Analysis of Static and Fatigue Damage in Aluminium/GFRP Hybrid Composites

Ahmad Saddy Mohamad Al-Azzawi

A thesis submitted for the degree of Doctor of Philosophy (Ph.D.) in Mechanical Engineering at Cardiff University.

Cardiff

United Kingdom

April 2017

Abstract

This study has focused on investigating the initiation, propagation and effects of damage in fibre-metal laminates (FMLs) specifically Glare® 4B under buckling, postbuckling and high cycle fatigue through the use of novel numerical and experimental techniques.

In terms of numerical analysis, a 3D user-defined cohesive zone model (CZM) has been generated to simulate delamination initiation and growth in specimens under static compressive stresses, using the software Abaqus. The generated models have been validated using a comprehensive literature review in order to gather reliable mechanical properties for the Glare® material constituents. Following this, a modified cohesive zone model (CZM) based on a trapezoidal traction-separation law has been developed by the author to simulate damage evolution under high cycle fatigue loading. This model was implemented through a user-written VUMAT subroutine working through the interface of Abaqus/Explicit software. This model is able to simulate elastic-plastic interfacial damage behaviour and as such is suitable for ductile adhesives including toughened epoxy unlike bilinear cohesive zone models which can only accurately simulate damage in brittle adhesives. This makes it suitable for modelling any material interface which incorporates ductile adhesives.

The numerical buckling results were validated using a series of experimental tests conducted on Glare® 4B specimens containing splice and doubler features in addition to flat specimens containing artificial circular delamination manufactured by Airbus Germany, demonstrating the ability of the models developed to predict the onset and propagation of damage. Experimental fatigue tests were then implemented on Glare® 4B specimens containing splice and doubler features manufactured in-house, to

obtain fatigue life for these types of joints, with fatigue parameters extracted from literature on similar grades of Glare® used to validate the trapezoidal traction-separation law based cohesive zone model. Static tests were monitored using Digital Image Correlation (DIC) to provide full-field displacement data and Acoustic Emission (AE) for the detection and location of the damage using traditional AE analysis and novel Delta-T techniques respectively, with Acoustic Emission (AE) using traditional AE analysis technique being used for damage detection under fatigue loading.

Finite element models were also generated to model the buckling and postbuckling behaviour of Glare specimens containing splice and doubler joints and showed good agreement with experiments in terms of in-plane and out-of-plane displacements. In experiments, artificial delaminations representative of those which could potentially be generated during manufacturing had a negligible effect on the compressive strength of specimens. Acoustic Emission (AE) was successfully used to detect and locate damage initiation and propagation under buckling loads.

Of particular importance in this body of work are the implementation of a trapezoidal traction separation model to predict the initiation and propagation of damage in elastic-plastic materials such as the resin used in the Fibre Metal Laminate Glare under high cycle fatigue and the detection and location of this damage using a bespoke mapping algorithm for the interpretation of Acoustic Emission data.

Keywords: FML, Glare, fatigue, buckling, postbuckling, damage modelling, delamination, Acoustic Emission (AE), Digital Image Correlation (DIC)

Declaration

This work has not previously been accepted in substance for any degree and is not currently submitted in candidature for any degree.

Signed Date

Statement 1

This thesis is being submitted in partial fulfilment of the requirements for the degree of Ph.D.

Signed Date

Statement 2

This thesis is the result of my own independent work/investigation, except where otherwise stated. Other sources are acknowledged by explicit references.

Signed Date

Statement 3

I hereby give consent for my thesis, if accepted, to be available for photocopying and for inter-library loan, and for the title and summary to be made available to outside organisations.

Signed Date

Acknowledgements

I would like to make my great gratitude to my academic supervisors Prof Carol Featherston, Dr Luiz Kawashita and Dr Rhys Pullin for their guidance, immense support and patience throughout my work. I would also like to thank Dr Matthew Pearson, Dr Mark Eaton and Dr John McCrory for their advice and help. My thanks also to the technical staff at Cardiff School of Engineering especially Garry Shipley, Ian King, Richard Rogers, Paul Leach, Steffan Jones and Harry Lane for their technical support throughout my experimental work.

Further gratitude and appreciation is expressed to my sponsor (Iraqi Ministry of Higher Education and Scientific Research/ Babylon University) for funding my study and giving me this unique opportunity.

Dedication

I dedicate this work to the spirit of the Prophet Mohammad, Fatima Al-Zahra and the infallible Imams (AS).

I dedicate this work to the spirit of my mother and my father who spent their life in raising me with compassion and tenderness and I feel that they are still supporting me with their praying.

I dedicate this thesis to my wife for her great patience, encouragement, understanding and support during the hard years of living away from home without which completion of this research wouldn't have been possible.

I dedicate this work to my lovely son Hussein and my beautiful daughter Jana for giving me the hope and helping me to keep smiling throughout my hard times during study.

Finally I would also thank my brothers and my sisters and the rest of my family who support me and are always pushing me forward, I would like to thank my friends for giving me advice over the years.

Table of Contents

Nomenclature

Symbol or Acronym	Meaning	Units
2D	Two-dimensional	
3D	Three-dimensional	
a	Crack length	mm
Arall	Aramid Reinforced ALuminium Laminates	
C	Modified Paris law multiplier	
CFRP	Carbon Fibre Reinforced Polymer	
CZM	Cohesive Zone Model	
$\mathrm{d}a/\mathrm{d}N$	Crack growth rate	mm/cycle
D_{e}	Damage evolution variable	
D_{f}	Fatigue damage variable	
D_{i}	Damage initiation variable	
D_{rate}	Fatigue damage after every time step (d_t)	
D_{s}	Static damage variable	
D_{t}	Total damage variable	
ΔG	Strain energy amplitude	N/mm
E	Young's modulus	MPa
FE	Finite Element	
FEA	Finite Element Analysis	
FML	Fibre Metal Laminate	
FRP	Fibre Reinforced Polymer	
$\emptyset$	Power law parameter	
G	Elastic shear modulus	MPa
G_a	Strain energy release rate amplitude	N/mm
G_{I}	Energy release rate for mode I loading	N/mm
G_{IC}	Mode I fracture energy	N/mm
G_{II}	Energy release rate for mode II loading	N/mm
G_{IIC}	Mode II fracture energy	N/mm
G_{max}	Maximum strain energy in mode II	N/mm
G_{TC}	Total fracture energy	N/mm
GFRP	Glass Fibre Reinforced Polymer	
Glare	Glass fibre Laminate Aluminium Reinforced Epoxy	
K	Cohesive stiffness	$\mathrm{N/mm^3}$
$L_{\mathrm{I.P}}$	Element characteristic length	mm
LEFM	Linear Elastic Fracture Mechanics	
m	Modified Paris law exponent	
ML	Metal Laminate	
MSD	Multiple-site damage	
N	Number of fatigue cycles	cycle
N_{f}	Number of fatigue cycles to failure	cycle
P_{I}	Applied load in mode I	kN
P_{II}	Applied load in mode II	kN
PTFE	Polytetrafluoroethylene	
R	Stress ratio	
S_{12}	In-plane shear strength	MPa
σ	Current stress for the cohesive law	MPa

σ_{I}	Mode I traction stress	MPa
σ_{II}	Mode II traction stress	MPa
σ_{o}	Yield stress for the cohesive material	MPa
SDEG	Scalar stiffness degradation variable	
SDV	Solution-dependent state variable	
SG	Back-face strain gauge	
t	Time	s
UD	Uni-directional	
U_{I}	Mode-I separation displacement	mm
U_{II}	Mode-II separation displacement	mm
U_x	Displacement along the x-axis	mm
U_y	Displacement along the y-axis	mm
X_{C}	Fibre direction ultimate compressive strength	MPa
X_{T}	Fibre direction ultimate tensile strength	MPa
Y_{C}	Transverse direction ultimate compressive strength	MPa
Y_{T}	Transverse direction ultimate tensile strength	MPa
t_{f}	Failure time	s
ω	Frequency	Hz

Chapter 1 - Introduction

1.1 Overview

This thesis includes experimental and numerical investigations on fibre-metal laminate structures containing artificial delaminations representative of those which might arise either during the manufacturing process, for example in trapping additional materials whilst manufacturing a joint, or in service due to impact. Fibre metal laminates provide a potentially attractive alternative to metals and fibre composites in applications such as aerospace structures. However, due to their additional complexity they have significantly more failure modes whose effect on load carrying capability must be understood and be capable of being predicted in order for them to be used optimally in aircraft design. The work presented here focuses on the development of models which enable the prediction of the behaviour of these materials when subject to different types of loading including quasi-static compression and tension-tension fatigue representative of in-service loading that are essential for design purposes. These models are validated using a series of tests on specimens supplied by Airbus and therefore representative of the manufacturing processes used in industry, supplemented by further specimens manufactured in-house.

1.2 Background

Aerospace manufacturers are continuing to focus their attention on the use of enhanced composite materials which are lightweight and durable, for the fabrication of the primary parts of an aircraft [1]. Fibre Metal Laminates (FMLs) are one family of composites which are increasingly used in industrial applications. Of these GLARE® (Glass fibre Reinforced Aluminium) has recently been incorporated into the fuselage

skin of the Airbus A380 and is of interest due to its high fatigue tolerance, specific strength and stiffness, and resistance to impact and lightning strikes [2]. The first FML, ARALL was manufactured in 1945. ARALL comprises aramid fibre/epoxy laminate and aluminium-alloy and was developed and used to manufacture the Fokker F-27 aircraft wing structure. Following this, in 1987, Delft University of Technology developed the glass fibre-reinforced aluminium laminate (Glare®), which is manufactured from alternating metallic aluminium sheets and glass fibre reinforced composite layers [1]. Glare® offers a 15-30% reduction in specific weight compared with aluminium and has advantages over CFRP's including improved impact, fire and corrosion resistance and increased damage tolerance [3]. Its commercial use has increased progressively and applications include the A380 fuselage, the ECOS3 blast-resistant Unit Load Device (a freight container designed to contain explosion and fire), the Learjet 45, the cargo floors of the Boeing 737, and the cargo doors of the latest models of the C-17 Globemaster III. Despite their advantages, however, FMLs present additional challenges in terms of understanding the increased number of damage mechanisms arising both during manufacture and in operation. In order to manufacture large panels there is a need to introduce joints. For a typical metal sheet of thickness between 0.3 mm and 0.4 mm the maximum width of material is normally 1.65 m, whilst a fuselage skin panel requires sheets of up to 2 m or wider. Aluminium sheets are therefore positioned side by side with gaps in between. The gaps are staggered through the thickness to prevent loss of strength with the fibre layers providing load transfer; this is known as 'splicing'. Joints can also be strengthened by adding additional layers externally or internally to reduce stresses, and these are known as 'doublers'. Examples of both types of joints are shown in Figure 1.1.

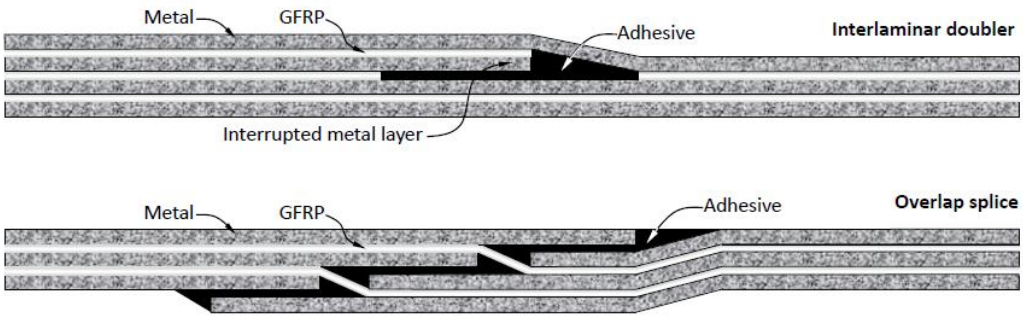

Figure 1.1: Schematic representations of the doubler (top) and splice (bottom) joining techniques for Glare® (adapted from [1]).

Although solving size restrictions, these features involve further manufacturing processes and therefore the possibility of introducing defects such as delaminations. This research examines potential damage arising from this manufacturing process, as well as from potential in-service damage. A detailed understanding of the damage process under an applied load, especially buckling and high cyclic loads is needed in order to use FML extensively in engineering applications. In this research numerical and experimental investigations of delamination initiation and propagation in adhesive joints such as splices and doublers (Figure 1.1) are carried out under both quasi-static compression and constant high cycle tension-tension fatigue stresses. Glare® specimens for the buckling tests were supplied by Airbus Germany and specimens for fatigue tests were manufactured in-house by the author.

1.3 Methodology

This study concentrates on the investigation of interlaminar delamination in the adhesive joints (splices and doublers) of Glare® 4B laminate structures specifically in metal-fibre interfaces under both buckling and constant high cycle fatigue stresses in addition to delamination and buckling behaviour of structures containing an initial circular delamination defect. These investigations were implemented using both numerical and experimental methods. Numerical analysis was carried out utilising the software Abaqus/Explicit 6.12 and included two parts; firstly, using a 3D user-defined

cohesive zone model (CZM) to simulate delamination initiation and growth and bulk damage models to predict failure in the continuum materials of specimens under static compressive stresses. The material properties for the model were obtained from a comprehensive literature review. Secondly, using a 2D modified CZM based on a trapezoidal traction-separation law developed by the author to simulate damage evolution in Glare® fibre-metal laminate specimens containing adhesive joints under high cycle fatigue loading. This model was implemented through a user defined VUMAT subroutine working with the interface of Abaqus/Explicit software. The numerical fatigue results were validated using experimental data from Alderliesten [4]. Experimental work again included quasi static compression and high cycle fatigue testing and they were monitored using a combination of digital image correlation (DIC) to provide full-field displacement information and Acoustic Emission (AE) to monitor and detect localised damage. SEM micrographs were also used to characterise the damage in these laminates and provide further validation alongside the AE results.

1.4 Research aims and objectives

The work described in this thesis aims to:

a) Develop novel modelling techniques to enable the prediction of the initiation and propagation of damage in the FML Glare® arising both during manufacture and in-service loading. Validate these techniques using experimental data.

b) Apply these techniques to examine the effect of such damage on the performance of FML structures under typical in-service loading including buckling and high cycle fatigue.

The objectives of this research can be summarised as follows:

1. Manufacture Glare® 4B coupons by hand layup and using standard autoclave techniques.

2. Incorporate doubler and splice features during the layup process.

3. Conduct buckling and fatigue tests to identify buckling and postbuckling behaviour and fatigue life.
4. Develop 3D FE models to predict the growth of artificial delaminations designed to reflect manufacturing defects in adhesive joints (splices and doublers) and impact damage under compression loading.
5. Develop 2D FE models to predict delamination initiation and growth in adhesive joints (splices and doublers) under high cycle fatigue loading.
6. Validate the predicted numerical results with the experimental results for both static buckling and fatigue.

1.5 Statement of novelty

This work investigates the ability to detect and monitor the progression of damage within fibre-metal laminates (Glare®) using both experimental and numerical techniques. The work focuses on studying delamination in Glare® 4B laminate under buckling and high cycle fatigue loads. The novelty of this research is highlighted below:

- High fidelity three-dimensional FE models were generated in order to study buckling and postbuckling behaviour of Glare® 4B laminates in complex structures.
- These FE models were successfully predicted delamination in Glare® fibre-metal laminate specimens containing splice joints, while those containing doubler features did not exhibit delamination under compression.
- The FE models are able to predict the effect of plasticity on buckling and postbuckling characteristics of Glare® laminates.
- The FE models successfully predict a number of different damage mechanisms in GFRP layers using a modified Hashin theory including matrix and fibre compression in addition to shear damage.
- Imperfection sensitivity is considered. Firstly, the effect of geometric imperfections

based on the first eigenmode of the specimen (scaled to have a maximum amplitude equal to that measured in the corresponding real specimens) and secondly, load eccentricity, which is accounted for by the introduction of an asymmetrical linearly distributed in-plane displacement component superimposed on the cross-head displacement. The introduction and study of the effects of these imperfections in the context of a fibre metal laminate joint is unique.

- The acoustic emission Delta-T technique was successfully used for the first time to monitor the position and level of damage propagation on FML structures including internal features.
- In experiments artificial delaminations representative of those which could potentially be generated during manufacturing had a negligible effect on the compressive strength for both splice and doubler specimens, a finding which was replicated both experimentally and numerically.
- The effect of damage representative of that caused by impact on the buckling and postbuckling behaviour of Glare® fibre-metal laminate was successfully examined using both 3D FE models and experimental tests.
- A series of Glare® 4B specimens were manufactured by the author (the first time in the UK for research purposes). These specimens were used to examine the interlaminar damage behaviour of splice and doubler joints included in Glare® laminate structures under high cycle fatigue loading.
- A novel cohesive zone model (CZM) incorporating a mixed mode trapezoidal traction-separation law has been developed to simulate delamination growth in Glare® specimens containing both splice and doubler features under both quasi-static and high cycle fatigue tension loadings.
- The fatigue life of Glare® specimens containing both splice and doubler features was determined experimentally through high cycle fatigue tests.

- AE results were successfully used to validate both static and fatigue results in terms of delamination propagation detection via high cumulative energy events and different amplitudes ranges.

1.6 Published outputs

As a result of this research, a total of three journal papers and seven conference papers have been written.

1.6.1 Journal papers

- Ahmad S.M. Al-Azzawi, J.P. McCrory, L.F. Kawashita, C.A. Featherston, R. Pullin, K.M. Holford. Buckling and Postbuckling Behaviour of Glare® Laminates Containing Splices and Doublers. Part 1: Instrumented tests, Composite Structures 2017.
- Ahmad S.M. Al-Azzawi, L.F. Kawashita, C.A. Featherston. Buckling and Postbuckling Behaviour of Glare® Laminates Containing Splices and Doublers. Part 2: Numerical Modelling, Composite Structures 2017.
- Ahmad S.M. Al-Azzawi, L.F. Kawashita, C.A. Featherston. Fatigue Damage in Fibre Metal Laminate Adhesive Joints: Numerical and Experimental Investigation, under review, Composites Science and Technology 2017.

1.6.2 Conference papers

- Ahmad S.M. Al-Azzawi, J.P. McCrory, L.F. Kawashita, C.A. Featherston, R. Pullin, K.M. Holford. Delamination Characteristics Of Splices And Doublers In Glare® Laminates During Buckling, In 11th World Congress On Computational Mechanics (WCCM XI). July 20 - 25, 2014: Barcelona, Spain.
- Ahmad S.M. Al-Azzawi, J.P. McCrory, L.F. Kawashita, C.A. Featherston, R. Pullin, K.M. Holford. Buckling And Postbuckling Behaviour Of Glare® Laminates Containing Splices And Doublers: Experimental And Numerical Investigations, in 3rd Int.

Conference on Buckling and Postbuckling Behaviour of Composite Laminated Shell Structures. 25-27 March 2015: Braunschweig, Germany.

- Ahmad S.M. Al-Azzawi, L.F. Kawashita, C.A. Featherston. Delamination Characteristics Of Glare® Laminates Containing Doubler And Splice Features Under High Cycle Fatigue Loading, in the 24th UK Conference of the Association for Computational Mechanics in Engineering. 31 March – 01 April 2016: Cardiff University, UK.
- Ahmad S.M. Al-Azzawi, L.F. Kawashita, C.A. Featherston. The effect of circular delaminations on the buckling and postbuckling behaviour of Glare® laminates under compression, in the 11th Int. Conference of Advances in Experimental Mechanics. 5-7 September 2016: University of Exeter, UK.
- Ahmad S.M. Al-Azzawi, L.F. Kawashita, C.A. Featherston. A constitutive model for elastic-plastic behaviour and delamination damage in fibre metal laminates, Proceedings of the 25th UKACM Conference on Computational Mechanics, 12 –13 April 2017, University of Birmingham, United Kingdom.
- Ahmad S.M. Al-Azzawi, L.F. Kawashita, C.A. Featherston. Modelling Fatigue Damage in Fibre Metal Laminate Adhesive Joints, accepted for presentation at 21st International Conference on composite Materials (ICCM-21) in Xi'an, China, 20-25 August 2017.
- Ahmad S.M. Al-Azzawi, M.S. Al-Saymaree, L.F. Kawashita, C.A. Featherston. Quasi-static Damage in Fibre Metal Laminate Adhesive Joints: Experimental Investigations, accepted for presentation at 20th International Conference on Composite Structures (ICCS-20), Paris, France, 4-7 September 2017.

1.7 Outline of thesis

This chapter provides background information on the subject of the research. The aims and objectives of this research have been identified. Also an outline of the experimental

and numerical methods used in the analysis in addition to the monitoring techniques used in this work and the novelty contained within the research have been described. The following chapters contain the details of this research.

Chapter 2 includes an overview of the background researches carried out by others to investigate the buckling, postbuckling and fatigue behaviour of fibre composite laminates and fibre-metal laminates structures containing adhesively bonded joints. This includes work to determine the effects of defects encountered during experiments on such structures including geometric imperfections and load eccentricity, in addition to the effect of impact damage represented by insertion of artificial circular delaminations on the buckling and postbuckling characteristics of FMLs far-field structures.

Chapter 3 provides information on the manufacturing processes, materials used and the techniques used for monitoring the experiments including Digital Image Correlation, Acoustic Emission and Scanning Electron Microscopy instrumentations and techniques.

Chapter 4 provides a description of the experimental investigations undertaken to determine the effect of artificial delaminations representative of those originating from manufacturing on two different types of joints (doublers and splices) as well as the effect of circular delaminations, representative of those which might occur due to impact on buckling and postbuckling behaviour.

Chapter 5 discusses the development of 3D finite element models incorporating a bilinear cohesive zone model and continuum (bulk) material damage models to examine the progressive damage and failure behaviour of the specimens tested in Chapter 4.

Chapter 6 presents the development of a user-defined code (VUMAT) implemented as a subroutine in Abaqus/Explicit. This code is written in FORTRAN programming language and is based on a cohesive zone model using a traction-separation law with

a trapezoidal shape. This model enables prediction of the damage at the interfaces of elastic-plastic materials (in this case at the interfaces between the aluminium and GFRP layers of the Glare® laminates) under both quasi-static and high cycle fatigue loading.

Chapter 7 describes modelling developed to predict delamination growth in Glare® laminates again containing adhesively bonded joints (splices and doublers) under high cycle fatigue loading using the (VUMAT) code developed in Chapter 6, The numerical results from this code are validated with experimental fatigue results from Alderliesten [4].

Chapter 8 outlines the conclusions and future work.

Chapter 2 - Background and Theory

2.1 Introduction

This chapter reviews the main experimental and numerical studies that have been undertaken to investigate the buckling, postbuckling and fatigue behaviour of fibre-metal laminate (FML) structures and the effect of delamination damage originating from either manufacturing defects or impact on this behaviour. Of particular interest is work carried out on specimens with adhesively bonded joints and those looking at the effect of circular delaminations typical of the damage caused during impact. Figure 2.1 shows a block diagram of the structure for this chapter.

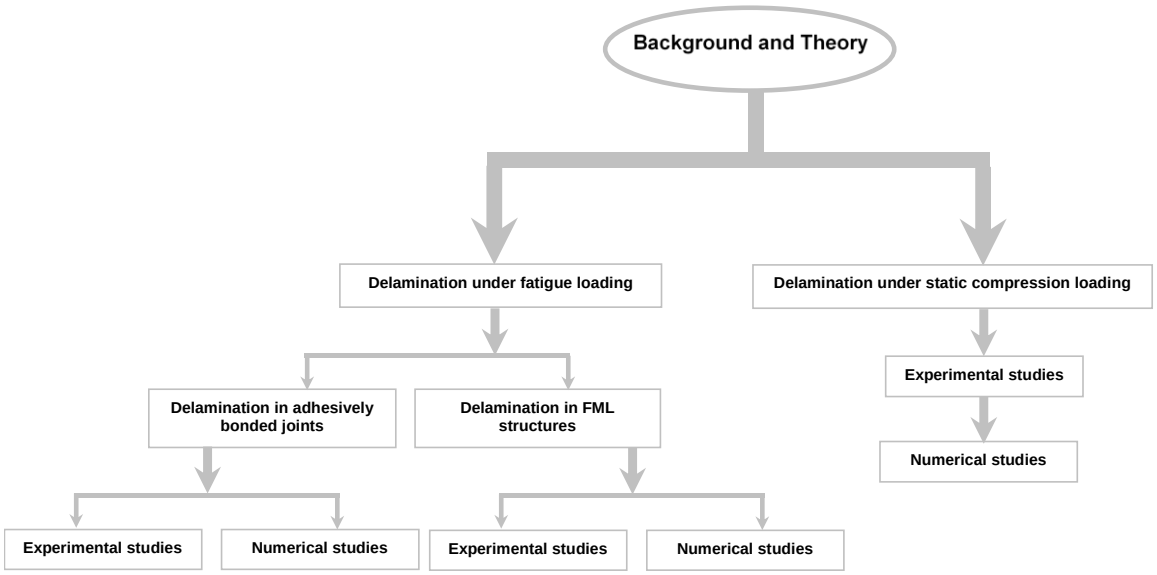

Figure 2.1: Structure of background and theory chapter.

2.2 Delamination of FMLs under in-plane compression (buckling)

2.2.1 Experimental studies

Many experimental studies have been conducted in order to study the effect of delaminations on the buckling behaviour of composite laminates and more recently

fibre-metal laminate materials.

The effect of delaminations on fibre composites was studied by Clarke and Pavier [5, 6] who examined the buckling behaviour of axially loaded composite plates and found that under compressive load the presence of initial delaminations extending across the specimens width and over 1/5 of the specimens length had a significant influence on their strength. Delamination growth during the buckling and post-buckling of HYE-3574 OH carbon/epoxy composites with artificial delaminations was also studied experimentally by Gu and Chattopadhyay [7]. The buckling mode was found to be closely related to the location and length of the delamination. Kutlu and Chang [8] investigated the compressive response of T300/976 composite panels containing multiple delaminations. Both flat and cylindrical panels with various ply orientations were tested. Experimental results demonstrated that delamination propagation significantly affected the postbuckling response in both cases, particularly in the case of multiple delaminations. The effect of delaminations on the postbuckling behaviour of CFRP composite laminated rectangular plates was also studied experimentally in [9]. This study found that after buckling occurs, delaminations can be expected to grow due to high interlayer shear stress. This growth is likely to be rapid and extensive before failure. In [10] experimental and numerical studies on the buckling of GFRP laminates containing a single delamination were carried out on rectangular plates. Artificial delaminations were introduced between fabricated laminate plies using embedded rectangular PTFE films of 13 μm thickness. Different fibre orientation angles were found to affect the critical buckling load, which was greatest for the 0° fibre orientation angle. This was the case for all aspect ratios and widths of delaminations.

In terms of the buckling and postbuckling behaviour of flat and curved fibre-metal laminate panels these were first investigated by Verolme [11-13]. Results showed that FML panels exhibited similar buckling and postbuckling behaviour to their metallic counterparts apart from the fact that the damage in the FMLs started with a local delamination, while the corresponding metallic panels exhibited plastic deformation.

Botelho *et al.* [14] studied the compressive properties of the hybrid composites Glare® and Caral and the polymer composites CFRP and GFRP. Results revealed that the axial compressive strength for unidirectional polymer composites was mainly controlled by the buckling modes of the fibres [15]. The compressive strength of fibre-metal laminates (FMLs) on the other hand which was much lower than that of the CFRP was limited due to the weak interface between the composite layers and the aluminium alloy. SEM micrographs showed damage at this interface leading to bucking of the corresponding aluminium layer. Mania and York [16] studied the buckling behaviour and load carrying capacity of thin-walled FML open cross-section profiles subjected to static axial compression loading. Uni-axial compression buckling strengths obtained using semi-analytical and finite element methods were compared with experimental results. Laminate tailoring strategies, based on the use of buckling factor contours mapped onto lamination parameter design spaces, were used to improve the compressive buckling load capacity for short columns of open cross-section. Kolakowski *et al.* [17] investigated the elasto-plastic buckling of thin-walled FML short columns/profiles subjected to axial uniform compression. They incorporated transverse shear effects and elasto-plastic material models based on different strain-hardening plasticity theories into their models and were able to demonstrate that the buckling modes in the elastic and elastic–plastic ranges are not always identical. Kamocka and Mania [18] considered both micro and macro mechanics to study flat plates manufactured from FMLs. The properties of these specimens were determined using the Rule of Mixtures and the analytical results were verified by experimental tests. After demonstrating the sensitivity of the performance of these structures to material properties the authors highlighted the need for accurate sub-laminate material data. McCarthy *et al.* [19] performed an experimental analysis at microscopic scale to monitor the progression of damage including buckling in pin-loaded fibre-metal laminates. Damage was investigated using SEM micrographs taken at different load levels up to the failure load. Different damage mechanisms were observed for instance

at 90% of the failure load as shown in Figure 2.2, plastic deformation in the aluminium layers was noticed in addition to delamination at the interface between the outer aluminium layers and their adjacent 0° GFRP layers. Delamination was also noticed between the 0° and 90° fibre plies with fibre kinking progressing to form micro-buckles in the 0° fibre plies eventually leading to fibre breakages in some of these plies. Experimental studies conducted by Remmers and de Borst [20] presented delamination buckling in 'Glare® 2' on a microscopic level both experimentally using Scanning Electron Microscopy (SEM) technique and numerically using the interface element model given by Kachanov [21].

Incorporation of the effects of geometric imperfections and load eccentricity on the buckling and postbuckling behaviour of structures is important in obtaining an accurate prediction of their response. The effect of such defects on composite laminates has also been studied by many researchers. However, comparatively less has been done to investigate their effects on fibre-metal laminates. Koiter [22] examined the effect of geometrical imperfections on the elastic buckling load of a cylindrical shell under uniaxial compression. This work was extended to both cylinders and spheres by Hutchinson [23] for loadings that produce biaxial membrane stresses. It was found that reducing the transverse membrane stress component leads to an increase in the axisymmetric initial imperfection (the normal deflection of the middle surface of the unloaded shell) and this behaviour is similar for both cylindrical and spherical shells. Hilburger and Starnes Jr. [24] showed that non-linear analysis can be used to determine accurate, high-fidelity design knockdown factors that can be used for predicting composite shell buckling and collapse loads in the design process. This can be achieved by considering traditional imperfections (geometric shell-wall mid-surface imperfections) and non-traditional imperfections (shell-wall thickness variations, local shell-wall ply-gaps associated with the fabrication process, shell-end geometric imperfections, non-uniform applied end loads, and variations in the boundary condition

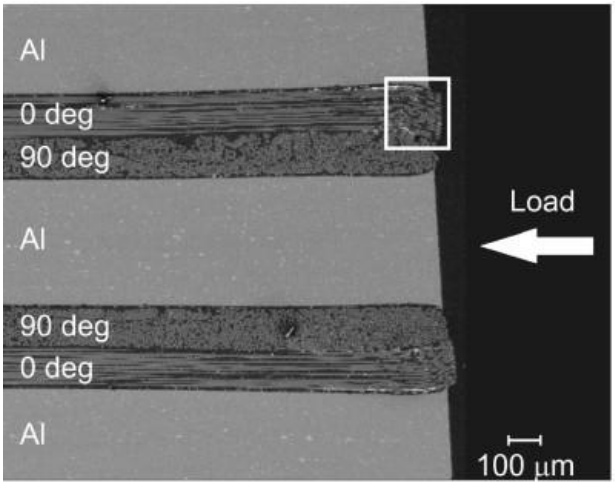

(a)

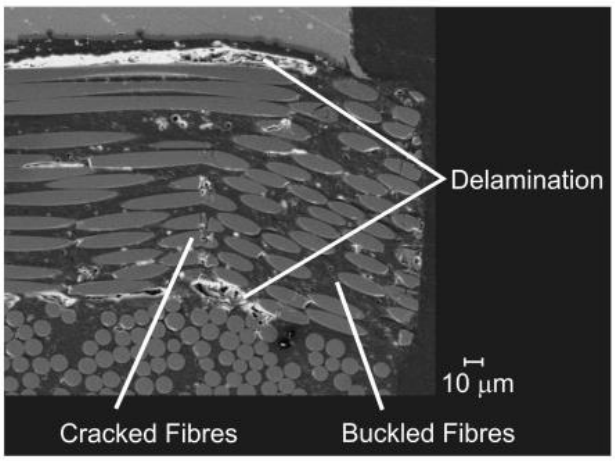

(b)

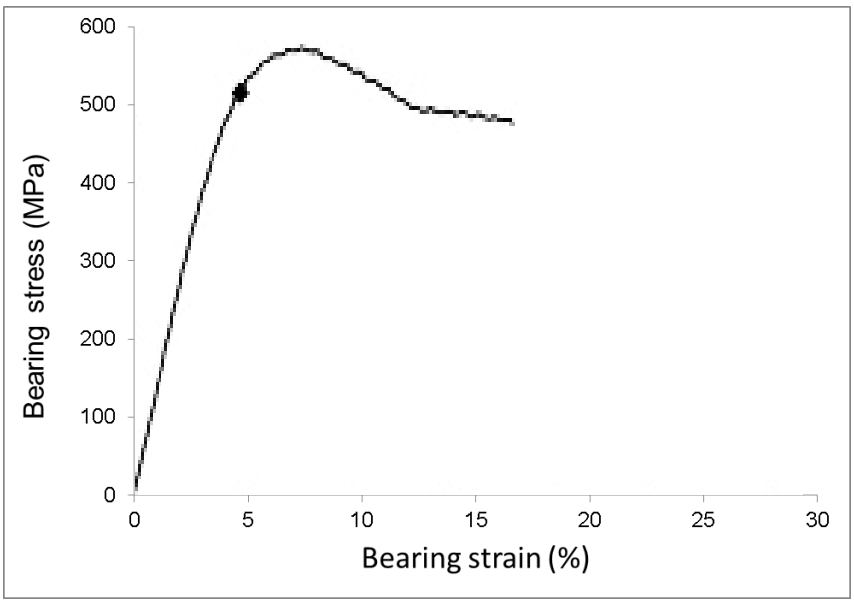

(c)

Figure 2.2: SEM micrograph of a bearing specimen (w/d = 6, e/d = 6) at 90% of the failure load: (a) 60× magnification, (b) 400× magnification (c) position at which the micrographs were taken on the bearing stress-strain curve (Figure reproduced from[19]).

including the effects of elastic boundary conditions) which could be combined to form the basis of a generalised imperfection signature for a composite shell that includes the effects of variations or uncertainties in the shell-geometry, fabrication-process, load-distribution and boundary stiffness parameters. Tsouvalis *et al.* [25] investigated the effect of initial imperfection magnitude on the buckling loads of cylinders under external hydrostatic pressure and found a good correlation between experimental and modelling results, and Featherston [26] performed a similar study on a simple aerofoil under combined shear and in-plane bending. In [24] Hilburger reports the results of experimental and analytical studies of the effects of initial imperfections on the buckling response and failure of unstiffened thin-walled compression-loaded graphite epoxy cylindrical shells, results that include the effects of traditional and non-traditional imperfections and uncertainties on the nonlinear response characteristics. Experimental and analytical investigations were conducted to examine the effects of the inherent mechanical couplings exhibited by fully anisotropic (*i.e.* unsymmetrical) graphite/epoxy laminates on the buckling loads and mode shapes of short rectangular plates in [27]. The results indicated that these couplings, especially those which relate stretching and bending behaviour, cause out-of-plane deflections prior to buckling and hence reduce the buckling load significantly. Eglitis *et al.* [28] performed experimental and numerical studies on the buckling of concentrically and eccentrically compressed composite cylinders. Although using values of knockdown factors which were estimated from linear eigenvalue analyses, both experimental and numerical results showed good correlation.

With respect to FMLs, the study completed by Mania *et al.* [16] on buckling behaviour and load carrying capacity of thin-walled FML open cross-section profiles, was extended in Mania *et al.* [17, 29] to investigate the buckling and postbuckling response of different FML profiles, with further work [30] highlighting the need to consider the effect of imperfections on the buckling and postbuckling behaviour in order to accurately predict the consequent reduction in performance.

In terms of the effects of joints, buckling in adhesively bonded GFRP composite flanges containing splice joints and with an initial debond were experimentally investigated by Kwon and Kim [31]. Although the flange length and width were found to affect the buckling behaviour strongly, their influence on debond crack initiation (which was seen to originate in the corners of the free edge of the buckled flange, where the highest peel stresses are found due to the post-buckled flange deformation) was only slight. The consequent growth of the debond crack was found to be strongly dependent on its initial length but weakly dependent on flange width.

In this study we extended the work of previous authors, focusing on examining the effect of delamination damage on the buckling and postbuckling characteristics of Glare® FML specimens containing two different types of joints (doublers and splices) based on a series of experiments. Also, Acoustic Emission and in particular the Delta-T source location technique, in combination with DIC and SEM monitoring systems were used for the first time to study the damage behaviour of FML structures.

2.2.1 Numerical studies

A number of numerical studies have also been performed in order to understand the buckling and postbuckling behaviour of composite panels containing delaminations. Delamination initiation and growth under compressive loading was investigated numerically for slender composite laminates using FE models based on the use of cohesive elements by Wang *et al.* [32]. They concluded that for composite laminates with embedded delaminations the propagation shape is affected by the depth of the

delamination, rather than its size. Under an axial compressive load, the damage propagation width was found to expand as the depth increased from 10% to 25% of the total specimen thickness. Mohammadi *et al.* [33] also developed a cohesive zone model to predict delamination propagation in laminated composites containing single and multiple through-the-width delaminations during buckling. They found that for specimens with multiple delaminations damage propagation was unstable causing a sudden drop in the load carried accompanied by a global buckling load which was much lower than for a similar specimen with a single delamination. Wang and Zhang [34] developed a B-spline finite strip method to study the buckling, postbuckling and delamination propagation in debonded composite laminates under compression. Extensive numerical studies were conducted to validate their theory [35]. The study concluded that unstable delamination propagation was often caused by mode-I fracture while mode-II fracture led to stable delamination growth in the cases examined. Chirica and Beznea [36] developed an FE model to predict the buckling behaviour of composite plates with a central elliptical delamination. They found that the aspect ratio of the delamination had a significant effect on the relationship between in-plane loading and displacement. Akbarov *et al.* [37] developed a three-dimensional model using the theory of viscoelasticity for anisotropic bodies to study delamination around two types of artificial crack (band-crack, edge-crack) introduced into a rectangular plate under compressive loading. They concluded that the mode of buckling delamination around the two types of cracks depended only on the initial infinitesimal imperfections of the edge-surfaces of these cracks. Eaton [38] investigated the propagation of delaminations in simply supported composite panels under compression using an FE model and then validated the results experimentally using acoustic emission to monitor the initiation and propagation of damage. The effect of the mechanical couplings exhibited by fully anisotropic graphite/epoxy laminates on the buckling loads and mode shapes of composite panels were studied by conducting analytical investigations by [27]. The numerical results correlated well with experimental results conducted by the

same authors and discussed in the previous section. Further analytical models have been developed by [8] enabling the prediction of the compression response of laminated composite panels containing single and multiple delaminations.

In terms of FMLs, less work has been done. Obrzalek and Vrbka [39, 40] performed numerical studies on the buckling of FMLs and concluded that depending on the in-plane orientation and out-of-plane position of an artificial delamination, the buckling load can drop by up to 30% and 50%, respectively. They also found that the buckling and postbuckling behaviour of the plates was greatly affected by the delamination's geometrical shape. Furthermore, McCarthy *et al.* [41] developed a 3D FE model using Abaqus software to study delamination in fibre-metal laminate pin-hole joints. The model incorporated a three-dimensional continuum damage mechanics approach for the composite plies, a plasticity model for the aluminium layers and a delamination model between layers. Cohesive elements, which are part of the Abaqus software, were used in areas of the model where delamination was expected (such as the interfaces near the pin-hole). They found that delamination occurs between the layers immediately adjacent to the pin and remains localised in a small region surrounding the pin-hole (of the order of 1 mm from the hole's edge) throughout the analysis as shown in Figure 2.3. The joint is severely affected when compressive fibre damage initiates, resulting in very low residual stiffness and a long plateau region in the bearing stress–strain curve.

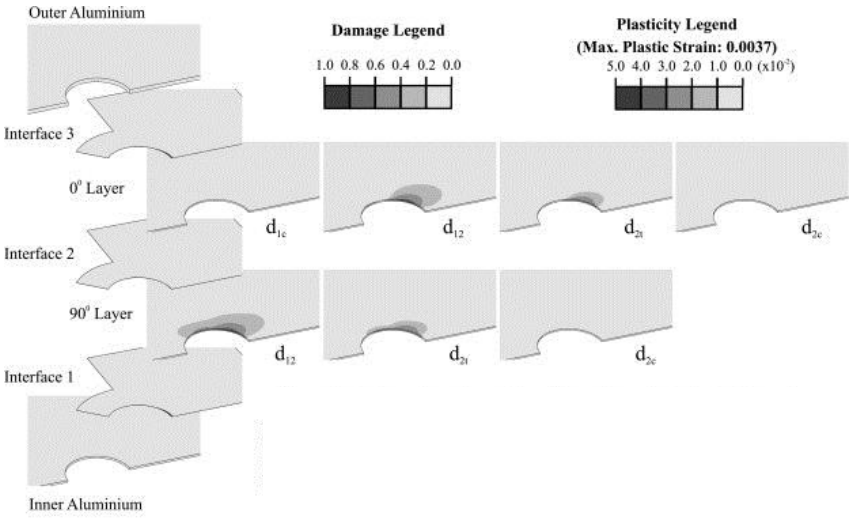

(a)

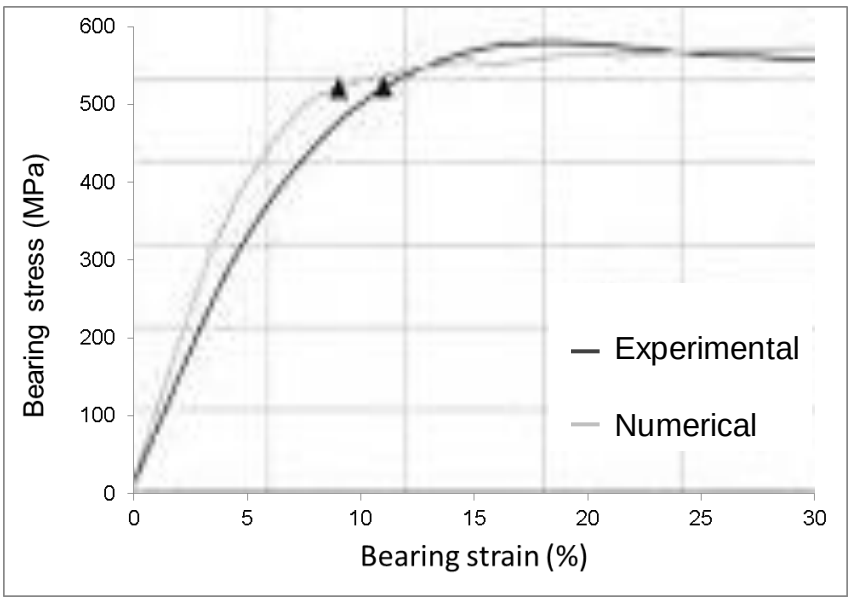

(b)

Figure 2.3: (a) Damage distribution in the various layers of the bearing specimen at 300 MPa bearing stress and 1.2% bearing strain (b) position of the micrographs taken on the bearing stress-strain curve (Figure reproduced from[41]).

Geometrical imperfections and load eccentricity have also been shown to have a significant effect on the buckling and postbuckling behaviour of composite laminates. This was confirmed by many researchers [24-26, 28, 42] who have developed FE models to correlate their experimental investigations mentioned in the previous Section on geometrical imperfections and load eccentricity on buckling properties. More recently, Degenhardt [43], Saullo [44] and Ismail [45] developed numerical

models for cylindrical shell structures introducing different types of geometrical and load imperfections. Singer *et al.* [46] showed that the buckling and postbuckling behaviour of a rectangular plate depended strongly on both in-plane and out-of-plane boundary conditions and that knockdown factors predicted by numerical analyses of the cylinders can be used to account for these effects. For design purposes, however, more accurate imperfection values such as experimentally measured geometric imperfections and load eccentricity [28] need to be adopted in order to ensure robust models.

Few researchers again have studied the effect of geometrical imperfection and load eccentricity on buckling and postbuckling behaviour of FMLs. Bi [47], used an elasto-plastic constitutive model to study the buckling and postbuckling behaviour of FMLs including Glare® considering the elasto-plastic deformation of the metal layers. The analysis was implemented using the classical nonlinear plate theory. A simplified three-dimensional rectangular plate model was used and the equations solved using the finite difference method. The effects of initial imperfections in the form of the first eigenmode with different amplitudes (0.05, 0.1 and 0.15 of the thickness) were numerically investigated. The authors concluded that by increasing the amplitude of the initial imperfection, the deflection of the plate increases reducing the stiffness prior to buckling. During postbuckling, the imperfection has a lesser effect than the plasticity. Mania *et al.* [17] investigated the buckling and postbuckling response of the FML profile/column analytically and numerically and compared the results with those found experimentally. They found that in practice structural imperfections decrease the real buckling load and analytical or FEM results should be used as an upper bound estimation. Wittenberg and de Jonge [48] studied Glare® plates subjected to unidirectional compression or shear. The authors proposed the application of correction factors to take into account the yielding of the aluminium and the magnitude of any imperfections.

In this thesis the buckling and postbuckling of a series of panels containing both splice

and doubler joint features with and without delaminations within the joints is studied using models developed in Abaqus/Explicit. Both delamination and bulk damage are considered using a combination of cohesive zone elements and bulk damage models. Geometric and load imperfections are incorporated. Results are validated based on the results of the experimental work.

2.3 Delamination in adhesively bonded joints

Delamination in adhesively bonded structures under fatigue loading has been studied by a number of researchers using a variety of different approaches. These include experimental and numerical studies which investigate delamination initiation and propagation. These studies are highly relevant to the understanding of delamination in FMLs so a literature review of the topic is presented here.

2.3.1 Experimental studies

Experimental studies can be divided into two types according to Crocombe *et al.* [49], namely 'total life' and 'initiation/propagation' studies.

2.3.1.1 Total life

A number of studies have been conducted using a total life or S-N curve method to examine the fatigue life of adhesive joints. In the total life method, specimens are tested under high cycle or low cycle fatigue loading until final failure. Tests can be repeated under different conditions including constant or variable amplitude stress, differing frequency and constant or variable load ratio R. The results are then presented as a graph of stress or load versus the number of cycles to failure to generate the well-known S-N curve or the fatigue life curve. Fatigue loading can be presented either in terms of maximum fatigue stress or maximum fatigue force, were the later can be calculated from quasi-static tests using ultimate tensile load [50] as follows:

$$F_{\max} = \rho * F_{\text{ultimate}} \tag{2.1}$$

where, $F_{\max}$ is the maximum fatigue load and ρ is the fatigue severity (for example if we apply fatigue load at 70% severity this means ρ is equal to 0.7) and F_{ultimate} is the ultimate tensile load. Most of the total life experimental studies performed have

Group 1: Exponential model Group 2: Power-law model

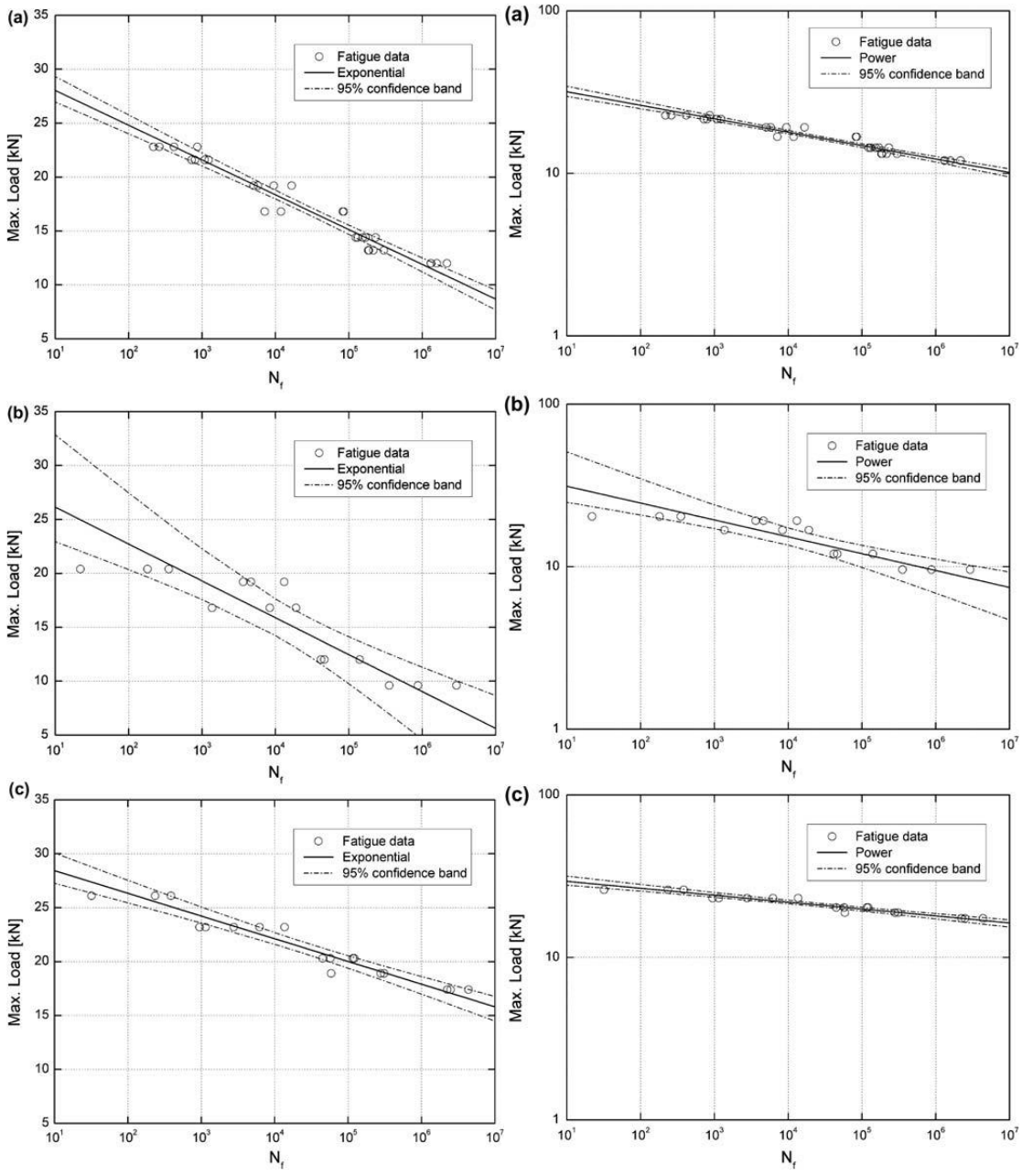

Figure 2.4: Experimental and numerical total fatigue life curves for adhesively bonded double-lap joints in GFRP specimens with R-ratios (a) $R = 0.1$,(b) $R = -1$, (c) $R = 10$ [54].

adopted a typical S-N curve approach based on maximum fatigue stress with constant load ratio R and constant frequency while other researchers such as [51-53] have explored the effects of changing mean stress and load ratio. The effect of load ratio on the total fatigue life of double-lap joints in GFRP specimens was presented by Vassilopoulos *et al.* [54]. Figure 2.4 shows a comparison of fatigue life curves from experimental results and those obtained from two numerical phenomenological linear regression models (exponential , group 1, and power law, group 2) for a number of different load ratios including tension ($R = 0.1$), compression ($R = 10$) and reversed loading ($R = -1$). Good correlation is seen between the numerical and the experimental fatigue life curve results for both group 1 and group 2 models for both tension and compression. However, for reverse loading where experimental results show significant scatter fatigue behaviour is not accurately modelled using either approach.

2.3.1.2 Crack initiation and propagation

Whilst many studies for evaluating the fatigue life of adhesive joints especially those based on un-notched specimens adopt the total life technique, other investigations have been conducted using the crack length measurement method. This method can be used for evaluating the fatigue life of geometries including adhesive joints by measuring crack initiation and growth along with the number of cycles to failure, with many different techniques used to make these measurements and also to try to distinguish between crack initiation and propagation regions. This review will provide an overview of experimental studies that have been conducted to achieve this.

Dessureault and Spelt [56] studied the effect of crack starting conditions on fatigue crack initiation and propagation. Fatigue tests were carried out on double cantilever beam specimens (mode-I), cracked lap shear specimens (mixed-mode I/II) and end notch flexure specimens (mode-II) with a load ratio of 0.1 and a frequency of 30 Hz. Crack initiation was studied using a microscope. The first visible micro crack in the fillet

was used to define the crack length. Three starting conditions including an intact fillet, a pre-existing crack and a fast mode-I pre-crack were considered. It was found that under mode-II and mixed mode conditions, the difference in crack initiation time for different starting conditions was negligible. In contrast, under mode-I conditions a pre-existing fatigue crack needed two or three times longer to initiate than a fast mode-I pre-crack. This was considered to be due to blunting of the crack tip or some self-toughening mechanism.

Crocombe *et al.* [49] tested aluminium-adhesive and composite-adhesive single lap joints with different configurations under fatigue loading at a load ratio of 0.1 and a frequency of 2 Hz. They employed the backface strain technique to inspect the damage initiation phase. It was found that for the joints with an intact adhesive fillet the damage initiation phase, even at high loads (50% of static failure load), occupied about half of the total fatigue life. Moreover, it was observed that removing the adhesive fillet of the joints eliminated the initiation phase and reduced the fatigue life. They also investigated the application of the backface strain technique and determined optimum gauge specification and location.

Quaresimin and Ricotta [57] studied the influence of overlap length and fillet corner geometry on the fatigue response of single lap joints composed of carbon/epoxy laminates bonded with an epoxy adhesive. Fatigue tests were conducted on the joints at a load ratio of 0.05 and a test frequency in the range of 10-15 Hz depending on the applied stress level. Fatigue damage evolution was monitored using visual and microscopic observations. A crack length of 0.3 mm was considered for the threshold value of crack initiation. The crack initiation phase was observed to be in the range of 20% to over 70% of the total fatigue life, depending mainly on the overlap length and stress level. It was found that the joints with shorter overlap length had a greater ratio of damage initiation to total fatigue life. Moreover, by increasing the overlap length, longer damage propagation life was achieved leading to a better fatigue performance of the bonded joints. The presence of a spew fillet (Figure 2.5) was found to make 25%

improvement in the fatigue strength. The crack growth rate was found to be very sensitive to the level of load and insensitive to the overlap length.

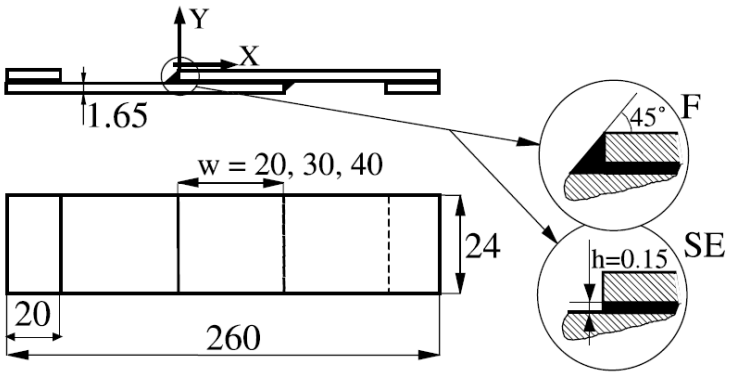

Figure 2.5: Geometry of single lap bonded joint (mm). SE, square edge joint; F, spew fillet joint [57].

Azari *et al.* [58] investigated the effect of starting condition (fatigue pre-crack and fillet) and testing approach (including force and displacement control) on the fatigue threshold of adhesively bonded joints. The fatigue threshold was defined as the maximum strain energy release rate that caused 10^6 mm/cycle crack growth rate. The effects of mode mixity and crack growth rate on the crack path and failure mode were studied. Cracked lap shear, asymmetric double cantilever beam and double cantilever beam joints were subjected to fatigue tests under both load and displacement control at a frequency of 20 Hz and load ratios of 0.1 and 0.5. It was found that the starting condition did not influence the fatigue threshold provided that the crack path was cohesive and not interfacial after crack initiation. Fatigue testing under displacement control was suggested as a more preferential testing approach in determining the fatigue threshold as it provided the same threshold and crack growth rate as those obtained from load control but more conveniently and in a shorter time. The crack path was observed to be dependent on the mode mixity and the crack growth speed with increasing the mode mixity and/or decreasing the crack growth rate driving the crack closer to the interface and making the bond strength highly sensitive to the interface bond strength. At higher crack growth rate and/or mode-I the crack path was driven

further from the interface and was consequently less sensitive to the interface condition. The relation between the crack growth rate and the crack path could not be attributed to environmental conditions since all tests were carried out in dry conditions (11-15% relative humidity). However, the authors provided two possible reasons for this relationship. One reason was that increasing the local mode mixity might increase adhesive stiffness around the crack tip when the crack growth rate was very low. The other possible reason was local toughening at the crack tip. Thus, when the cyclic loading continues for a long period, a local toughened zone forms around the crack tip that causes the crack to follow the weaker path around the outside of this zone and to deflect towards the interface. Kawashita and Hallett [59] developed a novel model for investigation of the effect of load ratio on crack propagation in composite laminates.

Figure 2.6 shows the experimental Paris law curve results for cut-ply composite specimens which were used to validate the developed numerical CZM results at different load ratio ranges. The results using crack tip tracking formulation for the normalised strain energy shown good correlation with the experimental Paris law results.

Several techniques have been utilised for monitoring and characterising damage initiation and propagation in adhesively bonded joints including:

- Micro-level techniques;
- Backface strain techniques;
- Digital image correlation (DIC);
- Acoustic emission (AE).

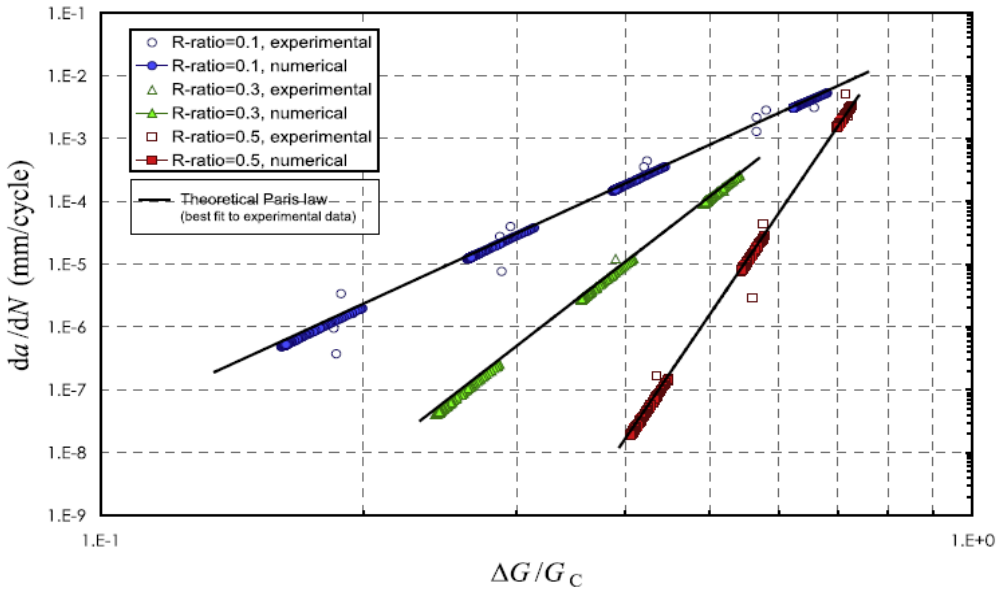

Figure 2.6: Experimental and numerical Paris curves for cut-ply specimens with various R-ratios [59].

A micro-video camera under a stroboscope light source was used by Ishii *et al.* [60], while Cheuk *et al.* [61] and Quaresimin and Ricotta [57] used Scanning Electron Microscopy (SEM) and an optical microscope to produce clearer images. The main problem around the use of such devices however is the fact that this requires the specimens to be removed from the test machine closing the cracks which are consequently unloaded. This is the case in particular for small elastic cracks generated in adhesively bonded joints which close completely once unloaded making their length difficult to measure.

The backface strain technique was applied to adhesively bonded joints by both Zhang *et al.* [55] and Khoramishad *et al.* [62] who conducted experiments on single lap joints to identify crack initiation and growth by considering the change in the direction of backface strain variations during fatigue cycles. Figure 2.7 indicates how the crack initiation life and the site of crack initiation can be determined. The readings for the backface strain gauge 1 (SG1) and strain gauge 2 (SG2) have similar values over the period of crack initiation, however as the crack begins to propagate there is sudden change with SG1 decreasing whilst SG2 increases in region (c). This can be explained

by the fact that as a crack propagates the local deformation at the location of the nearer strain gauge (SGI in Figure 2.7 (c)) relaxes and the joint becomes more asymmetric, thus a larger moment is induced in the other substrate. Although not explicitly stated, this response only occurs if the strain gauge is placed outside the overlap and in this case, the sensitivity is very low.

DIC techniques are favoured by many researchers as they involve a non-destructive approach and are able to measure full-field displacements and strains making them one of the most suitable in-situ techniques. DIC was used by Khan [63] to measure the shape of delaminations in FML structures. It was also used by Lemmen [64] to measure delamination in thick adherent tests.

AE has been used by researchers including [65-67] to monitor damage in composite materials and adhesively bonded joints structures. AE signals generated during initiation and propagation of damage can be used to be both locate and characterise damage. Location is traditionally a triangulation process based on a signal's time of arrival (TOA) at the three nearest sensors. In anisotropic materials such as composites and in structures with complex geometries (changes of thickness, holes) in which the assumption of constant velocity is invalid more complex approaches such as the Delta-T technique which maps the transmission of AE across the whole structure can be used [68]. By looking more closely at the signals themselves *e.g.* absolute energy, count, amplitude, duration [69] the level of damage can be estimated and frequency-based approaches [70, 71] among others allow the damage to be characterised. Many researchers [65, 72-75] have adopted AE to detect damage in composite materials under fatigue loading.

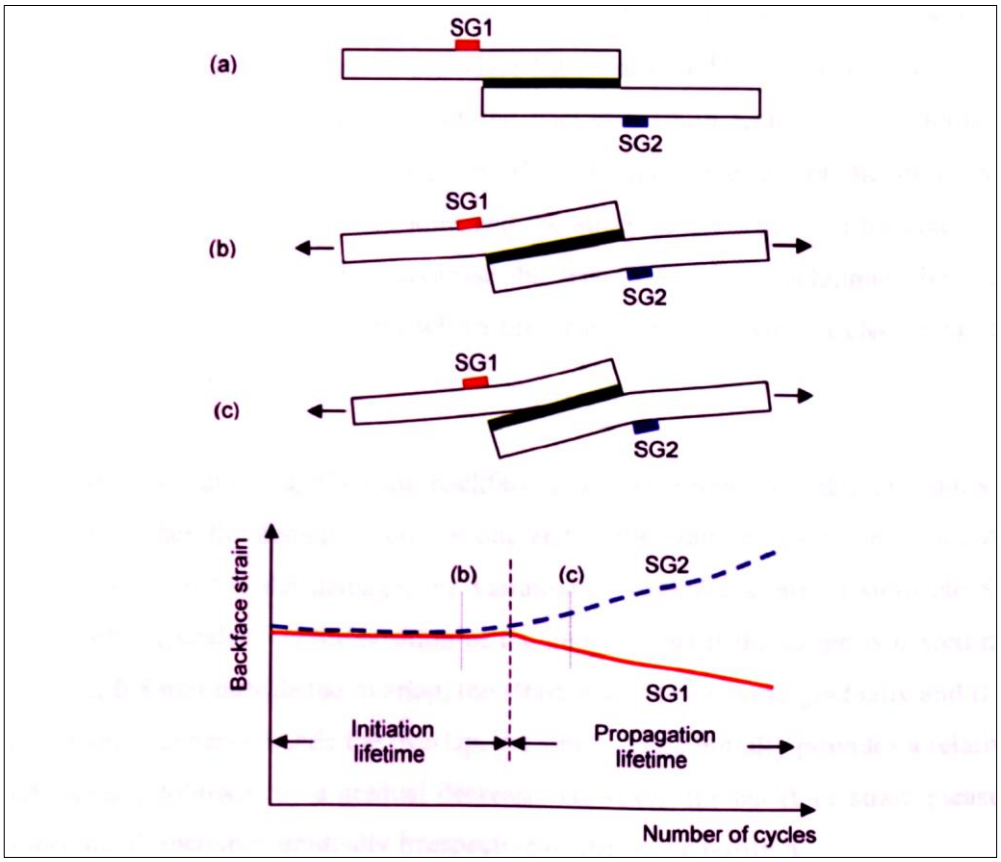

Figure 2.7: Backface strain detection of fatigue crack initiation [62].

In this thesis a fatigue total life approach will be used to study design life and damage tolerance of FML structures including adhesively bonded joints subject to high-cycle fatigue loading. In addition, Acoustic Emission and in particular the Delta-T technique will be used to detect and locate damage in FML structures subject to high-cycle fatigue. These results, combined with the Paris law parameters for Glare® reported by Alderliesten [4], will be used to validate models generated using a new cohesive zone model to predict fatigue damage initiation and propagation at the interfaces of FML specimens.

2.3.2 Numerical studies

This Section reviews the numerical methods employed to study the fatigue failure behaviour of adhesively bonded joints. According to Khoramishad [62], fatigue modelling for adhesively bonded joints can be divided into five approaches - total life,

continuum damage mechanics (CDM), fracture mechanics, stress singularity and cohesive zone modelling (CZM).

2.3.2.1 Total life method

The design life of a component subjected to fatigue can be determined through either a stress-life or strain-life approach. If the amplitude of the total strain is such that there is significant plasticity, then the fatigue life is likely to be short and we have Low Cycle Fatigue (LCF), which typically means less than 10^4 cycles. In these cases we use a strain life approach. If the stresses are low enough that the strains are elastic, the lifetime is likely to be long and we have High Cycle Fatigue (HCF), which is typically over 10^6 cycles, where stress-life approaches are commonly used. The latter has however, not been utilised extensively for adhesively bonded joints. Normally, in applying the stress-life approach, the structure needs to be modelled under cyclic loading with constant amplitude with different load severities (which can be calculated experimentally based on the static strength of the same structure). The fatigue life for the structure can then be estimated based on the applied stress versus number of cycles to failure at different stresses with the results plotted as a S-N curve. An example of experimental and numerical fatigue life or (load versus number of cycles) curves for adhesively bonded joints in single lap joint (SLJ) specimens is shown in Figure 2.8 [62] with the nominal stress (S) defined as the applied load amplitude divided by the bonded area. It should be noted that in adhesively bonded joints, calculating the average stress relative to the maximum stress might not be easy. This is because once crack propagation takes place the bonding area will change and the average stress and accordingly the relationship between the average and the maximum stress will change. Hence the S-N curve will not only be material dependent but also geometry dependent. In other words, an S-N curve obtained for one joint may not be applicable to other joints with different geometries but similar adhesive materials. The test setup and boundary conditions can also affect the results

significantly. The numerical S-N curves are usually plotted for given maximum stresses against number of failure cycles as follows:

$$\sigma_{\max} = a\left(N_f\right)^{b} \tag{2.2}$$

where $\sigma_{\max}$ is maximum fatigue stress, N_f is number of failure cycles and a and b are constants which can be obtained from power law curve fitting experimental S-N curves. The constants can be dependent on parameters such as material, geometry, surface condition, environment and stress ratio.

Although the stress-life approach can be useful in predicting the fatigue lifetime, this method is not able to indicate the damage or the evolution of the damage during the fatigue loading. Therefore, residual strength, following partial fatigue damage, cannot be determined using this method. Another deficiency of the stress-life approach is that the initiation and growth phases of fatigue lifetime are not differentiated. It is worth noting that some researchers (Zhang *et al.* [55], Crocombe *et al.* [49]) have tried to enhance the capability of the method by combining it with other methods like the backface strain technique.

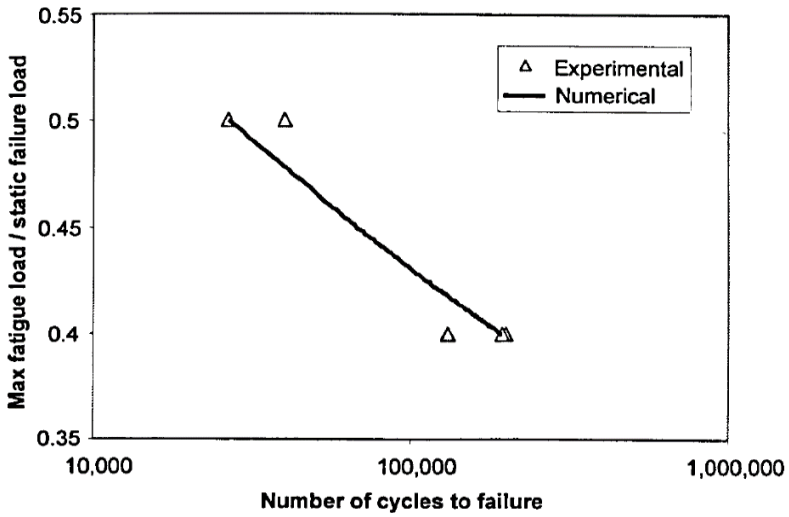

Figure 2.8: Comparison between the experimental and numerical load-life fatigue data of the SLJ specimen [62].

2.3.2.2 Continuum damage mechanics (CDM)

CDM theory can be described as the damage theory concerned with macroscale

cracks or defects and developed based on damage variables. This theory has been adopted by many researchers [76-79] to predict the fatigue life of composite materials including adhesively bonded joints. In this method, a damage parameter (D) is defined to specify the effective stress corresponding to a certain amount of damage. The damage parameter is zero for an undamaged material and one for a fully damaged material. According to this theory, the initiation of a macro-crack occurs when the accumulated damage reaches a critical value (between zero and one) and damage accumulation can be expressed in terms of a number of cycles to failure. This approach was first introduced for modelling damage in metals and later conducted on adhesive bonded joints in 1997 when Ganghoffer *et al.* [80] developed an elasto-plastic continuum damage model for simulating damage in the interface of two contacting bodies such as rubber and glass, for the thin intermediate layer within the frame of continuum thermodynamics. A damage model based on a scalar damage parameter (D) was also introduced by Imanaka *et al.* [81] to investigate fatigue damage evolution in adhesively bonded butt joints as follows:

$$D = 1 - \left\{1 - 2qN\{(A+B)^{2n+1} - (B-A)^{2n+1}\}\right\}^{\frac{1}{2n+1}} \tag{2.3}$$

Where D is the damage variable, n is a material constant, N is the number of cycles, A is the nominal stress amplitude, B is the nominal mean stress and q is a variable which can be calculated as follows:

$$q = \frac{(1-2v)^{n+1}(1+v)^{n+1}}{3(2^{n-1})E^{n+1} \cdot S^{n}(1-v)^{n+1}} \tag{2.4}$$

where v is Poisson's ratio, S is a material constant and E is Young's modulus.

CDM was employed to predict fatigue damage in an aluminium/epoxy single lap joint by Hilmy *et al.*[79]. They considered a damage equation as a function of cycles and stress:

$$D = 1 - \left\{1 - (\beta + m + 1)\alpha\left(\Delta\sigma_{eq}\right)^{\beta+m} R_v^{\beta/2} N\right\}^{\frac{1}{\beta+m+1}} \tag{2.5}$$

where σ_{eq} is the Von Mises equivalent stress, R_v is a triaxiality function, m is a material constant related to strain hardening and α and β are damage parameters. However, they only predicted the number of cycles to damage initiation.

2.3.2.3 Fracture mechanics

The fracture mechanics approach can be employed to predict the fatigue crack propagation for adhesively bonded joints. The most widely used approach is the use of the Paris law which can be plotted by calculating the crack growth rate ($\mathrm{d}a/\mathrm{d}N$) from a linear fitting to the relationship between the delamination length along the adhesive joint interface and the number of failure cycles. The maximum strain energy release rate and the change in strain energy can then be calculated from area under the curve of the traction-separation relation. The Paris law curve can then be plotted as the logarithmic relationship between crack growth rate ($\mathrm{d}a/\mathrm{d}N$) and normalised strain energy release rate (G_a/G_c) as shown in Figure 2.9. Paris law-based models have been widely employed as an efficient engineering tool for fatigue life prediction especially in lightweight structures and are used in this work to predict damage evolution in FMLs structures including adhesive joints.

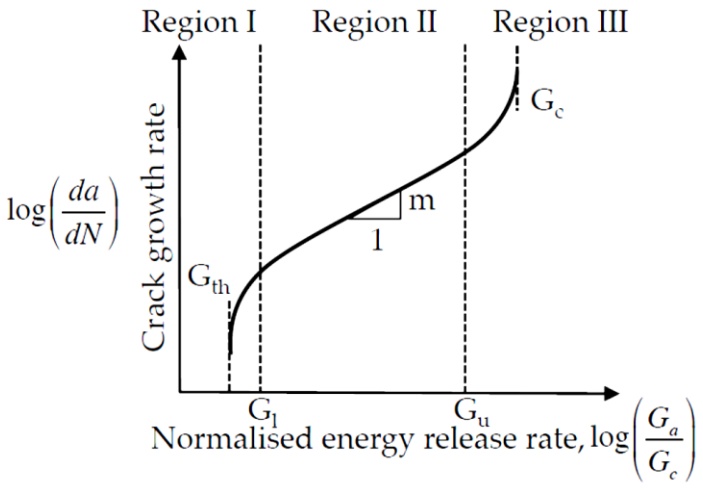

Figure 2.9: A typical fatigue crack growth curve.

A large number of researchers have adopted the Paris law in modelling crack propagation in adhesively bonded joints. Wahab *et al.* [82, 83] used this approach to predict damage evolution in single lap joint (SLJ) and double lab joint (DLJ) specimens comprising CFRP composite laminates bonded with epoxy adhesive. Using a modified Paris law [84]:

$$\frac{da}{dN} = DG_{max}^{n}\left(\frac{1-(G_{th}/G_{max})^{n_1}}{1-(G_{max}/G_c)^{n_2}}\right) \quad (2.6)$$

(where G_{th} is the fatigue threshold strain energy release rate, G_c is the facture toughness, G_{max} is the maximum strain energy release rate, n, n_1, n_2 are fatigue parameter constants which can be obtained from an experimental S-N curve) and integrating from initial crack length (a_0) to the final crack length (a_f) they were able to predict the number cycles to failure. They also extended previous work by Curley *et al.* [85] for calculating strain energy by using an automatically generated finite element analysis so it could be generalised for any adhesively bonded joints.

2.3.2.4 Stress singularity

Researchers examining the life of bonded joints agree that stress singularity has a significant effect on crack initiation fatigue life. Imanaka *et al.* [86] developed a formula to estimate crack initiation life-time (equation 2.7) based on a stress singularity parameter and this equation can be used to estimate the endurance limit for single lab joints (SLJs):

$$\sigma_{ij} = \frac{K_{ij}}{r^{\lambda}} \quad (2.7)$$

where σ_{ij} is the stress component, r is the distance from singular point, K_{ij} is the stress intensity factor and λ is the order of stress singularity which can be estimated from the shape of the joint.

2.3.2.5 Cohesive zone model (CZM)

The CZM method combines the classical fracture mechanics concept of a critical strain energy release rate for crack propagation with the damage mechanics assumption of a zone ahead of the crack tip where a gradual, irreversible loss of material stiffness is observed. This approach is advantageous over linear elastic fracture mechanics theory (LEFM) for modelling crack growth in that it removes the need for singularity at the crack tip [39] and so is able to predict the crack growth behaviour of uncracked structures. The cohesive zone model was first introduced by Barenblatt and Dugdale [87, 88] with Dugdale proposing the concept of a cohesive traction equal to the yield stress for the material considered and separation occurring between two adjacent surfaces in a region called the cohesive zone when this is exceeded and Barenblatt [87, 89] using a similar approach to solve instability problems in brittle materials subject to fracture. Hillerborg *et al.* [90] used a similar model to study the fracture behaviour of concrete. Cohesive zone models based on such traction-separation laws are found to be an efficient approach in predicting damage at the interface of two solid bonded surfaces when the adhesive layer is very thin. As the joint is loaded traction increases until it reaches a critical value $\boldsymbol{\sigma}_{\mathrm{o}}$ at which point damage initiates. Following this it decreases indicating the growth of the damage. The separation, U, is the value of displacement which is U_{o} at initiation and U_{f} at final failure. A cohesive element fails when the separation reaches the maximum value U_{f} at zero stress. In this case the strain energy is equal to the critical strain energy or fracture toughness, G_{c}, and can be calculated by integration of the traction–separation relation to give the area under the curve. The shape of the traction–separation curve is identified according to the fracture behaviour of the material. A number of models have been proposed by different researchers a discussion of which will follow.

Needleman [91] introduced polynomial traction–separation law (Figure 2.10 (a)) in order to analyse the void initiation and propagation from initial debonding up to final

separation. This model is attractive for the cases when interfacial strength is low and the high stress degradation associated with cracks in homogeneous material do not develop. In these cases use of a polynomial traction-separation law enable standard finite element methods to be extended to incorporate interfacial integrals. Xu and Needleman [92] also proposed an exponential model to predict damage in brittle materials see Figure 2.10 (b). Mi *et al.* [93] proposed the bilinear traction-separation law see Figure 2.10 (c) which involves a simple linear relationship with a constant stiffness up to the critical yield stress and then stress degradation also with a linear slope up to final failure. The trapezoidal traction-separation law shown in Figure 2.10 (d) has been adopted by many researchers [94-103] to model interface damage behaviour in elastic-plastic materials under static loading.

In this thesis a trapezoidal traction-separation law is developed to model both static and high cycles fatigue damage in the FML interfaces using cohesive elements.

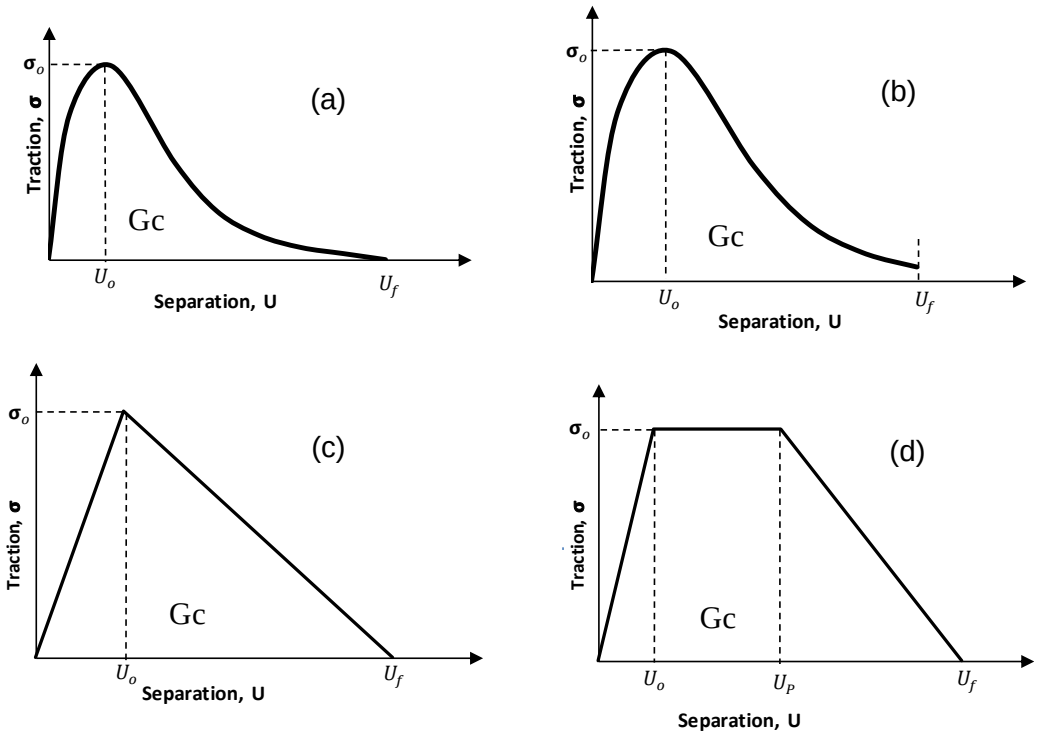

Figure 2.10: Typical traction-separation law shapes, (a) polynomial, (b) exponential (c) bilinear, (d) trapezoidal.

2.3.3 Cohesive zone models for fatigue

Cohesive zone models have been widely used for predicting delamination in adhesively bonded structures under fatigue loading. The developed models can be classified according to the applied load into three types (see Figure 2.11) as follows:

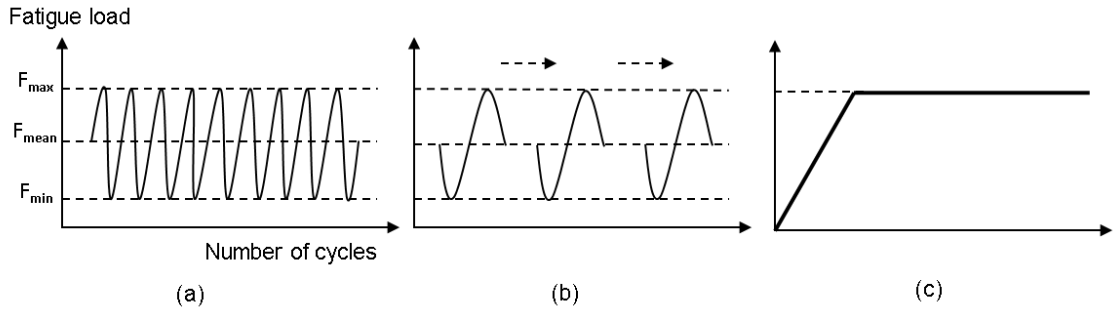

Figure 2.11: Schematic of different approaches in modelling high cycle fatigue loading based on CZM (a) Cycle-by-cycle, (b) Cyclic extrapolation and (c) Envelope maximum load.

2.3.3.1 Cycle-by-cycle analysis

CZM for homogenous cycle-by-cycle analysis was implemented by Roe and Siegmund [104] in order to investigate adhesively bonded structures. A sinusoidal fatigue load was applied in both normal and shear directions (see Figure 2.12). Normal stress σ and shear stress τ were combined with phase angle β using the following expression,

$$\beta = \tan^{-1}(\tau/\sigma) \tag{2.8}$$

The cycle-by-cycle approach is illustrated in Figure 2.11 (a). This approach has not been adopted in this thesis as according to many researchers [59, 105, 106], it is computationally expensive and practically impossible in the case of high cycle fatigue.

2.3.3.2 Cyclic extrapolation analysis

Using CZM for every single cycle was considered impractical due to computational cost as mentioned also due to the fact that convergence is difficult to achieve for high cycle fatigue simulation. An alternative technique has therefore been adopted by other researchers (Van Paepegem [107], Ural and Papoulia [108], Cocojaru [109] and Turon *et al.* [110]) in order to reduce the computational time. This technique is called cyclic

extrapolation or cycle-jump and it can be implemented for certain number of cycles at equal intervals and then extrapolated to obtain the total number of fatigue cycles to failure.

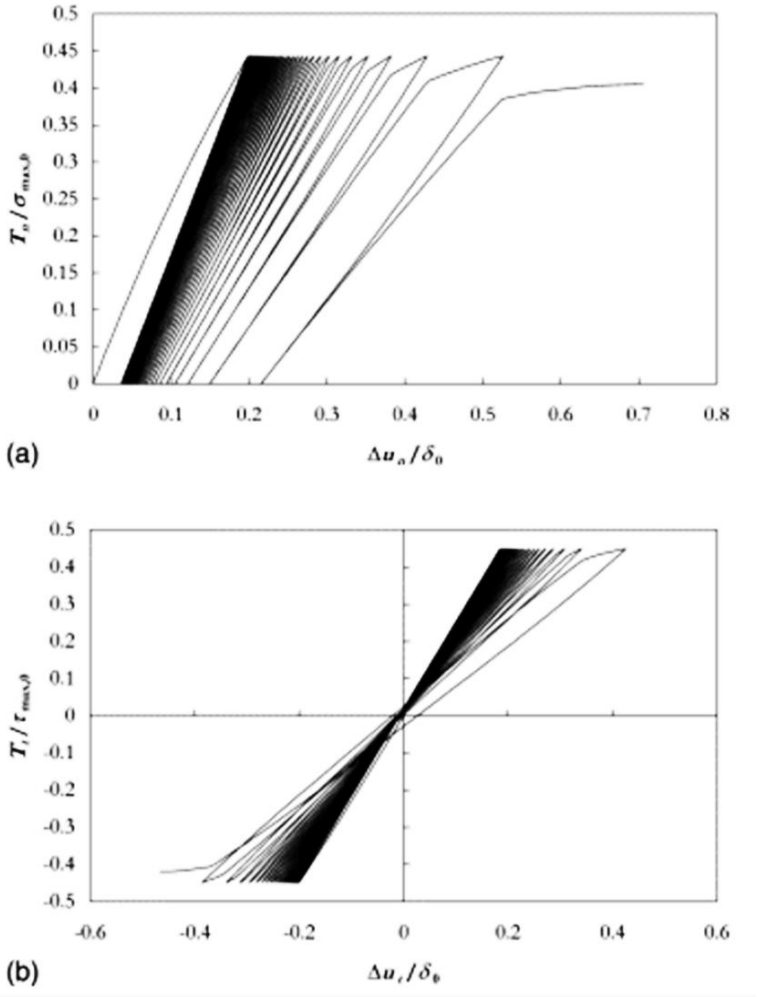

Figure 2.12: Prediction CZM response under load-controlled conditions (a) normal, (b) shear traction-separation behaviour (Roe and Siegmund [104]).

A schematic of the cyclic extrapolation technique is shown in Figure 2.11 (b). However, this approach is still computationally expensive especially for high cycle fatigue analyses and also for complex FMLs structures.

2.3.3.3 Envelope analysis

The envelope load damage model has been widely employed recently by researchers including Harper and Hallett [105], Kawashita and Hallett [59] and de Moura *et al.* [106] in the analysis of delamination propagation in composite materials under high cycle

fatigue loading using mixed-mode CZMs. In each case the maximum fatigue model developed by Robinson *et al.* [111] is used. A schematic representation of this model is shown in Figure 2.11 (c). A detailed description of the implementation of envelope fatigue loading in finite element analysis is given in chapter 6: Section 6.3.

As this technique has proved to be highly efficient in terms of computational cost and accuracy, it has been utilised in this thesis to model the effects of high cycle fatigue on adhesively bonded FML joints using CZMs based on a mixed mode trapezoidal traction-separation law.

2.4 Delamination in FML structures

Fatigue crack propagation mechanisms in fibre-metal laminates (FMLs), including 'Glare', can be divided into crack growth in the aluminium layers and delamination growth at the interface between the aluminium and glass fibre reinforced polymer (GFRP) layers. Both experimental and numerical studies have been conducted to investigate these damage mechanisms. Marissen [112] studied the crack growth behaviour of **A**ramid **R**einforced **AL**uminium **L**aminates (ARALL) under different types of fatigue loading. He developed a model for the calculation of crack growth rates, based on analytical solutions for the stress-strain system in cracked Arall by considering the influence of delamination growth as a function of strain energy release rate and adhesive shear deformation which was validated by experimental results. Takamatsu *et al.* [113] studied fatigue crack growth of Glare3-5/4 by conducting fatigue tests under constant amplitude loading. They observed that fatigue crack growth of Glare® 3-5/4 is about 8-9% higher than that of a 2024-T3 aluminium alloy as well as confirming the order of the assumed residual stress in Marissen's formula [112]. Wu and Guo [114] investigated the characteristics of fatigue growth for the FML 'Glare' under constant and variable amplitude loading both experimentally and theoretically. They developed two models to predict crack growth under constant amplitude loading, one of which depends on the fatigue damage mechanism whilst the other

phenomenological model is based on the characteristics of the steady crack growth. The damage-based model required complicated analyses included consideration of bridging stresses and delamination growth variables, while the phenomenological model does not. They also observed retardation of the crack growth caused by an overload, although the effect on delamination was minor. Alderliesten [4] found that the failure of Glare® specimens subject to fatigue involves crack propagation and delamination growth under constant–amplitude loading. The stress intensity factor at the crack tip in the metal layers of the FML was found to determine the extension of the crack under cyclic loading. The investigation incorporated both theoretical and experimental programmes but was restricted to through the thickness cracks. Alderliesten and Homan [115] investigated fatigue behaviour and damage tolerance issues related to the application of Glare® in a fuselage skin with respect to material characteristics and airworthiness requirements in comparison to monolithic aluminium alloys. They studied crack initiation and propagation in Glare3–3/2–0.3 and compared the results with the monolithic aluminium 2024-T3. They validated and justified different approaches compared to monolithic aluminium based on a large number of experimental results and they found that in comparison to monolithic aluminium, Glare® has a high damage tolerance.

Alderliesten [116] then proposed a model to describe the propagation of fatigue cracks in the aluminium layers and the corresponding delamination growth at the aluminium/fibre interfaces perpendicular to the crack. In this model the stress intensity factor at the crack tip is a function of the far-field opening stress and the crack closing bridging stress in the aluminium layers. The bridging stress along the crack length is calculated on the basis of the crack opening relations for the individual mechanisms. It is then used to calculate the delamination extension, using a correlation between the delamination growth rate and the energy release rate. It is believed that the presented model is generally applicable to any fibre-metal laminate, as long as the material properties of the constituents are known and a Paris relation for the metal layers and

for the delamination at the interface is available or can be determined.

Singh *et al.* [117] investigated fatigue crack growth and related damage mechanisms experimentally in a hybrid laminate (CFRP/aluminium). A simplified empirical model was applied to determine an effective stress intensity factor applied to the crack tip in the alloy material. The fatigue crack growth rate in the hybrid laminate, characterised using the effective stress intensity factor, was demonstrated to be in reasonable agreement with the data for monolithic aluminium alloy, showing that the methods used to partition the load were reliable. Using data from embedded fibre-optic strain sensors, they demonstrated that the stress is not constant along the length of the bridging fibres, and there is compelling evidence to suggest that this is due to a diffuse delamination boundary that extends over several millimetres. It is thus evident that a complex combination of damage mechanisms and stress states exists in the delamination zone of even the simplest fibre-metal laminate structures. The delaminated area between the far-side skin and the core grew more slowly than that between the near-side skin and the core so that only the near-side delamination zone could be recorded as shown in Figure 2.13.

Khoramishad [118] developed a strain–based fatigue damage model for his cohesive element in order to model delamination in adhesively bonded joints in composite laminate structures. This model incorporated different fatigue variables into the cohesive zone model parameters defined by,

$$\Delta D = \begin{cases} \Delta N \alpha (\varepsilon_{\max} - \varepsilon_{th})^{\beta} & , \quad \varepsilon_{\max} > \varepsilon_{th} \\ 0 & , \quad \varepsilon_{\max} \leq \varepsilon_{th} \end{cases} \tag{2.9}$$

$$\varepsilon_{\max} = \frac{\varepsilon_n}{2} + \sqrt{\left(\frac{\varepsilon_n}{2}\right)^2 + \left(\frac{\varepsilon_s}{2}\right)^2} \tag{2.10}$$

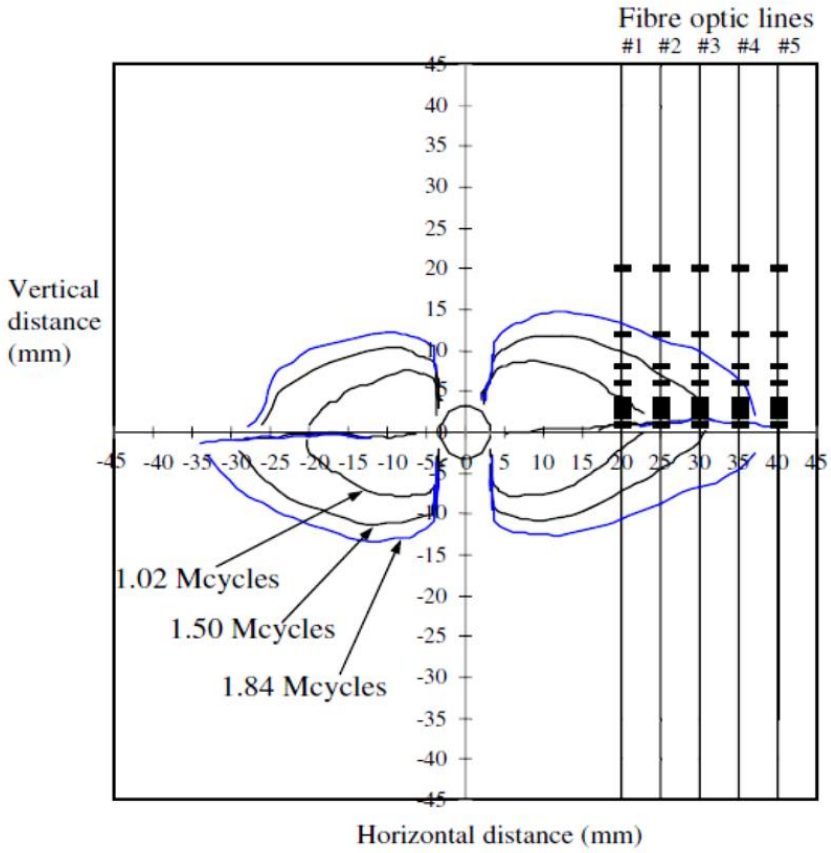

Figure 2.13: Delamination profiles in panel H-R01 [117].

where $\varepsilon_{\max}$ is the maximum principal strain, ε_{th} is the threshold strain below which no fatigue failure occurs, ε_n and ε_s are the normal and shear strains respectively and the parameters α, and β are material properties. The effect of the fatigue load ratio R was also considered by introducing a load correction factor γ, to the damage model as reported in equations 2.11 and 2.12,

$$\Delta D = \begin{cases} \Delta N \alpha [(\varepsilon_{\max} - \varepsilon_{th}) \gamma^n]^\beta & , \quad \varepsilon_{\max} > \varepsilon_{th} \\ 0 & , \quad \varepsilon_{\max} \leq \varepsilon_{th} \end{cases} \tag{2.11}$$

$$\gamma = \frac{(1-R)/2}{1-\left[\frac{P_{\max}}{2P_s}(1+R)\right]^m} \tag{2.12}$$

It should be noted that when applying γ to the strain in the damage evolution law, the ductility needs to be taken into account. This is because, for a given change in stress, a more ductile material exhibits larger strain variations. This is accounted for by incorporating the power n in the damage evolution law (equation 2.11). This model was

implemented by coupling the Abaqus/Standard software with the FORTRAN user subroutine GETVRM. Although this model has been developed for modelling fatigue damage in composite laminates, it has also been used by other researchers to model damage in FML structures as will be explained later. Katnam *et al.* [119] investigated the effect of load ratio on the fatigue behaviour of adhesively bonded joints using both experimental and numerical approaches. The progressive damage of the adhesive material was modelled using a cohesive zone approach with a bilinear traction-separation response. They found that the developed numerical model accurately predicted the effect of load ratio on the fatigue lives of both the FM73M OST and the AV119 single lap joints. Furthermore, their existing experimental data for FM73M OST correlated well with the predicted adhesive fatigue damage initiation and propagation. Crocombe and Sugiman [120] conducted experimental and numerical investigations on metal laminate (ML) doubler joints and hybrid fibre-metal laminate (aluminium-Glare) doubler joints under fatigue tension loading. The numerical analyses were implemented using Khoramishad's cohesive zone model [118] which enables simulation of damage in the adhesive joints for both (ML) and (FML) interfaces. Experimental tests were carried out to validate the results and showed good agreement. The authors found that the static strength of hybrid joints is higher when the fibre direction is parallel to the loading direction than when the fibre is perpendicular to the loading direction. Also butts that exist in the ML and hybrid FML doublers joints loaded in tension shown in Figure 2.14, decrease their static and fatigue performance, particularly where the butt position is close to the stringer edge. Fatigue failure is still initiated in the aluminium layer close to the stringer edge where high stresses exist due to secondary bending and load transfer. Therefore, the design of laminate structures with the doubler joints loaded in tension should, where possible, minimize the stress concentration in the aluminium layer close to the stringer edge by using technique such as stringer run out (tapering).

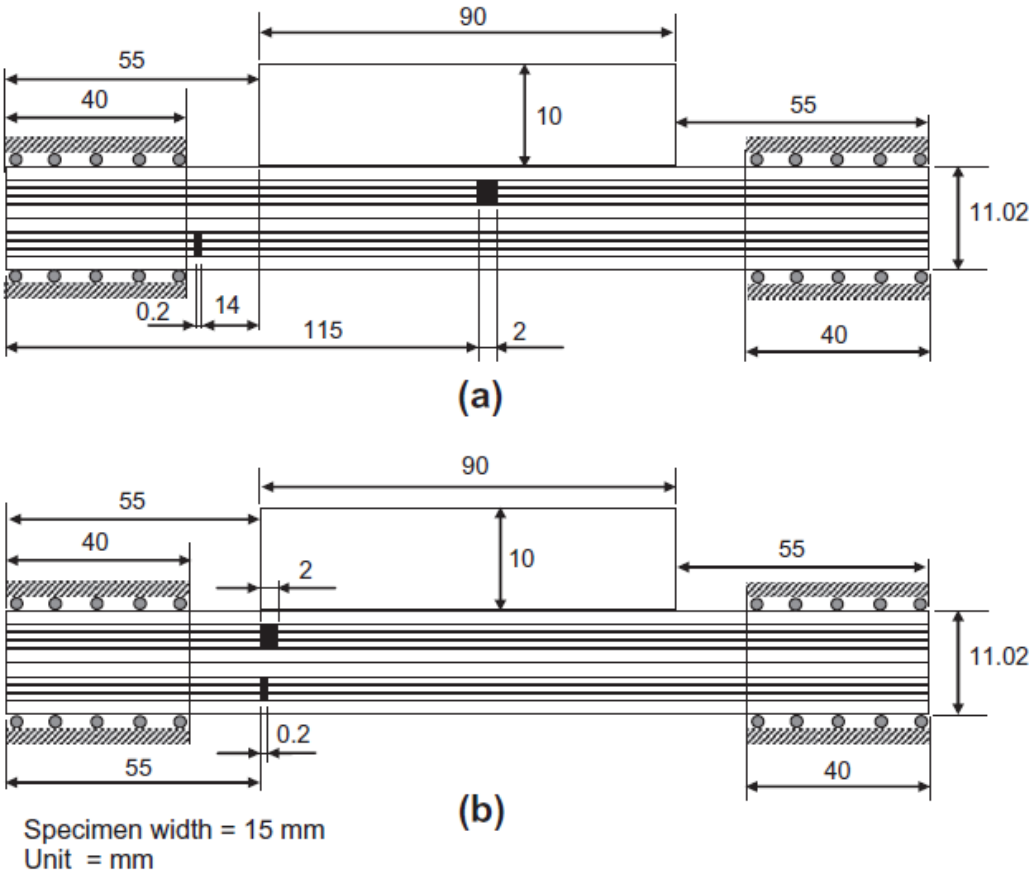

Figure 2.14: Hybrid FML specimens, (a) CH-B1, (b) CH-B2 [120].

Gupta *et al.* [121] studied crack paths in fibre-metal laminates experimentally under static and fatigue off-axis loading. They observed the damage modes and failure mechanisms which occurred and found that although the metal is under external tensile loading, the fibre bridging due to the off-axis effect produces a component of shear at the crack tip in the metal. These two loads combine together to produce the effect of crack turning because of mixed-mode loading. The use of the mixed-mode parameter to incorporate the effects of the fibre-bridging was therefore thought to have the potential to provide a better understanding and estimation of the crack paths in FMLs. Yang *et al.* [122] investigated fatigue crack growth behaviour of Glare3-3/2 laminates with multiple-site damage (MSD). In FMLs with MSD, the combination of fibre bridging, load transferring, the toughness of the aluminium sheet and the secondary bending effect, controlled the fatigue crack growth rate. They concluded that for specimens with

multiple through-thickness open holes, when fatigue cracks emanated from the open holes and propagated, the crack growth rate was faster than for the case without the interaction of the cracks. They also noticed that the propagating cracks tended to bypass each other and form an eye-shaped region before linking-up. However in specimens with multiple surface cracks, cracks propagated and linked up directly instead of bypassing each other. Wilson [123] predicted a generalised model for the growth of damage in fibre-metal laminates under fatigue loading by considering FMLs which may consist of any arbitrary configuration of fibre-reinforced composite laminae combined with metallic layers .The generalised bridging load and strain energy release rate formulations were validated by comparison to finite element models of FML with non-uniform, arbitrary crack and delamination configurations. The overall model predictions of crack and delamination growth were validated through a series of fatigue crack growth tests on a variety of thick FML configurations, including some with non-uniform thickness layers, asymmetry, differing metal alloys, and different arrangements of composite prepreg and adhesive plies. Chlupová and Kozák [124] studied the damage of the fibre-metal laminate 'Glare' subjected to fatigue loading with positive mean stress. They investigated fatigue crack initiation and growth in addition to delamination shape and the surface area of notched specimens experimentally. A model using Abaqus software was used to predict fatigue life in terms of number of cycles to crack initiation depending on the amplitude of the local plastic deformation and the local stress at the notch root, see Figure 2.15. Furthermore, they observed that the shape of delamination in Glare® laminate can be approximated by an ellipse. More recently Hosseini-toudeshky and Mazaheri [125] developed an elastic–plastic constitutive damage model to simulate delamination initiation and propagation in FML structures. However, the last two models [124, 125] were limited to only a low-cycle fatigue loading regime.

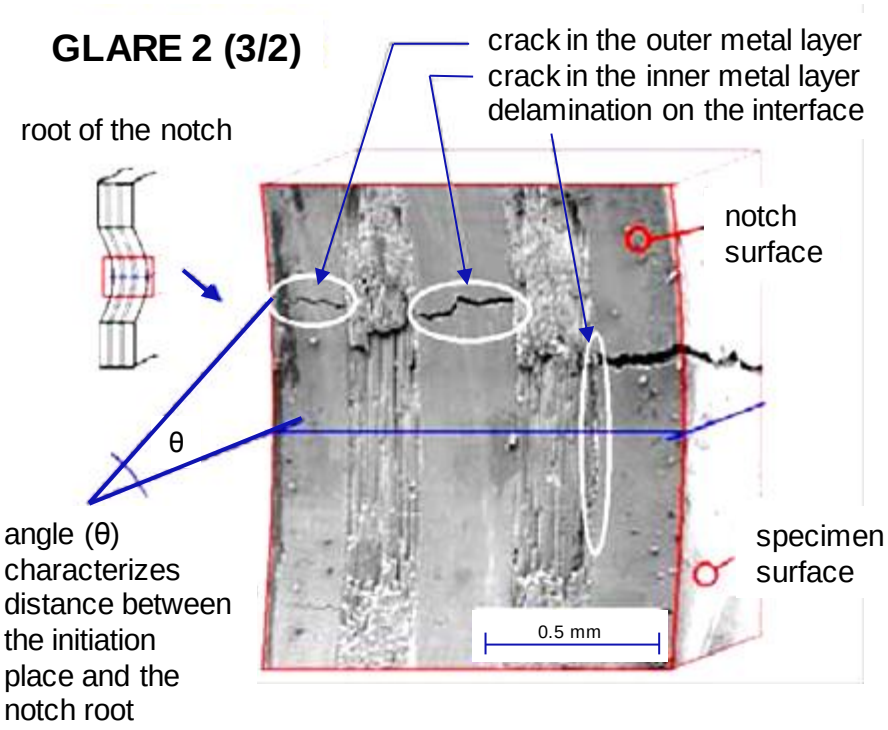

Figure 2.15: Deflection of crack initiation angle.

2.5 Chapter summary

The state of the art pertaining to the initiation and propagation of damage in FML structures under static and fatigue loading has been investigated.

In terms of static damage literature relating to the effects of delamination damage on the buckling and postbuckling behaviour of panels subject to quasi static loading has been explored with the results of both experimental and numerical studies being presented. An overview of studies considering load eccentricity and geometrical imperfection has been included due to their importance in the accurate prediction of buckling behaviour. Both fibre composites and FMLs have been considered.

Research into fatigue damage in FMLs in terms of crack growth in the metal layers and delamination in the interface layers in addition to the delamination of adhesively bonded joints has been summarised. Numerical techniques for predicting the total fatigue life of structures including the S-N curve method and for modelling the initiation and propagation of damage including the Paris law and cohesive zone models and modelling fatigue loading in a computationally effective way have been summarised.

Chapter 3 - FML Manufacture and Testing

3.1 Introduction

This chapter describes the processes and techniques used to manufacture the specimens and to monitor them during testing. Whilst the specimens used for the quasi-static buckling tests were supplied by Airbus GmbH, those for the fatigue tests were manufactured in-house. The process developed in order to manufacture these is detailed here. During testing, specimens were monitored using acoustic emission (AE) to monitor damage initiation and growth and digital image correlation (DIC) to determine full-field displacements and strains. A high magnification camera was also used to monitor crack propagation. On completion of the tests, Scanning Electron Microscopy (SEM) was used to determine failure mechanisms. Each of these processes is discussed in detail.

3.2 Specimen design

Specimens for both buckling and fatigue tests were manufactured from the fibre metal laminate Glare®, which is a hybrid material consisting of alternating metal and composite layers. The metal layers in Glare® are made from the aluminium alloy Al-2024-T3 and the composite layers are assembled from between two and four (depending on the grade) unidirectional (UD) S-2 glass fibre/FM 94 epoxy prepreg layers [1] as seen in Figure 3.1. The number of layers expressed as (n+1)/n *e.g.* 3/2 gives the number of metal layers (n+1) and the number of composite layers (n). The composite layers are oriented either in one direction only, resulting in UD-laminate layers, or in two directions, resulting in cross-ply laminate layers. The resin used is epoxy FM94, which is a very tough adhesive material.

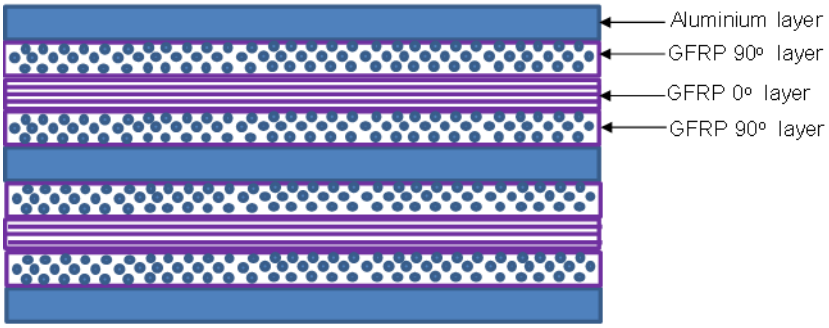

Figure 3.1: Schematic of the Glare® 4B-3/2 laminate.

In this work, specimens were manufactured from Glare® 4B which consists of 0.4 mm thick 2024-T3 aluminium sheets and GFRP layers each having 3 plies with the layup [90º/0º/90º] and a cured ply thickness of 0.133 mm.

3.3 Specimen manufacture

The manufacture of FMLs including Glare® requires a number of stages to be completed in order to obtain the final laminated panels. These stages include the preparation of the aluminium sheets using an etching process, the cutting of the GFRP plies and then the hand layup and curing of the laminate. Following curing, specimens are cut to the required dimensions. Further detail on each of these steps is provided below;

3.3.1 Surface treatment

In order to obtain a good bond between the aluminium and GFRP plies pre-treatment of the aluminium sheets is required to remove the oxide layers from the aluminium surface. This is done by mechanical abrasion of the aluminium surface using a wire brush followed by chemical treatment. Both acidic (low pH) and alkaline (high pH) solutions are used for this purpose. The chemical treatment typically comprises three steps: degreasing, alkaline cleaning and acid etching [126]. The preparation of the sheets for the specimens used in this study was performed according to [126, 127].

The first step included mechanical abrasion using Scotch-Brite™ abrasive sponges, followed by degreasing through the application of the cleaner Methyl Ethyl Ketone (MEK). The second step involved immersing the sheets in a solution of 100 g/L of water of sodium hydroxide (NaOH), at 60 °C for 1 min, as shown in Figure 3.2. The third step involved etching. This can be achieved using a number of different methods depending on the etching solution utilised. The most common methods are: chromic–sulphuric acid etching (CAE) using chromic–sulphuric acid solution and potassium dichromate [128], *Forest Product Laboratory* (FPL) treatment using sulphuric acid solution and potassium dichromate [129], and sulfo-ferric acid (P2) treatment using sulphuric acid and ferric sulphate [130]. The most effective method has been shown to be one which incorporates chromic–sulphuric acid etching (CAE) [127]. This etching treatment was therefore adopted in this work and was conducted by immersing the aluminium sheets in a water solution of 330 mL/L chromic-sulphuric acid (97% v/v) and 50 g/L potassium dichromate; at 60 °C for 15 min. During both the second and third steps, magnetic stirring was used to ensure an even temperature distribution and a thermocouple measured the temperature.

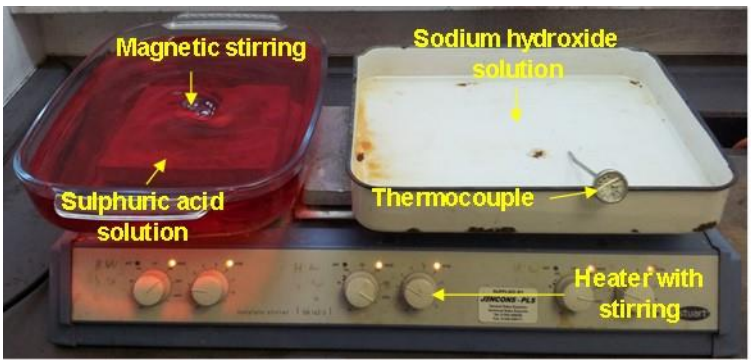

Figure 3.2: Aluminium etching process.

After steps two and three, the sheets had to be rinsed in tap water for 20 minutes. They were then dried in an oven at 40 °C for 30 minutes. An anodising step [131] can also be introduced in order to reduce corrosion which can occur due to the etching process. This is appropriate when the aluminium sheets will be exposed to harsh conditions in

service, but unnecessary for the present study where specimens will only experience laboratory conditions. In addition to this consideration ageing and durability are out of the scope of this study.

3.3.2 Hand layup

Following preparation of the aluminium sheets, the Glare® material was laid up by hand (Figure 3.3). Further detail on the exact lay-up for individual tests is given in Section 4.2.1 for the buckling specimens, and Section 7.3 for the fatigue specimens.

Figure 3.3: Hand layup.

3.3.3 Vacuum bagging and curing

Following lay-up, the material was bagged and attached to the vacuum system in the autoclave as shown in Figures 3.4 and 3.5. For the FM 94 adhesive system [132], the material needed to be heated to 120 °C at a rate of (1.7 - 2.8 °C) per minute with a pressure of 1.86 bar and vacuum 0.9 bar applied. The temperature, pressure and vacuum then need to be held for 60 minutes before cooling at a rate of 3 °C min^{-1}. This gives a total cure time of approximately 210 minutes including cooling.

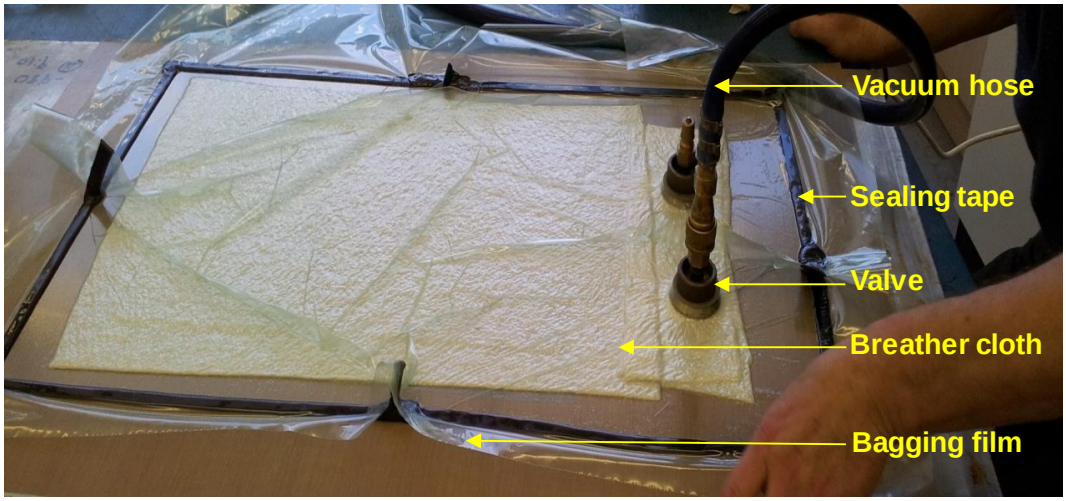

Figure 3.4: Vacuum bagging process.

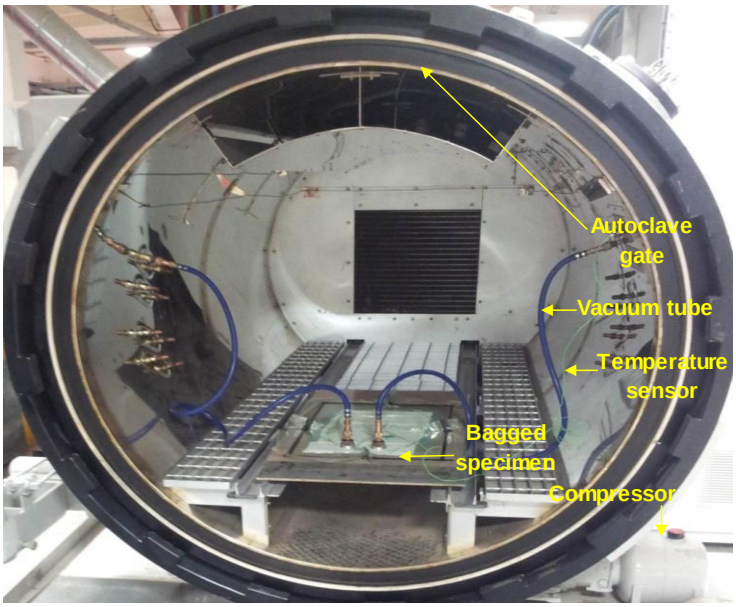

Figure 3.5: Autoclave process.

3.3.4 Specimen cutting

A number of methods can be used to machine Glare. When choosing an appropriate method consideration should be given to the surface quality required (machining can cause delamination and create geometrically imperfect edges) and the effect on tool wear (which can be rapid due to the abrasive nature of the GFRP). Tool wear, for example, can be eliminated by using processes such as water and laser jet machining, however, in both cases, edge quality is an issue, with both processes producing relatively rough edges limiting their application [126].

In this work, the cutting process was performed in two stages as shown in Figure 3.6. In the primary stage, specimens were cut to size using a Toyo tile saw. Following this, a carbide milling cutter was used to achieve a high-quality finish and geometric accuracy. The latter was recommended in [133] for cutting highly abrasive materials such as the GFRP included in the Glare® laminate.

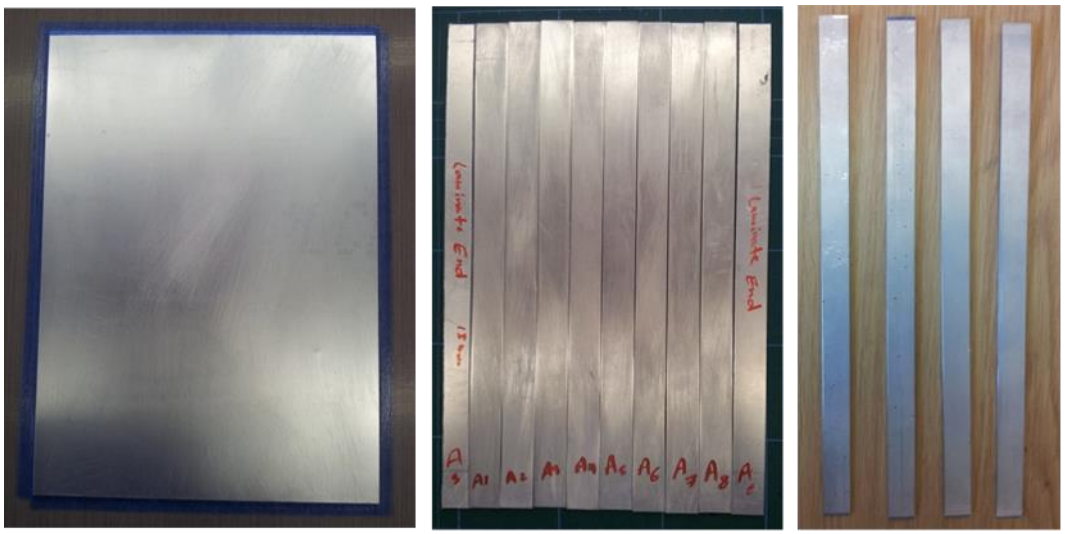

Figure 3.6: Cutting the Glare® panel, (a) pristine panel, (b) stage-1 using the tile cutter and (c) stage-2 using the milling cutter.

3.3.4.1 Tile cutter

A 500 W Titan tile saw was used to cut the Glare® panels into specimens of the required width (see Figure 3.7) by wet-cutting using a diamond blade cutting was achieved without generating significant heat which might have affected the material properties of both the resin and the aluminium. The cutter used also had the benefit of being only 1 mm thick, minimising the amount of material lost during the cutting process. Despite these advantages, the tile saw was not able to generate a smooth cut and avoid delamination, therefore it was necessary to go through another stage of cutting using a carbide milling cutter to achieve this.

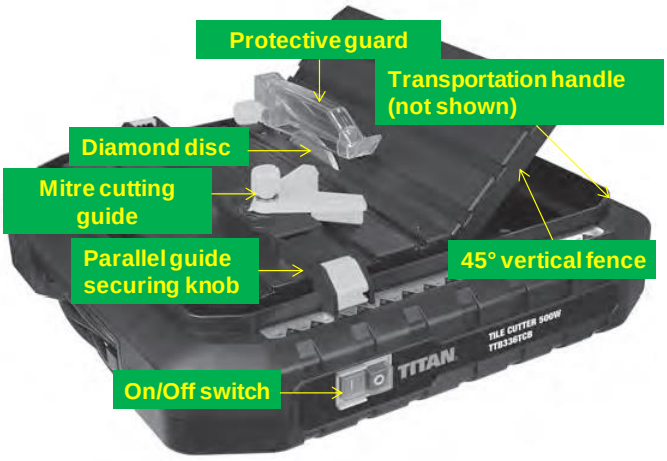

Figure 3.7: The tile cutter used in this work.

3.3.4.2 Carbide milling cutter

A relatively high-speed cutting device and low feed rate are recommended in [1], particularly when machining harder (glass fibre based) fibre metal laminates. Milling of Glare® laminates was carried out using a plain milling machine fitted with a spiral tooth cutter to ensure a smooth finish (in comparison to a straight tooth cutter). Diamond cut solid carbide cutters are recommended when cutting glass based products and were used here. Typically, when using tooth cutters, a depth of cut of about 1.5 mm and cutter surface speed of 1200 – 1800 mm/min may be used. For glass based materials as in this case, using diamond cut solid carbide tooling, a 10 mm diameter cutter at a cutter speed of 2000 – 3000 rpm and a feed rate of 500 mm/min is recommended and was used here see Figure 3.8.

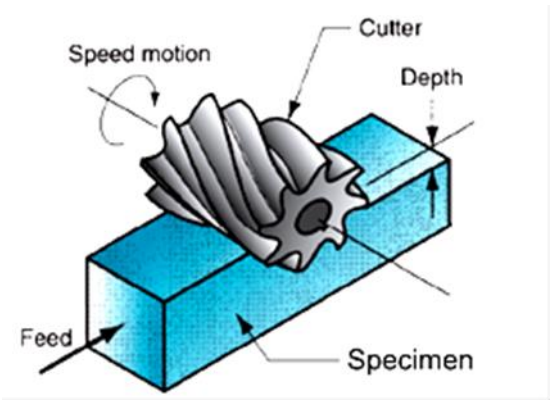

Figure 3.8: Milling cutting process.

3.4 Monitoring techniques

In this study, three systems were used to monitor both the static and the fatigue behaviour of Glare® laminates during testing. These systems were acoustic emission (AE) which was used to detect the initiation and propagation of damage, a high magnification video camera to measure the crack length from the edge of the specimens, and digital image correlation (DIC) which was used to measure surface displacements.

3.4.1 Acoustic emission instrumentation and techniques

AE is a physical phenomenon by which elastic energy is generated from a mechanical source such as a defect, in the form of elastic waves which propagate through the material. When these reach the surface, they cause surface deformations which can be detected using piezoelectric transducers [134], Analysis of these signals in terms of their relative arrival time at a group of sensors and the characteristics of the wave itself allows the initiation and growth of damage to be identified and located [135], [136]. This method has advantages over other ultrasonic techniques in that it is passive and does not require an input signal to be generated and it is highly sensitive [137]. The following sections detail the particular experimental setup used in this work and outline the methods used to locate the damage which occurs.

3.4.1.1 AE wave mechanisms

Emission from AE sources can be categorised as either transient or continuous. Continuous AE signals come from sources such as machine vibrations, friction and flow or leakage noise. Transient waves which are used in this work, are burst type signals with an obvious start and end point which originate from sources such as abrupt and permanent changes in material including fractures, crack growth, corrosion and defect related deformation processes (Vallen [138]).

If the two surfaces of the structure through which these waves propagate are sufficiently close together for example in the case of a plate as we have here, many reflections and mode conversions occur. The waves couple together into more complex surface waves known as Lamb waves. Two families of Lamb wave modes exist: the symmetric or extensional modes which are mostly in the plane and the asymmetric or flexural modes which are mainly out-of-plane. Both can be seen in Figure 3.9. Within these two modes, there are particular frequencies which carry the majority of the elastic energy. These are known as the zero order modes and are designated S_0 (symmetric) and A_0 (antisymmetric). Higher order wave modes exist, however, they have lower amplitudes and contain little energy and are often difficult to detect.

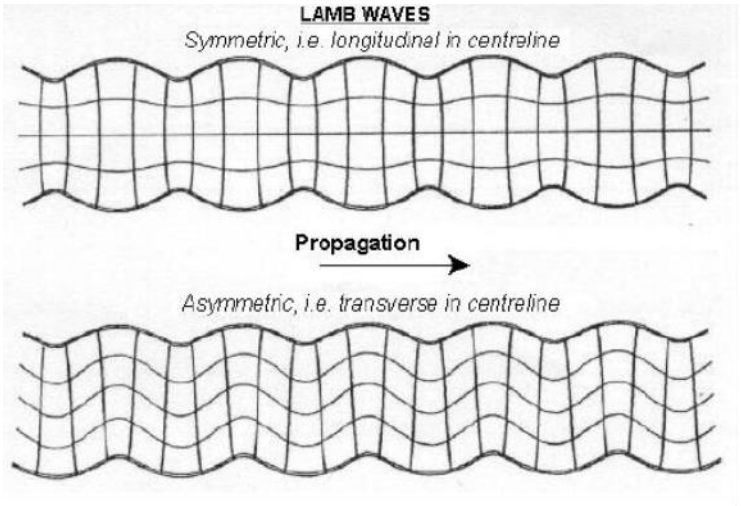

Figure 3.9: Lamb wave modes in a solid plate[139].

For a fixed plate thickness, different frequency components of the Lamb waves travel at different velocities. This variation is plotted in dispersion curves such as the one shown in Figure 3.10 with velocity plotted on the vertical axis and frequency (or thickness-frequency) on the horizontal axis (in this case generated using the commercially available, DISPERSE software).

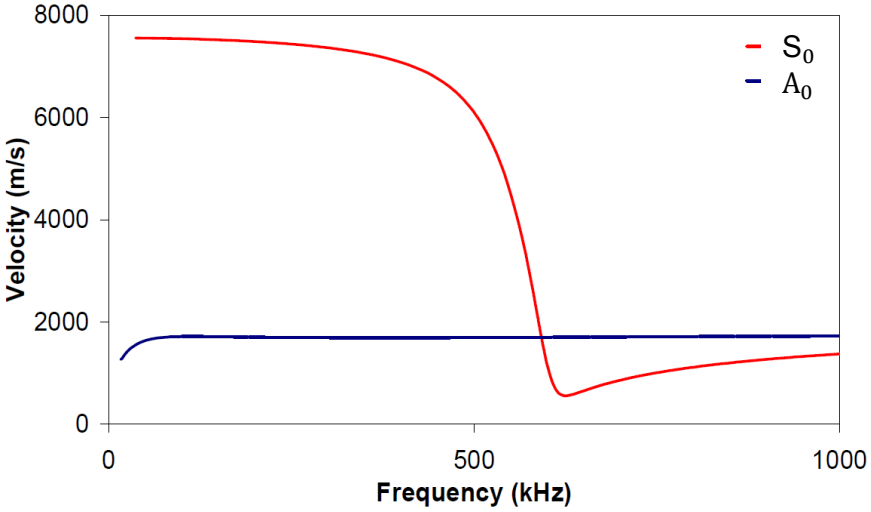

Figure 3.10: Typical dispersion curves for a 2.15mm thick cross-ply laminate[38].

From the figure, it can be seen that the S_0 mode travels at a higher velocity at low frequencies with the velocity determined by the in-plane stiffness of the plate. The A_0 mode however is slow and highly dispersive, because its velocity is determined by the out-of-plane stiffness of the plate (which is much lower) and depends strongly on thickness. This difference results in the form of the transient wave an example of which is shown in Figure 3.11 in which we can see that the So mode which travels fastest, arrives first, followed by the A_0 mode which is slower.

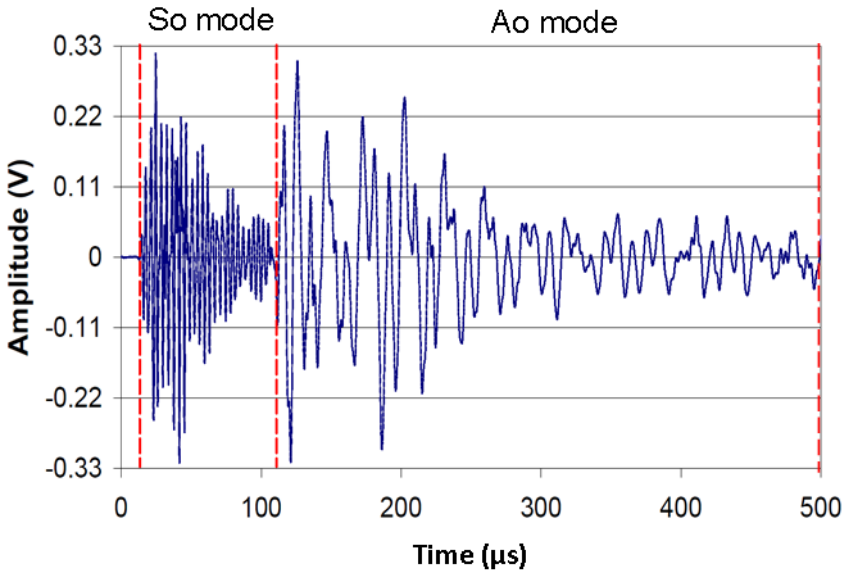

Figure 3.11: A typical AE lamb wave with signal modes separation.

A full understanding of the effects of propagation on the AE signals is essential for AE analysis particularly when considering anisotropic materials such as the Glare® material used in this study because the material properties and therefore the propagation characteristics vary with direction which needs to be accounted for particularly for example when dealing with location. More information can be found in Rindorf [139], Pollock [140] and Gorman and Prosser [141].

3.4.1.2 AE sensors

An acoustic emission sensor is a piezoelectric element that produces a measurable voltage signal which is proportional to the physical parameter it is monitoring.

In order to detect the surface displacement resulting from an AE event, suitable piezoelectric transducers are used. A typical piezoelectric transducer construction is presented in Figure 3.12. When stress waves (Lamb waves) arrive at the specimen surface, small displacements will occur. The piezoelectric element detects this mechanical movement and converts it into an electrical signal. The frequency response of the transducer is defined by the geometry.

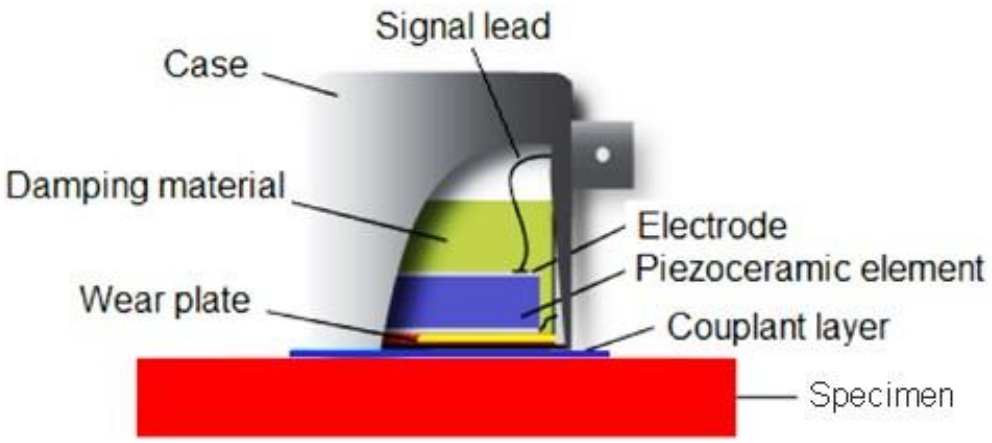

Figure 3.12: Schematic diagram of a typical AE sensor bonded on a specimen surface (Figure reproduced from [142]).

Generally, AE sensors are categorised into two types; wideband and resonant. Resonant sensors are biased towards particular frequencies, at which the piezoelectric material oscillates at a greater amplitude than at other frequencies. The working range of a typical resonant or narrow-band sensor within 1 MHz span is presented in Figure 3.13 for a sensor with a resonant frequency of 0.29 MHz. This behaviour improves the detection sensitivity if the expected frequency of the desired signals matches the resonant frequency of the transducer.

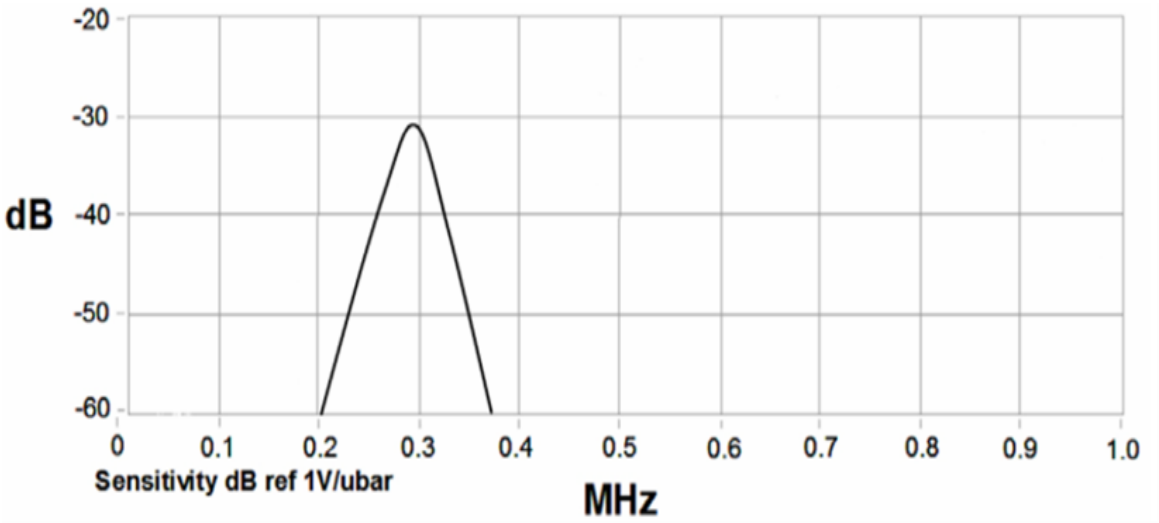

Figure 3.13: Theoretical resonant frequency transducer response [143].

Wideband sensors have a flatter frequency response and work across a much larger frequency range than that of resonant sensors whilst maintaining a good level of sensitivity. A typical flat frequency response is presented in Figure 3.14. Wideband sensors are often used in research applications, especially when frequency analysis or identification of wave modes is required.

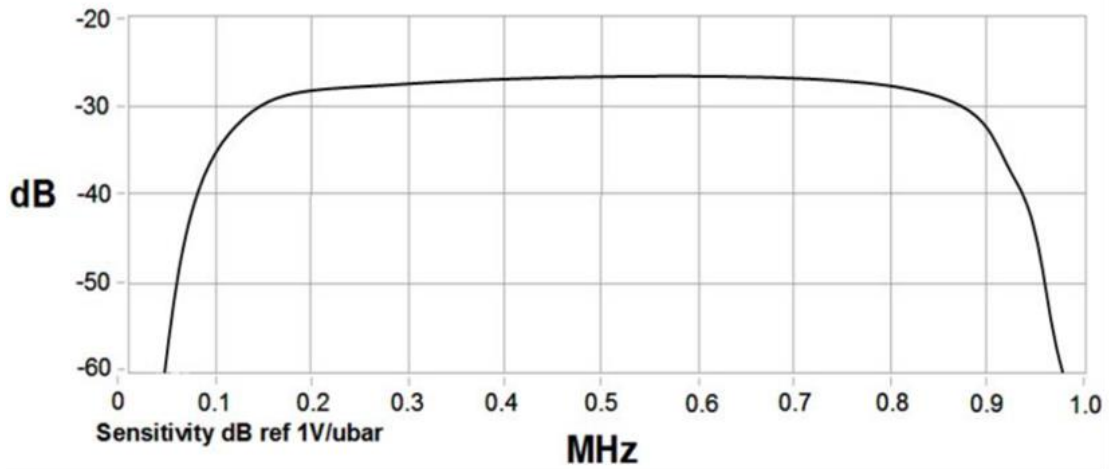

Figure 3.14: Theoretical frequency response of a wideband sensor [143].

In this study, two types of sensors were used, the WD wideband and Nano-30 resonant sensors, both manufactured by Mistras™ Group. The working frequencies, resonant frequencies and dimensions of both sensors are given in Table 3.1, with examples of typical calibration certificates for each shown in Figure 3.15. The Nano-30 which has clear peak frequency at approximately 300 kHz (seen from the calibration certificate) has an 8 mm diameter and is therefore most suitable for mounting on small specimens or those in which only a small area is available for mounting the sensor. The WD wideband sensor which has a relatively flat frequency response without any dominant peaks has a higher resonant frequency in comparison and can therefore be used to localise damage in complex structures such as the Glare® laminate used here which generate a range of frequency activity during damage initiation and propagation which is difficult to distinguish using low resonant frequency sensors.

Table 3.1: Manufacturers specifications of the AE sensors used throughout this work [144].

Sensor Type	Dimensions $d^* \times t^*$ (mm)	Operating Frequency Range (kHz)	Resonant Frequency (kHz)
Wideband (Mistras™ WD)	18 × 17	100-1000	650
Resonant (Mistras™ Nano-30)	8 × 8	125-750	300

(d^* = sensor diameter, t^* = sensor thickness)

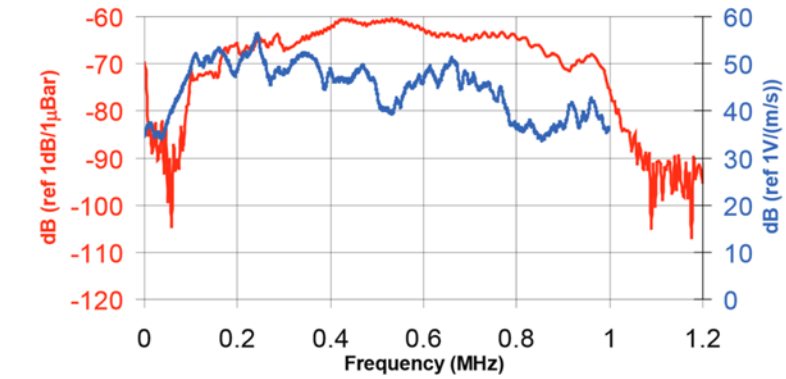

(a) WD

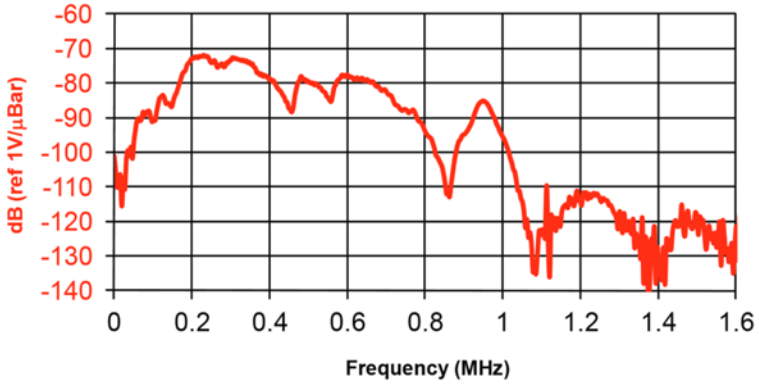

(b) Nano 30

Figure 3.15: Typical calibration certificates for (a) WD and (b) Nano-30 sensors (Sensitivity dB ref. 1 V/µbar).

3.4.1.3 Sensor mounting and acoustic couplant

The quality of the signals recorded by the AE sensors is critical to the success of the test method. If the sensor is placed directly on the specimen surface a very weak signal is produced by the sensor. At the interface, air gaps (due to the microstructure of the two contacting surfaces) cause energy transmission loss in the acoustic wave because the acoustic impedance of air is much lower than that of the test specimen and the sensor surface. Poor quality signals will limit the test method's ability to detect defects in a structure. To ensure good acoustic wave transmission between the sensor and the specimen and to hold the sensor in position, a couplant needs to be used. A couplant can be defined as any material which aids the acoustic wave transmission between

sensor and specimen surface by filling any gaps between the two surfaces and expelling the air to increase the transmission of energy. In order to achieve the optimal energy transmission between the sensor and the specimen surface, correct couplant selection is essential. There are many considerations when selecting the correct couplant for an AE test such as test duration, couplant stability, the frequency of sensors removal, test environment and the type of wave to be detected. According to [145] the selected couplant should:

a) Be appropriate to the test environment;

b) Not cause any damage to the structure or transducer;

c) Be suitable for the type of motion detected.

The different types of couplants used include liquid, gel, grease and adhesive couplants. Silicone rubber compound adhesive was used in this work because it can be applied as a fluid to achieve a thin, bubble free couplant and at the same time provide a permanent bond between the sensor and the structure under test [143]. This thin layer can provide excellent sound transmission with a relatively strong bond. Furthermore, silicone rubber compound works well on rough surfaces and has good resistance to bond failure if surface movement might occur during the test and is therefore suitable for vertical mounting applications. This type of bond enables easier sensor removal after use with lower risk of sensor damage compared with other commonly used methods such as cyanoacrylate bonding.

In this study, a silicone couplant (multi-purpose silicone sealant Loctite™ 595) was used at the interface. A mechanical clamp was applied initially as shown in Figure 3.16 and then removed when the silicone was dry dried after 24 hours.

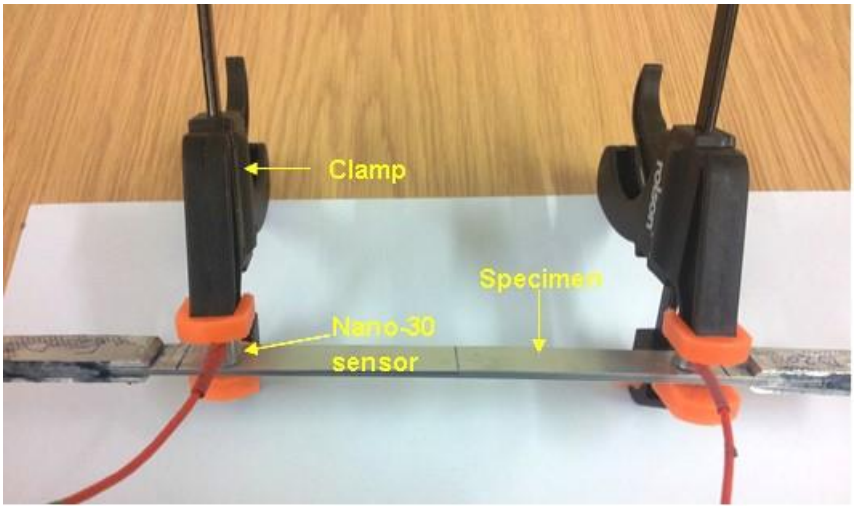

Figure 3.16: AE sensors position on the specimen with proposed mechanical clamp.

3.4.1.4 Data acquisition and storage

The PCI-2 data acquisition system manufactured by Mistras™ Group Limited (MGL) was used in this study (board diagram [5]). This system utilises a series of PCI-2 boards, each of which has two low noise AE channels with the potential to use up to four boards to provide a maximum of 8 channels. Data was recorded with a 5 MHz sample rate, recording over 1.2 ms for each hit received to ensure the capture of full waveforms since using high acquisition and processing rates along with the capture of full waveforms leads to a much deeper understanding of AE wave propagation.

3.4.1.5 AE pre-amplifier

A pre-amplifier located close to the sensor, provides gain to allow the signal to be translated along a length of cable (so, if necessary, the main AE hardware can be placed hundreds of metres from the structure under test) and low frequency filtering to remove undesirable mechanical noise, before passing to the processor for digitisation via a coaxial cable. The AE signals in this work were amplified using a 2/4/6 pre-amplifier which is a voltage pre-amplifier with switch-selectable gain ranges of 20, 40 and 60 dB (Figure 3.17). This amplifier has a band pass filter, with a range of 100–1200 kHz. The gain was set to the default value of 40 dB and a threshold of 45 dB was

chosen, which was just above the background noise level. This selection of threshold was based on previous research on isotropic materials.

Figure 3.17: PAC's 2/4/6 Pre-amplifiers.

3.4.1.6 Hsu-Nielson (H-N) source

After the sensor is installed and connected to the monitoring equipment, and before monitoring begins, the system sensitivity (performance) needs to be checked. This involves simulation of the AE source and the most common technique for doing this uses the Hsu–Nielsen source [146], shown in Figure 3.18. This technique is a cheap and effective method for sensitivity assessment and is based on pencil lead breaks. The test is conducted using the H-N pencil which uses a grade 2H lead with a 0.3 or 0.5 mm diameter which is broken at an angle of 30° against the surface of the structure being monitored. A repeatable angle can be achieved by using the PTFE guide ring the 'Nielson Shoe' which is fixed to the end of a retractable pencil. This generates an intense acoustic signal, similar to the natural AE sources that the sensors detect as a strong burst. The test also verifies the quality of the acoustic coupling between the AE sensor and the surface of the structure under test. It is essential to have enough AE sources (pencil lead breaks) at each node to provide reliable results and to eliminate erroneous data and this can be achieved by conducting at least five sources at each node [147]. In all tests during this investigation, a properly mounted sensor on a specimen's surface responded to a H-N source with an amplitude of 98 to 100 dB generated adjacent to the sensor.

The recommended procedure for pencil lead breaks is as follows[147];

a) The lead feed button on the pencil is pressed repeatedly until the lead protrudes.

b) The end of the lead is levelled with the end of the guide tube by pressing the tip of the pencil perpendicularly towards an even surface while the feed button is pressed down.

c) The button is pressed a few times to cause the lead to protrude about 3 mm.

d) The pencil is guided obliquely towards the test object until the guide ring rests on the surface.

e) The pencil is pivoted about the point of contact towards a steeper position to cause the lead to break.

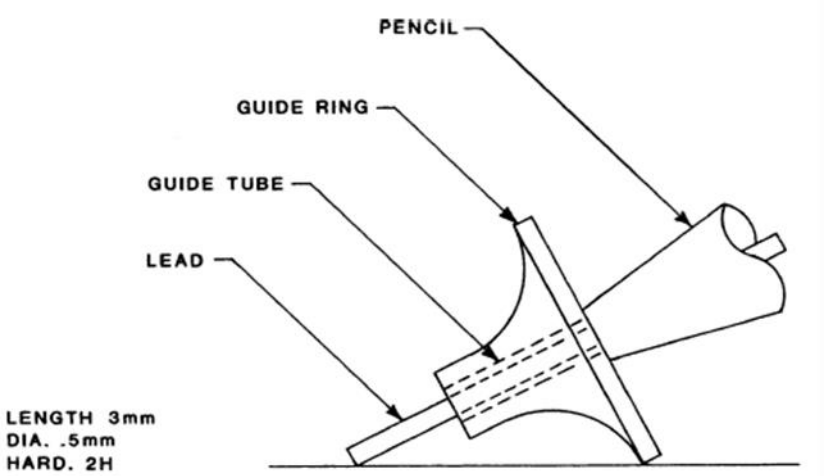

(a) Nielsen Shoe on Hsu Pencil Source.

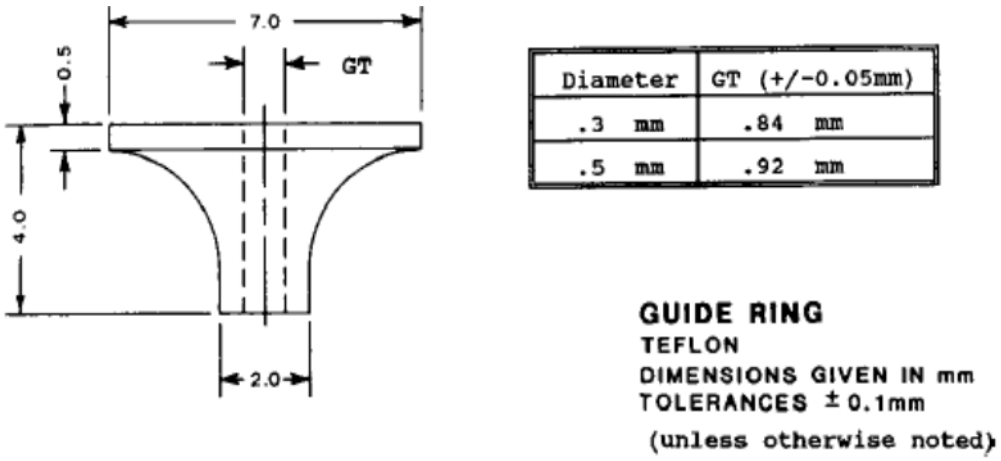

(b) Nielsen Shoe.

Figure 3.18: The H-N source method and guide ring, after [146].

3.4.2 AE source location

3.4.2.1 Time of arrival (TOA)

Identification of the location of a source of damage using AE data is traditionally achieved using a triangulation technique based on the difference in signal arrival times between the transducers located closest to the damage. By using a known wave velocity the location of an AE event can be estimated by minimising the error between the measured and calculated difference in arrival times. A detailed description of this method is given by Miller [148]. This technique has been used extensively to identify AE source location in isotropic and homogenous structures. However, in real structures the wave speed is rarely constant due to thickness changes and anisotropy (for example in composite materials where the wave velocity is dependent on the propagation direction with the wave velocity of the fastest propagating mode being considerably higher in the fibre direction). In addition to these, geometric features such as holes, lugs and structural discontinuities will have a considerable effect on the propagation path and velocity [68, 149, 150].

These factors mean that the assumptions relied upon by the TOA technique are invalid in certain circumstances and hence will introduce errors in the source location calculation. In order to improve arrival time estimation, a number of approaches have been investigated. The method used in this study is Delta-T source location which is described next.

3.4.2.2 Delta-T source location

As discussed in the previous section, one of the major assumptions made for TOA location is a constant wave velocity. It is known that due to their inhomogeneity, wave velocities in composite materials exhibit a directional dependency, thus creating an inherent inaccuracy in location. To overcome the location problems created by the complexity of these structures and inhomogeneity of materials a novel method of

source location has been developed in which an AE location array is mapped with an H-N source placed at a grid of known positions. A detailed description of the “Delta-T” mapping technique which showed an improvement over TOA location of over 50% in complex structures can be found in Baxter [143]. Improved location using the “Delta-T” Technique requires a number of steps according to [38] as follows:

- **Determine the area of interest** - Delta-T source location can provide complete coverage of a part or structure or it can be employed as a tool to improve source location around specific areas of expected fracture, which could be identified via finite element modelling.
- **Construct a Map System** - A grid is placed over either the entire component or a specific area of interest within which AE events will be located; the higher the resolution of the grid the greater the accuracy. The grid resolution can be increased around features of interest but should not be smaller than one wavelength, this being the minimum location resolution possible. It should be noted that sources are located with reference to the grid and not the sensors and it is not required that sensors be placed within the grid.
- **Obtain time of arrival data from an artificial source** – An artificial source (nominally an H-N source) is conducted at the nodes of the grid to provide AE data for each sensor. The artificial source is performed several times at each node to provide an average result and to eliminate any erroneous data. It is not essential to have AE data from every node in the grid because missing data points can be interpolated from surrounding nodes.
- **Calculate Delta-T map** – Each artificial source results in a difference in arrival time or Delta-T for each sensor pair (an array of four sensors has six sensor pairs). The average Delta-T at each node is stored in a map for each sensor pair. The resulting maps can be visualised as contours of constant Delta-T, such as those shown in Figure 3.19 for a steel plate containing numerous holes.

- **Locating real AE data** – The Delta-T values from a real AE event are calculated for each sensor pair. A line of constant Delta-T equivalent to that of the real AE event can then be identified on the map of each sensor. By overlaying the resulting contours, a convergence point can be found that indicates the source location. As with time of arrival, a minimum of three sensors is required to provide a point location and more sensors will improve the location. In theory, all the lines should intersect at one location, however, in practice, this is not always the case. Thus in order to estimate a location all convergence points are calculated and a cluster analysis provides the most likely location.

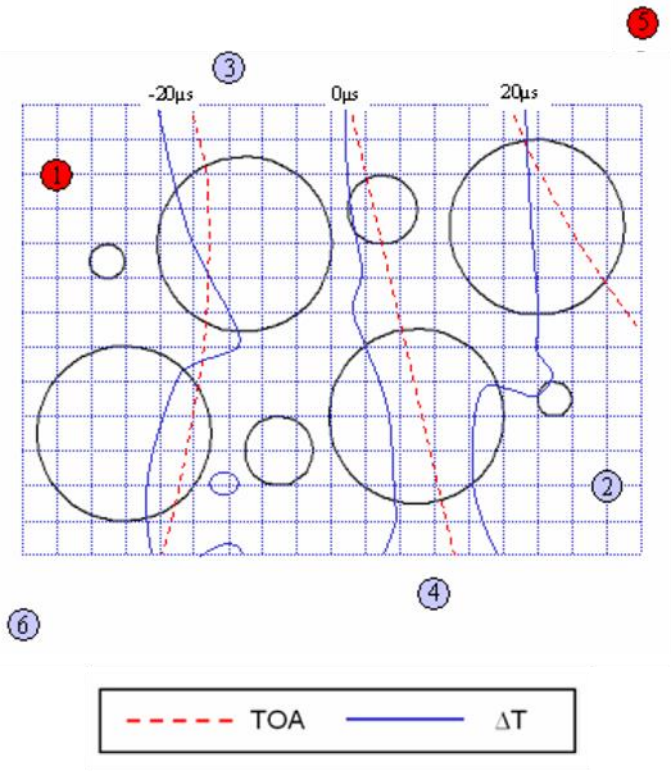

Figure 3.19: An example of a Delta-T location map in a steel plate containing holes [143].

3.5 High magnification video camera

A single video camera with high magnification micro-lenses was used to capture images to measure the crack length through the thickness of the doubler specimens used for the fatigue tests in chapter 7. This was done using a Q-400 Camera (focal length 75 mm, sensor size 2/3”-CCD and minimum object distance (MOD) 700 mm)

fitted with C-mount compact Pentax Ricoh precision lenses manufactured by Jos. Schneider Optische Werke Kreuznach GmbH (Figure 3.21). Extension tubes were used to increase the image distance between the lens and the camera sensors, allowing the lens to focus on objects at a shorter distance than would be possible without a spacer (Figure 3.21). This decreased object distance increases the magnification of the image on the camera sensor while decreasing the depth of field. In these experiments, a two C/CS mount lens extension tubes each 40 mm long were to create high-resolution images of the area of interest (see Figure 3.21).

This test was conducted under monotonic loading and the images were captured manually, taking snapshots approximately every 1 kN and then stopping the test when the pre-cracked length reached 1mm. This test was repeated for a series of specimens. Specimens were polished using a silicon carbide abrasive paper with a grade 1200 Cw and then cleaned using an acetone cleaner to get a smooth and shiny surface for good images and then labelled with a scale unit of 1 mm using a thin marker pen. An image taken through the thickness of the sections is shown in Figure 3.20 from the pre-cracked doubler specimen.

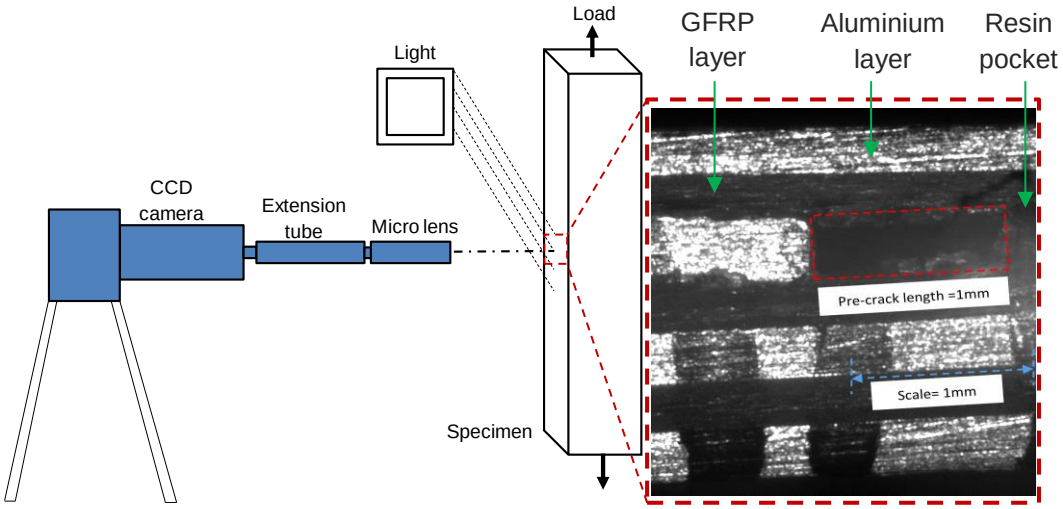

Figure 3.20: Micro-video camera setup for through-thickness crack measurement left and 2D micro-image for pre-cracked doubler specimen (particularly doubler joint section) right.

Figure 3.21: (a) C-Mount compact micro lenses, (b) Extension tube set.

3.6 Digital image correlation (DIC) system

Digital Image Correlation (DIC) is an optical measurement technique that can be used to carry out full-field, non-contact, two or three-dimensional measurement of the shape, displacements and strains of the specimens throughout testing [151]. By monitoring surface profile in real time this information can then be used for example to provide useful information to enable the user to distinguish possible failure mechanisms such as delamination.

DIC works by directly detecting the surface displacements of the structure under investigation from digital images of a random speckle pattern applied to its surface using a process of pattern recognition and tracking. Using either 1 (for 2D tracking) or 2 (for 3D tracking) camera. As the test proceeds images captured from the deformed specimens are compared with a reference image taken prior to testing and therefore representative of the undeformed specimen to match subsets of pixels (square sets of

pixels as indicated by the red box in Figure 3.22) using an image correlation algorithm [152] and tracking these throughout the test to allow displacement profiles to be determined. For each pair of image subsets are moved through the entire field of view with a fixed increment or step size (the number of pixels that the subset is moved within the field of view for each displacement calculation) to characterise the displacement across the whole field of view.

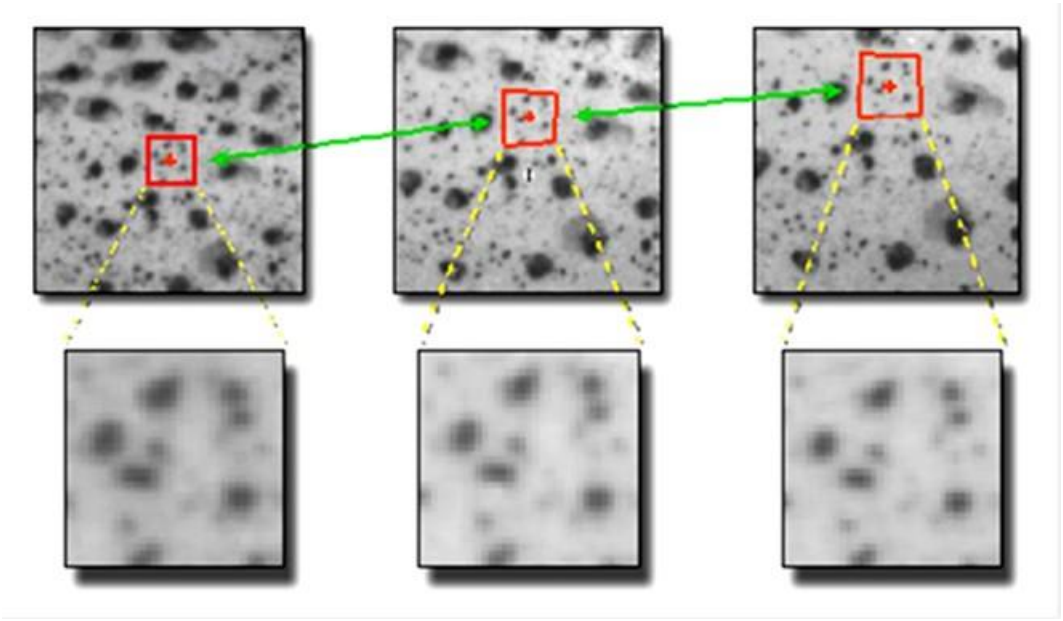

Figure 3.22: DIC Image correlation process example, Figure reproduced from correlated solutions [152].

3.6.1 Speckle pattern

Specimens need to be prepared via application of a random speckle pattern on their surfaces. This can be done in a number of ways depending on the size of speckle pattern required. In this work it was achieved by first spraying a uniform white primer to the specimen surface. A fine speckle pattern was then created using black primer, applying only light pressure to the release valve to get a random speckle with homogenous density (Figure 3.23).

Figure 3.23: Speckle pattern of the pristine specimen used in buckling tests (Chapter 4).

3.6.2 DIC Calibration

Calibrating the DIC system is key to ensuring that the measured results are accurate. DIC calibration provides the metric information to relate the ideal model of the camera to the actual physical device and to determine the position and orientation of the cameras with respect to a global reference system. This information includes two kinds of parameters, intrinsic parameters and extrinsic parameters. The intrinsic parameters indicate the internal geometric and optical characteristics of the camera, such as the focal length of the lens, lens distortions and the distances between the lenses and the CCD image device. The extrinsic parameters indicate the external geometric relation between the camera and the specimen, in terms of a rotation matrix and a translation vector. With the calibration data, the DIC system can translate the image coordinates to the geometric coordinates.

The cameras are calibrated for a given test space using a calibration target (Figure 3.24) chosen based on specimen size and working distance. The target should be between 100% and 200% of the desired field of view and should be positioned a suitable distance from specimen according to the type of lenses used. The target consisting of a grid of dots of known spacing is placed in front of the camera. A series

of images are acquired rotating the target between images. Based on these images and information about the grid the intrinsic and extrinsic parameters can be calculated and the system is calibrated.

Figure 3.24: Calibration target.

3.6.3 DIC set-up

The set up used in this work to monitor the buckling and postbuckling behaviour of the specimens is shown in Figure 3.25. A pair of greyscale cameras (in this case two 2/3-inch grey scale CCD Limess™ sensors), each with a resolution of 1600 × 1200 pixels, fitted with lenses of focal length 28 mm to enable a working distance of (300-600 mm) were then used to capture the movement of the speckle pattern applied to the specimen. The cameras were fitted to a bar mounted on a tripod and directed towards the specimen with a typical angle of 50^{o} between the two cameras as shown in Figure 3.25 [37]. Calibration was performed with a target comprising a 9 × 9 grid with dimensions 40 mm × 40 mm (Dantec Dynamics) (Figure3.24). A calibration residuum (the average uncertainty of the found markers in the unit of pixels and which should usually have a value of less than 0.3 depending on the type of calibration target used in the test [151]) of < 0.1 pixels was considered acceptable.

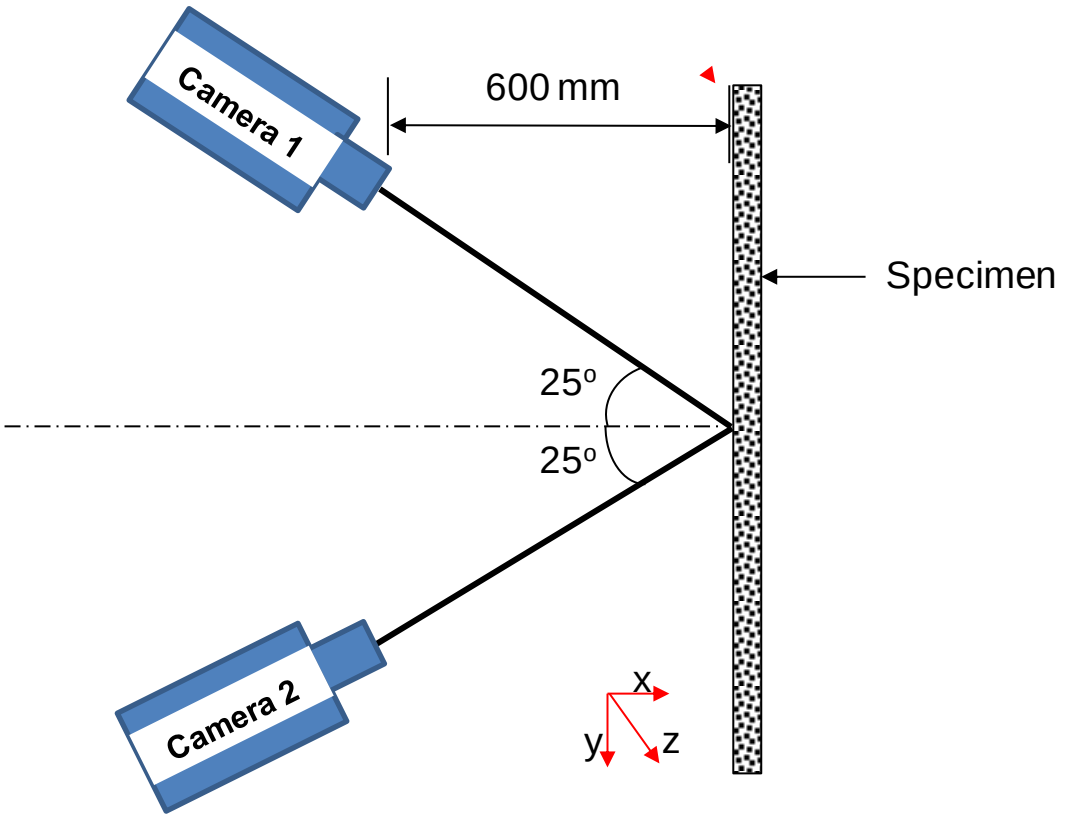

Figure 3.25: Schematic for the 3D DIC system calibration procedure.

Tests were lit using a HiLis™ monochromatic LED system. Images were captured manually in approximately 1 kN steps and post-processed using the ISTRA 4D software with a subset size 17 pixels. Whilst the default size of the subset is 29 pixels a number of studies have indicated that the optimum value is between 17 and 21 pixels [153]. The spatial resolution was 2 mm and was calculated based on the actual width of the specimen and the width of the DIC image in pixels. The default step size of 5 pixels which has been shown to be suitable for situations where the specimen exhibits a uniform or slowly varying displacement and strain response as is the case for the buckling experiments performed here was chosen in this study. A step size of 1 pixel was also considered but typically resulted in a significant amount of noise in the data that needed to be filtered out in the post-processing. A numerical investigation conducted by Wang *et al.* [154] using 1, 3, 5, and 7 pixels step sizes concluded that the influence of the step size on the displacement field is minor. Figure 3.26 shows an

example of the results from the 3D DIC system used in this work, presenting a typical contour of the out-of-plane displacements measured for the pristine far-field specimen under compression load. More details on experimental setup are given in Chapter 4.

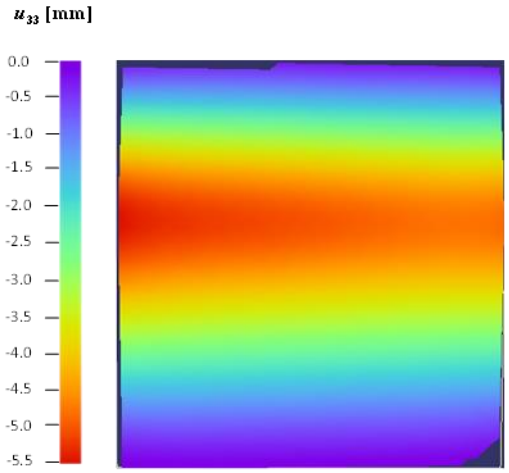

Figure 3.26: Typical DIC contour for the out-of-plane displacements of one of the pristine specimen used in buckling tests in Chapter 4.

3.7 Scanning Electron Microscopy (SEM)

The final technique discussed in this chapter is scanning electron microscopy which was used to allow the damage mechanisms present following the quasi static tests described in Chapter 4 to be identified and located. Sections were taken to enable areas both remote from and within the joints in the specimens to be examined for both splice and doubler features. These sectioned specimens were finished by grinding with wet silicon carbide paper and polishing with acetone cleaner. A carbon coating, which gives a more suitable matt finish in comparison to the alternative gold coating for metallic specimens, of 10-20 nm was applied by thermal evaporation. Specimens were then examined using a SEM type (FEI/Philips XL30 FEG ESEM) with the setup shown in Figure 3.27. Micrographs were captured under high vacuum using a 30 µm aperture and 20 kV accelerating voltage with a working distance of 10-12 mm between the specimens and the aperture.

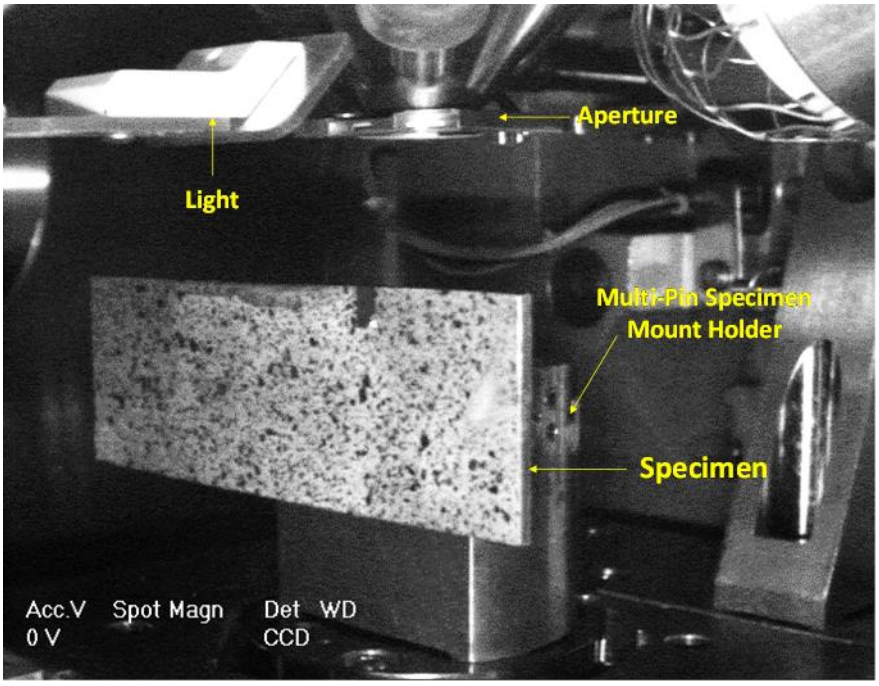

Figure 3.27: SEM experimental setup.

3.8 Chapter summary

The techniques used to manufacture the Glare® specimens used for fatigue testing, along with details of the acoustic emission, DIC, high magnification video camera and SEM utilised throughout this research are described in this chapter.

Chapter 4 - Buckling/Postbuckling of FMLs with Internal Features: Experiments

4.1 Introduction

This chapter focuses on examining the effect of two different types of joints (doublers and splices) with and without artificial delaminations in addition to the effect of a circular artificial delamination, on the buckling and post buckling characteristics of Glare® fibre-metal laminates (FMLs) plates based on a series of experiments. Specimens containing these joints were tested under in-plane compression and monitored using digital image correlation (DIC) for visualisation of three-dimensional full-field displacements and acoustic emission (AE) monitoring to detect damage. The AE analysis was implemented using the novel Delta-T location algorithm used for the first time to monitor damage initiation and propagation in complex FML structures, enabled the detection and location of damage events. Results were validated using Scanning Electron Microscopy (SEM) to determine the damage mechanisms present. The experimental results were validated via three-dimensional Finite Element (FE) models generated using Abaqus/Explicit software and a detailed explanation of this numerical analyses and the FE models used is discussed in Chapter 5.

4.2 Experimental methods

4.2.1 Specimen design

Specimens measuring 140 mm × 80 mm (unsupported dimensions; when clamped 100 mm × 80 mm) were manufactured incorporating longitudinal splice and transverse doubler features as shown in Figure 4.1. These specimens were made by Airbus

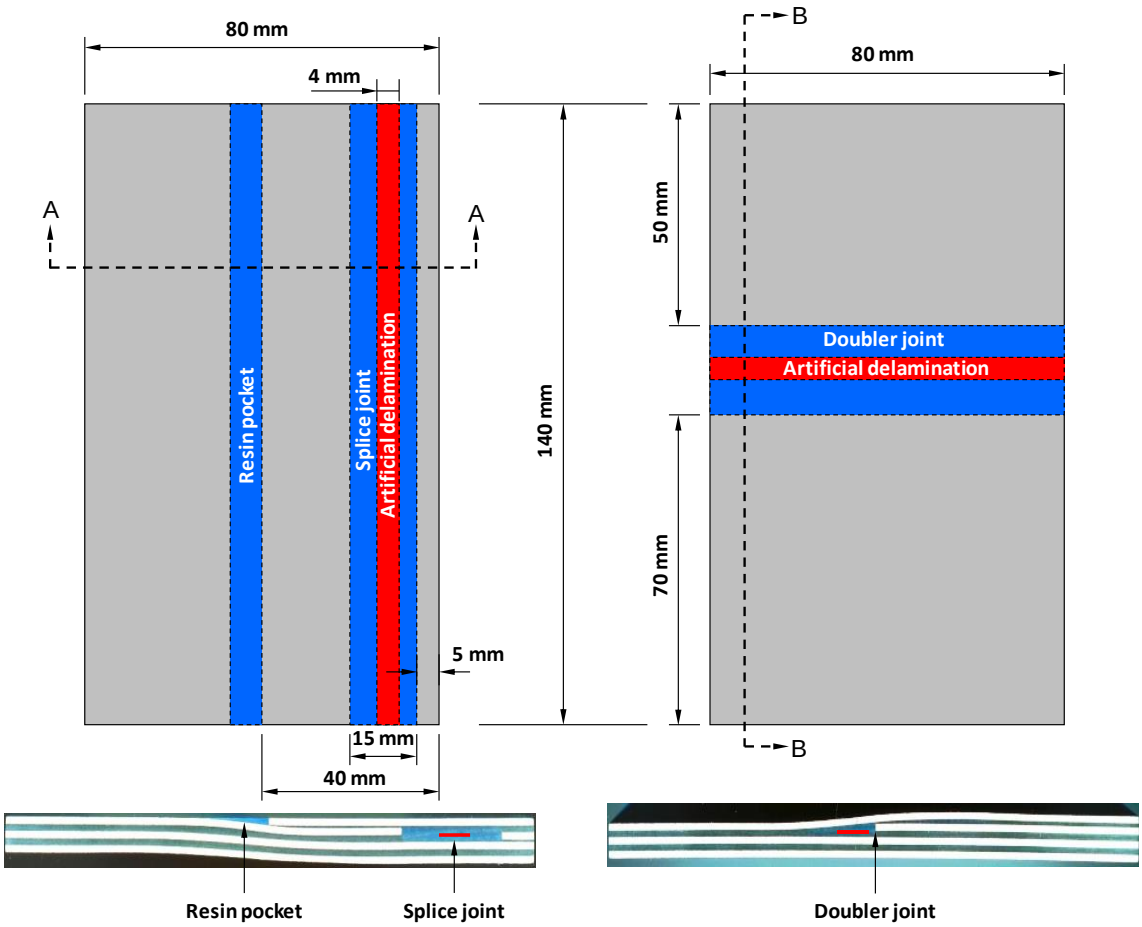

Figure 4.1: Layout of Glare® 4B specimens, (a) longitudinal splice and (b) transverse doubler.

Germany GmbH from 0.4 mm thick sheets of aluminium alloy 2024-T3 and Hexcel™ S2-glass/FM94 glass fibre reinforced polymer (GFRP) unidirectional prepreg. Each GFRP 'layer' has 3 plies with the layup [90°/0°/90°] and a cured ply thickness of 0.133 mm. The layup on one side of the joint was '3/2' (three layers of aluminium and two layers of GFRP prepreg) and on the other '4/3' (four layers of aluminium and three layers of prepreg), according to the standard designation of commercial 'Glare® 4B' shown in Table 4.1[1]. Artificial delaminations were introduced by embedding a 4 mm wide strip of PTFE film of thickness 10 µm. This artificial delamination is representative of those which could potentially be generated during manufacturing.

In addition, specimens without splice or doubler features were also investigated. These

are referred to as 'far-field' specimens, since they represent the FML in regions far enough from the splice/doubler joint so that the latter do not influence their stress state when loaded. Two types of far-field specimens were considered, namely *pristine* and those with *artificial circular delaminations*. These delaminations had a diameter of 50 mm and were created by inserting a circular film of PTFE, 10 μm thick, into the interface between the first aluminium layer and the first GFRP ply, as shown in Figure 4.2.

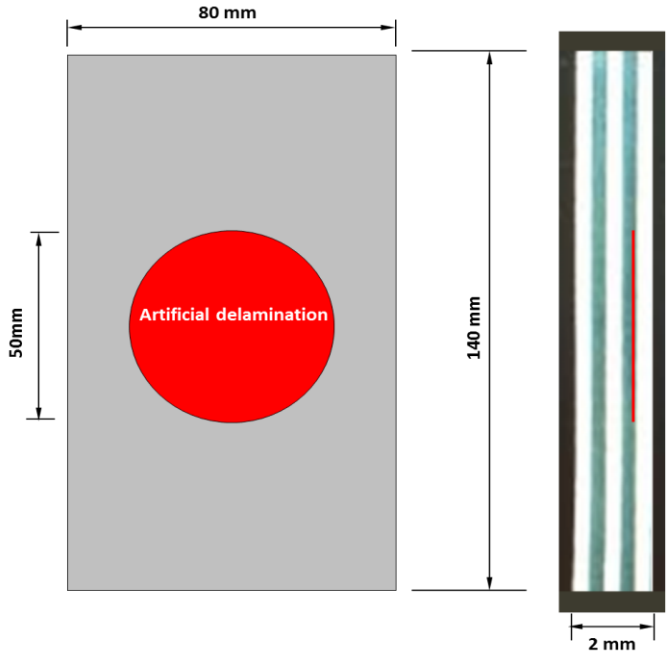

Figure 4.2: Layout of a 'far-field' specimen (i.e. without splice or doubler features) of Glare® 4B-3/2 with a circular delamination.

Table 4.1: Standard grades of commercial Glare® laminates[1].

Grade	Sub-Grade	Alloy	Metal sheet thickness [mm]	GFRP sub-laminate layup	Main beneficial characteristics
Glare® 1	-	7475-T761	0.3 – 0.4	0 / 0	fatigue, strength
Glare® 2	Glare® 2A	2024-T3	0.2 – 0.5	0 / 0	fatigue, strength
Glare® 2	Glare® 2B	2024-T3	0.2 – 0.5	90 / 90	fatigue, strength
Glare® 3	-	2024-T3	0.2 – 0.5	0 / 90	fatigue, impact
Glare® 4	Glare® 4A	2024-T3	0.2 – 0.5	0 / 90 / 0	fatigue, strength (especially in 0° direction)
Glare® 4	Glare® 4B	2024-T3	0.2 – 0.5	90 / 0 / 90	fatigue, strength (especially in 90° direction)
Glare® 5	-	2024-T3	0.2 – 0.5	0 / 90 / 90 / 0	impact
Glare® 6	Glare® 6A	2024-T3	0.2 – 0.5	+45 / -45	shear, off-axis properties
Glare® 6	Glare® 6B	2024-T3	0.2 – 0.5	-45 / +45	shear, off-axis properties

The far-field specimens were made by Airbus Germany GmbH as well from same grade of aluminium and GFRP materials described earlier for the splice and doubler specimens. The layup was '3/2' (three layers of aluminium and two layers of GFRP prepreg), according to the standard designation of commercial Glare® 4B shown in Table 4.1.

4.2.2 Test setup

The specially designed test rig shown in Figure 4.3 was manufactured from stainless steel 304. Specimens are held in place with two pairs of clamps. The frame was mounted in a Zwick® servo-hydraulic testing machine (fitted with a 500 kN load cell) as shown in Figure 4.4. The rig is designed such that when tension is applied, the loading plates apply a compressive load to the specimen with axial movement of the rig being facilitated by four bronze journal bearings. The machine was operated under displacement control with a crosshead velocity of 0.1 mm/min. A total of six types of specimens were tested, namely splice, doubler and far-field specimens with and without artificial delaminations, with two repeats each, totalling 12 specimens.

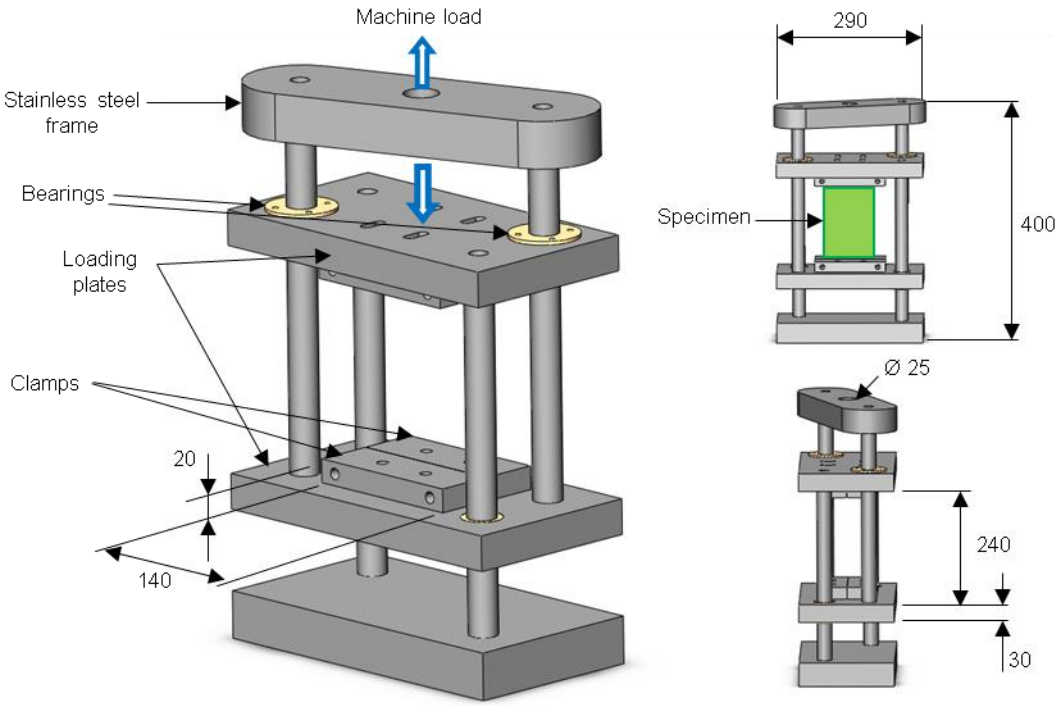

Figure 4.3: Buckling rig design (dimensions in mm).

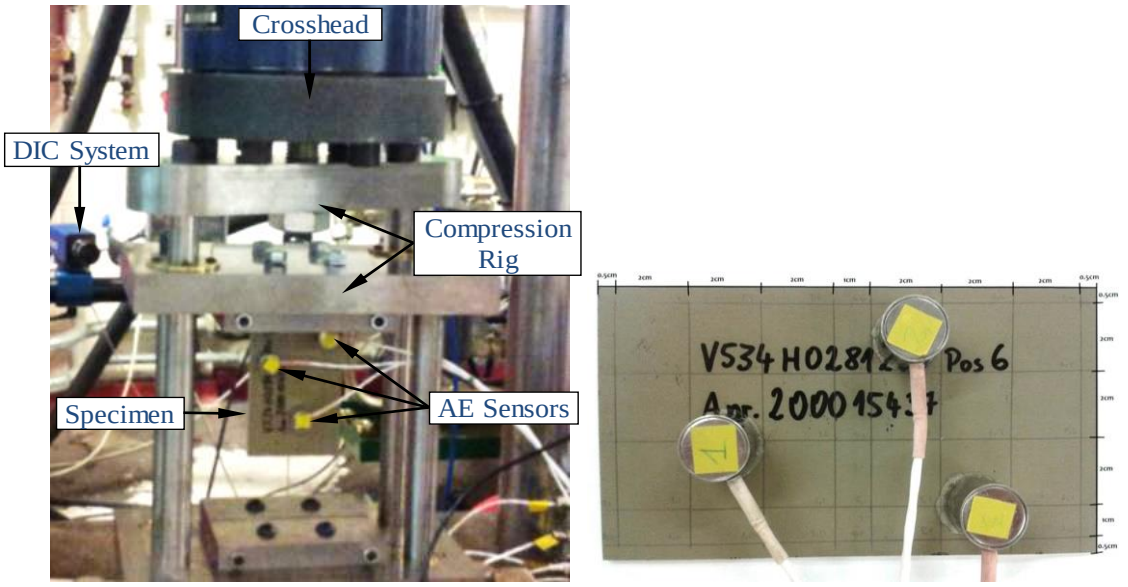

(a) (b)

Figure 4.4: Experimental setup (a) and position of WD AE sensors on the specimen (b).

4.3 Instrumentation

4.3.1 Digital Image Correlation (DIC) system

Specimens were monitored using a Dantec™ Dynamics Q-400 DIC system described in Chapter 3, Section 3.6.

4.3.2 Acoustic Emission (AE) system

Three Acoustic Emission (AE) sensors were mounted on both splice and doubler specimens to monitor damage events during the buckling and postbuckling regimes (see Figure 4.4). The 18mm diameter wideband (WD) sensors used in this work were supplied by Mistras™ Group and had a frequency range of 100-1000 kHz. These were chosen because they cover a wide range of waveform frequencies which enable them to detect the different types of energy produced from different materials incorporated into the Glare® laminate. As for the far-field specimens, four (Nano-30) AE sensors manufactured by Mistras™ Group were used. These have a frequency response range of 125-750 kHz and diameter of 8 mm and they were bonded onto the specimen as

shown in Figure 4.5. These sensors were used to monitor damage for the far-field specimens instead of the wideband sensors used for the splice and doubler specimens due to narrow space causing by relatively big size artificial delamination that need to be monitored. Both types of sensors were bonded to the specimens using multi-purpose silicone sealant Loctite™ 595. The sensors were connected to a Mistras™ Group PCI2 acquisition unit with a 45 dB threshold (as recommended by previous studies including Büyüköztürk and Taşdemir [155], Pearson [156] and Al-jumaili [134] for a wideband differential transducer) and a sampling rate of 5 MHz, recording over 1.2 ms to capture full waveforms, through pre-amplifiers with a 40 dB gain and a built-in band pass filter of 20-1200 kHz.

Event locations were calculated using the bespoke 'Delta-T Mapping' location algorithm described in Chapter 3 in section 3.4.2.2 In the present work the Delta-T method has been applied for the first time in the monitoring of damage development in Glare® laminates. The sensitivity and accuracy of the method make it a strong candidate for the monitoring of FML structures containing anisotropic laminae [157] and internal features (such as splices and doublers) which are prone to high cycle fatigue damage.

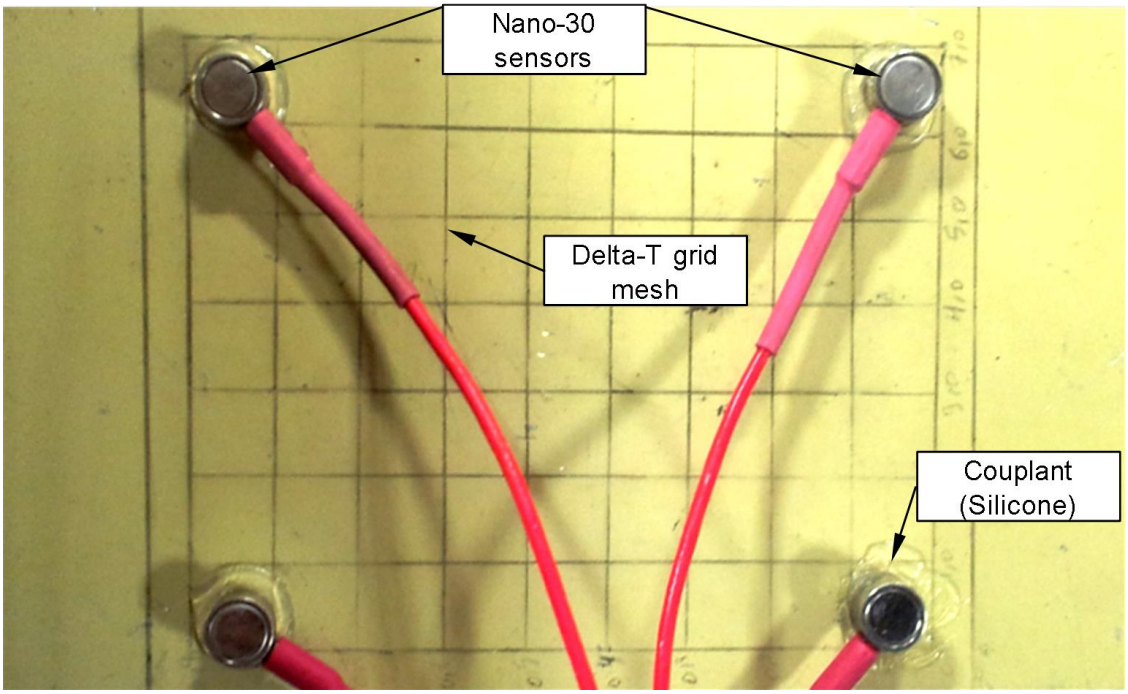

Figure 4.5: AE sensor positioning for far-field specimens.

4.3.3 Scanning Electron Microscopy (SEM)

Specimens were studied following testing using scanning electron microscopy to allow the damage mechanisms present to be identified and located. Sections were taken to enable areas both remote from and within the joints to be examined for both splice and doubler features (the locations at which these sections were taken are shown in Figure 4.6 for both splice and doubler specimens). These sectioned specimens were finished by grinding with wet silicon carbide paper and polishing with acetone cleaner. Specimens were then examined using a SEM type (FEI/Philips XL30 FEG ESEM) as shown in Figure 3.27. Further details on experimental setup are provided in Section 3.7.

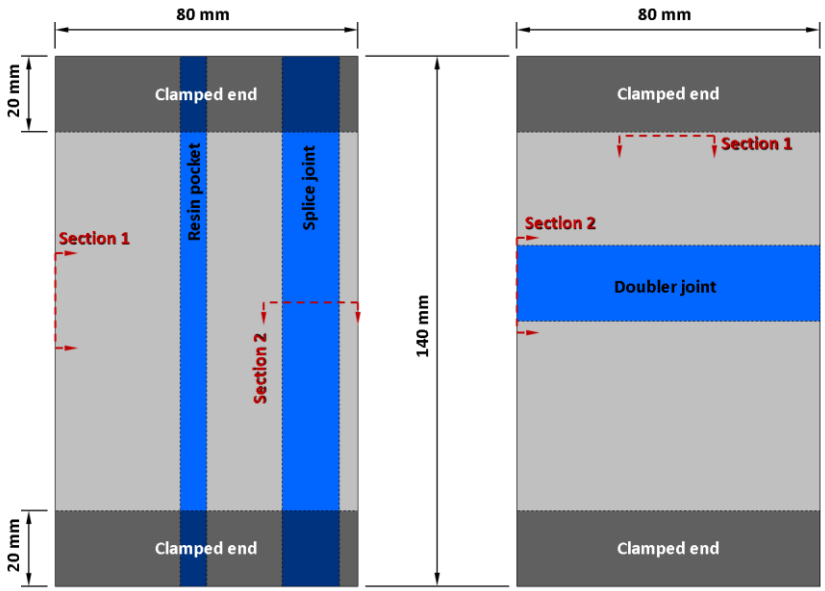

Figure 4.6: Sections of the Glare®4B specimen observed under SEM, (a) longitudinal splice and (b) transverse doubler.

4.4 Results and discussion

4.4.1 Splice specimens

Figures 4.7 and 4.8 show the load *versus* in-plane displacement curves and section stress *versus* normalised in-plane displacement curves for the splice specimens, respectively (Specimen 1 of the laminates with defects suffered from slippage in the rig

and has therefore not been considered). The normalised displacement is the ratio between in-plane displacement and initial specimen length, *i.e.* $\Delta x/l_0$, where l_0 = 100 mm for all specimens and section stress is defined as the load divided by the cross-sectional area of the specimen, while the. It should be noted that 'section stresses' are global measures and may not reflect the local stress states in each of the material constituents. Approximate 'lamina stresses' can be recovered during the initial elastic regime via the assumption of uniformity of in-plane strains. This will be discussed later in this chapter, based on the material strengths provided in Section 5.2.3. The in-plane displacements were obtained from the DIC data rather than the machine cross-head displacement as the former is more accurate (since it is not affected by the compliance of the machine). In terms of the ultimate compressive loads for the splice coupons the experimental values are 13.66 kN and 13.72 kN (corresponding to section stresses of 77.86 MPa and 78.20 MPa) for the specimens with and without defects respectively. The effect of the inserted delamination on both pre and postbuckling stiffness and ultimate strength therefore appears to be negligible. This could be due to the relatively small delamination size relative to the specimen size, or the fact once global buckling has started to occur the deformation of the specimen tends to close any delamination initiated by the insertion of this localised defect which is in front of the specimens neutral axis and therefore sits between plies which are under tension during bending, which consequently has little effect on the performance of the joint under compression.

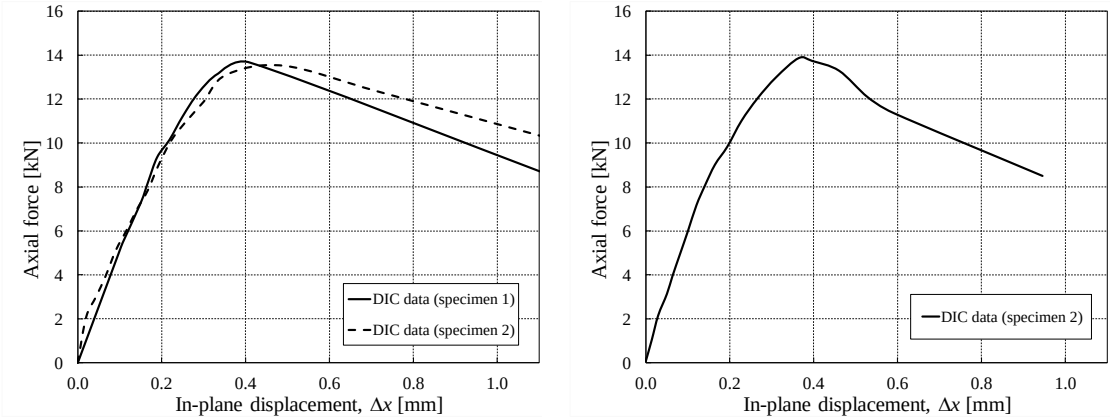

(a) (b)

Figure 4.7: Axial force versus in-plane displacement for splice specimens; (a) pristine and (b) with an artificial defect.

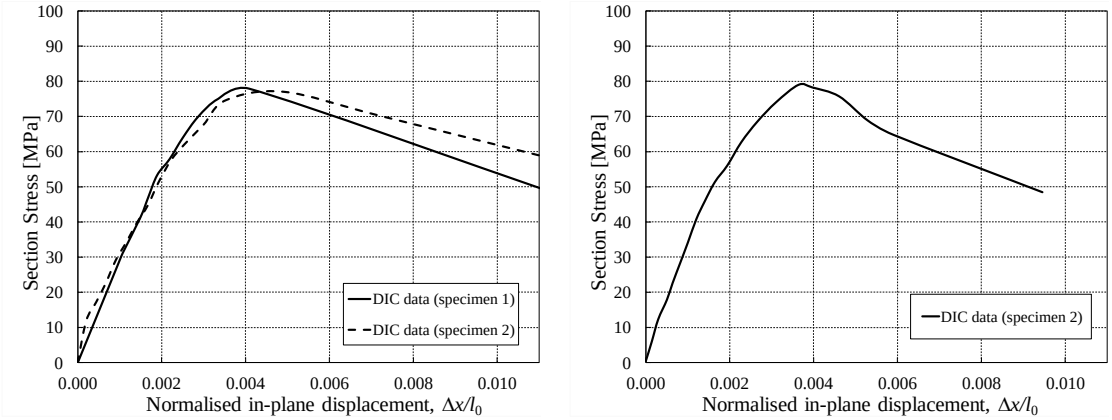

(a) (b)

Figure 4.8: Section stress versus normalised in-plane displacement for splice specimens; (a) pristine and (b) with an artificial defect.

Figure 4.9 shows the contours of the out-of-plane displacement at initial buckling (in-plane displacement Δx = 0.166 mm), peak load (Δx = 0.385 mm) and postbuckling (Δx = 0.809 mm), obtained from DIC data. These are compared with AE location data using the Delta-T algorithm described earlier. The results presented are for splice specimens incorporating an artificial defect, but the pristine specimens presented very similar behaviour indicating that the effect of the damage introduced on the mode shape and the amplitude of out-of-plane deformations is negligible. The plate is seen to buckle with a single half wave length in the loading direction as expected for a plate with free longitudinal edges under compression. Deformations to the left of the joint in

the thinner region of the specimen are higher than those to the right again as would be expected. With respect to the AE location data in Figure 4.9 and cumulative AE energy in Figure 4.10, at approximately Δx = 0.166 mm initially low-energy AE events are detected along the horizontal centreline in an area which coincides with the location of the embedded defect. This due to matrix cracking at the initial buckling load, as illustrated later by SEM micrographs (Figure 4.11). Then, at approximately Δx = 0.385 mm , a large number of high-energy AE events are detected all along the centreline of the specimen where the large out-of-plane displacements and high curvature at the ultimate compressive load lead to further matrix cracking, as also seen in SEM micrographs (Figure 4.12). Further events located in the area of the splice joint correspond to delamination initiation. Activity then begins to spread out along the joint at approximately Δx = 0.809 mm, indicating delamination in addition to shear damage in the matrix resin layers, with possible fibre breakage in 0^o fibre plies. Although some level of fibre failure is expected during the postbuckling regime, only indirect observations have been made via SEM as no clear 'kink band' is observed at these moderate levels of strain. Instead, fibre failure along 0° plies appear in the form of fibres with multiple fractures along their length, *e.g.* Figure 4.12 (b), which is likely to be a combination of fibre damage during the test with further damage during the cutting and polishing of SEM samples.

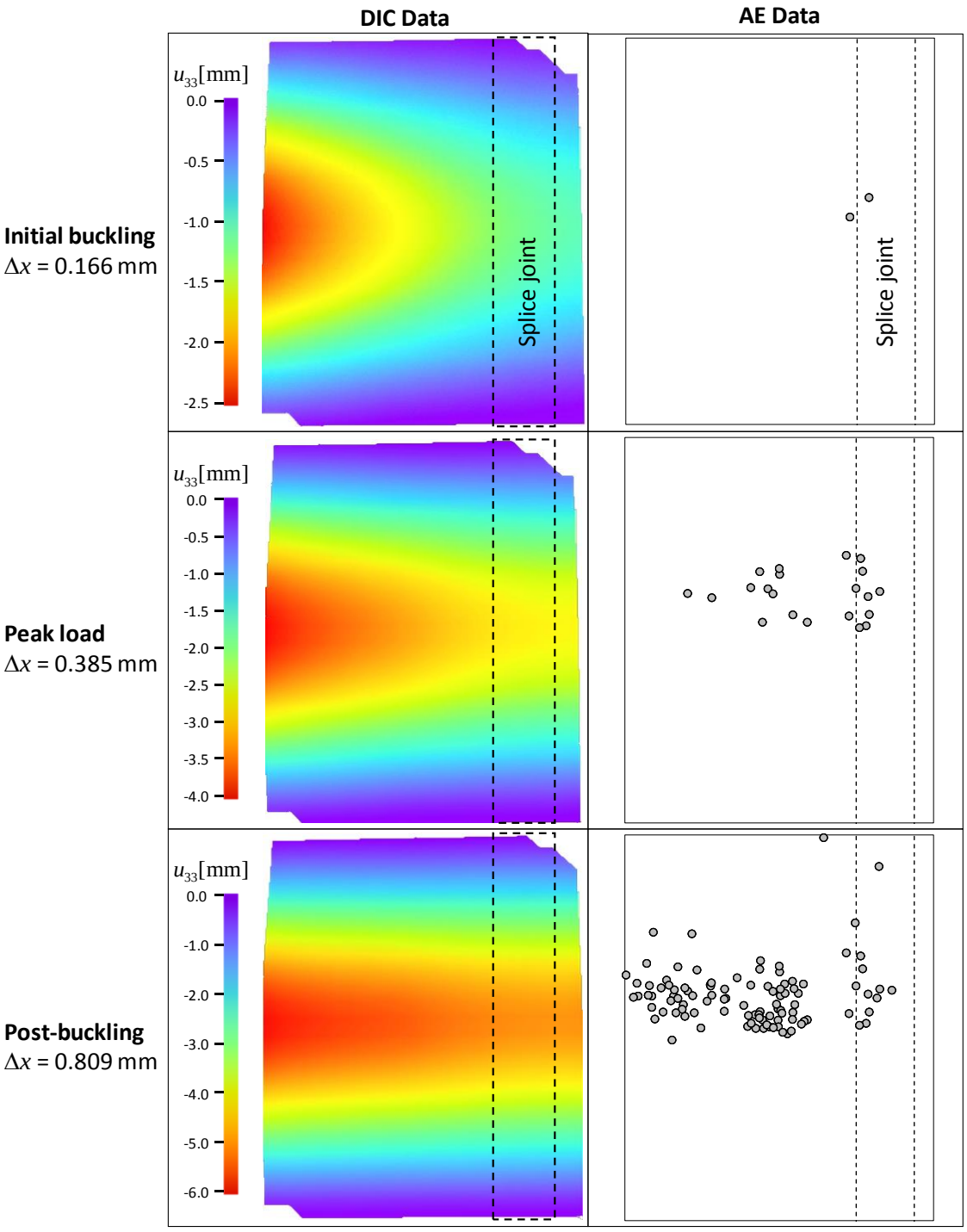

Figure 4.9: Contours of out-of-plane displacement, u_{33} (left) against location of AE events (right) for the splice specimen (with an artificial defect) at different in-plane displacements Δx (dashed lines indicate position of splice).

Figure 4.10 shows the cumulative energy of events occurring throughout the test period, against applied load. The first significant increase in the logarithmic cumulative energy occurs at an in-plane displacement of around Δx = 0.166 mm corresponding to

the matrix damage which accompanies initial buckling of the panel, indicating that AE can be used to predict the onset of buckling. A further large jump is observed when the load reaches the ultimate compressive strength at Δx = 0.385 mm indicating a high level of damage activity (potentially matrix cracking matrix shear damage, as suggested by the SEM micrographs) plus the initiation of macroscopic delamination, due to high levels of deformation and curvature at this point, as would be expected. This is followed by a gradual increase in energy which corresponds to delamination initiation and growth along the splice feature during postbuckling. Again, this interpretation is backed by the analysis of detailed nonlinear Finite Element models described in Section 5.4.1. [158].

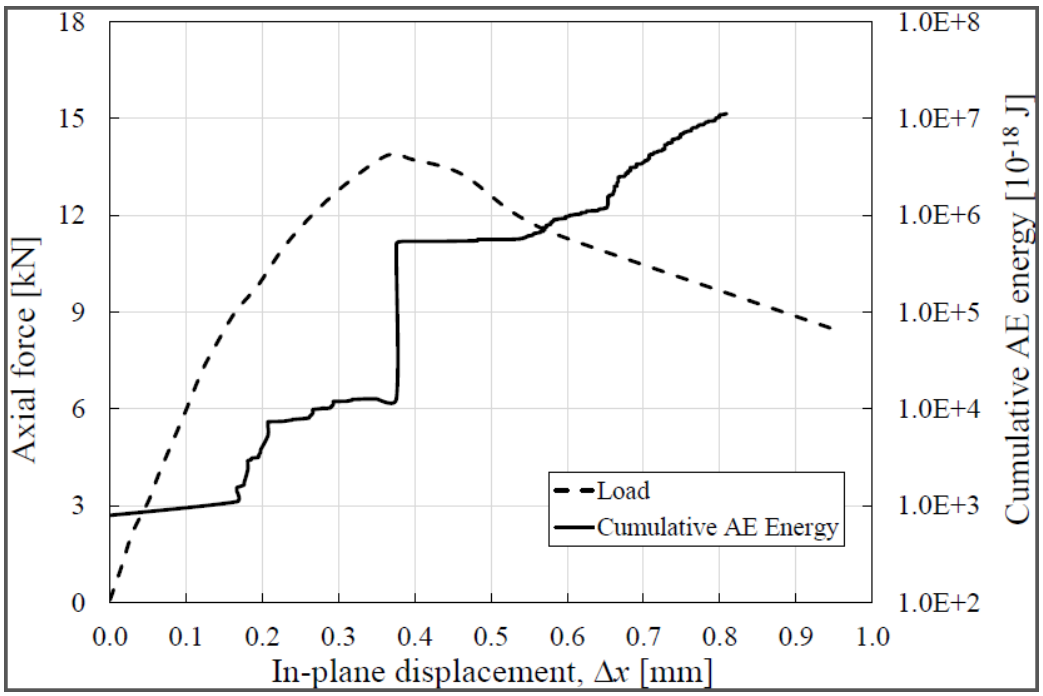

Figure 4.10: Load and cumulative AE energy versus in-plane displacement for the splice specimen with defect.

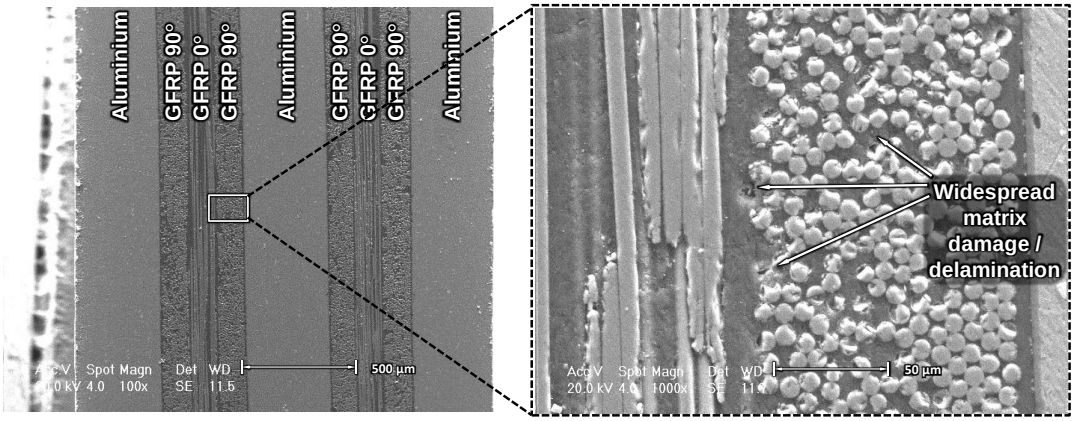

(a) (b)

Figure 4.11: SEM of splice specimens along Section 1 (side of specimen), with magnifications of (a) 100× and (b) 1000×.

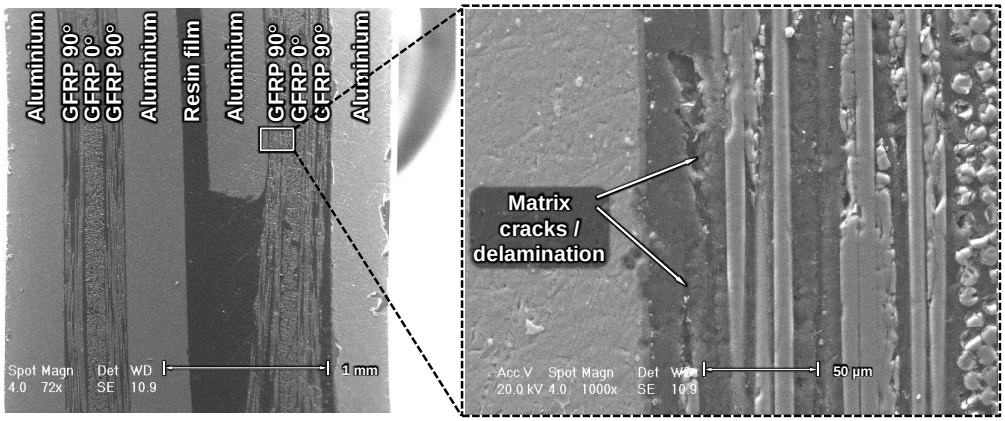

(a) (b)

Figure 4.12: SEM of splice specimens along Section 2 (across splice), with magnifications of (a) 72× and (b) 1000×.

4.4.2 Doubler specimen

The load *versus* in-plane displacement curves and section stress *versus* normalised in-plane displacement curves of doubler specimens with and without artificial defects are shown in Figures 4.13 and 4.14. As before, in-plane displacements were extracted from DIC data. The ultimate compressive loads for the specimens without defects are 13.78 kN and 13.69 kN (corresponding to section stresses of 85.27 MPa and 84.72 MPa) and for those with artificial defects are 14.65 kN and 15.49 kN

(corresponding to stresses of 90.66 MPa and 95.85 MPa). Clearly the presence of the defect is not having any significant impact on the buckling load of the doubler specimens, and this is believed to be for the same reasons as for the splice specimens. Using the concept of uniform strains, and utilising the material strengths presented in Chapter 5: Section 5.2, a simplified stress analysis shows that fibre damage will not occur in the 90^o GFRP plies outside the joint at peak load. Neither will matrix cracking nor shear damage between GFRP plies occur at this load for the same reason. Damage initiation is however predicted in the splice as the stresses in this thinner middle region are likely to exceed the ultimate normal and shear strengths for the FM94 epoxy resin.

Figure 4.15 shows the contours of the out-of-plane displacement for initial buckling (in-plane displacement Δx = 0.173 mm), ultimate load (Δx = 0.362 mm) and postbuckling (Δx = 0.824 mm), obtained from DIC data, which are again compared with AE event location data (Figure 4.15) and AE cumulative energy (Figure 4.16). The results shown correspond to one of the specimens with a defect but the pristine specimens give similar results. Out-of-plane displacements can be seen to be greatest along the doubler joint, which corresponds to the panel buckling with one half wave length along the length of the panel. It is also where a change in panel thickness occurs, with the thinner portion being above the joint. Examining the results from the acoustic emission monitoring, Figure 4.15, shows initial low-energy AE events detected in the upper portion of the panel just above the doubler joint, as well as at the point of highest curvature at around Δx = 0.16 mm corresponding to the onset of buckling. This is mostly due to matrix cracking as illustrated by the SEM micrographs (Figures 4.17 and 4.18). Then, at approximately Δx = 0.36 mm when the peak load is reached, a large number of high-energy AE events are seen (Figures 4.15 and 4.16). These again correspond to the joint and the thinner Section of the specimen where the out-of-plane displacements and curvatures are increasing significantly leading to matrix cracking in the resin layers as confirmed again by the SEM micrographs (Figures 4.17 and 4.18).

Following this point activity levels continue to increase as loading continues into postbuckling (Figure 4.15) particularly at the boundary of the joint with the thinner section, with the results of the SEM indicating this damage to be in the form of matrix cracking and shear damage as seen in Figures 4.17 and 4.18.

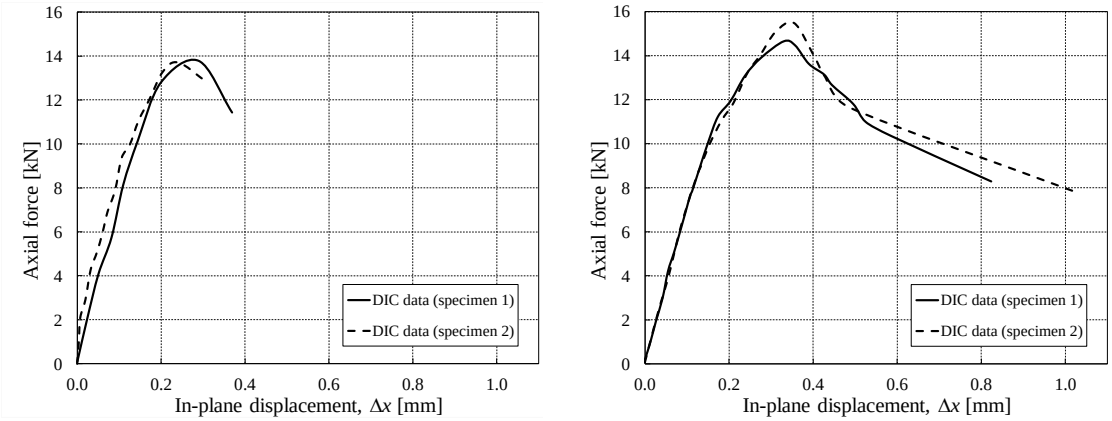

Figure 4.13: Axial force versus in-plane displacement for doubler specimens; (a) pristine and (b) with an artificial defect.

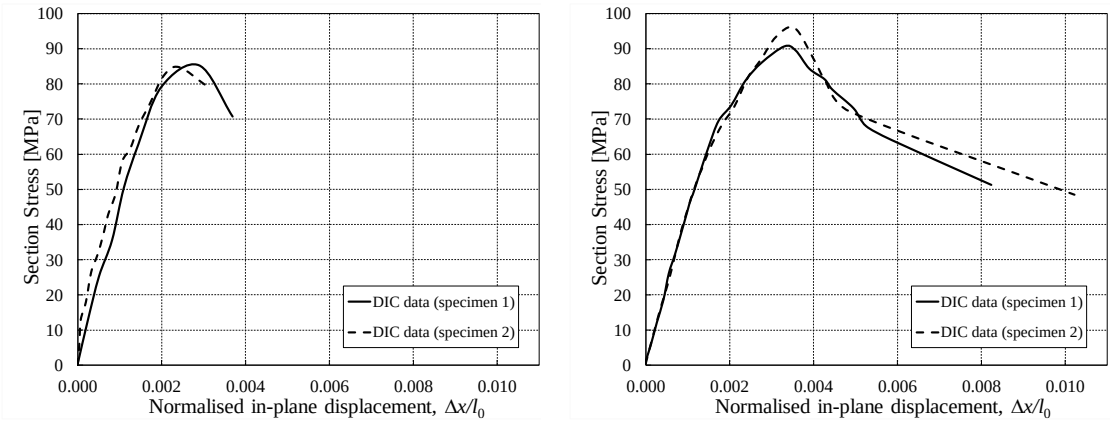

Figure 4.14: Section stress versus normalised in-plane displacement for doubler specimens; (a) pristine and (b) with an artificial defect.

In terms of AE energy the results in Figure 4.16 show there is a sharp increase in cumulative energy between 0.16 mm < Δx < 0.23 mm corresponding to widespread matrix cracking. A further large jump in energy can be seen at Δx = 0.36 mm due to the

large out-of-plane displacements and high curvature seen at ultimate load causing further matrix cracking. This is followed by a more gradual increase in energy up to the end of the tests at approximately Δx = 0.85 mm caused by a number of different damage mechanisms including matrix cracking and shear damage, as confirmed by SEM micrographs at the doubler joint region in Figure 4.18. No delamination initiation or propagation from the embedded defect was noticed in the SEM results. Again this can be explained by the fact that as the specimen begins to buckle globally, deformations act to close any delamination which might be initiated minimising their effect. This is supported by the fact that the increase in cumulative energy is more gradual for the doubler specimen than for the splice specimen due to the smaller number of damage mechanisms which are active. This is in agreement with the Finite Element analysis presented in Section 5.4.2.

As also shown in Figure 4.15, initial low-energy AE events were detected in the upper portion of the panel just above the doubler joint, as well as at the point of highest curvature which shows great levels of AE activity at around Δx = 0.16 mm which corresponds to the onset of buckling. Then at approximately Δx = 0.36 mm a large number of high-energy AE events are seen in the same region, corresponding to the peak load when out-of-plane displacements and curvatures increase significantly. The AE energy results shown in Figure 4.16 show a sharp increase in cumulative energy between 0.16 mm < Δx < 0.23 mm corresponding to widespread matrix cracking. A further large jump in energy can be seen at Δx = 0.36 mm due again to the large out-of-plane displacements and high curvature seen at ultimate load. This is followed by a more gradual increase in energy up to the end of the tests at approximately Δx = 0.85 mm. The increase in cumulative energy is more gradual for the doubler specimen than for the splice specimen. This suggests that the transverse doubler joint investigated here does not promote large scale delaminations as observed for the longitudinal splice joint. This is supported by the detailed Finite Element analysis presented in Section 5.4.

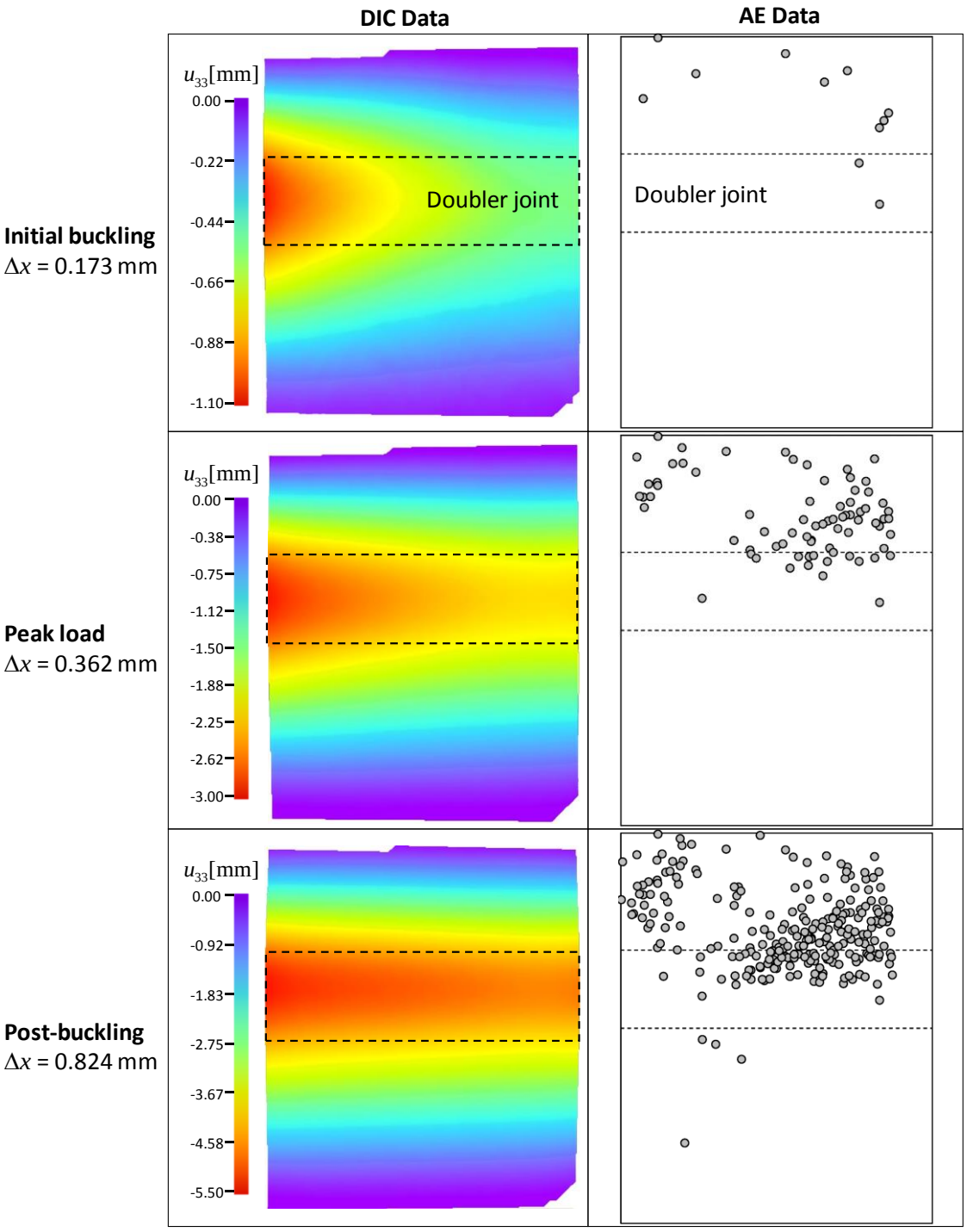

Figure 4.15: Contours of out-of-plane displacement, u_{33} (left) against location of AE events (right) for the doubler specimen (with an artificial defect) at different in-plane displacements Δx (dashed lines indicate position of doubler).

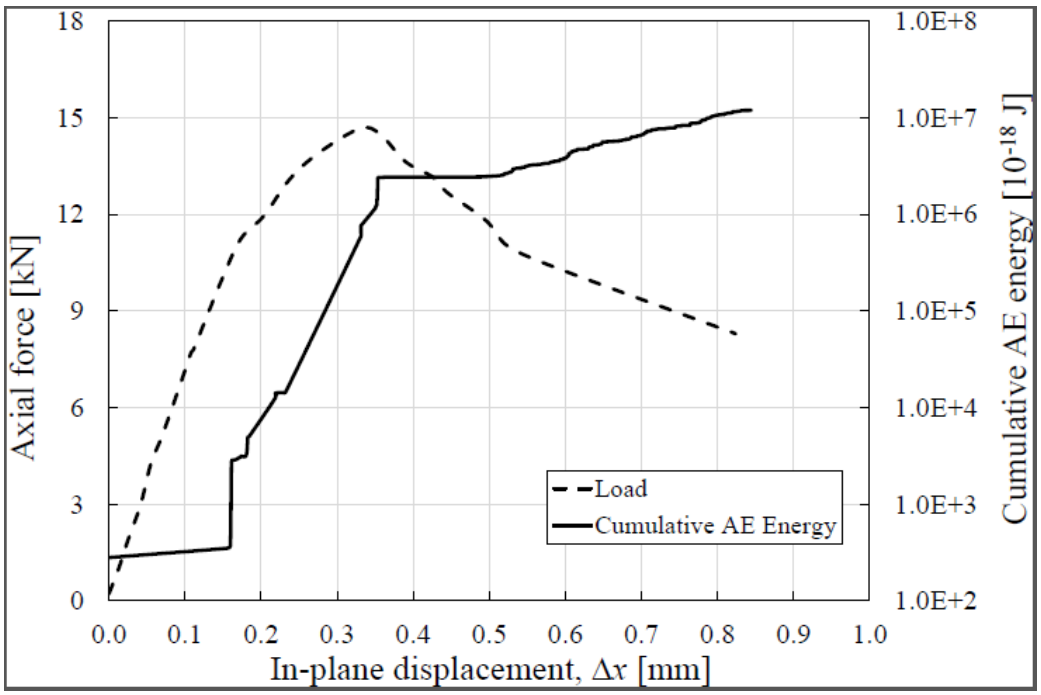

Figure 4.16: Load and cumulative AE energy versus in-plane displacement for the doubler specimen with defect.

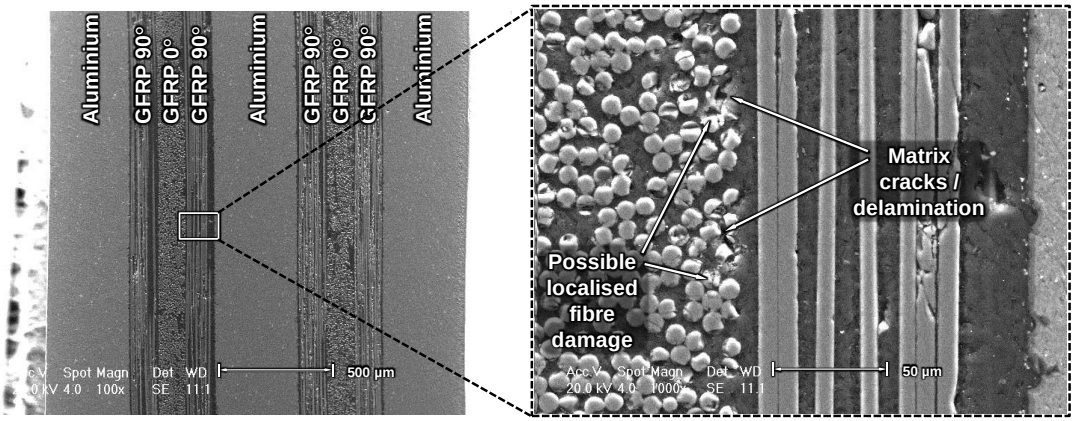

(a) (b)

Figure 4.17: SEM of doubler specimens along Section 1 (near the top grip), with magnifications of (a) 100× and (b) 1000×.

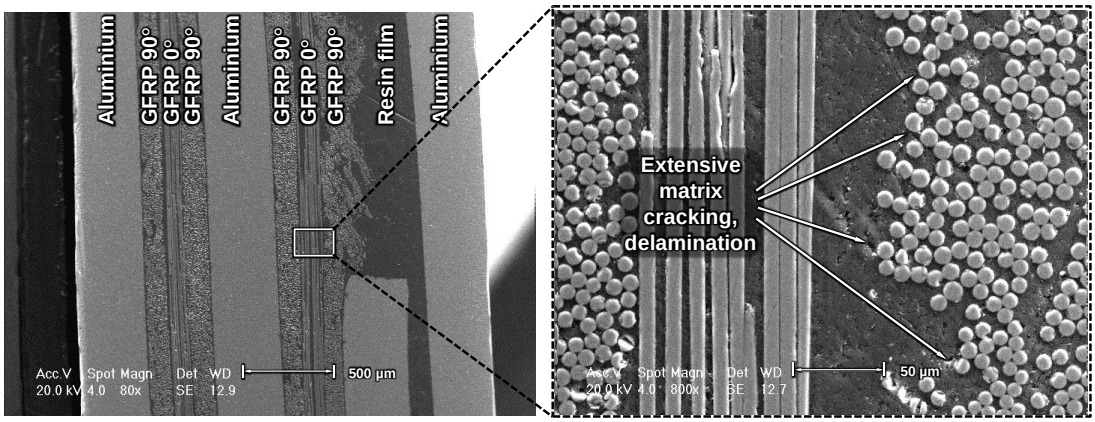

(a) (b)

Figure 4.18: SEM of doubler specimens along Section 2 (across doubler), with magnifications of (a) 80× and (b) 800×.

4.4.3 'Far-field' specimens

Figure 4.19 shows the experimental load-displacement curves of far-field specimens both with and without the circular delamination. The introduction of a large delamination (covering 62.5% of the width) at the point of maximum out-of-plane displacement has a significant effect on the buckling and postbuckling behaviour of the far-field specimen. DIC results show a good representation of this reduction in ultimate compression load from 11.18 kN to 10.75 kN for specimen (2) pristine and with defect, although both pristine specimen (1) and with defect specimen (1) show lower ultimate compressive load 10.65 kN to 9.28 kN due to specimens slipping and misalignment in the test machine. This reduction in properties can be seen to correlate well with the propagation of the delamination as detected by the FE model results which were described in Section 5.7.

A comparison between DIC out-of-plane displacement results and deformed tested specimens (Figures 4.20 and 4.22) presented that delamination occurs in both far-field with defect specimens and pop out as a half circle shape due buckling which occur prior to delamination onset and causing closing delamination in the buckled region.

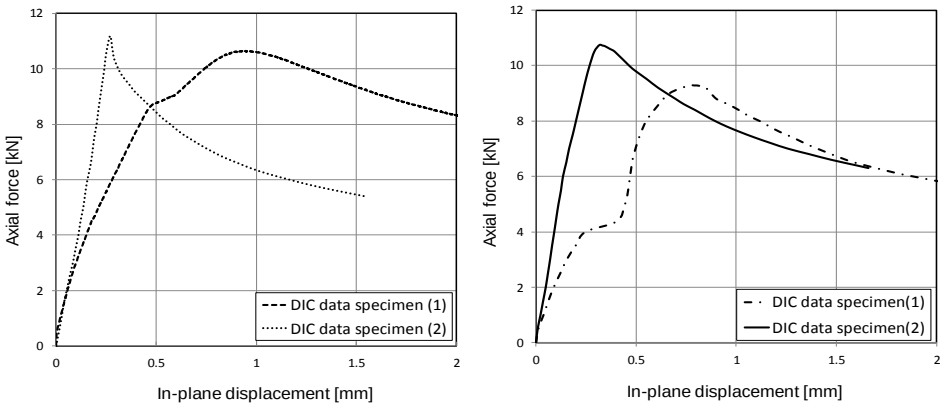

(a) (b)

Figure 4.19: Axial force versus in-plane displacement for far-field specimens; (a) pristine and (b) with an artificial defect (circular delamination).

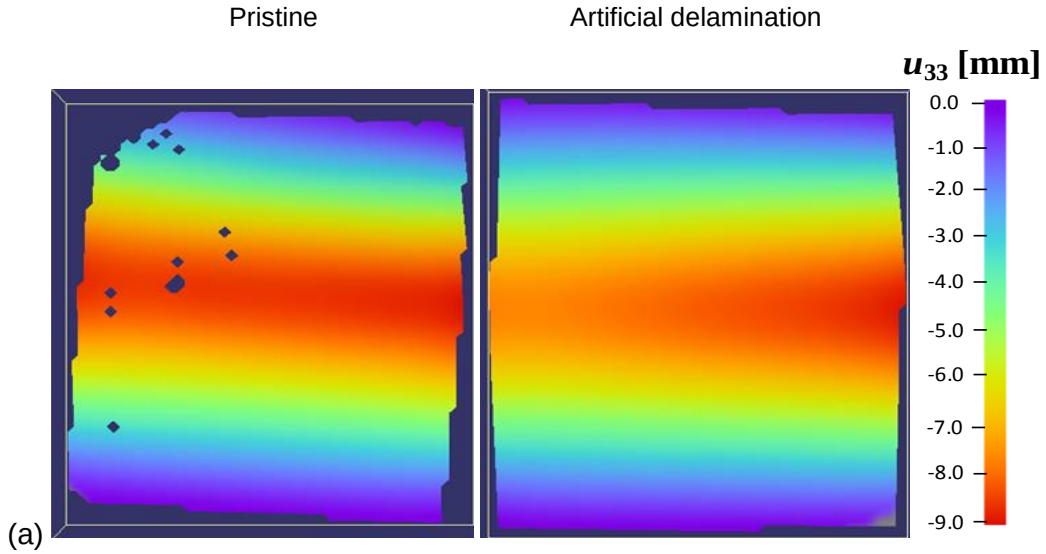

(a)

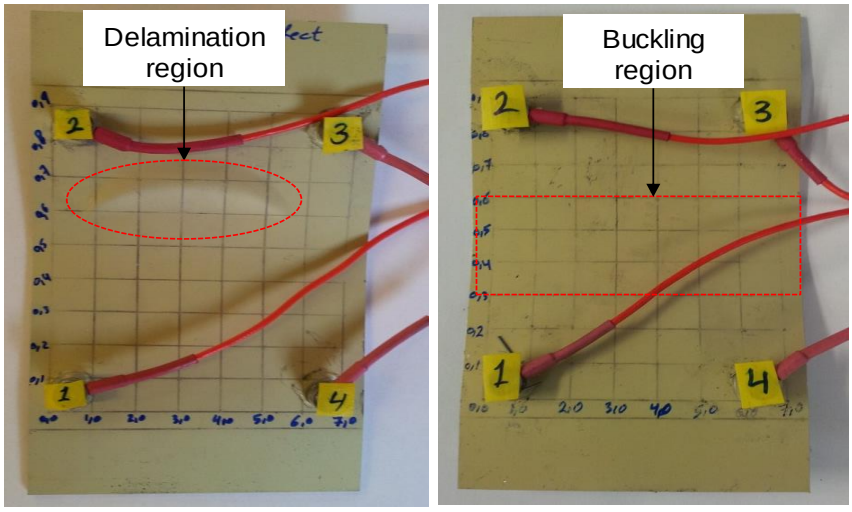

(b)

Figure 4.20: 'First round' far-field specimens with (right) and without (left) an artificial delamination at axial displacement Δx = 1.66 mm ; (a) out-of-plane displacement from DIC and (b) tested specimens.

However, position of the delamination is different either from top artificial delamination circle half for specimen(1) or from bottom circle half in the case of specimen(2) which might be a result of moving in PTFE film generated to the artificial delamination during manufacturing process for tested specimens or misalignments in the test rig. While pristine specimens (1) and (2) do not show any delamination.

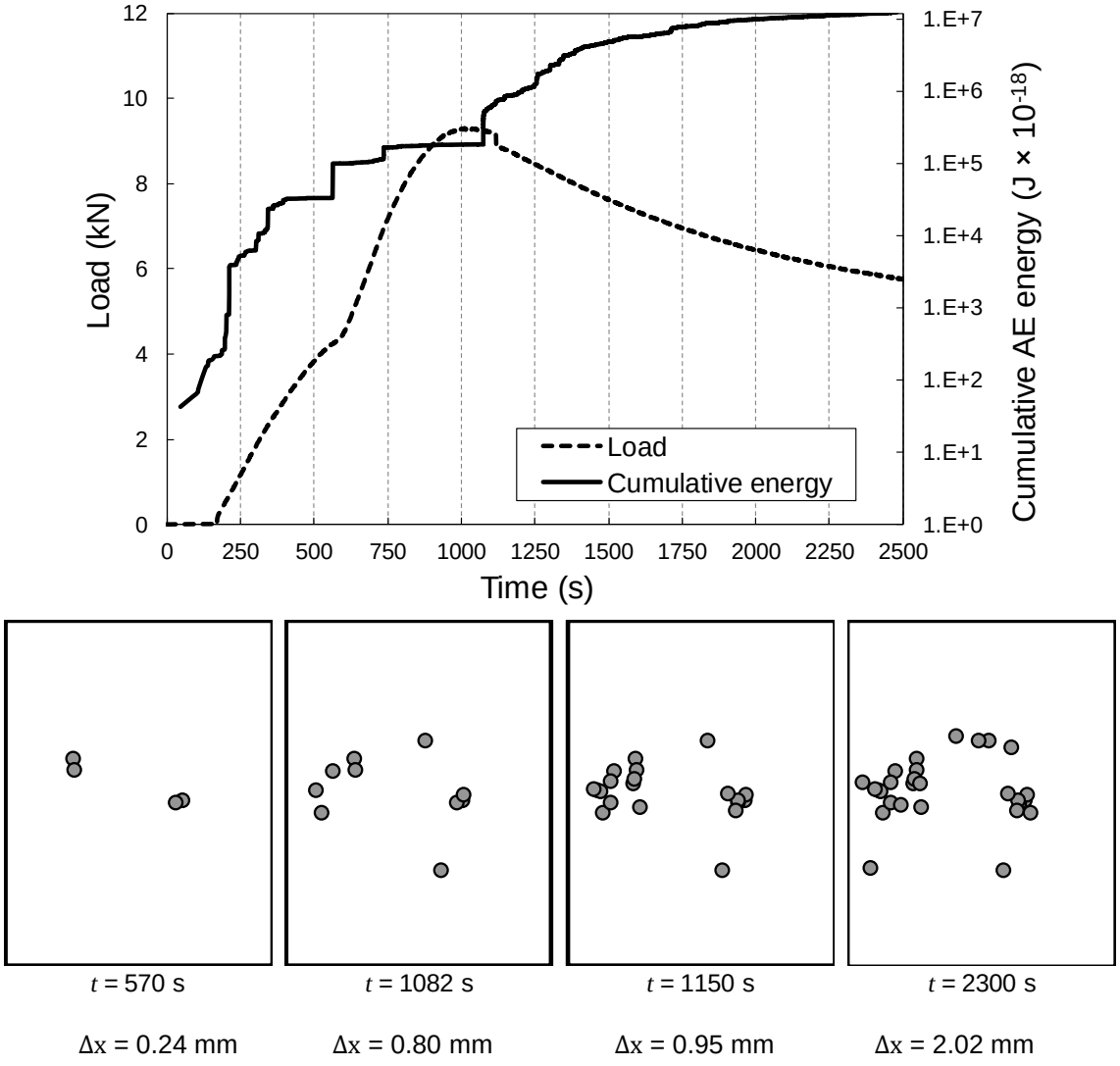

Figure 4.21: AE results for 'first round' far-field specimen with an artificial delamination; (top) cumulative AE energy / applied load versus time, and (bottom) Delta-T source location.

These results were confirmed via AE results for far-field with defect specimens shown in Figures 4.21 and 4.23 for both specimen (1) and (2) respectively. A delamination was noticed by a drop in axial force accompanied by a jump in AE cumulative energy at

time 1150 s and 700 s for both specimen(1) and (2) respectively. This was happen after a high jump in AE activity at ultimate compressive load (9.42 kN and 10.75 kN) for both specimen (1) and (2) which is mostly as a result of buckling failure events. This was followed by a steady increase in energy at postbuckling region up to the final failure. This exhibited how AE techniques can be used to detect and localised damage effectively and efficiently in FML structures.

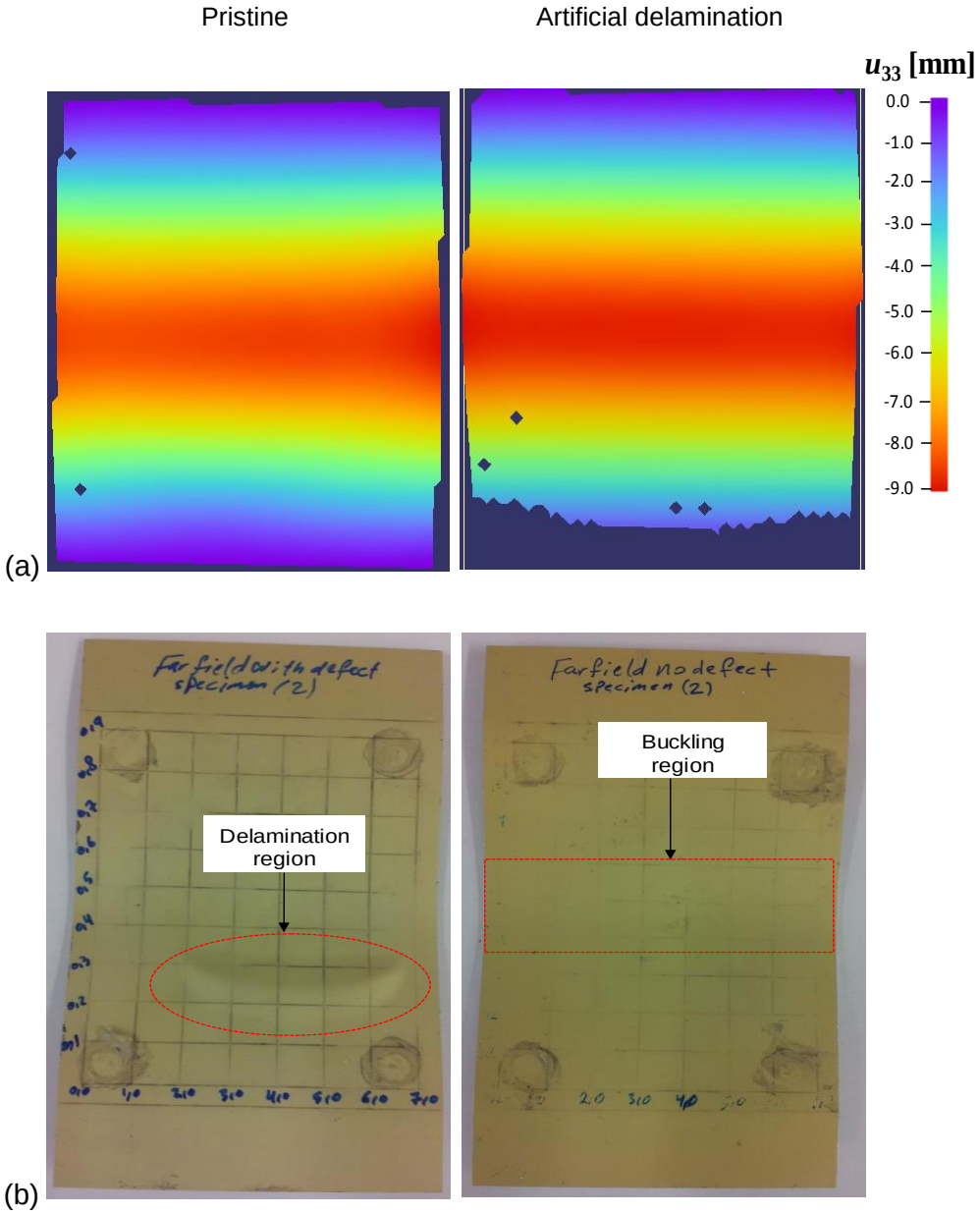

Figure 4.22: 'Second round' far-field specimens with (right) and without (left) an artificial delamination at axial displacement Δx = 2.02 mm; (a) out-of-plane displacement from DIC and (b) tested specimens.

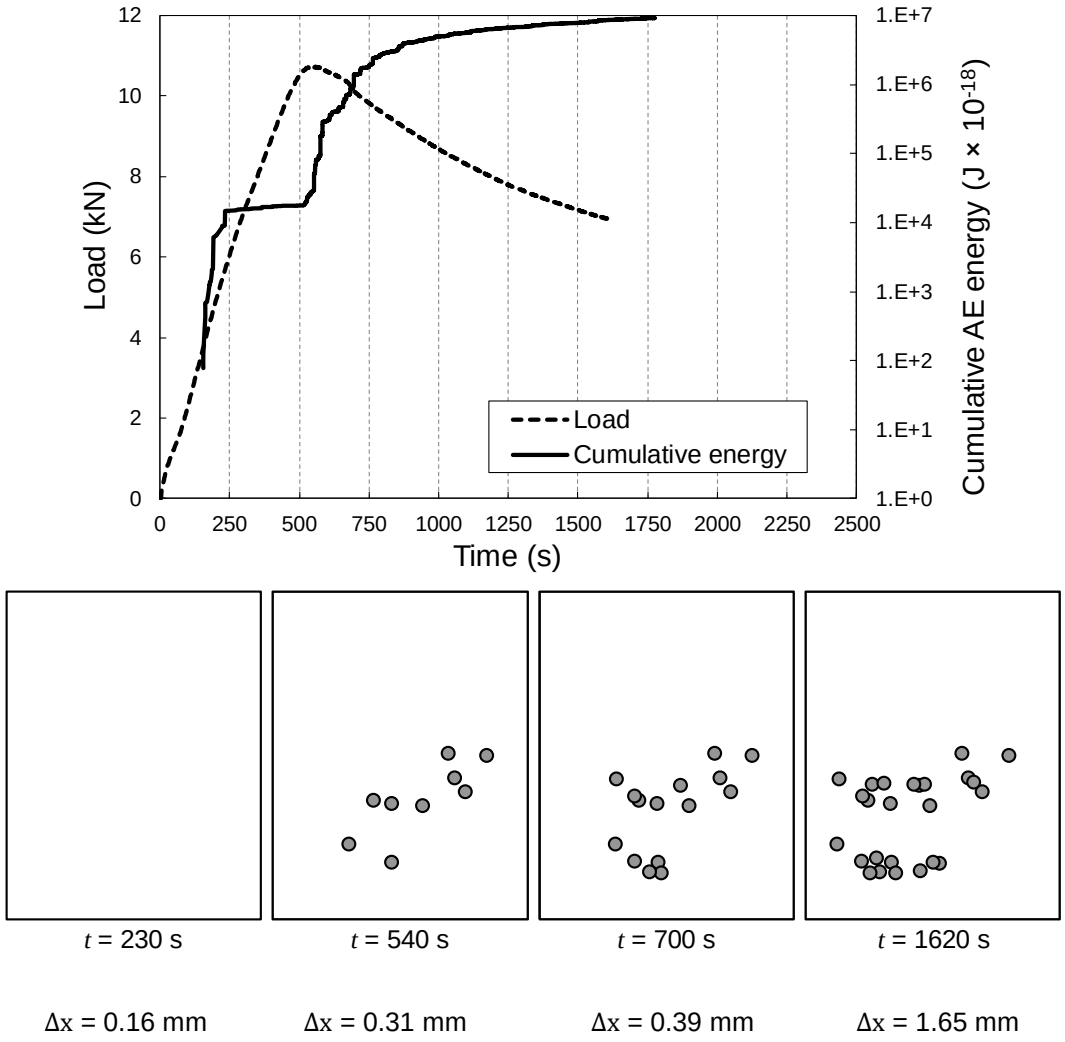

Figure 4.23: AE results for 'second round' far-field specimen with an artificial delamination; (top) cumulative AE energy / applied load versus time, and (bottom) Delta-T source location.

AE results for both two pristine specimens (Figure 4.24) shows similar behaviour therefore only one specimen is presented. A high jump in energy was observed at ultimate compressive load (11.18 kN) which is mostly as a result of buckling failure events followed by steadily increase in energy at postbuckling region which could be due to matrix cracks up to the final failure. Also AE location results present that AE signals in the middle of the specimen (high curvature region), starts at low intensity, and then intensity increased within time increment as the test progressed, which is due buckling onset followed by buckling failure as observed from experiments. Also other AE events were noticed in the lower part of the pristine specimens which are mostly due matrix cracks due to bending in this region.

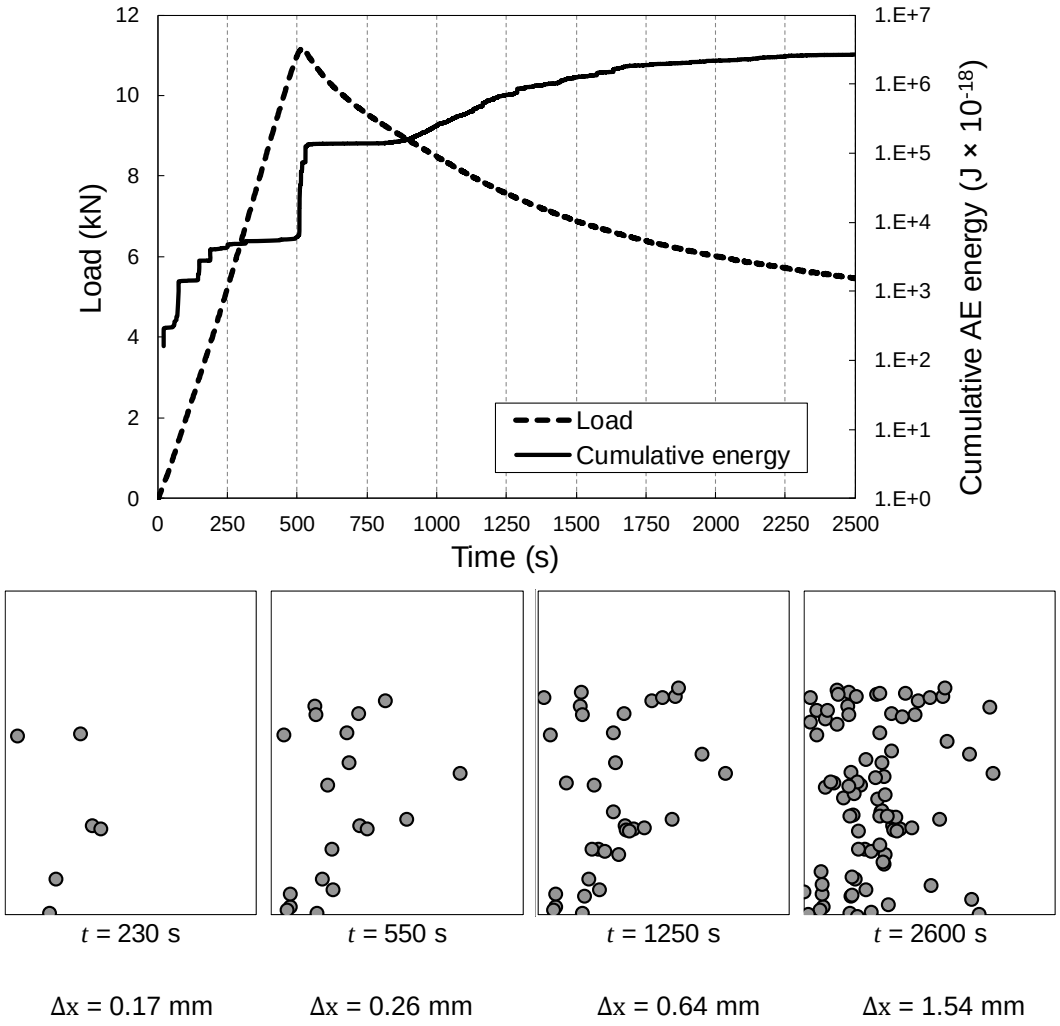

Figure 4.24: AE results for 'first round' far-field specimen without an artificial delamination; (top) cumulative AE energy / applied load versus time, and (bottom) Delta-T source location.

Comparing the AE data for both pristine and with defect far-field specimens shown in Figures 4.24 and 4.21, respectively, the ability of traditional AE analysis technique to successfully detect damage as it is occurring is clearly demonstrated. This is demonstrated by jumps in the cumulative energy at both initial buckling and peak loads for both types of the specimens followed by a steady increase in cumulative energy in the postbuckling region up to final failure. More significant however is its ability to locate the damage which in this case is clearly demonstrated by the concentration of AE events around the areas of highest out of plane displacement and hence curvature across the centre of the pristine specimen which is significantly different to the pattern of damage for the specimens containing circular delaminations, in which the events are

clearly located around the periphery of this delamination where damage propagation is occurring.

4.5 Chapter Summary

This chapter including a series of experiments was performed to examine the effect of splice and doubler joints in addition to the effect of circular delamination artificial defect, on the buckling and postbuckling behaviour of Glare® fibre-metal laminate specimens. Panels were tested under in-plane compression with and without the introduction of artificial defects. Tests were recorded using Digital Image Correlation (DIC) and Acoustic Emission (AE) monitoring systems. Also Scan Electron Microscopy (SEM) technique was used in order to validate experimental results from both DIC and AE monitoring for different damage mechanisms in both splice and doubler specimens. A bespoke Delta-T algorithm was implemented for accurate detection and localisation of damage from the recorded AE signals. Good correlation was observed between in-plane loads, out-of-plane displacements and AE event location which suggest that the postbuckling behaviour of both joints involves different damage mechanisms. The longitudinal splice joint did not promote early matrix cracking and the buckling point was characterised by a greater amount of delamination, as seen by a large jump in cumulative AE energy and the sudden increase in out-of-plane displacements. The transverse doubler joint on the other hand showed much more gradual damage behaviour during postbuckling, dominated by widespread matrix cracks. The ‘Delta-T’ AE location algorithm was successfully used to monitor damage development in the Glare® laminates. The location and sequence of AE events suggest that the method is particularly sensitive to early activity within the internal features which act as stress concentrations. Artificial delaminations representative of those which could potentially be generated during manufacturing (inserted in splice and doubler joints) had a negligible effect on the compressive strength of both types of joints, while the introduction of a large delamination (covering 62.5% of the width) at the point of

maximum out-of-plane displacement (inserted in the far-field specimens) has a significant effect on the buckling and postbuckling behaviour of the specimen ;yet the Delta-T algorithm was able to detect the presence of such defects at relatively low loads, suggesting that the method is a strong candidate for the in-service Structural Health Monitoring of Glare® structures. Finally, SEM technique enabled characterisation the different types of damage mechanisms in both splice and doubler specimens and has a good agreement with AE results.

Chapter 5 - Buckling/Postbuckling of FMLs with Internal Features: Modelling

5.1 Introduction

This chapter focuses on the development of a 3D finite element model using cohesive elements and continuum (bulk) material damage models to examine the progressive damage and failure behaviour of Glare® Fibre Metal Laminate (FML) specimens subjected to in-plane compressive loading. The specimens contained internal 'splice' and 'doubler' features in addition to others with an artificial circular delamination defect and were either pristine or contained simulated manufacturing defects in the form of artificial delaminations. The initiation and growth of delaminations at the inter-laminar interfaces, damage in the glass fibre reinforced polymer (GFRP) plies, ductile damage in the resin pockets (FM94 epoxy) and the onset of plasticity in the metal layers were examined. Geometric imperfections and load eccentricity were incorporated in an explicit dynamic nonlinear analysis implemented in the software Abaqus/Explicit. A series of buckling tests on specimens with and without artificial delaminations were conducted for validation, which are described in detail in Chapter 4. Tests were monitored using Digital Image Correlation (DIC) for visualisation of full-field displacements and strains whilst Acoustic Emission (AE) monitoring enabled detection and localisation of the onset and progression of damage. Results for 'Glare®4B' specimens incorporating longitudinal and transverse delaminations into both splice and doubler geometries respectively in addition to those with central circular delamination introduced in the far-field specimens structure are presented. These results revealed that in order for the finite element analyses to be accurate, all the damage and plasticity mechanisms described above need to be accounted for, as well as load

eccentricity and geometry imperfections. Finally the models' predictions are verified based on the results of experimental work including Scanning Electron Microscopy (SEM) micrographs which enable the damage found in different areas of the specimen to be characterised for comparison with that predicted by the model.

5.2 Finite element models

5.2.1 Specimen geometry

Three types of specimens were modelled, one incorporating a longitudinal splice and the other a transverse doubler in addition to a 'far-field' specimen with an artificial circular delamination (Section 4.2.1). Specimens measured 100 mm × 80 mm corresponding to the unsupported section of the 140 mm × 80 mm specimens tested for validation. Each had a lay-up type 'Glare® 4B' according to standard grades of commercial Glare® shown in [1] and a detailed description of this layup is provided in Section 4.2.1. Artificial delaminations were simulated by introducing 4 mm wide strips of polytetrafluoroethylene (PTFE) film of thickness 10 µm embedded in the splice and doubler structures. As for the far-field specimen model, the artificial circular delamination was simulated using a 50 mm diameter PTFE film of a thickness 10 µm inserting into the interface between the front aluminium layer and the first GFRP layer.

5.2.2 Finite element meshes

Three-dimensional, ply-by-ply finite element models were generated for all specimen types using the Abaqus/CAE software. The geometry and thickness of each layer were extracted from detailed scans of real specimens and a high fidelity structural mesh was generated to represent the internal geometry. The resulting meshes are shown in Figures 5.1, 5.2 and 5.3 for doubler, splice and far-field specimens, respectively. The layers of aluminium and the resin pockets were meshed using linear continuum (C3D8R) elements with the interfaces between layers modelled using 0.01 mm thick

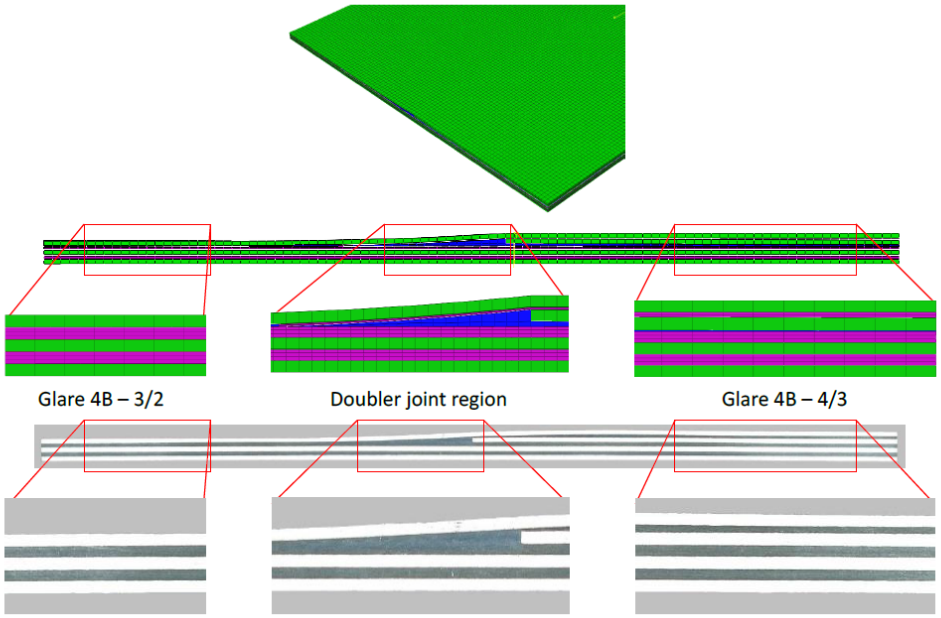

Figure 5.1: Finite element mesh of the doubler specimen (top) based on optical scans of real specimens (bottom) (images resized for clarity, not to scale).

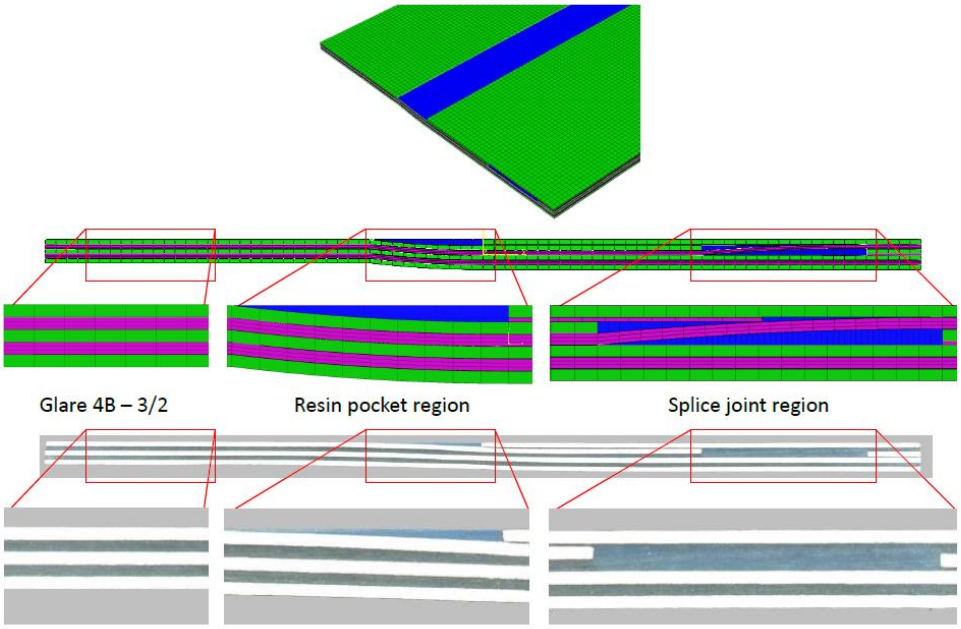

Figure 5.2: Finite element mesh of the splice specimen (top) based on optical scans of real specimens (bottom) (images resized for clarity, not to scale).

cohesive (COH3D8) elements and had a mesh size of unity (the thickness was chosen based on a review of the literature related to similar models for fibre laminates, the mesh size was determined through a mesh sensitivity analysis which is explained in

detail in Appendix-A). Three-dimensional 'continuum shell' elements (SC8R), each made of 8 nodes with 3 degrees of freedom (DoF) per node, were used for the composite plies to enable composite damage to be modelled in Abaqus. Individual layers of each of the laminates were meshed separately and then assembled using tie constraints between adjacent layers coupling all nodal degrees of freedom at the interface.

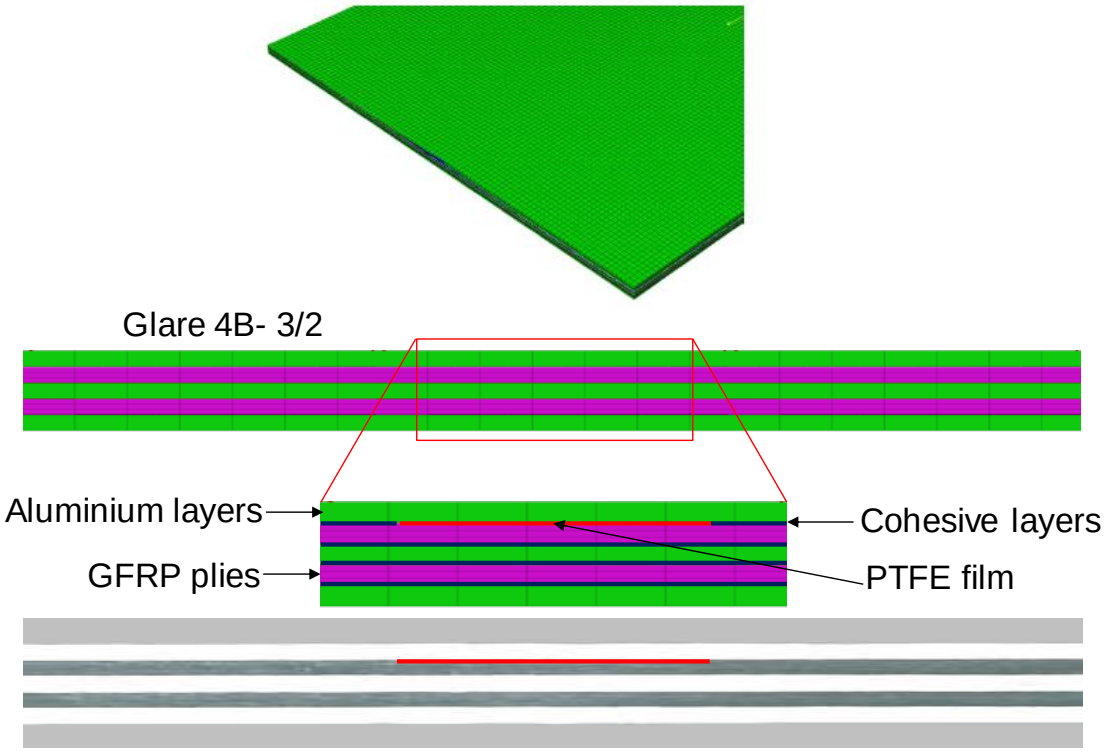

Figure 5.3: Finite element mesh of the far-field specimen (top) based on optical scans of real specimens (bottom) (images resized for clarity, not to scale).

5.2.3 Material properties

A comprehensive literature review was conducted on the mechanical properties of the Glare® material constituents. Properties for the aluminium alloy 2024-T3 were obtained from [4] and are summarised in Table 5.1. The plastic stress-strain curve from the same alloy was taken from [159] and is shown in Table 5.2. The mechanical properties for the S2-glass/FM94 GFRP material were given in [120] and are shown in Table 5.3.

Every interface in the laminate was represented by a Cohesive Zone Model (CZM) with bilinear traction-separation curves defined independently for modes I and II (further details in Section 5.2.7). The cohesive properties for GFRP-metal interfaces were obtained from [160] and are shown in Table 5.4. The cohesive stiffnesses $\mathrm{K_I}$ and $\mathrm{K_{II}}$ were however calculated based on the elastic properties of bulk FM94 resin, shown in Table 5.5, and the assumption that the interfacial stiffness is dominated by the deformation of a 10 μm thick resin rich layer, as described in [59] (it should be noted that these stiffnesses have only minor influence on the fracture initiation and propagation behaviour of the CZM, which instead is more strongly dependent on the initiation stresses, $\sigma_{\mathrm{I}}^{\max}$ and $\sigma_{\mathrm{II}}^{\max}$, and critical strain energy release rates, G_{IC} and G_{IIC}).

The fracture process resulting from the delamination of GFRP-metal interfaces is micro-mechanically different from the fracture process observed between the same metal and the same resin in the absence of fibres, since the presence of fibres precludes the development of a local plastic zone within the toughened epoxy material [161]. As a result, much higher fracture energies are expected within the resin pockets formed around the splice and doubler features contained in the laminates investigated here. Indeed, Katnam *et al.* [162] obtained the cohesive properties shown in Table 5.6 for fracture in a similar material system, but along a 100 μm thick unreinforced resin layer. The properties in Table 5.6 were therefore assumed for the interfaces formed around resin pockets in the splice and doubler features investigated here.

Finally, artificial delaminations were introduced via a reduction in cohesive properties along the interfaces to be covered by the PTFE strip. A range of different properties were taken from the literature all of which resulted in similar behaviour of the specimen due to the compressive stiffness of the PTFE film being relatively small compared to the cohesive stiffness used and the limited size of the embedded defect. The properties chosen are detailed in Table 5.7.

5.2.4 Loading and boundary conditions

Boundary conditions were applied at the top and bottom edges of the specimen corresponding to the effect of the clamps in the validation experiments. The bottom edge was restrained in all three DoFs to represent the fixed end condition, while the top edge was free to move in-plane but restricted in both other DoFs. Both sides of the specimens were left unconstrained as in the validation experiments. An initial

Table 5.1: Mechanical properties for aluminium alloy 2024-T3 [1].

Property	Value	Units
Young's modulus	72.4	GPa
Stress at 4.7% strain	420	MPa
Tensile yield strength, rolling direction	300	MPa
Tensile yield strength, transverse direction	299	MPa
Shear modulus	27.6	GPa
Poisson's ratio	0.33	-
Coefficient of thermal expansion	22×10^{-6}	$^{o}C^{-1}$
Mass density	2780	$kg\cdot m^{-3}$

Table 5.2: Plastic stress-strain data for aluminium alloy 2024-T3, transverse direction [159].

Plastic strain [%]	Stress [MPa]
0.000	300
0.016	320
0.047	340
0.119	355
0.449	375
1.036	390
2.130	410
3.439	430
5.113	450
8.000	470
14.710	484

Abaqus/Explicit thermal step was implemented to generate the residual stresses created during the curing process (based on a curing temperature of 120 ^{o}C followed by cooling to a room temperature of 20 ^{o}C giving a reference temperature for thermal analysis of -100 ^{o}C), using the thermal expansion coefficients shown in Tables 5.1, 5.3 and 5.5. Following this, a compressive load under velocity control was applied to the top edge of the specimen.

Table 5.3: Mechanical properties for S2-glass/FM94 prepreg material [120].

Property	Value	Units
Young's modulus, fibre direction, E_{11}	50.0	GPa
Young's modulus, transverse direction, E_{22}	9.0	GPa
Poisson's ratio, ν_{12}	0.33	-
Poisson's ratio, ν_{23}	0.04	-
In-plane shear modulus, G_{12}	3.5	GPa
Transverse shear modulus, G_{23}	3.0	GPa
Fibre-direction tensile strength, X_T	2000	MPa
Fibre-direction compressive strength, X_C	550	MPa
Transverse tensile strength, Y_T	43	MPa
Transverse compressive strength, Y_C	90	MPa
In-plane shear strength, S_{12}	93	MPa
Transverse shear strength, S_{23}	50	MPa
Critical SERR*, fibre direction, $G_{C,X}$	12.0	kJ·m^{-2}
Critical SERR*, transverse direction, $G_{C,Y}$	1.0	kJ·m^{-2}
Mass density, ρ [163]	2000	kg·m^{-3}
Coefficient of thermal expansion, fibre direction [4]	6.1 x 10^{-6}	^{o}C^{-1}
Coefficient of thermal expansion, transverse direction [4]	26.2 x 10^{-6}	^{o}C^{-1}

*Strain Energy Release Rate.

Table 5.4: Cohesive zone properties for GFRP-metal interfaces.

G_{IC} (kJ·m^{-2}) [160]	G_{IIC} (kJ·m^{-2}) [160]	$\sigma_{\mathrm{I}}^{\max}$ (MPa) [160]	$\sigma_{\mathrm{II}}^{\max}$ (MPa) [160]	K_{I} (N·mm^{-3})	K_{II} (N·mm^{-3})
0.45	1.0	40	40	2.189×10^{5}	0.823×10^{5}

Table 5.5: Mechanical properties for the FM94 resin [164].

Property	Value	Units
Young's modulus	2.19	GPa
Poisson's ratio	0.33	-
Mass density [164, 165]	1280	$kg \cdot m^{-3}$
Coefficient of thermal expansion [165]	$100x10^{-6}$	$^oC^{-1}$

Table 5.6: Cohesive zone properties for bulk resin-metal interfaces.

G_{IC} ($kJ \cdot m^{-2}$) [162]	G_{IIC} ($kJ \cdot m^{-2}$) [162]	σ_I^{max} (MPa) [166]	σ_{II}^{max} (MPa) [166]	K_I ($N \cdot mm^{-3}$)	K_{II} ($N \cdot mm^{-3}$)
2.0	4.0	50	50	2.189×10^5	0.823×10^5

Table 5.7: Mechanical properties for the PTFE film [167, 168].

Property	Value	Units
Young's modulus	480	MPa
Poisson's ratio	0.46	
Mass density	2150	$kg \cdot m^{-3}$
Coefficient of thermal expansion	10×10^{-5}	$^oC^{-1}$

5.2.5 Geometric imperfections

In order to represent the 'as-built' structures tested in the validation experiments geometric imperfections were introduced. In line with common practice, since their exact form was not known they were modelled in the form of the first mode shape (obtained by performing an eigenmode analysis in Abaqus/Standard, Figure 5.4) with an amplitude scaled to give a maximum 1.0 mm out of plane deformation corresponding to the deviations measured in the specimens tested (due to the manufacturing process and variations in thickness across the specimen). This is expected to provide conservative results.

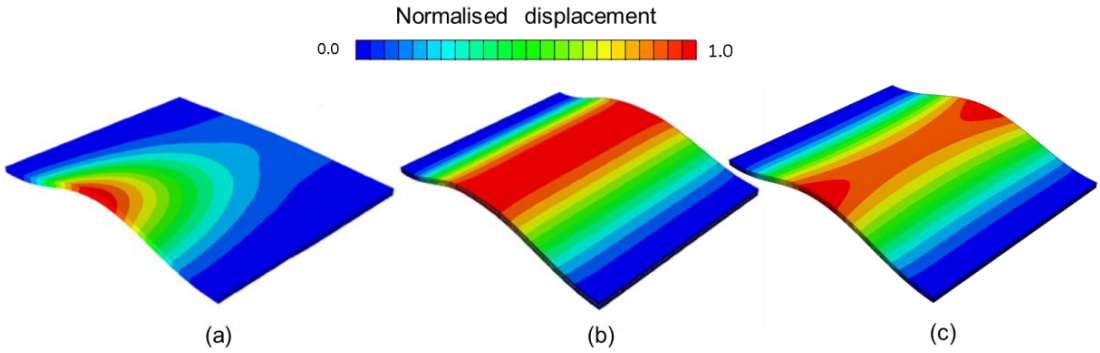

Figure 5.4: Geometrical imperfections based on the first eigenmode for (a) splice and (b) doubler specimens and (c) far-field specimens (normalised displacements magnified for clarity, not to scale).

5.2.6 Load eccentricity

In addition to geometric imperfections, load eccentricity caused by misalignments in clamping the specimen leading to an asymmetrical load distribution was also considered in the analysis. The value of eccentricity was based on measurements of the experimental set-up which indicated an average eccentricity of 0.7 mm based on readings from a digital inclinometer. This was achieved by implementing two load steps following the thermal loading step discussed in Section 5.2.4. As shown in Figure 5.5 the first step represented the load eccentricity which was introduced in the form of an asymmetric linearly distributed in-plane displacement component superimposed on the cross-head displacement and the second step represented the uniform compression load applied up to the final failure.

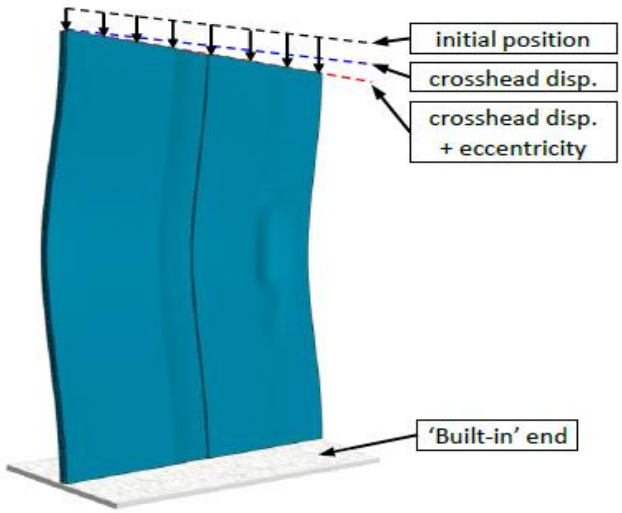

Figure 5.5: Load eccentricity introduced after the thermal step and before the main loading step.

5.2.7 Cohesive Zone Model

As mentioned earlier, one of the complexities of modelling the behaviour of fibre metal laminates is the increased number of damage mechanisms compared to modelling metallic or composite laminates. In order to accurately model the initiation and propagation of damage in the specimens a range of damage and fracture criteria were therefore introduced. The mixed-mode bilinear cohesive zone model (CZM) shown in Figure 5.6 was used to model delamination initiation and growth in the metal-fibre and fibre-resin interfaces. This model uses a quadratic nominal stress criterion to identify the onset of damage,

$$\left(\frac{\langle \sigma_{\mathrm{I}} \rangle}{{\sigma_{\mathrm{I}}}^{\max}}\right)^2 + \left(\frac{\sigma_{\mathrm{II}}}{{\sigma_{\mathrm{II}}}^{\max}}\right)^2 = 1\,, \tag{5.1}$$

where $\langle \cdot \rangle = \max(\cdot\,, 0)$. Propagation is then based on the strain energy release rates G_{I} and G_{II} for modes I and II respectively,

$$\left(\frac{G_I}{G_{Ic}}\right)^n + \left(\frac{G_{II}}{G_{IIc}}\right)^n = 1\ . \tag{5.2}$$

where n is a material-specific power law coefficient. In the absence of reliable mixed-mode fracture data for the various interface types in Glare®, it has been assumed here

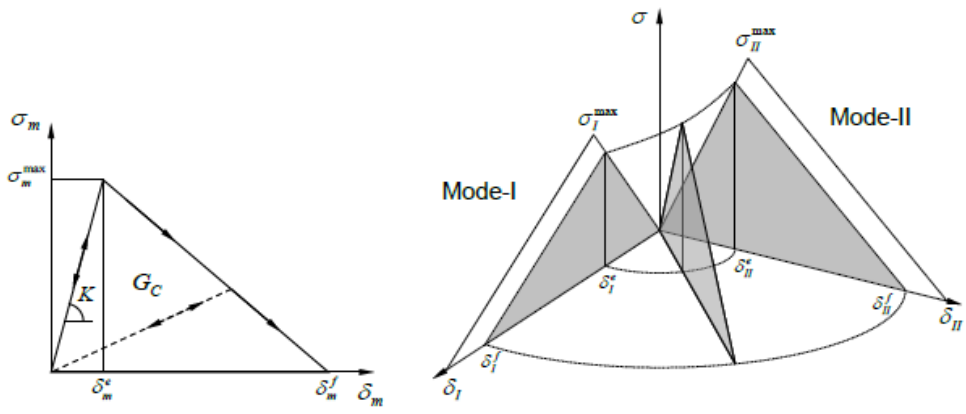

(a) (b)

Figure 5.6: Cohesive Zone Model (CZM) based on bilinear traction-separation curves (a) which are defined independently for modes I and II (b).

that n = 1 so that equation 5.2 turns into a linear interaction criterion instead [59]. The other interfacial material properties required to completely define the CZMs used in this work are provided in Tables 5.4 and 5.6.

5.2.8 Continuum damage and plasticity

Plastic deformation of the aluminium sheets was considered by introducing the stress-strain properties provided in Table 5.2. The resin pockets were assumed to strain-harden according to the Drucker-Prager yield criterion [169]. A ductile damage criterion was used to model damage in both the aluminium layers and the resin pockets [169]. This criterion assumes that the equivalent plastic strain at the onset of damage is a function of stress triaxiality and strain rate.

The mechanical properties used for both materials are shown in Table s 5.1 and 5.5, respectively. The Hashin damage criterion [170] was used to model damage in the GFRP plies. The model available in the Abaqus software (only applicable to continuum shell elements) is a 2D version of the original Hashin criteria with four damage variables, *i.e.* compressive and tensile failure along the fibre direction and the in-plane transverse direction (for simplicity the former are referred to as 'fibre failure' and the latter 'matrix failure'). The damage initiation criterion for fibre tension is,

$$\left(\frac{\sigma_{11}}{X_T}\right)^2 + \left(\frac{\sigma_{12}}{S_{12}}\right)^2 = 1 \tag{5.3}$$

and for fibre compression,

$$\left(\frac{\sigma_{11}}{X_C}\right)^2 = 1 \tag{5.4}$$

where X_T and X_C are the fibre-direction tensile and compressive strengths, respectively, and S_{12} is the in-plane shear strength. The initiation criterion for matrix tensile damage is,

$$\left(\frac{\sigma_{22}}{Y_{\mathrm{T}}}\right)^2 + \left(\frac{\sigma_{12}}{S_{12}}\right)^2 = 1\,, \tag{5.5}$$

and for matrix compressive damage,

$$\left(\frac{\sigma_{22}}{2\,S_{12}}\right)^2 + \left[\left(\frac{Y_C}{2\,S_{12}}\right)^2 - 1\right]\,\frac{\sigma_{22}}{Y_C} + \left(\frac{\sigma_{12}}{S_{12}}\right)^2 = 1\,, \tag{5.6}$$

where Y_{T} and Y_C are the transverse direction tensile and compressive strengths, respectively.

Once an initiation criterion is satisfied, the evolution of damage variables for each damage mode follows a bilinear stress-displacement curve similar to that of a cohesive formulation (Figure 5.6a). Integration point strains are converted into displacements via a 'characteristic length' which is based on element dimensions [169]. Three damage variables are tracked, 'fibre damage' d_{f}, 'matrix damage' d_{m} and in-plane 'shear damage' ds. The 2D stiffness matrix for that integration point then becomes,

$$C_{\mathrm{d}} = \frac{1}{D}\begin{bmatrix} (1-d_f)E_1 & (1-d_f)(1-d_m)\nu_{21}E_1 & 0 \\ (1-d_f)(1-d_m)\nu_{12}E_2 & (1-d_m)E_2 & 0 \\ 0 & 0 & (1-d_s)GD \end{bmatrix} \tag{5.7}$$

where $D = 1 - (1-d_f)(1-d_m)\nu_{12}\nu_{21}$, and the material response at the integration point is given by,

$$\sigma = C_{\mathrm{d}}\,\varepsilon \tag{5.8}$$

It should be noted that the damage variables are decomposed into tensile and compressive damage, *i.e.* d_{ft} and d_{fc} for 'fibre damage' and d_{mt} and d_{mc} for 'matrix damage', respectively.

5.2.9 Eigenvalue analyses

Linear eigenvalue analyses were conducted on all types of specimens to provide estimates of the buckling loads and to obtain the eigenmode shapes needed for modelling geometric imperfections. Abaqus/Standard (version 6.12) was used for all of

the eigenvalue analyses [169]. An eigenvalue buckling problem finds the loads for which the model stiffness matrix becomes singular.

The Lanczos solver is generally faster when a large number of eigenmodes are required for a system with many degrees of freedom, and was therefore used throughout. The output eigenmodes are normalised so that the maximum displacement component is one unit. As mentioned previously, scaled versions of these mode shapes, representative of the size of the amplitude of imperfections measured in the test specimens were used to model imperfections in the dynamic analyses, since they provide a conservative approach when the exact form of the geometrical imperfections is unknown [169].

5.2.10 Explicit dynamic analysis

As discussed, in order to predict the buckling behaviour of real structures it is important to take into account the various sources of nonlinearity, including geometric imperfections, plasticity and damage growth. In order to achieve this, the buckling experiments were analysed using the explicit dynamic solver Abaqus/Explicit (version 6.12) [171]. Whilst this software is ideally suited for analysing high-speed dynamic events, it has many advantages for the analysis of slower (quasi-static) processes which are beneficial here. The use of a large number of small time increments in Abaqus/Explicit is advantageous because each increment is relatively quick to compute (compared to the direct integration dynamic analysis procedure available in Abaqus/Standard) as it does not require convergence iterations. It also simplifies greatly the treatment of contact. The procedure uses diagonal (‘lumped’) element mass matrices whose inverses are simple to compute, significantly increasing computational efficiency. In addition, the vector multiplication of the inverse mass matrix by the inertial force requires only n operations, where n is the number of degrees of freedom in the model. The equations of motion for each node in the domain are integrated using the explicit central-difference integration rule. The explicit procedure requires no global

matrix operations and no tangent stiffness matrix calculation [171].

5.3 Results and discussion

A thorough sensitivity study was conducted on the effects of the various sources of nonlinearity described in Section 5.2 on the behaviour of splice, doubler and far-field specimens (see Appendix-A) in addition to consultation with the literature as described in chapter 2. The best agreement with experimental results was obtained when all the sources of nonlinearity were included, which suggests that the complex buckling and postbuckling behaviour of such features is defined by interactions between the various mechanisms. Therefore the results presented here are for models containing the full set of damage and delamination criteria discussed in Section 5.2.

5.3.1 Splice specimens

Figures 5.7 and 5.8 show the displacement behaviour (out-of-plane and in-plane respectively) for splice specimens obtained from the FE models alongside the experimental DIC system data for comparison (specimen 1 of the specimens with defects in Figure 5.8 suffered from slippage in the rig and has therefore not been considered). Considering first the out-of-plane displacement, the contour plots presented in Figure 5.7 illustrate the deformation at initial buckling, peak load and postbuckling, with corresponding in-plane displacementsΔx. Whilst the results presented are for specimens incorporating a defect, the pristine specimens presented very similar behaviour indicating that the effect of the damage introduced on the mode shape and the amplitude of out-of-plane deformations is negligible. The plate is seen to buckle with a single half wave length in the loading direction as expected for a plate with built-in ends and free longitudinal edges under compression. Deformations to the left of the joint in the thinner region of the specimen are higher than those to the right in the thicker region again as would be expected. Good qualitative agreement is observed between experimental and FE results in terms of the mode shape although the FE

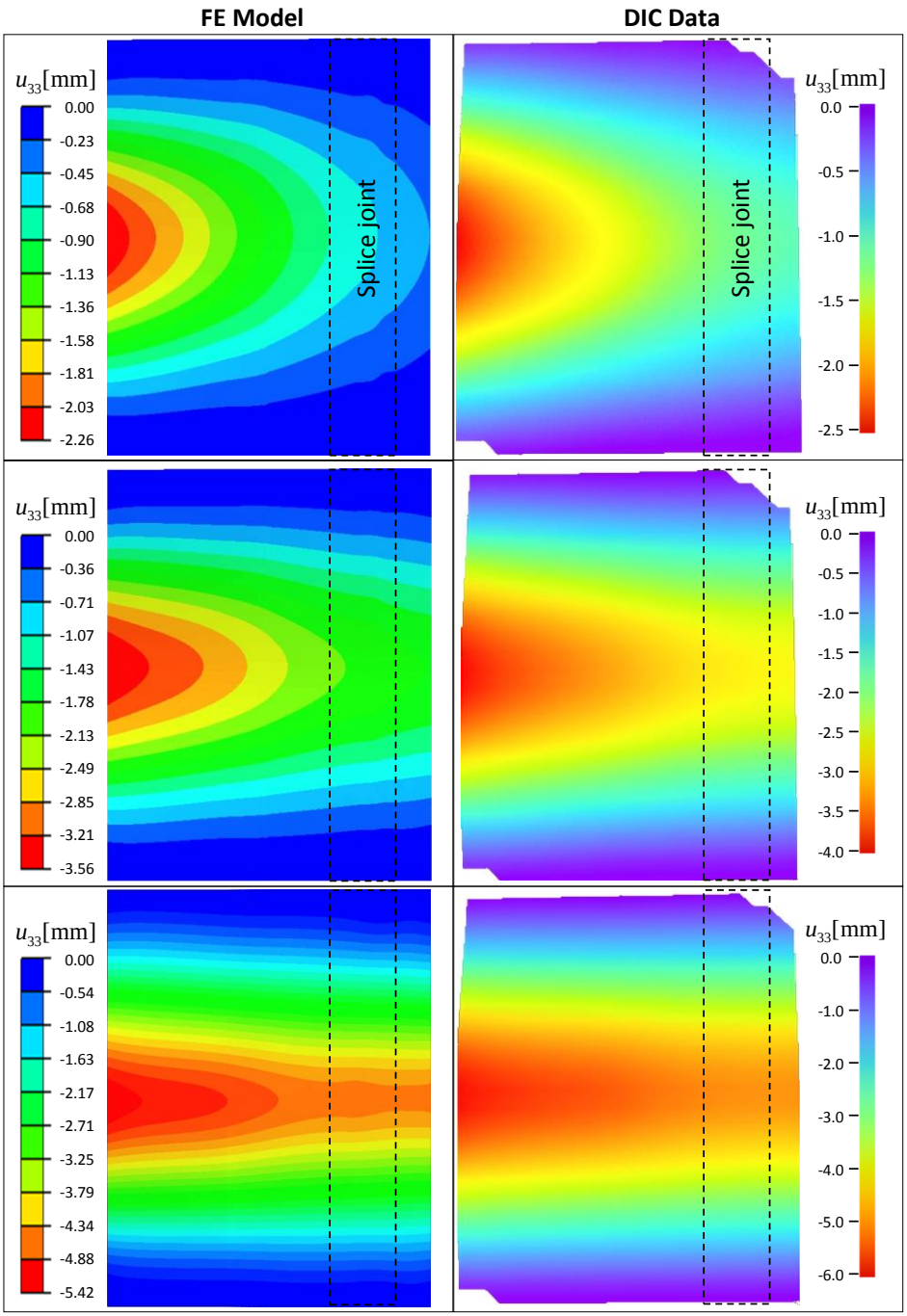

Figure 5.7: Out-of-plane displacements for the splice specimen with an artificial defect; FE predictions and DIC data at different in-plane displacements Δx (dashed line indicates position of splice).

model underestimates the displacement slightly.

In terms of axial load versus in-plane displacement it can be seen in Figure 5.8 that in terms of both the pre- and postbuckling stiffness there is a strong correlation between

the analytical and experimental results with only a slight overestimate of stiffness in the FE results. In terms of ultimate compressive loads, the FE model predicted 14.73 kN for both pristine and defective specimens, which overestimates the experimental values of 13.66 kN and 13.50 kN for pristine specimens and 13.86 kN for those containing a defect. This is potentially caused by the use of continuum shell elements which have a simplified treatment of through thickness stresses [173] when modelling the GFRP plies. The effect of the inserted delamination on both pre and postbuckling stiffness and ultimate strength appears to be negligible, possibly due to the relatively small size of the delamination.

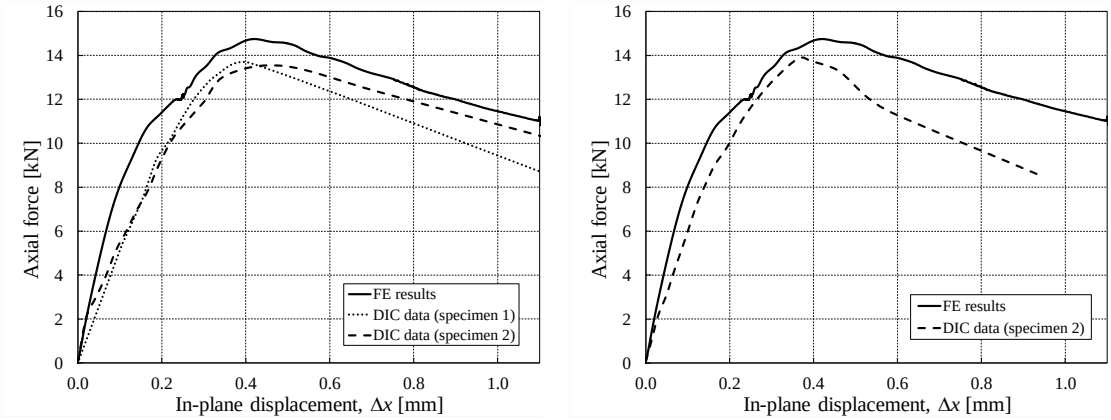

Figure 5.8: Axial force versus in-plane displacement for splice specimens; (a) pristine and (b) with an artificial defect.

The evolution of interface damage is shown in Figure 5.9 for the critical interface of the splice specimen with the defect with an interface damage value of one representing full delamination and a value of zero indicating no delamination. The results indicate the initiation of interface damage in the area of the splice at initial buckling (Δx = 0.184 mm) with the delamination propagating throughout buckling and full separation of the splice in the postbuckling region at Δx = 1.0 mm. Comparison with the AE data in Figure 5.10 showing the location of cumulative AE events in the specimen supports this prediction with activity seen to initiate in the centre of the splice and propagate along its

length as buckling proceeds. Further validation is provided by the SEM micrographs of the splice region (Figure 4.12) which clearly indicate the presence of delamination in this area. The pristine specimens tested presented very similar behaviour indicating that the effect of the initial delamination on the interfacial damage is negligible.

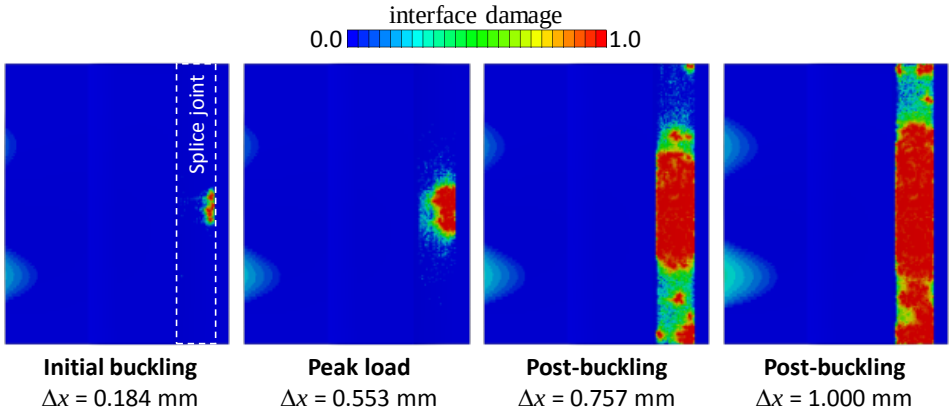

Figure 5.9: Numerical results for evolution of interface damage along the critical interface in the splice specimen with a defect (dashed line indicates position of splice).

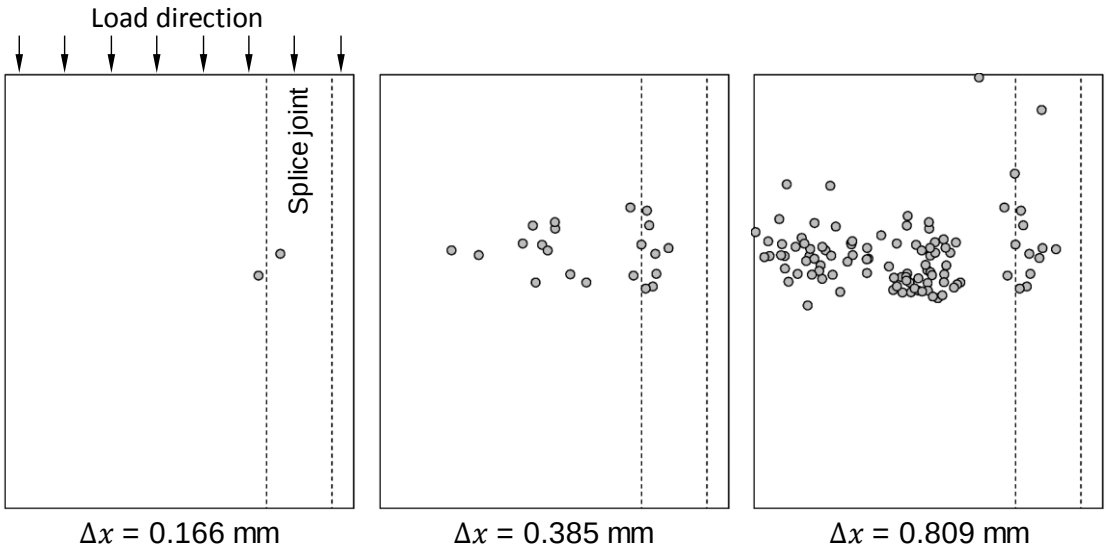

Figure 5.10: Acoustic Emission event locations in the splice specimen at different cross-head displacements Δx (dashed line indicates position of splice); after [172].

In terms of plasticity in the aluminium layers, Figure 5.11 shows the predicted plastic strain contours at a cross head displacement Δx = 1 mm which suggest considerable amounts of energy are being dissipated via plastic deformation of the metallic sheets.

Again the result shown is for the specimen with the defect, however the pristine specimens produce very similar behaviour indicating that the effect of this defect on the plasticity of the specimen is negligible. This result is confirmed by both SEM and visual inspection which show large residual curvatures in aluminium layers, in particular near the discontinuity at the joint. This is in direct correlation with the results of the FE model (Figure 5.11) which predicts higher levels of plastic strain in the joints than in the remainder of the specimen (including the areas of high curvature in the thinner part of the specimen).

The evolution of damage in the composite plies is shown in Figure 5.12 again for the specimen with a defect, with the pristine specimens presenting similar behaviour. As with the interface damage a value of one represents full composite ply damage while a damage value of zero represents no composite damage. The Hashin damage criterion for fibre compression (top of Figure 5.12) indicates that up to and during critical buckling there is no damage, with fibre breakage beginning during postbuckling. This damage is concentrated in the centre of the specimen near the splice joint where the combination of high curvature following buckling and the stress concentration coming from the discontinuity in the aluminium layers creates a weak region. Similar behaviour is noticed for matrix compression (middle of Figure 5.12) which indicates FE predicted matrix compression between the fibre layers during postbuckling. Finally, results for matrix shear (bottom of Figure 5.12) indicate that this occurs during postbuckling. Again peaks can be seen at centre of the specimens particularly in the splice joint for the reasons described above. The AE data presented in Figure 5.10 can again be seen to correlate well with the FE predicted damage with a large number of events detected in the centre of the specimen in the area of highest curvature during both buckling and postbuckling, indicating a high level of damage initiation and propagation in this area as predicted by the application of the Hashin criteria.

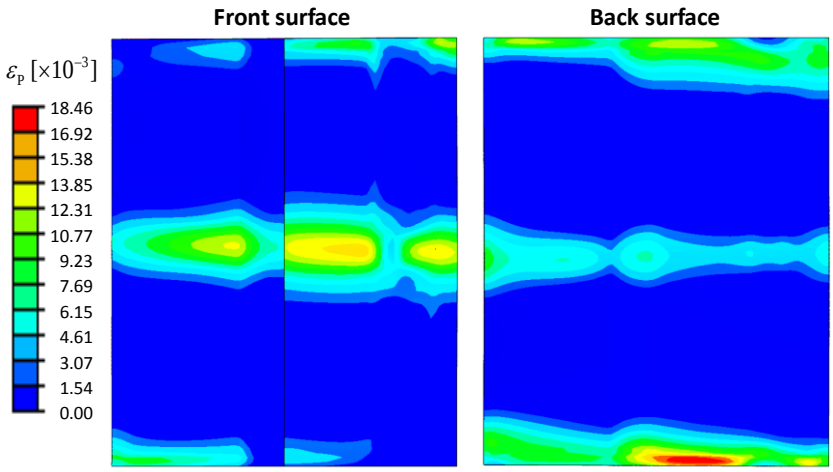

Figure 5.11: Contours of equivalent plastic strain in the FE model of the splice specimen (with an artificial defect) at Δx = 1 mm.

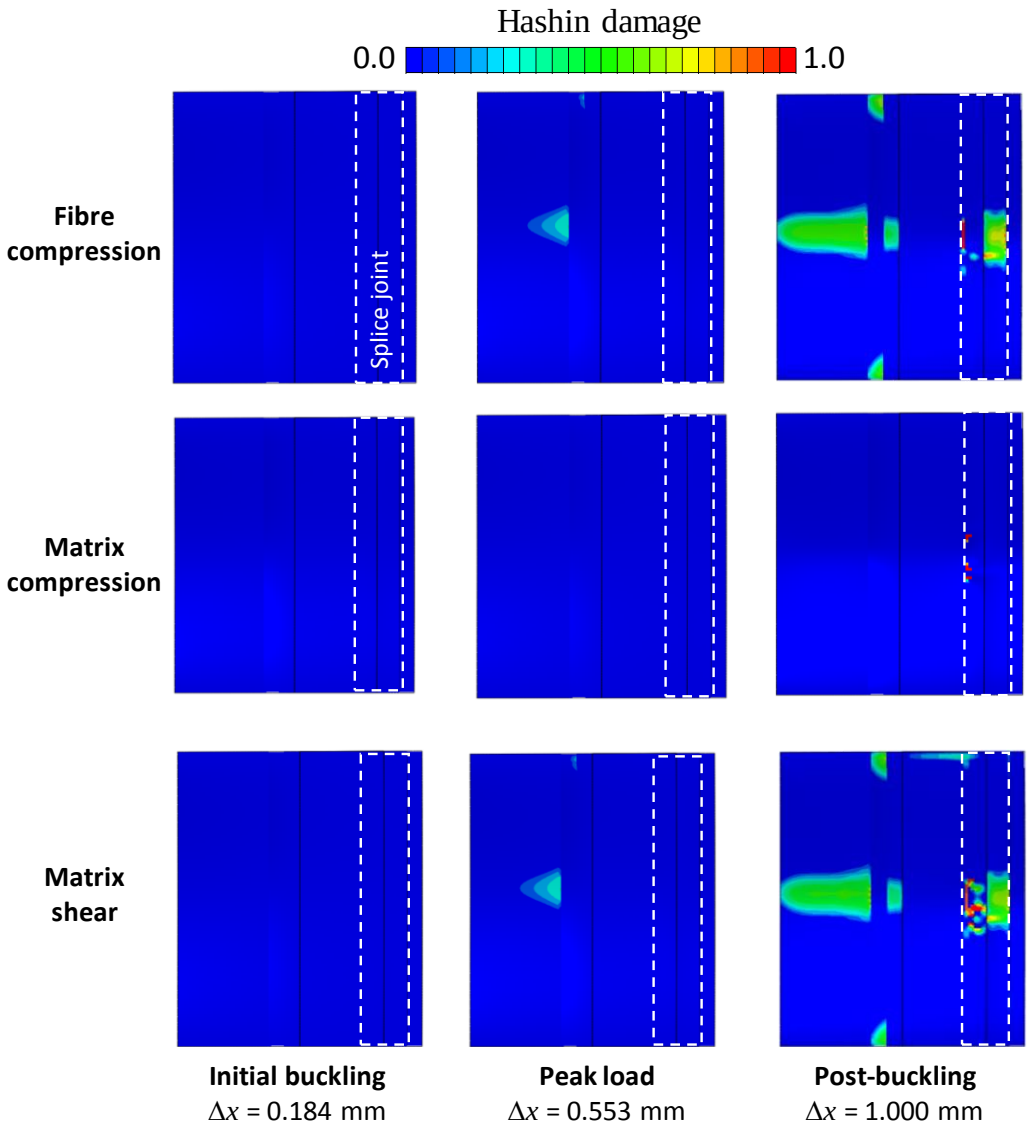

Figure 5.12: Hashin damage indices for GFRP layers in the splice specimen at three different stages of the buckling curve (dashed line indicates position of splice).

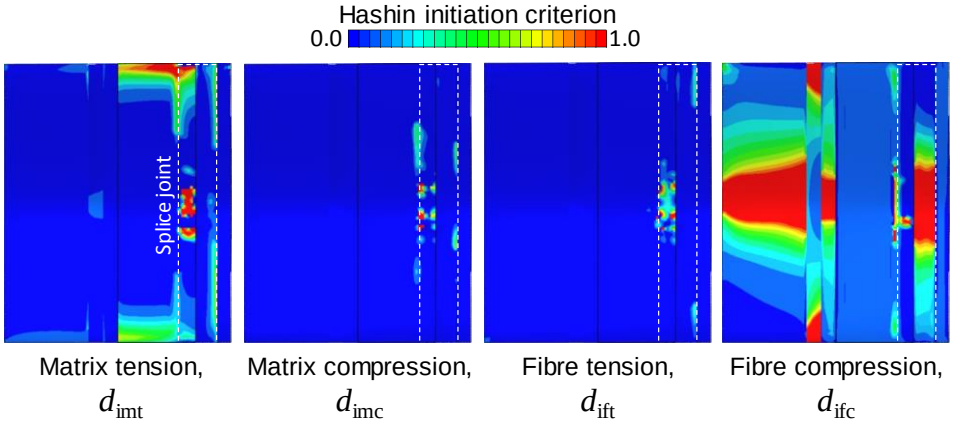

Figure 5.13: Hashin damage initiation variables for splice specimen.

SEM micrographs taken in this region of the panel outside the splice joint (Figure 4.11) indicate the presence of matrix cracking in this area, caused by the initiation (Figure 5.13) and evolution (Figure 5.12) of damage predicted by the Hashin criteria (with indices of less than one indicating partial damage as discussed in [174]).

In the joint itself, a range of different damage mechanisms can be seen from the SEM micrographs (Figure 4.12), including matrix cracking and shear damage in the matrix resin layers and some indirect evidence of fibre damage in the 0° GFRP layers, in the form of fractured fibres along the polished surface (it should be noted that this fracture combines any damage introduced during the test, with further damage introduced when cutting and polishing the specimens). This correlates well with the predictions of the Hashin damage criterion in terms of both initiation and evolution.

5.3.2 Doubler specimen

For the doubler specimens, Figures 5.14 and 5.15 show the out-of-plane and in-plane displacement behaviour obtained from the FE model compared with that from the experimental DIC system data. The out-of-plane displacement is shown at initial buckling, peak load and postbuckling, corresponding to in-plane displacements Δx shown separately for model and experiment. The results presented are for specimens

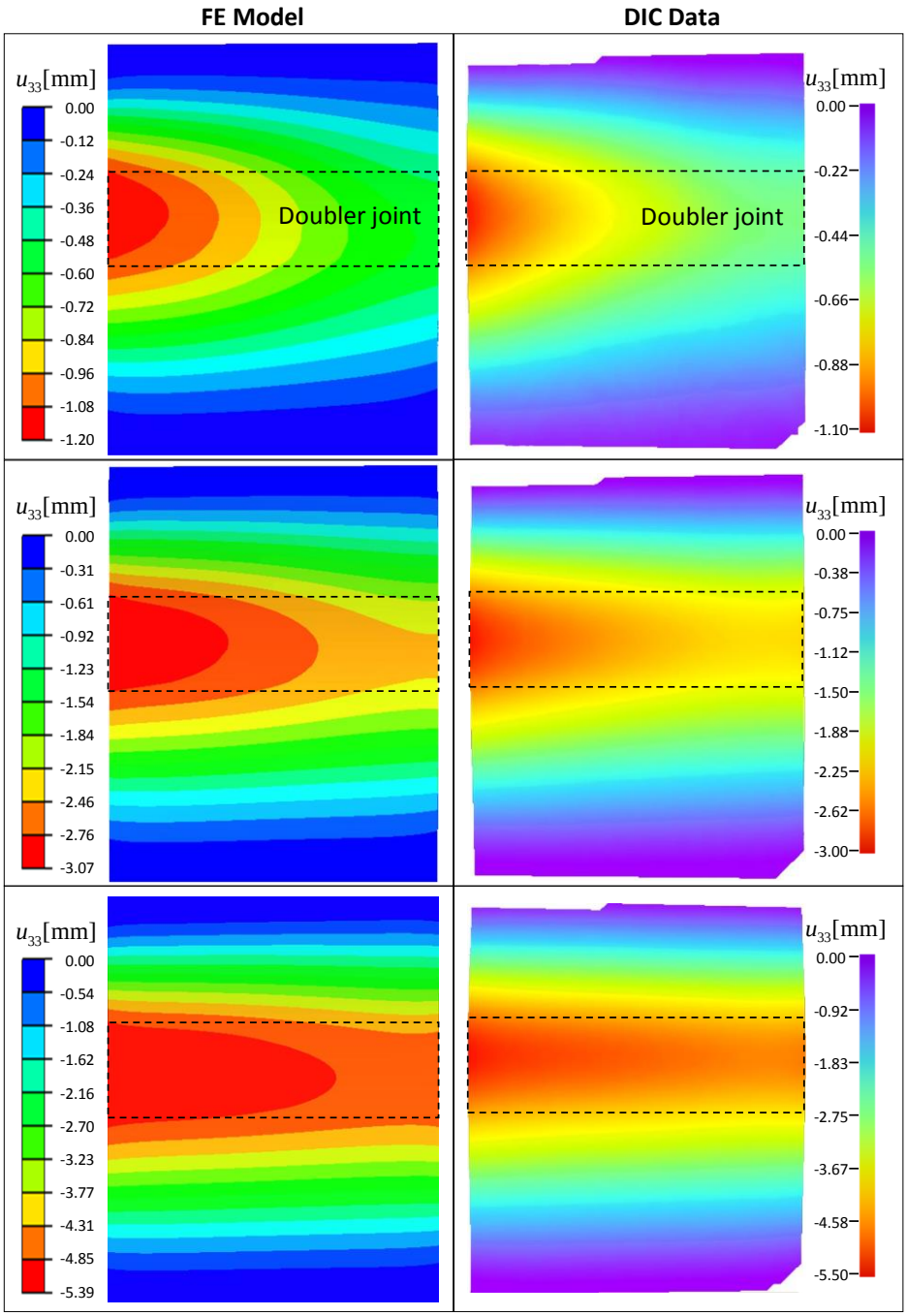

Figure 5.14: Out-of plane displacements for the doubler specimen with an artificial defect; FE predictions and DIC data at different in-plane displacements Δx (dashed line indicates position of doubler).

incorporating a defect, but the pristine specimens presented very similar behaviour indicating that the effect of the introduced initial delamination on the buckling and postbuckling behaviour is also negligible for the doubler specimen. The plate is again seen to buckle with a single half wave length in the loading direction as expected. Deformations towards the top of the joint in the thinner region of the specimen are

higher than those nearer to the bottom, again as would be expected. Good qualitative agreement is observed between experimental and FE results in terms of the mode shape although the FE model underestimates the displacement slightly.

Axial load versus in-plane displacement for the FE model is compared with that measured during the experimental work in Figure 5.15. It can be seen that for both the pristine doubler specimens and those incorporating defects, there is strong correlation between the experimental pre-buckling stiffnesses and the FE results, while the postbuckling stiffnesses are overestimated by the model . In terms of ultimate compressive load the FE model predicts a value of 14.89 kN for both pristine and defective specimens whilst experimental values are 13.69 kN and 13.78 kN for pristine specimens and 14.65 kN and 15.49 kN for defected specimens. As mentioned earlier this is believed to be due to the use of shell elements which neglect the through thickness stresses to model the composite layers [173], resulting in an overestimation of their stiffness which is particularly significant in areas of high curvature such as the thinner part of the doubler specimens during postbuckling, while showing very good correlation in elastic and initial buckling regions. In terms of interface damage the model indicates no delamination growth either remote from or within the doubler joint. This is confirmed by the SEM micrographs in Figures 4.17 and 4.18.

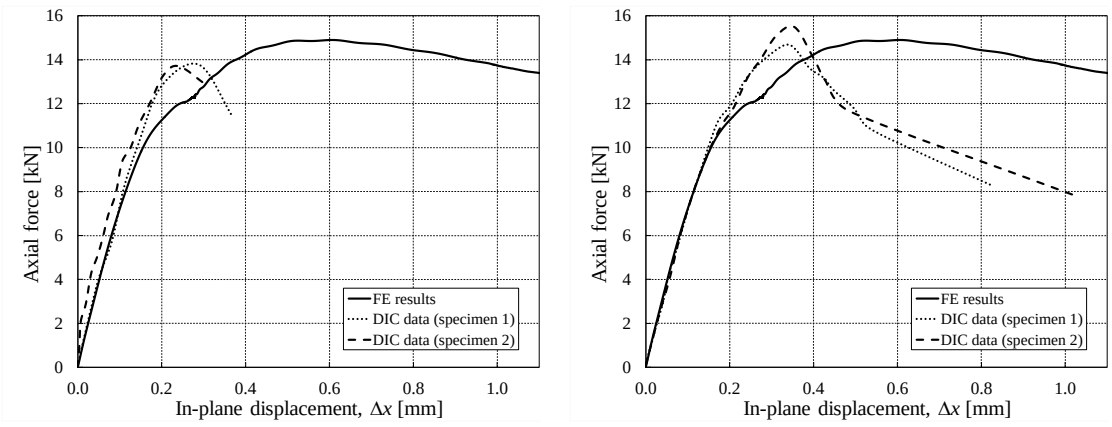

Figure 5.15: Axial force versus in-plane displacement for doubler specimens; (a) pristine and (b) with an artificial defect.

Figure 5.16 shows the FE contours of plastic strain for the doubler specimen with a defect at a cross head displacement Δx = 1 mm. This result is again confirmed by SEM micrographs and visual inspection which show considerable residual curvatures in the aluminium layers, in particular at the ends of the discontinuous layers in the doubler joint. As for the splice model, a considerable amount of energy appears to be dissipated via plastic deformation of the metallic sheets.

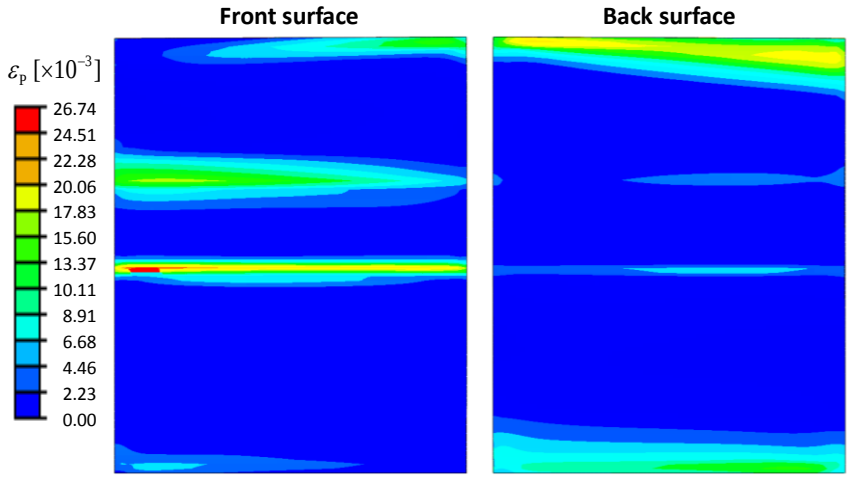

Figure 5.16: Contours of equivalent plastic strain in the FE model of the doubler specimen (with an artificial defect) at Δx = 1 mm.

The evolution of damage in composite plies is shown in Figure 5.17 for the doubler specimen with defect with the pristine specimens presenting similar results. The Hashin damage criterion for fibre direction compression (top of Figure 5.17) indicates that this damage mode initiates during buckling and continues to increase throughout postbuckling with the damage concentrated in the centre of the specimen particularly in the doubler joint as where the highest out-of-plane displacement occurs due to buckling and the discontinuous aluminium layers result in a region of high stress concentration. FE results for transverse direction compression (middle of Figure 5.17) suggest that this damage mode initiates between the fibre layers at the left hand side of doubler joint in the critical buckling region and increase during postbuckling to both sides of the doubler joint. Finally, the FE results for matrix shear (bottom of Figure 5.17) show that this damage mode occurs between the fibre layers at critical buckling and grows during postbuckling in the region of the doubler joint.

The location of the damage predicted using the Hashin criterion is again supported by the AE data shown in Figure 5.19. It shows a high level of activity in the thinner, upper part of the specimen particularly during postbuckling and up to final failure indicating this is where the majority of damage occurs, thus confirming the capability of the Hashin damage criterion to predict damage in Glare® in the buckling and postbuckling regimes.

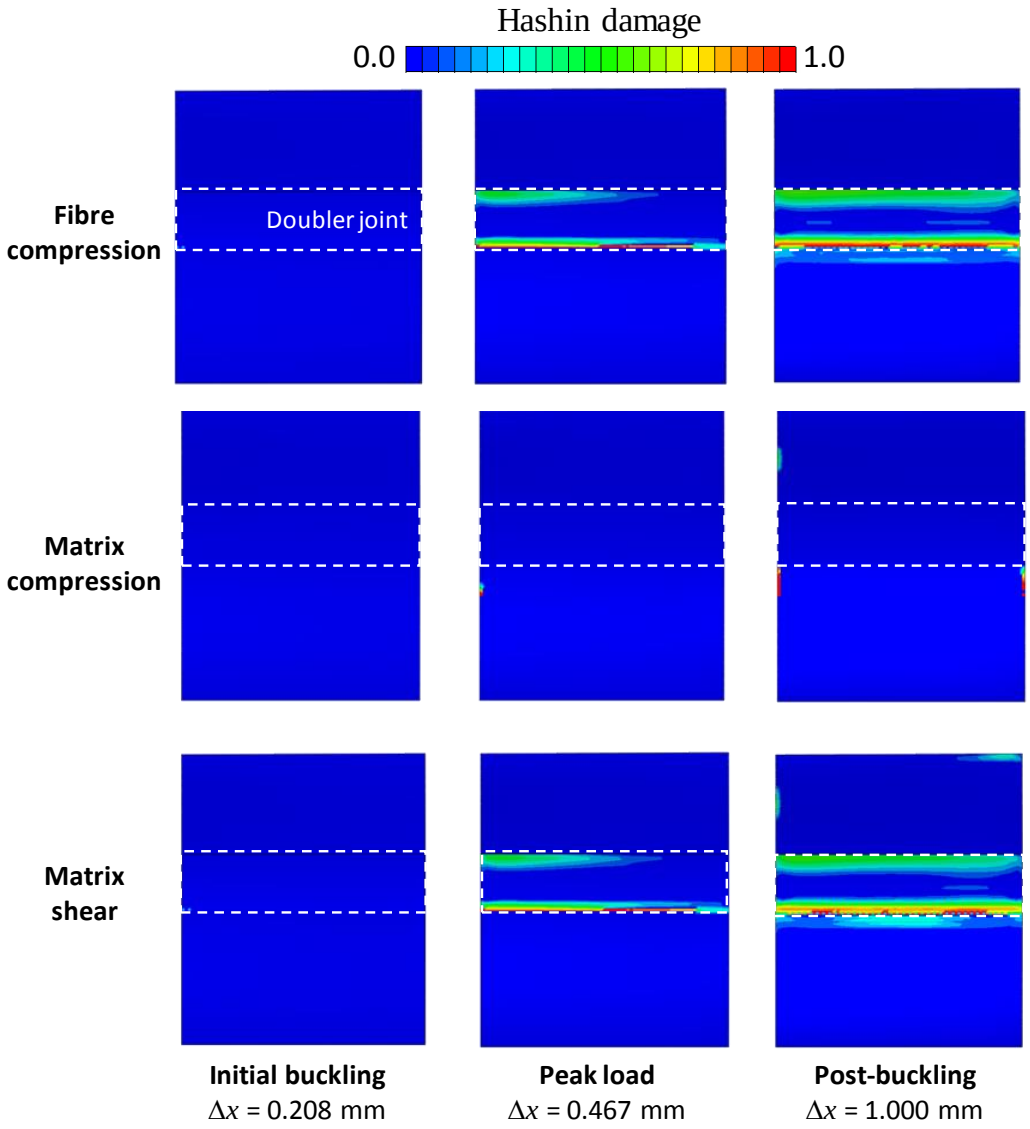

Figure 5.17: Hashin damage indices for GFRP layers in the doubler specimen at three different stages of the buckling curve (dashed line indicates position of doubler).

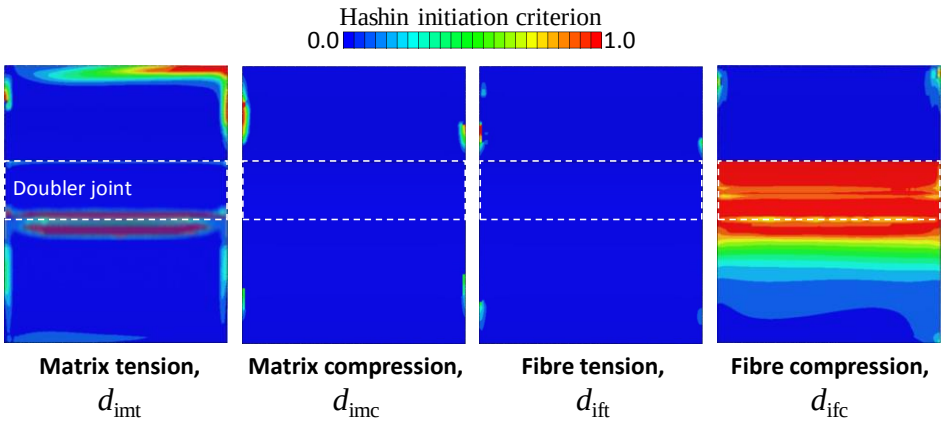

Figure 5.18: Hashin damage initiation variables for doubler specimen.

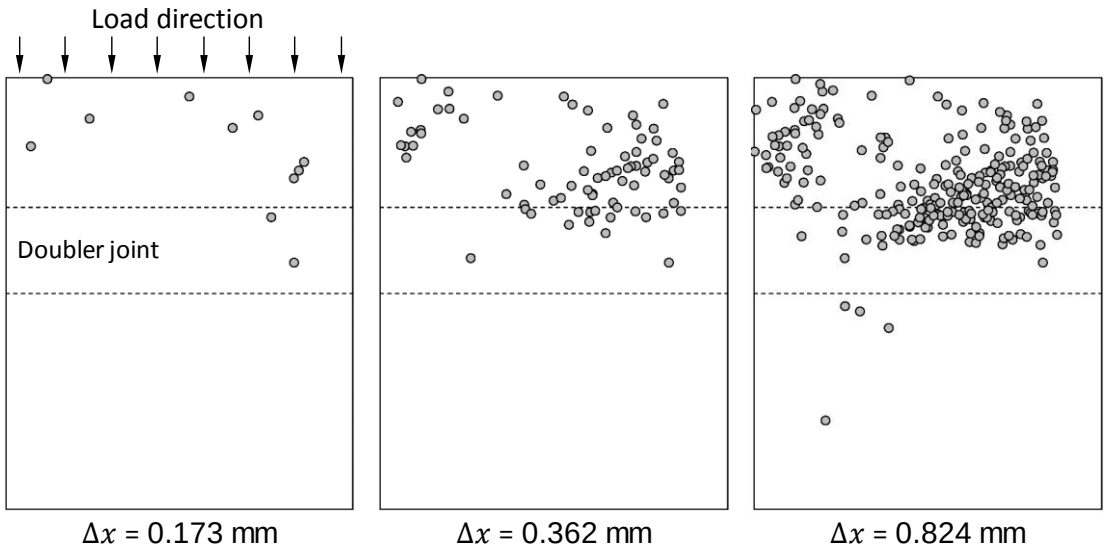

Figure 5.19: Acoustic Emission event locations in the doubler specimen at different cross-head displacements Δx (dashed line indicates position of doubler); after [172].

SEM micrographs from this region (Figure 4.18) indicate that the damage is mostly in the form of matrix cracking as was predicted by the FE model in which the Hashin damage initiation variable for matrix tension (Figure 5.18) reaches one in this area with lower levels of damage evolution corresponding to in plane shear (Figure 5.17). It should be noted however that the FE model did not predict widespread damage within the thin section as suggested by the AE data, but instead it highlighted damage initiation and evolution within the doubler joint and near the upper grip, where local curvatures were high. Possible reasons include local variations in material properties, further geometric imperfections, and the possibility of AE event location being affected by reflections. Future work is required to clarify this issue.

5.3.3 Far-field specimens

For far-field specimens with defect, Figure 5.20 shows the progressive increase in AE events located around the periphery of the delamination as it grows, in particular around the area where we see the most out-of-plane displacement (Figures 4.20 and 4.22). Excellent correlation with the FE model was observed, which predicts delamination growth as well as matrix cracking along the horizontal centreline where the highest curvature is seen. The evolution of interface damage is for the critical interface of the far-field specimen with the defect with an interface damage value of 1 representing full delamination and a value of zero indicating no delamination. The results indicate the initiation of interface damage in the area of the high curvature at initial buckling (t = 570 s) and peak load (t = 1082 s) with the matrix cracking throughout buckling and delamination onset and growth around the area where we see the outer aluminium layer come out (Figure 4.20) in the post-buckling region at (t = 1150 s). While we cannot see delamination very clearly for the second half of the circular delamination region due to buckling which causes delamination closure as a result of opposite direction out-of-plane deflection. Analyses continue with more matrix cracking in the high curvature region and delamination propagation around the top half circular delamination up to the final failure and these results were confirmed via AE activities in the same regions.

Comparison with the AE data for the pristine far-field specimens shown in Section 4.4.3, the location of cumulative AE events in the specimen show similar behaviour with AE activity seen to initiate in the centre of the far-field with defect specimen and propagate along its length as buckling proceeds which are mostly due to matrix cracking. The FE analyses for the pristine specimens support these results and presented no delamination occur in the critical interface layers and is therefore not presented here.

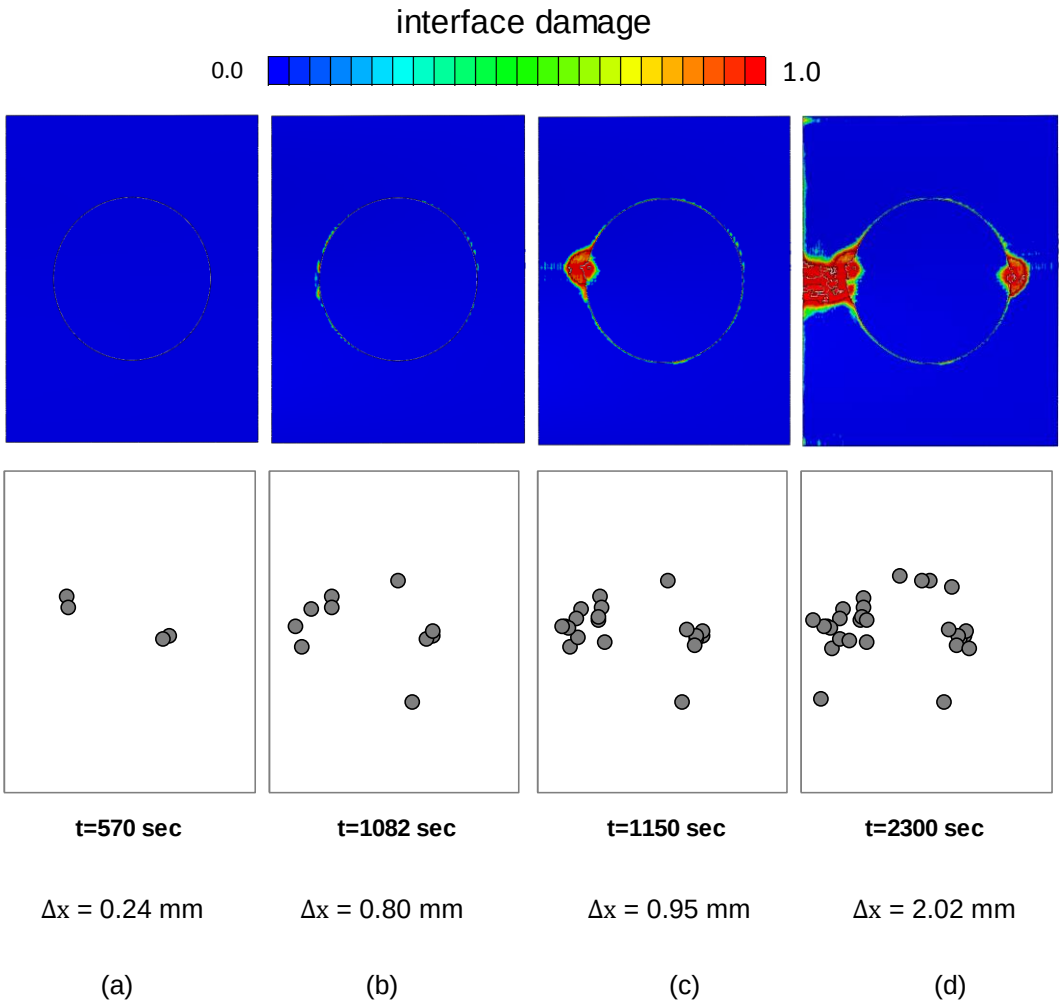

Figure 5.20: AE Results & FE model comparison for far-field with defect specimen at (a) initial buckling (t = 570 s), (b) peak load (t = 1082 s), (c) postbuckling (t = 1150 s) and (d) postbuckling (t = 2300 s).

Figure 5.21 shows the load-displacement behaviour predicted by the model which is also in a good agreement with experimental results for both pristine and with defect specimen 2 (the first specimens of both types of far-field specimens to be tested (pristine and with defect) suffered from slippage in the rig and have therefore not been considered for comparison with the FE analyses). A comparison between FE analyses for pristine and with artificial circular delamination models (Figure 5.21-c) shows a reduction in postbuckling stiffness (28.2 %) for the defected specimen model which showing the suitability of the model in assessing the effects of this type of delamination damage.

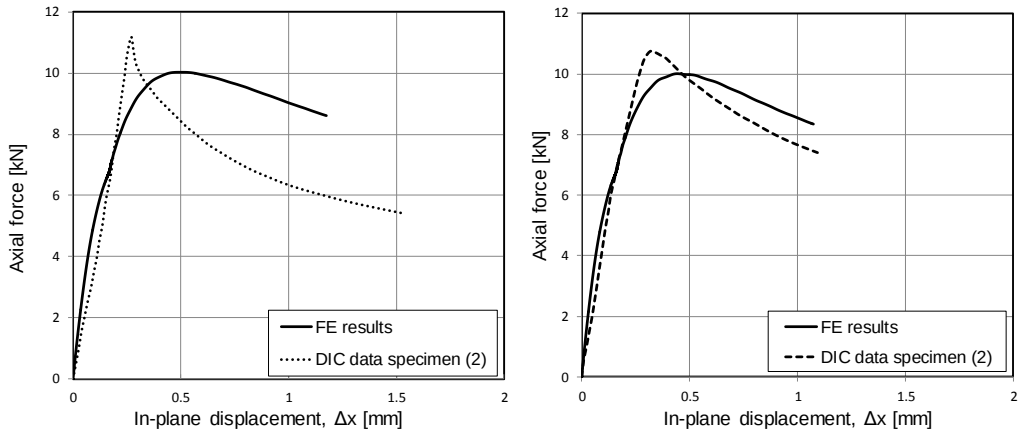

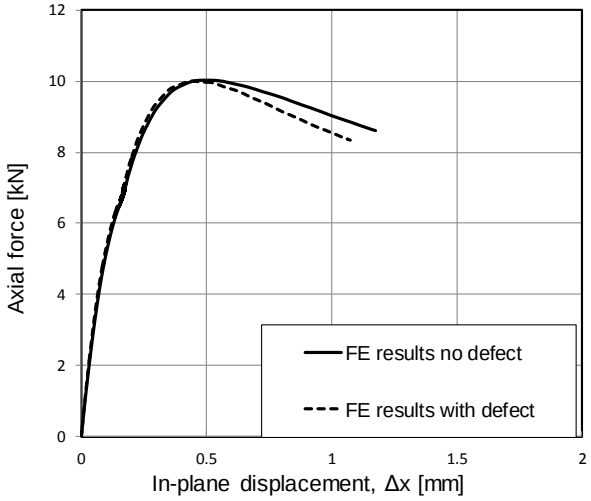

Figure 5.21: Axial force versus in-plane displacement for far-field specimens; (a) pristine and (b) with an artificial defect and (c) FE model comparison between pristine and with defect far-field specimens.

5.4 Chapter summary

This chapter included numerical studies to determine the buckling and postbuckling behaviour of Glare® laminates with splice, doubler and artificial circular delamination features. The results showed good agreement with experiments in terms of in-plane and out-of-plane displacements thus validating the models used.

The gradual evolution of interface damage (delamination) is effectively modelled by a cohesive zone model in both splice and far-field specimens' models, which also predicts the lack of delamination in the doubler model. A considerable amount of

energy is dissipated via plastic deformation of the metallic sheets in all cases. The FE models predict damage in GFRP layers due mostly to fibre direction and transverse direction compression. In addition, delamination between composite plies is observed in both splice and doubler regions. These findings are supported by acoustic emission data collected during validation of the experiments. Relatively small embedded artificial delaminations typical of those potentially introduced during manufacturing had a negligible effect on the compressive strength of both splice and doubler specimens, while a relatively large artificial delamination in proportion to the specimen width has a noticeable effect on the compressive strength of far-field specimens and postbuckling stiffness, a finding which was also validated by the experimental and numerical results.

Chapter 6 - Fatigue Numerical Model and Validation

6.1 Introduction

This chapter focuses on the development of a constitutive damage model capable of simulating the damage at the interfaces of elastic-plastic materials (in this case at the interfaces between the aluminium and GFRP layers of the Glare® laminates) under high cycle dynamic loading. The model uses a mixed mode trapezoidal traction separation law to addresses the problem of defining the damage behaviour of elastic-plastic materials under high cycle fatigue and is to the author's best knowledge entirely novel, previous solution available in the literature having dealt with static and/or single mode analysis as discussed in Chapter 2.

This model is used to define the material properties of cohesive layers in a series of models of increasing complexity designed to validate the approach proposed. Models are written in FORTRAN 77 programme and implemented in Abaqus/Explicit software using the user subroutine VUMAT. This subroutine enables the mechanical constitutive behaviour of a material to be defined and implemented in an explicit model (an alternative UMAT subroutine is available for implicit modelling). At each increment of the analysis VUMAT reads and updates the state variables according to a user defined constitutive equation. By interfacing with Abaqus/Explicit it takes advantage of the use of relatively quick to compute small time increments and efficient convergence is achieved from diagonal ("lumped") element mass matrices. A complete description of these features and instructions on how to write VUMAT subroutines basis is given in [169].

6.2 Mixed mode trapezoidal traction-separation law

An overview of the cohesive zone model (CZM) and its development was presented by the author in Chapter 2, with cohesive elements used in the static models developed in Chapters 4 and 5.

Cohesive zone models have been widely used for predicting delamination in adhesively bonded structures under fatigue loading. Models used in these analyses which are mostly based on a bilinear traction-separation law have been found to be a particularly efficient approach for elastic materials. This approach however has not been found to be accurate for elastic-plastic materials where a trapezoidal traction-separation law proved to be more efficient in predicting the plastic flow of ductile adhesives [175].

The trapezoidal traction law shown in Figure 6.1 has been adopted by many researchers [94-103] to model interface damage behaviour in elastic or elastic-plastic materials in either mode-I or mode-II under static loading. In this work, a mixed mode trapezoidal traction-separation law has been developed to model first static and then high cycle fatigue damage in fibre metal laminate (FML) structures including adhesively bonded joints. The deterioration due to the influence of fatigue loading is then simulated by degrading the trapezoidal traction-separation response based on a fatigue damage variable derived from the Paris law of the material and the elapsed number of load cycles.

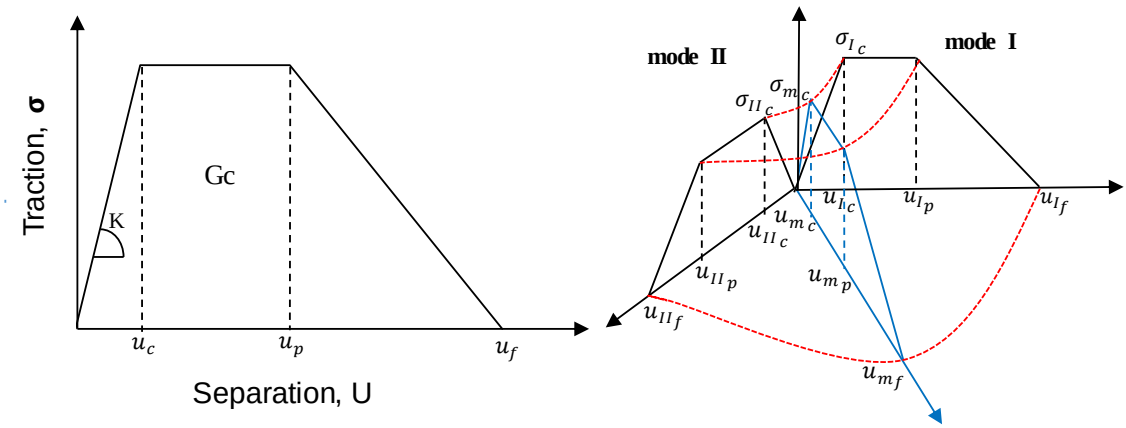

Figure 6.1: Mixed mode trapezoidal traction law.

As discussed previously CZM can be implemented in Abaqus/Explicit using either 2D (COH2D4) or 3D (COH3D8) cohesive elements. Whilst the static analyses described in earlier chapters, used 3D elements a 2D cohesive element has been adopted for fatigue modelling for simplicity, as both the splice and doubler specimens to be studied have symmetrical through thickness cross-sections (width-direction propagation can be neglected for narrow, prismatic tension-tension specimens but not for the wider buckling specimens). Figure 6.2 shows pure mode-I and pure mode-II failure modes for these elements. More details can be found in the Abaqus software manual [169]. In this work mixed mode failure will also be considered.

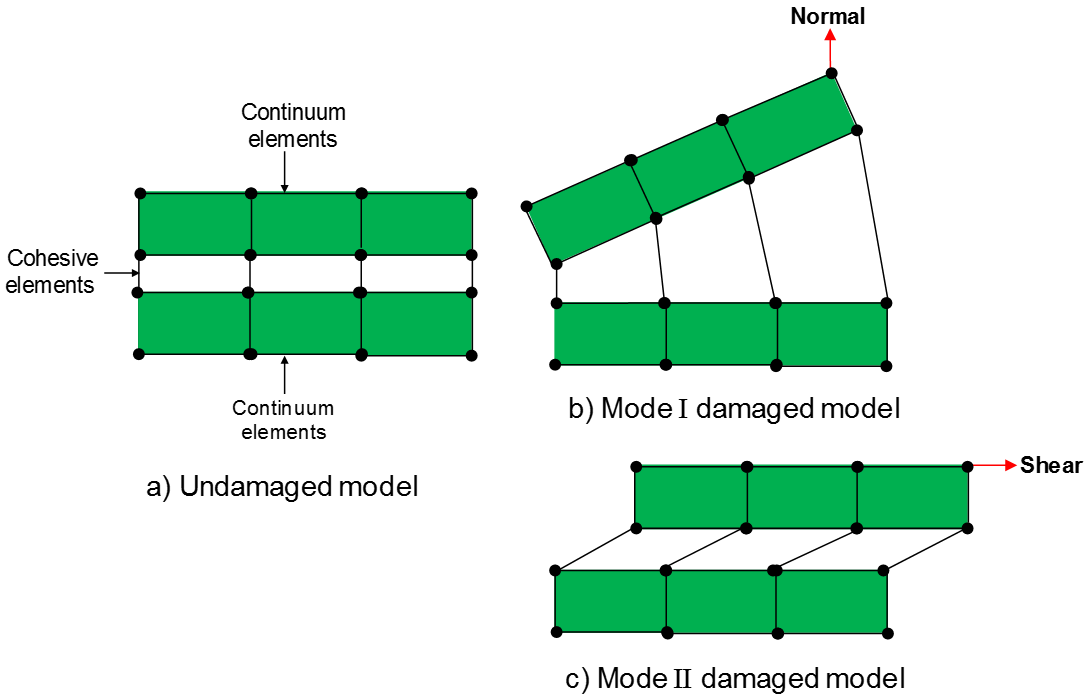

Figure 6.2: Cohesive modes of failure in two dimensions.

6.3 Modelling fatigue in Abaqus using the VUMAT subroutine

The cohesive zone models developed were then utilised in the two-stage fatigue loading analysis shown in Figure 6.3. In the first step static loading up to the maximum fatigue load value was applied after which the second step including the fatigue envelope approach described in Chapter 2 and shown in Figure 6.3 (a) began. This process required the use of two VUMAT codes to simulate both quasi-static and high

cycle fatigue damage behaviour with the static VUMAT subroutine following the trapezoidal traction law, and the fatigue VUMAT subroutine following the Paris Law. This fatigue degradation process is illustrated in Figure 6.3 (b) and is based on a total damage variable which is the sum of both static and fatigue damage variables. This fatigue damage variable (D_f) is zero at the end of static step and is then updated according to the Paris law for each increment. During analysis, it increases up to certain value $D_{f,t1}$ at simulation time t_1 which is identified by the user and which indicates the start of the 'fatigue degradation at constant stress' region. Fatigue degradation then continues to increase following the trapezoidal traction law up to damage variable $D_{f,t2}$ at simulation time t_2 at the softening stress region. The process continues until final fatigue failure occurs when (D_f) reaches one and the number of cycles is equal to the number of failure cycles, at which point all cohesive stress components vanish.

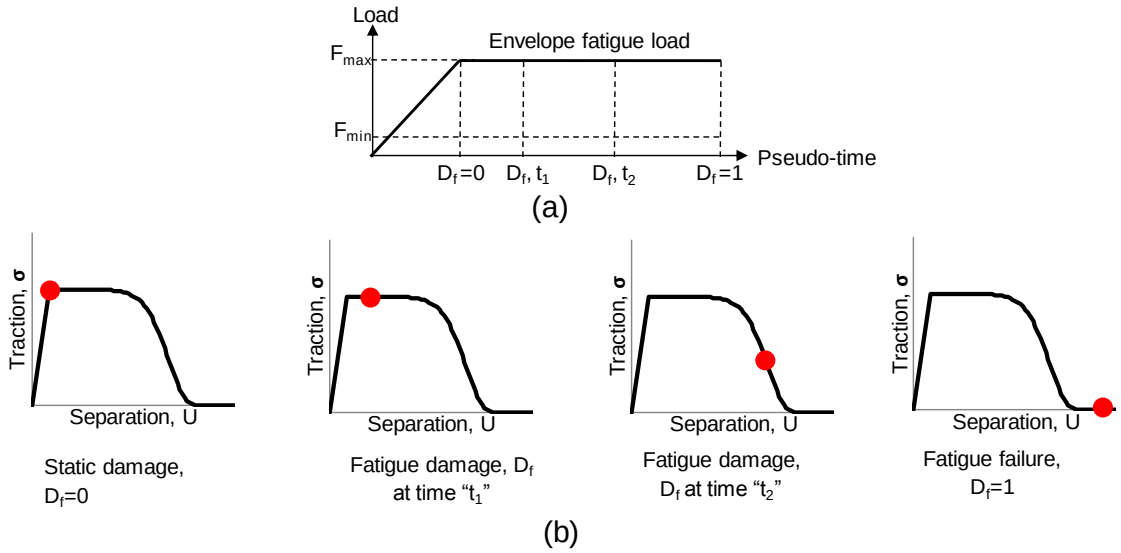

Figure 6.3: (a) Fatigue envelope loading, and (b) fatigue degradation process for the cohesive zone model.

To increase the accuracy of the model, a user defined variable was introduced to allow the fatigue analysis at a certain time increment of the total simulation time. This permitted the model to start at any time increment automatically whenever a smaller time increment size was required to reduce the computational time for the model which

has a significant important in fatigue analysis, facilitating a balance between the total simulation time and the fatigue degradation start and end times. A detailed explanation of the calculation of both static and fatigue damage variables is discussed in Sections 6.2.2 and 6.2.3, respectively.

6.3.1 Quasi-static damage model

The first stage in this work was to develop a static VUMAT code and to build it into an interface with the Abaqus/Explicit software. For this, a trapezoidal mixed mode modified cohesive zone model (Figure 6.1) was adopted. This code is described in the flowchart shown in Figure 6.4.

The VUMAT subroutine calls for blocks of material points at each increment and is provided with the material state data for each material point including stresses and solution – state dependent variables (SDVs) by the main programme. The state variables include the strain increments that can be used to calculate separation under mode-I, $U_{\boldsymbol{I}}$ and mode-II, $U_{\boldsymbol{II}}$. This enables updated stresses including normal stresses $\sigma_{\boldsymbol{I}}$ and shear stresses $\boldsymbol{\sigma_{II}}$ for both mode-I and mode-II, respectively, to be calculated at each integration point for each element and updated using the history delivered from the main programme. These stresses are then used to calculate the damage initiation variable $(D_{\boldsymbol{i}})$. After this damage initiation can be predicted using a quadratic nominal stress criterion (equation 6.1) [169]. Strain energy release rates $G_{\boldsymbol{I}}$ and $G_{\boldsymbol{II}}$ are then calculated from the areas under the trapezoidal traction-separation curves for mode-I and mode-II (equations 6.2 and 6.3), respectively. Finally damage evolution variable $D_{\boldsymbol{e}}$ is calculated using a power law failure criterion (equation 6.4) based on strain energy and the power law parameter, ϕ determined from best fit to mixed-mode delamination data from the literature [176]. Delamination growth is mostly described in terms of the strain energy release rates [166]. The energy release rate of the interface between aluminium 2024-T3 and FM94 reinforced with S2 glass fibre used here is based on experiments performed by Vesco *et al.*[177]. An important aspect of the

mixed mode case is the lower total energy G_c required compared to the pure mode-I and mode-II situations. Neither the Benzeggagh-Kenane criterion, as described by Wen-Guang Jiang *et al.* [176] and Camanho *et al.* [178], nor the power law with the power constant (ϕ) equal to 1 or 2 can correctly describe the experimental behaviour as obtained by Vesco *et al.* [177]. A better relation for this specific case is the power law with the power $\phi = 1/2$ [166].

$$(\frac{\sigma_I}{\sigma_{Ic}})^2 + (\frac{\sigma_{II}}{\sigma_{IIc}})^2 = D_i \tag{6.1}$$

$$G_I = \int_0^u \sigma_I \ du_I \tag{6.2}$$

$$G_{II} = \int_0^u \sigma_{II} \ du_{II} \tag{6.3}$$

$$(\frac{G_I}{G_{Ic}})^\phi + (\frac{G_{II}}{G_{IIc}})^\phi = D_e \tag{6.4}$$

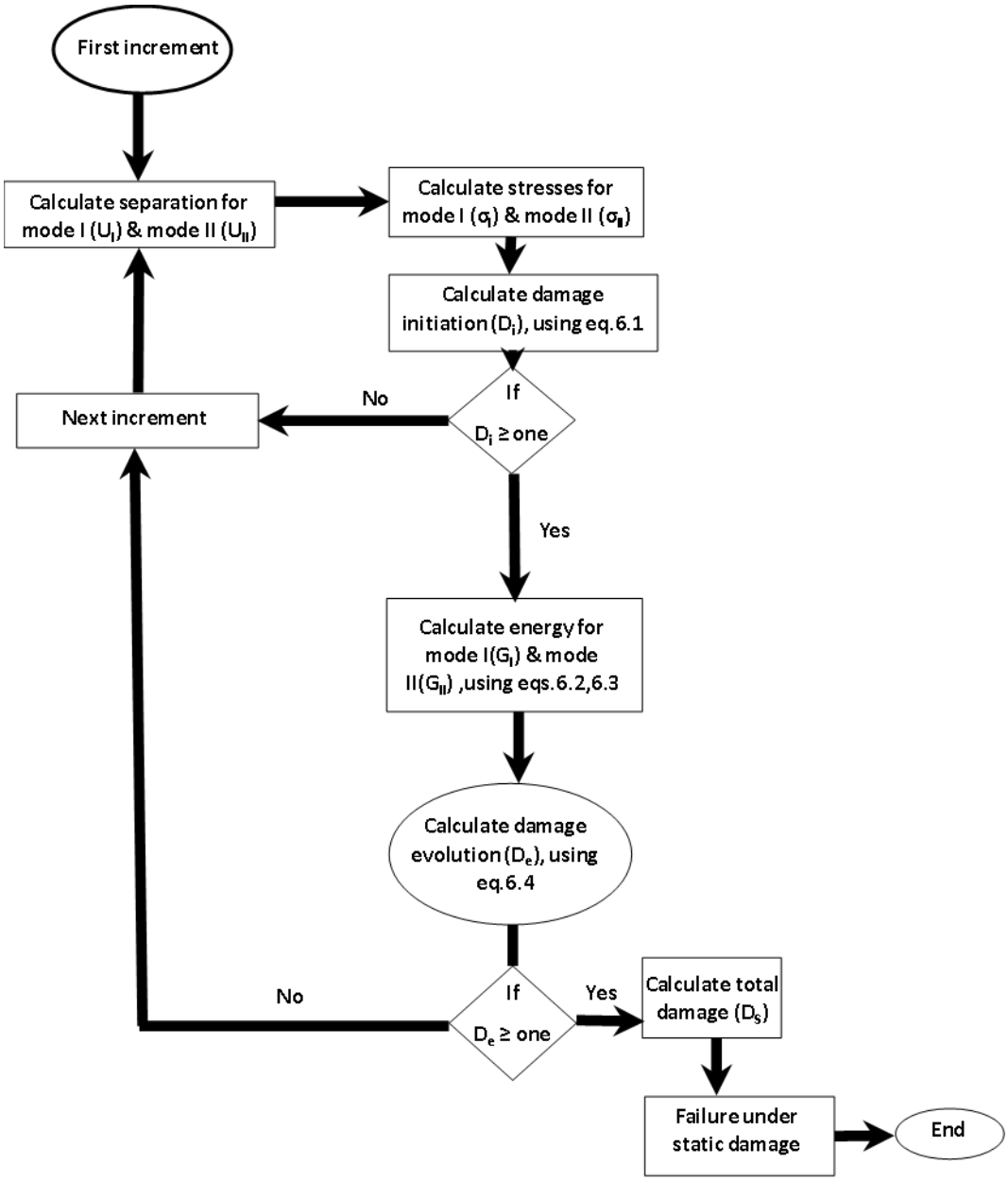

Figure 6.4: Static damage model flow chart.

6.3.2 Fatigue damage model

A fatigue analysis was then developed based on the static damage model by incorporating cyclic degradation using a fatigue damage degradation law. This code can be explained by reference to the flowchart in Figure 6.5. The fatigue damage approach adopted in this model to calculate crack growth rate is a normalised Paris law according to [166, 177] as follows:

$$\frac{\mathrm{d}a}{\mathrm{d}N} = C\left(\frac{\Delta G}{G_c}\right)^m \tag{6.5}$$

where $\mathrm{d}a/\mathrm{d}N$ is the crack growth rate (the increment in crack area with increasing number of cycles) and *C* and *m* are best fit coefficients to experimental data in a log-log plot for crack length *a* versus number of cycles *N*. The total critical strain energy G_c is a material property for the interface cohesive layer (Chapter 5: Table 5.4) and it represents the area under the curve of the trapezoidal traction–separation relation for pure mode-II as in this study we consider only pure mode-II to simulate delamination crack growth under fatigue loading. This is because delamination is the predominant failure mode as noticed from experiments. The change in mode-II strain energy can be calculated as in [166, 177] as follows;

$$\Delta G = (1 - R^2).\, G_{\max} \tag{6.6}$$

where, R is the load ratio (which can be calculated from division of minimum fatigue load over the maximum fatigue load) and for this study its value is equal to 0.1 from experiments and $G_{\max}$ is the maximum strain energy in mode-II. The fatigue damage variable D_f is calculated based on effective element length $(L_{I.P})$ which is the length associated with a single cohesive integration point in the direction of crack propagation. The delamination will propagate with a distance $L_{I.P}$ after a certain number of cycles to failure N_f with a constant crack growth rate $\frac{da}{dN}$ which is calculated using the Paris law given in equation 6.5 based on both pure mode-II strain energy release rate ratio and experimental fatigue parameters as follows;

$$N_f = L_{I.P} \cdot {}^{1}\Big/\frac{\mathrm{d}a}{\mathrm{d}N} \tag{6.7}$$

$$t_f = {}^{N_f}\Big/_{\omega} \tag{6.8}$$

$$D_{\mathrm{rate}} = {}^{dt}\Big/_{t_f} \tag{6.9}$$

$$D_f = D_f + D_{\mathrm{rate}} \tag{6.10}$$

where t_f is the failure time of each element in the direction of crack propagation, ω is

the user-defined loading frequency and D_{rate} is the calculated fatigue damage after every time step (dt) in the explicit analysis.

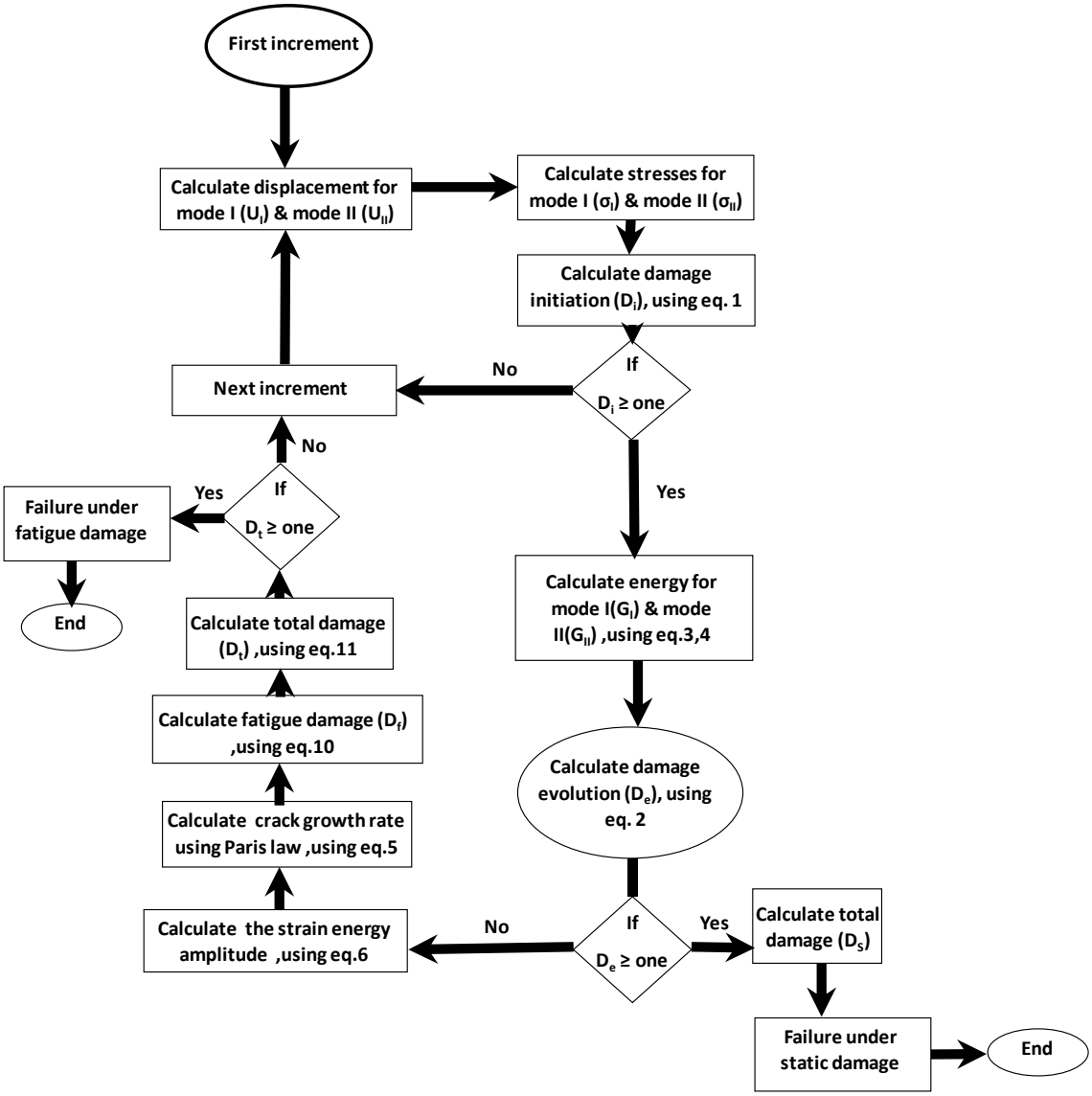

Figure 6.5: Fatigue damage model flow chart.

Finally the total damage variable (D_t) can be calculated from summation of static damage variable (D_s) and fatigue damage variable (D_f) according to [59, 105, 179] as follows:

$$D_t = D_s + D_f \tag{6.11}$$

6.3 Unloading/Reloading

As discussed above, the fatigue model developed in this work is based on modelling the envelopes of forces versus simulation time (pseudo-time). As the number of elapsed cycles increases and interfaces degrade, the cohesive elements 'soften' and displacements increase for a constant prescribed peak load. However, since this model is analysed in an explicit dynamic solution, minor local oscillations in force and displacement envelopes may occur. Therefore a rigorous treatment of unloading/reloading paths is required for the model to be valid, as explained in this section.

If the separation of the corresponding cohesive surfaces happens to be smaller than in the previous loading state, the 'unloading' path is followed. Unloading is prescribed to be directed back to the origin of the traction-separation space [169] see Figure 6.6. The traction components during unloading are then calculated as follows;

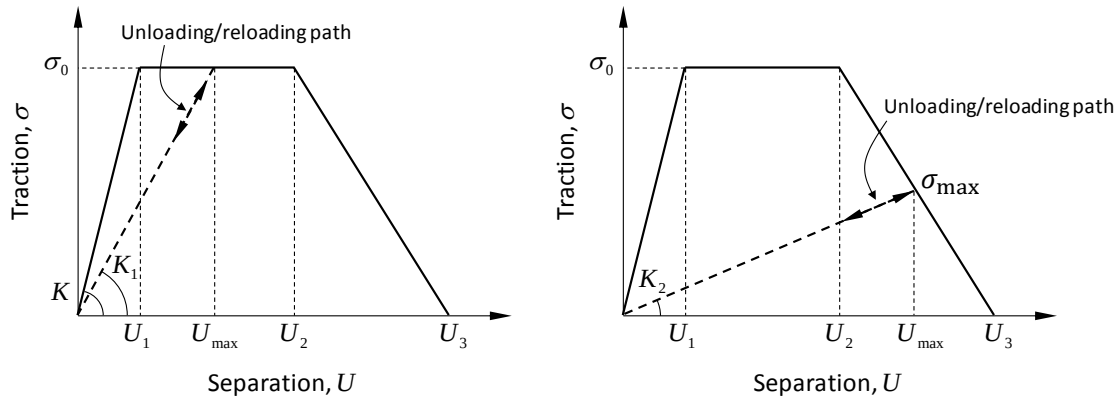

Figure 6.6: Unloading/reloading path for mixed mode trapezoidal traction law for (a) the constant stress-region and (b) the softening region.

For the constant stress-region Figure 6.6 (a)

When

$U \geq U_{\max}$ → Loading

$$\sigma = \sigma_o \tag{6.12}$$

$U < U_{\max}$ → Unloading

$$K_1 = \frac{\sigma_o}{U_{\max}} \tag{6.13}$$

$$\sigma_{\text{unloading}} = K_1 \cdot U \tag{6.14}$$

If $D_t = 0$

$$\sigma_{\text{unloading}} = \sigma_{\text{reloading}} \tag{6.15}$$

If $D_t > 0$

$$K_1 = K_1 \cdot (1 - D_t) \tag{6.16}$$

$$\sigma_{\text{reloading}} = K_1 \cdot U \tag{6.17}$$

For the softening region, Figure 6.6 (b):

$U \geq U_{\max}$ → Loading

$$\sigma = \sigma_o \cdot \frac{U_3 - U}{U_3 - U_2} \tag{6.18}$$

$U < U_{\max}$ → Unloading

$$\sigma_{\max} = \sigma_o \cdot \frac{U_3 - U_{\max}}{U_3 - U_2} \tag{6.19}$$

$$K_2 = \frac{\sigma_{max}}{U_{\max}} \tag{6.20}$$

$$\sigma_{\text{unloading}} = K_2 \cdot U \tag{6.21}$$

$D_t = 0$ → Reloading

$$\sigma_{\text{unloading}} = \sigma_{\text{reloading}} \tag{6.22}$$

$D_t > 0$ → Reloading

$$K_2 = K_2 \cdot (1 - D_t) \tag{6.23}$$

$$\sigma_{\text{reloading}} = K_2 \cdot U \tag{6.24}$$

where U is the displacement at the current increment, $U_{\max}$ is the maximum displacement up to the current increment (*i.e.* the 'envelope' displacement), σ_o is the yield stress for the cohesive layer, σ is the current stress for the cohesive layer, U_1, U_2, U_3 are user-defined displacements defining the trapezoidal law, D_t is the total damage variable, K_1 is the unloading/reloading stiffness in the constant stress region, and K_2 is the unloading/reloading stiffness in the softening region.

6.4 Element deletion

Each cohesive element has a number of integration points also called material points and for 2D cohesive elements (COH2D4) there are two per element (see Figure 6.7). Material point deletion can be used to delete damaged elements, once all material points are flagged as deleted. Once a material point has been flagged as deleted, it cannot be reactivated. Once an element is deleted stress and strain for that element are set to zero and the analysis can continue without the need for re-meshing [169]. The state variable can be used to control the element deletion flag in VUMAT. For instance, specifying a state variable of SDV5 indicates that the fifth state variable is the deletion flag in VUMAT. The deletion state variable should be set to a value of one or zero. A value of one indicates that the material point is active, while a value of zero indicates that Abaqus/Explicit should delete the material point from the model by setting the stresses and strains to zero. The block of material points passed to the VUMAT code remains unchanged during the remainder of the computation and deleted material points are not removed from the block.

Figure 6.7: Schematic of a two-dimensional cohesive element (COH2D4).

6.5 Numerical modelling

6.5.1 Simplified models

Having developed the cohesive zone model to be used in modelling high cycle fatigue it was incorporated into a series of models of increasing complexity to enable the required material properties to be determined and the model to be validated. Material properties were obtained first using a quasi-static model and then validation was achieved through use of the fatigue model.

6.5.2 Three-element model

Initially, a simplified model using three elements was generated as shown in Figure 6.8, in order to validate the modified cohesive zone approach using the trapezoidal traction law for both pure mode-I and mode-II under quasi-static and fatigue loading. The simplified model incorporates three cohesive elements with a constant thickness of 0.01 mm. Element 1 is subjected to vertical and horizontal loads or displacements representing mode-I and mode-II damage failure modes respectively whilst the other two elements are fixed in both the x and y axes. The two-dimensional cohesive elements (COH2D4) are used; each element is 0.25 mm in length. The properties of the cohesive materials used are as given in Table 5.4.

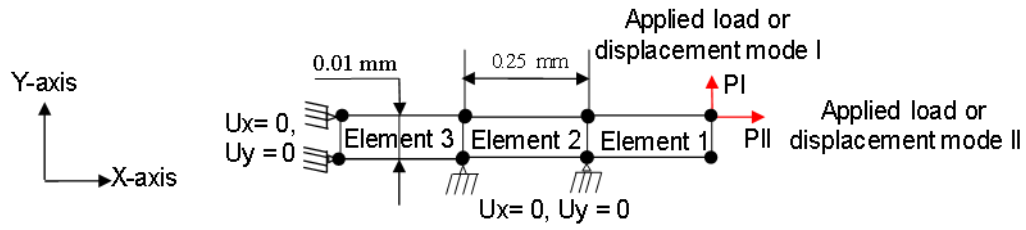

Figure 6.8: Three element model.

6.5.2.1 Quasi-static loading

The traction separation curves for static loading for both mode-I and mode-II obtained using the VUMAT code for this model are compared with the bilinear CZM available in

Abaqus software library and the results can be seen in Figure 6.9.The mode-I VUMAT results in Figure 6.9 (a) show that a yield stress of 40 MPa is reached in the damage initiation region at a displacement of 1.827×10^{-4} mm for a normal stiffness 2.189×10^{5} N/mm^3 and this is identical to the Abaqus results in the elastic region. The VUMAT results then show damage evolution starting with an increasing level of displacement under constant stress up to a separation of 6.86 µm for the constant-stress region in accordance with the trapezoidal law, followed by a linear degradation in stress up to failure displacement 16.0 µm at zero stress in the softening region. Abaqus results however, in accordance with the bilinear damage model implemented show immediate linear degradation in stress with increasing displacement up to 45.67 µm which is significantly higher than the VUMAT separation. Pure mode-II results (Figure 6.9 (b)) show similar behaviour in the elastic region with a shear yield stress of 40 MPa but a much lower shear stiffness of 8.32×10^{4} N /mm^3 as would be expected. Damage initiation is predicted by both the VUMAT code and Abaqus at a displacement of 4.86×10^{-4} mm. Stress then remain constant for the VUMAT code during the constant-stress region (up to a 15.18 µm separation) with a degradation in stress up to a failure displacement of 35.3 µm in the softening region. Mode-II Abaqus results however again follow a bilinear law where damage evolution starts with increasing in displacement up to 100 µm accompanied by stress softening to zero. Finally it can be seen for both mode-I and mode-II VUMAT results that the standard trapezoidal traction law reported via Hutchinson [94] is achieved.

A comparison of the contours obtained by plotting the Abaqus static damage variable (SDEG) and the VUMAT code static damage variable (SDV) is presented in Figure 6.10 (a). Both mode-I and mode-II results shown very similar damage behaviour for element 1 with a damage value of one shown in red .The other two elements which have fixed boundary conditions show no damage with blue indicating damage variable value of zero.

Since for both mode-I and mode-II the static damage variable shows excellent

agreement between Abaqus and VUMAT, only mode-I results are compared in Figure 6.10 (b), which demonstrates that for both VUMAT and Abaqus, damage increased steadily with increasing simulation time up to maximum value at (D=1) and then remained constant up to the final failure.

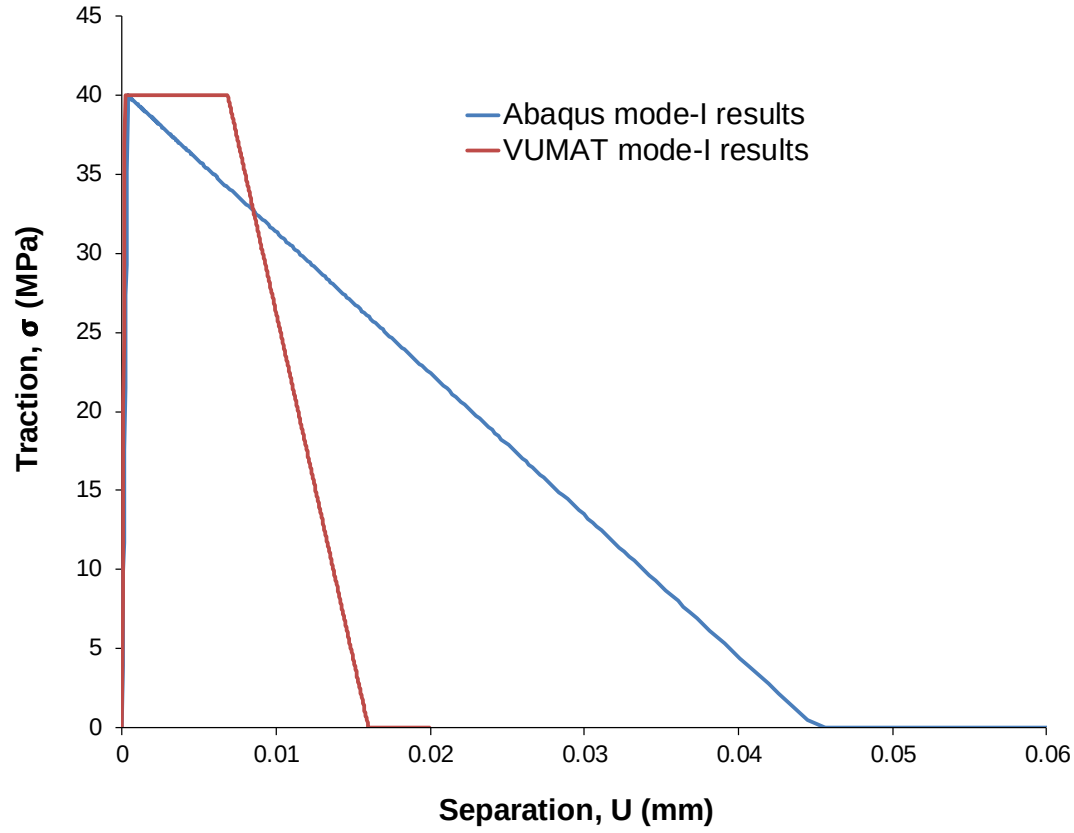

(a)

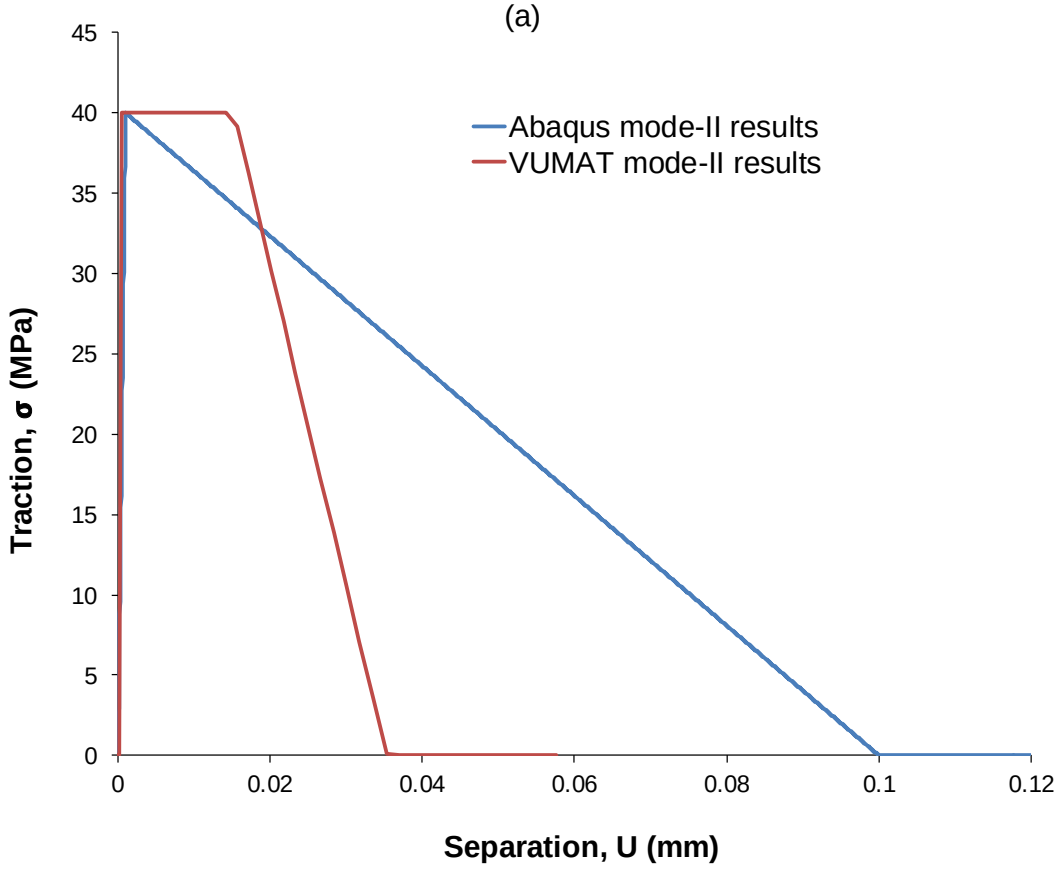

(b)

Figure 6.9: Comparison between the VUMAT code and Abaqus' built-in cohesive law for a three-element simplified model in (a) pure mode-I and (b) pure mode-II.

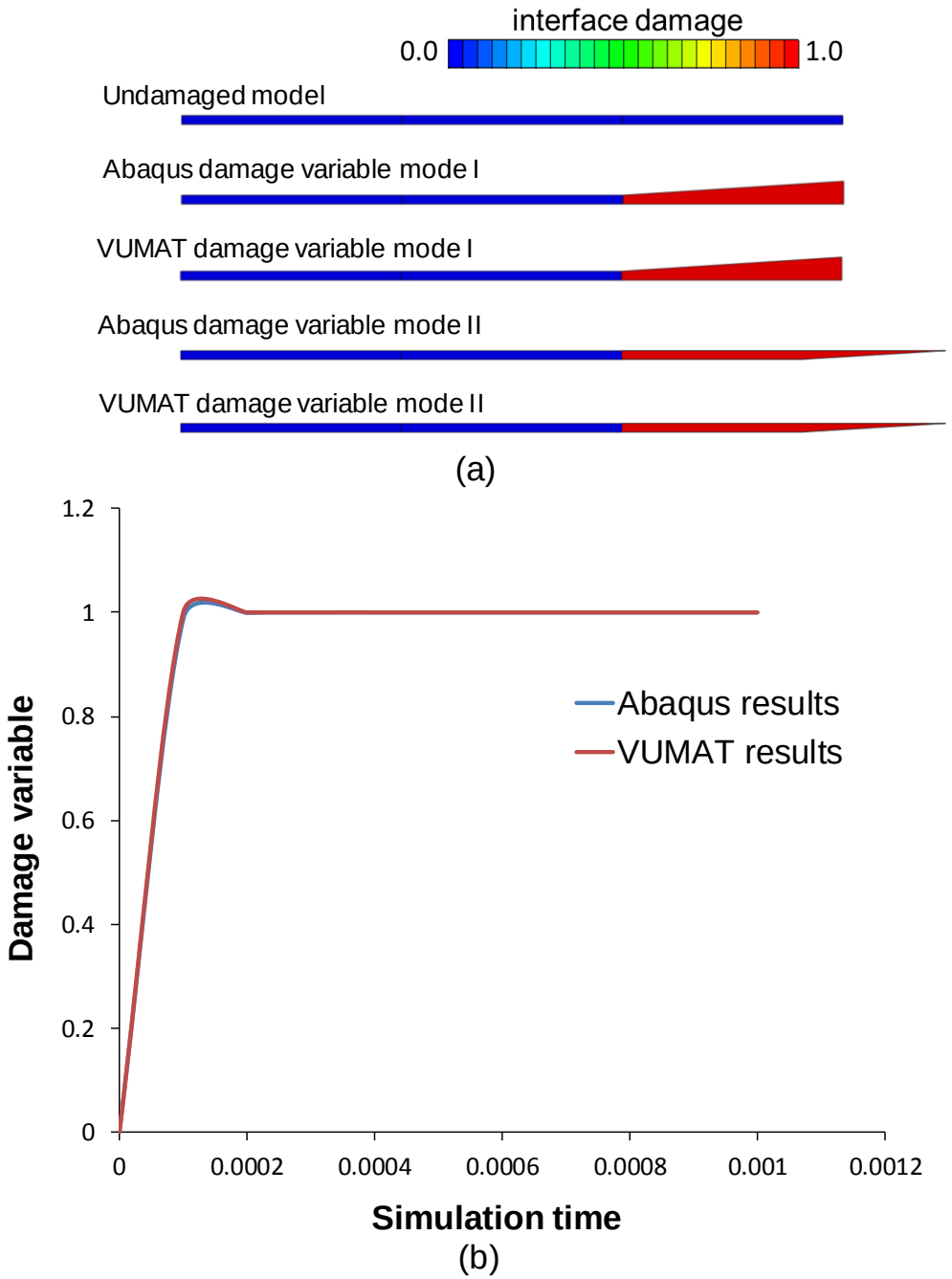

Figure 6.10: Static damage variable comparison between VUMAT code results (SDV) and Abaqus software results (SDEG) for simplified model in mode-I and mode-I (a) contour plots (b) damage variable versus simulation time.

6.5.2.2 Fatigue loading

Fatigue results for the three element model under fatigue loading are again presented only for element 1 since no damage occurs in elements 2 and 3 due to fixed boundary conditions assigned to them in order to simplify analysis. The traction-separation curves plotted in Figure 6.11 show identical behaviour in both static and fatigue

behaviour in the purely elastic region as expected but also at the beginning of the static softening region before fatigue damage occurs. Following this fatigue damage starts at a user-defined start time (0.0002 s in this example) in the constant-stress region at a stress of 40 MPa leading to early degradation in stresses at a displacement of 5.2 µm in comparison with the static result which starts softening at a displacement of 15.5 µm. The first element fails at a displacement of 17.9 µm under fatigue whilst the failure displacement is 35.7 µm under pure mode-II static load.

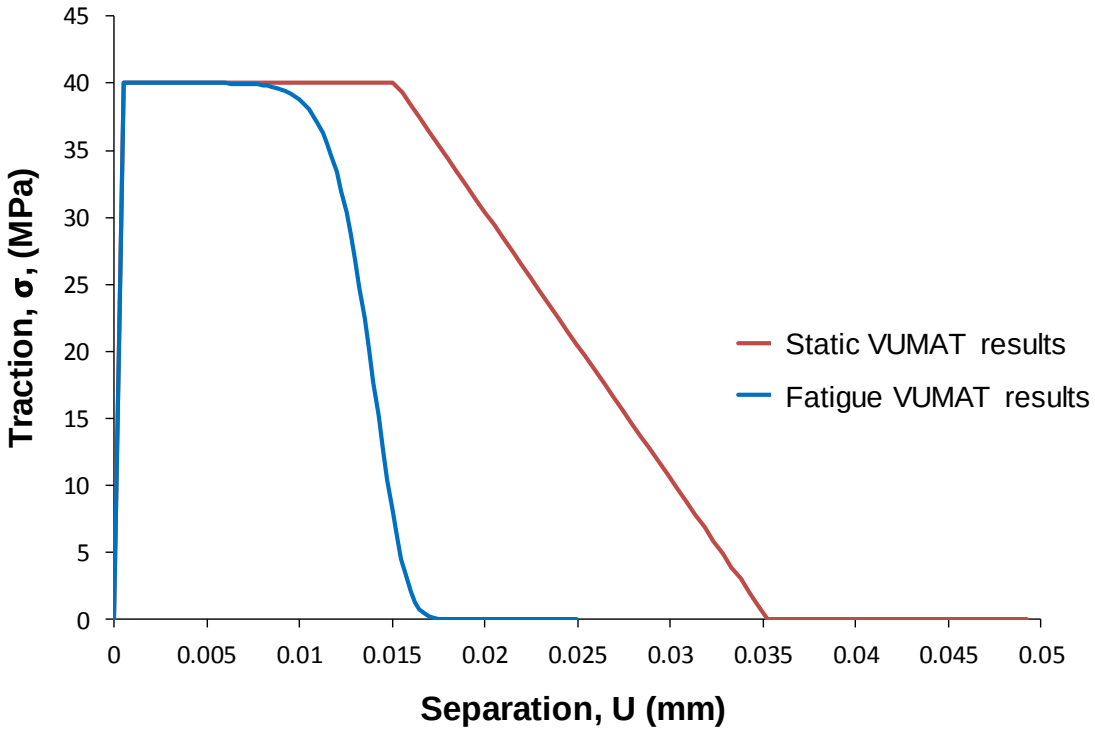

Figure 6.11: Traction-separation curve comparison between static and fatigue 70% severity using pure mode-II VUMAT code for simplified three element model.

6.5.3 Cut-ply specimen model

A more complicated cut-ply model was then generated as shown in Figure 6.12. This model incorporates two aluminium layers with different thicknesses bonded using cohesive elements. The aluminium layers are 0.4 mm (upper) and 0.1 mm (lower) thick. Each layer comprises 200 elements 0.25 mm long and is one element thick. The elements used are linear two-dimensional continuum elements (CPS4R). The

interfaces are meshed using two-dimensional cohesive elements (COH2D4) 0.01 mm thick. The model has a fixed boundary condition at the LHS edge nodes and also along the bottom nodes. The properties of aluminium and cohesive materials used in this model are given in chapter 5 (Tables 5.1 and 5.4) for aluminium and cohesive properties are the same used in Section 6.5.2. RHS edge elements are subjected to horizontal loads or displacements representing mode-II damage failure mode.

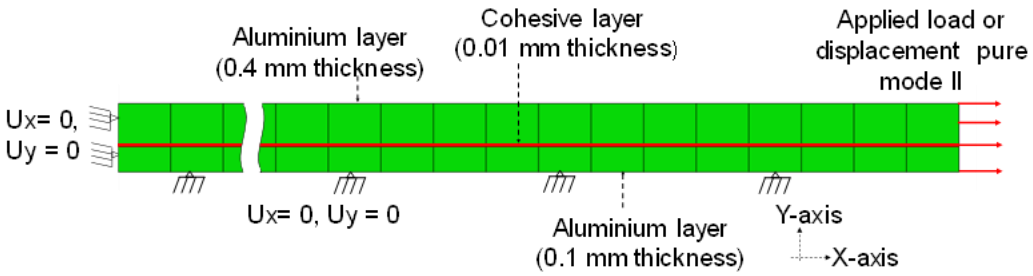

Figure 6.12: Cut-ply specimen model.

6.5.3.1 Quasi-static loading

The traction-separation curves for the cut ply model based on both pure mode-I and mode-II VUMAT code are shown in Figure 6.13.

A good representation of the trapezoidal traction law reported via Hutchinson [94] is achieved. For mode-I indicates a normal yield stress of 40 MPa is reached at the damage initiation region at a displacement of 1.827×10^{-4} mm for a normal stiffness of 2.19×10^{5} N/mm^3 and that the stress then remains constant during the constant-stress region up to a displacement of 6.86 µm. During softening stress degrades up to a failure displacement of 16.0 µm.

For pure mode-II the curve shows similar behaviour with a shear yield stress at 40 MPa but as shear stiffness is lower than direct stress in the normal direction 8.32×10^{4} N/mm^3 damage initiation occurs at a displacement of 4.86×10^{-4} mm, with stress remaining constant for the constant-stress region up to displacement 15.18 µm

and then softening up to a failure displacement of 35.30 µm.

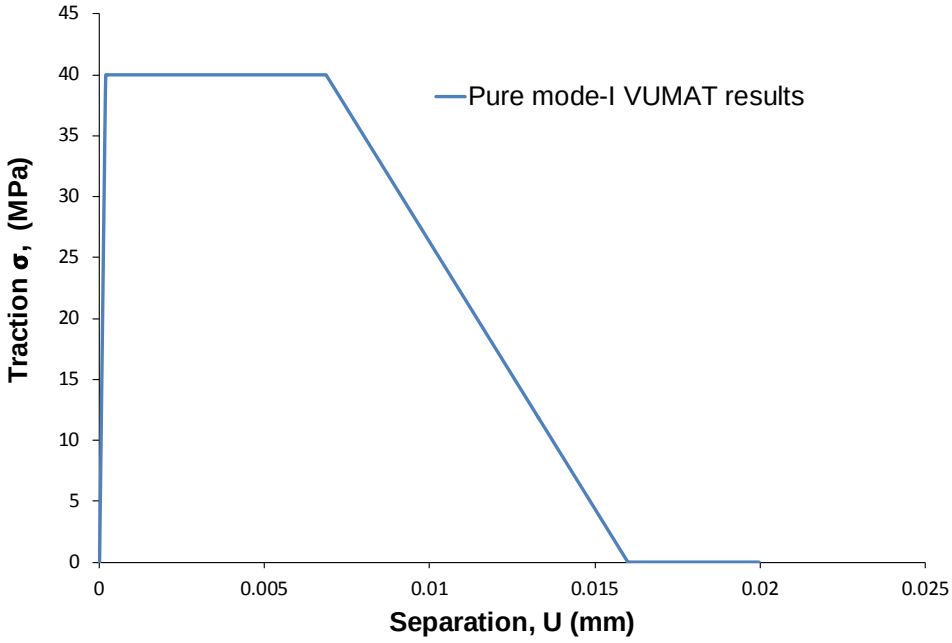

(a)

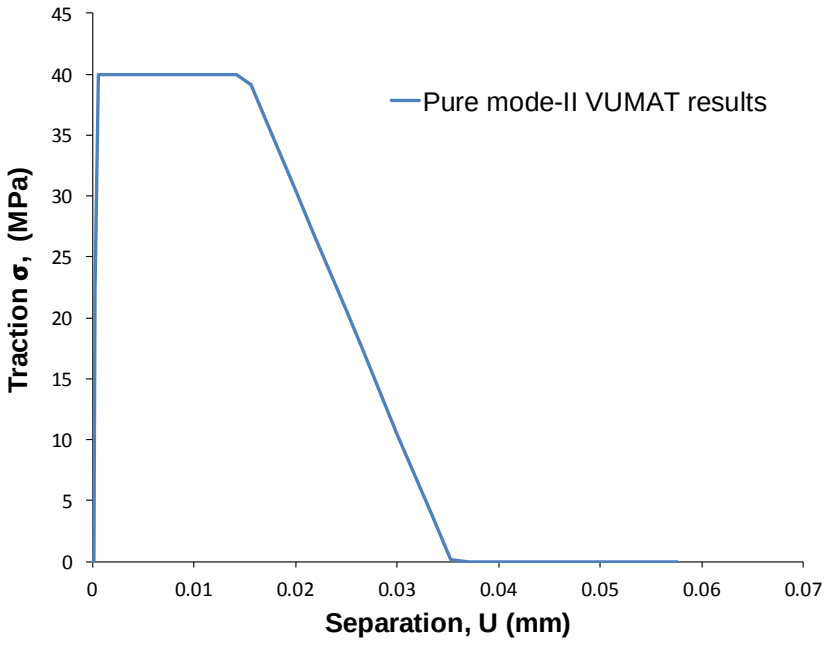

(b)

Figure 6.13: Traction-separation curve for simplified model using VUMAT code for (a) pure mode-I, (b) pure mode-II.

6.5.3.2 Fatigue loading

The traction-separation curves for the cut ply model under cyclic loading are shown in Figure 6.14. These show that both static and fatigue curves are identical in the purely elastic region and the initial part of the static softening region before fatigue damage is

incurred. After this fatigue damage initiates at the user-defined start time of 0.0003 s in the constant-stress region at 40 MPa leading to an early degradation in stress over a displacement range of 1.36 – 4.382 μm for all of a series of four-sample results taken from four cohesive elements starting from 1.25 mm from the right hand side edge of the model representing the predicted stable crack growth.

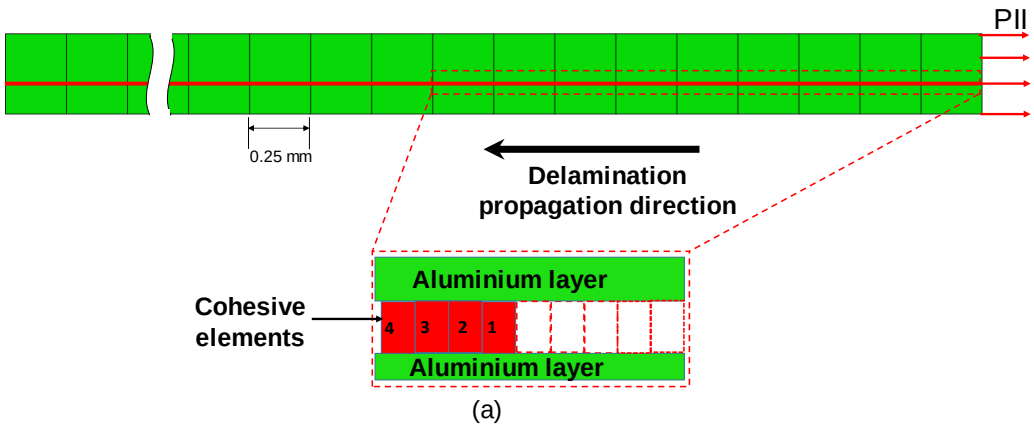

(a)

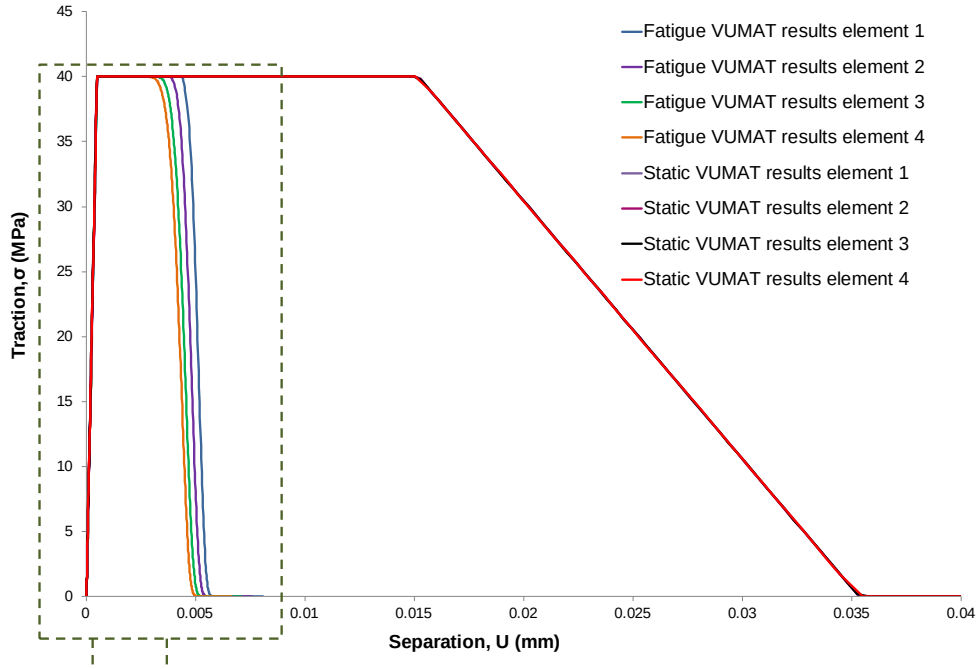

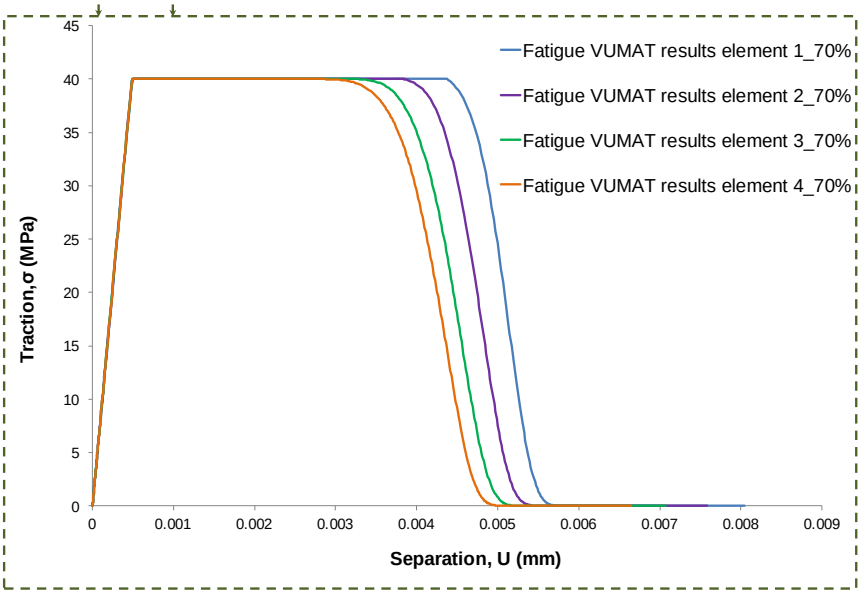

(b)

Figure 6.14: (a) Cohesive elements used in the simplified cut-ply model (data for four cohesive elements starting 1.25 mm from the RHS edge), and (b) traction-separation curve comparison between static and fatigue (70% severity).

In order to validate the fatigue parameters used which were taken from experimental data reported by Alderliesten[4], the response for different severities was predicted using the VUMAT code as shown in Figure 6.15. For clarity results for only four cohesive elements out of the 200 elements modelled are shown for four different severities (70%, 60%, 50% and 40%) and compared with experimental Paris law results. The maximum strain energy release rate for pure mode-II (G_{II}) is calculated for each severity and the results for strain energy ratio are plotted against crack growth rate to obtain the Paris curve. A power law fitting was used to get fatigue parameters with very good correlation observed between predicted and experimental results.

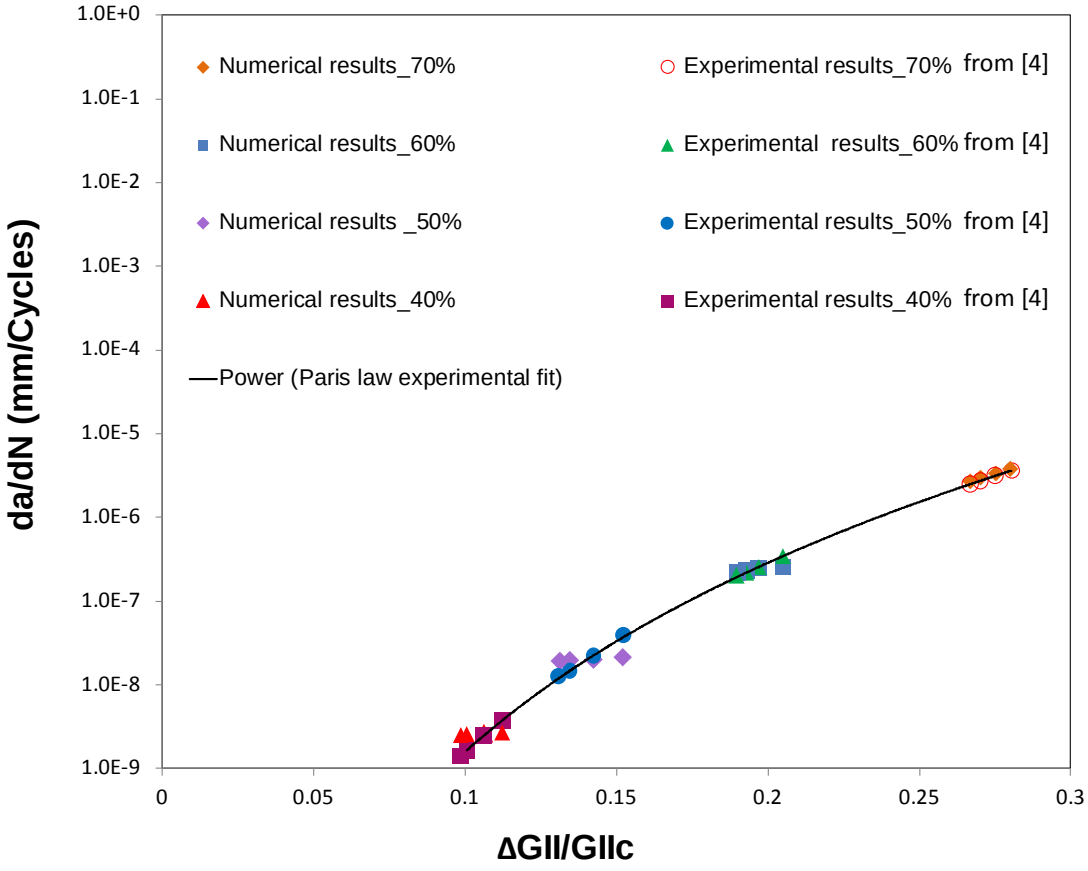

Figure 6.15: Experimental from [4] and numerical Paris curve for simplified model at R- ratio R=0.1 and severities (70%, 60%, 50% and 40%) for a series of cohesive elements at delamination length start at 1.25 mm from crack tip element.

6.6 Chapter summary

This chapter presents the development of a user-defined subroutine (VUMAT) to define the high cycle fatigue damage behaviour of elastic plastic material such as that at the interface between the metallic and GFRP layer of the fibre metal laminate Glare® within the Abaqus/Explicit software. The code is based on a cohesive zone model for mixed mode loading using a combination of trapezoidal traction-separation and Paris laws not currently available within the literature or proprietary codes such as Abaqus. The developed fatigue damage model is based on a normalised Paris law which is a function of the change in strain energy and critical strain energy. This has advantages over other fatigue damage models in the literature which depend either on stress or strain, being based on strain energy represented by the area under the traction-separation curve and therefore a function of both stress and strain. The predictive fatigue damage model also accounts for the load ratio effect and this is incorporated by using the change in strain energy which is calculated as a function of the load ratio and the maximum strain energy. The predicted static damage model has been validated against results obtained from the Abaqus software and the fatigue damage model has been checked against experimental fatigue results for the Paris law by Alderliesten [4]. Models based simplified geometries including a three element model and a cut-ply model were generated and analysed using the predicted damage model for both mode-I and mode-II under static and fatigue loads. It was found that the developed static model correlates very well with Abaqus results obtained using a bilinear law. It was also found that the developed fatigue model successfully predicted the experimental Paris curve. Thus, the model was validated as being able to simulate delamination propagation in FMLs interfaces and adhesive joints effectively.

Chapter 7 - Fatigue Damage in Fibre Metal Laminates with Internal Features

7.1 Introduction

This chapter focuses on the modelling of damage initiation and propagation in Glare® laminates containing adhesively bonded joints (both splices and doublers) under high cycle fatigue loading. This was achieved using the modified cohesive zone model (CZM) presented in Chapter 6 to represent interlaminar damage in the high toughness adhesive of metal-fibre interfaces. The CZM was implemented through a user – written VUMAT subroutine in the Abaqus/Explicit software. Damage in the bulk material constituents of the laminate (aluminium, composite and resin pocket) was not considered in this analysis which concentrates on the application of the novel CZM to investigate damage at the interfaces but could be added if required.

A two-stage experimental testing programme was performed in order to support the numerical analyses. Firstly, quasi-static tests were used to obtain the ultimate tensile strength (UTS) of the manufactured specimens and hence determine appropriate values for the severity and maximum load for the fatigue testing. Then, fatigue life curves were extracted for specimens containing both splice and doubler specimens in order to study fatigue behaviour of FMLs including these features.

Tests were monitored using digital image correlation (DIC) to determine in-plane displacement during the quasi-static tests in order to plot load versus in-plane displacement curves for the specimens and hence determine the UTS needed to calculate the severities for the fatigue tests and acoustic emission (AE) to enable the initiation and propagation of damage to be detected during the fatigue tests.

Further details on both these techniques have been given in Chapter 3.

7.2 FE models

To model the fatigue behaviour of both splice and doubler joints, two-dimensional FE models representative of the specimens to be tested were created, one for each joint. Models were 153 mm × 2.56 mm representing the gauge sections without tabs. This was achieved by extracting the geometry and thickness of each layer from detailed scans of the actual specimens, shown in Figure 7.1, and then meshing the continuum (bulk) material (aluminium, composite and the resin pocket) using two-dimensional linear continuum elements (CPS4R) as shown in Figures 7.2 and 7.3.

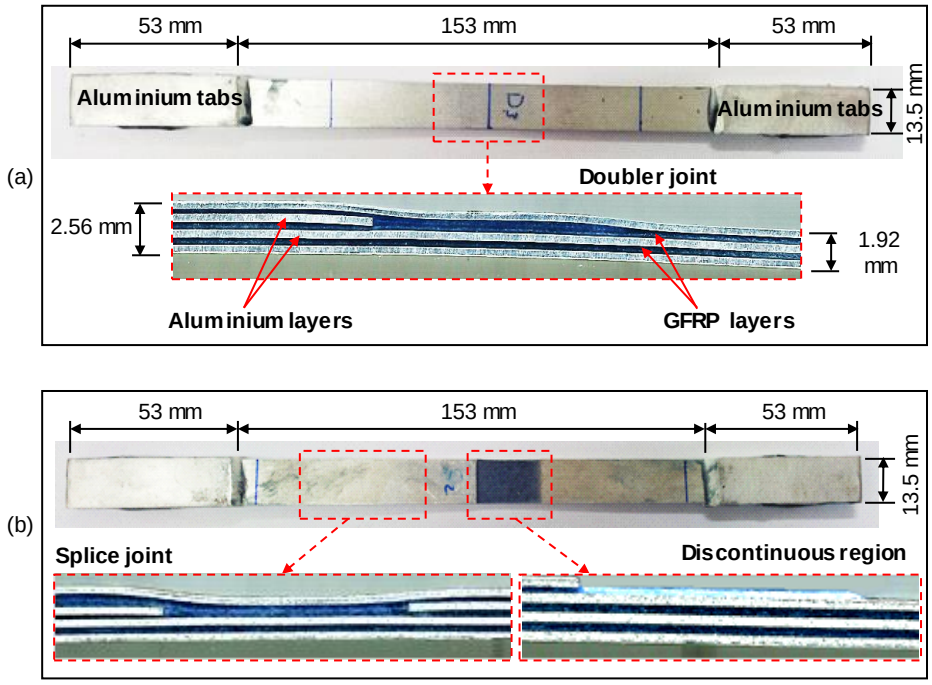

Figure 7.1: Specimen design for (a) doubler (b) splice (images resized for clarity, not to scale).

The interfaces were meshed using two-dimensional cohesive elements (COH2D4). The cohesive layers were 0.01 mm thick and had a mesh size of unity (the thickness was chosen based on a review of the literature related to similar models for fibre laminates). The mesh size was determined through mesh sensitivity analysis which is explained in detail in Appendix-A. The mechanical properties used for the aluminium, GFRP, bulk FM94 resin and cohesive layers were the same as those used in Section 5.2.3.

Load control was implemented with forces applied to all edge nodes along the left side of the specimen for both splice and doubler models (Figures 7.2 and 7.3), and the right side was fixed in both horizontal (x) and vertical (y) directions. Top and bottom edges were left free in order to simulate experiments.

Analyses were conducted in Abaqus/Explicit with the cohesive zone model implemented through the use of a VUMAT subroutine implementing first the quasi-static and then the fatigue damage models described in Sections 6.2.2 and 6.2.3, respectively. As the experimental static tests (see Appendix-B) showed that crack growth for both splice and doubler specimens was mostly mode-II, therefore only mode-II VUMAT code was implemented for both models.

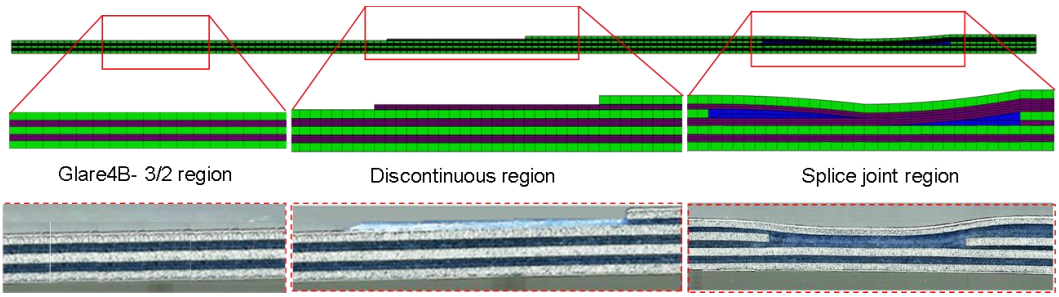

Figure 7.2: Finite element mesh of the splice specimen (top) based on optical scans of real specimens (bottom) (images resized for clarity, not to scale).

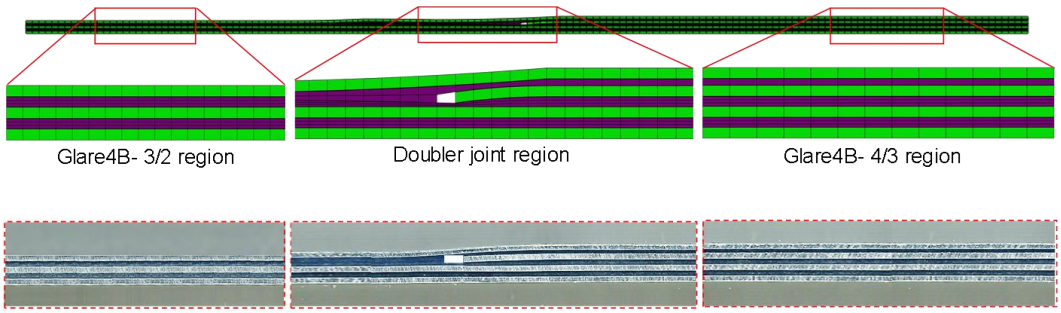

Figure 7.3: Finite element mesh of the doubler specimen (top) based on optical scans of real specimens (bottom) (images resized for clarity, not to scale).

7.3 Experimental test setup

Tests were conducted on specimens containing splice and doubler features as shown in Figure 7.1. Specimens measured 153 mm × 13.5 mm for the gauge section- with 53 mm × 13.5 mm aluminium end tabs bonded onto each end. These specimens were manufactured in-house as described in Chapter 3. They consisted of 0.4 mm thick sheets of aluminium alloy 2024-T3 and Cytec™ S2-glass/FM94 glass fibre reinforced polymer (GFRP) unidirectional prepreg with a lay-up corresponding to the specification for Glare® 4B (Table 4.1)[1]. Each GFRP 'layer' had 3 plies with the layup [90°/0°/90°] and a cured ply thickness of 0.133 mm. The layup one side of the joint was '3/2' (three layers of aluminium and two layers of GFRP prepreg) and on the other '4/3' (four layers of aluminium and three layers of prepreg). They were tested under first static and then fatigue load using an MTS servo-hydraulic (50 kN) machine as shown in Figure 7.4.

Static tests were monitored using digital image correlation to derive accurate measurements of the in-plane displacement. The DIC system and set-up described in Chapter 3, section 3.6 was used to monitor the in-plane displacement of the surface of each of the specimens.

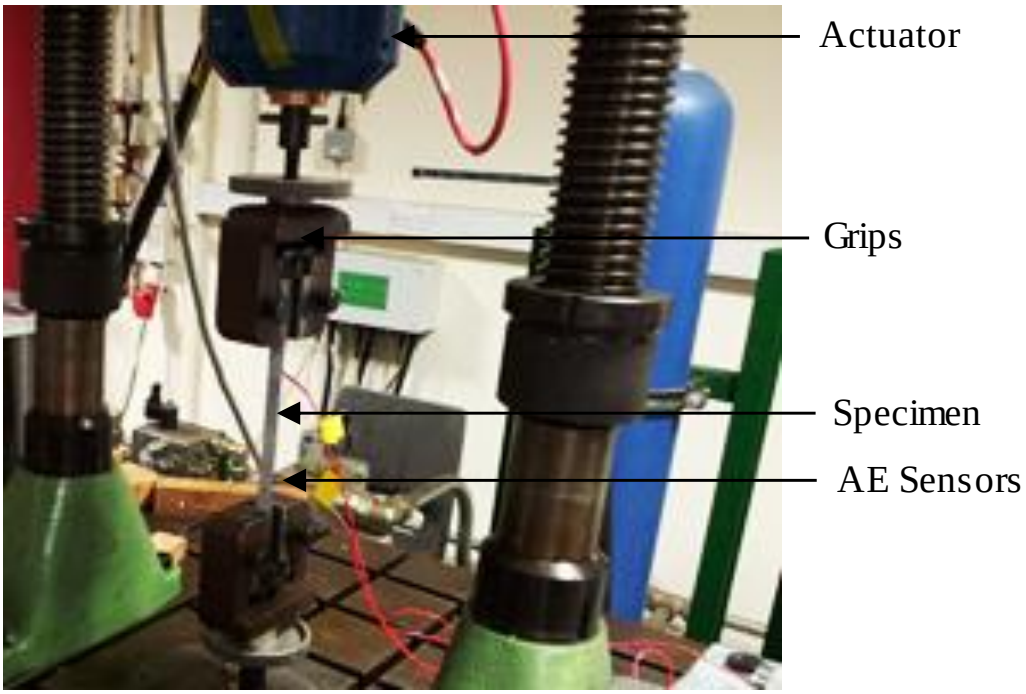

Figure 7.4: Experimental fatigue test setup.

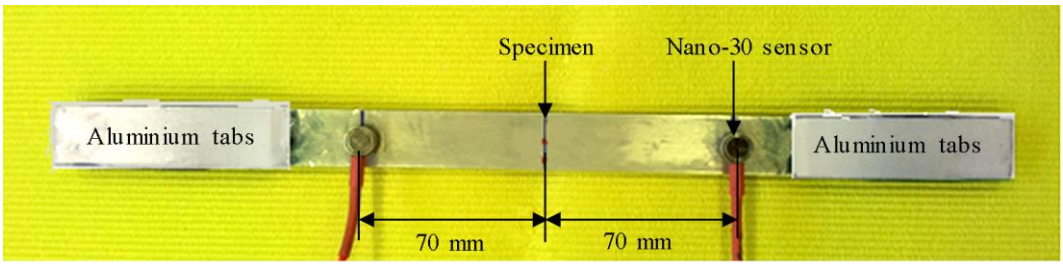

Figure 7.5: AE sensors position on Glare® 4B specimen.

Two Nano-30 Acoustic Emission (AE) sensors were mounted on the specimens to monitor damage events during both static and fatigue tests. These sensors; supplied by Mistras Group™ have a mid-band frequency range of 125-750 kHz. They were chosen since due to their small size (8 mm diameter) they could easily be mounted on the relatively small surfaces of the specimen available. In addition to this practical consideration, the Nano-30 AE sensor has a resonant response up to 300 kHz and a good frequency response making it suitable for monitoring the signals expected. They were bonded to the specimens using multi-purpose silicone sealant *Loctite*™ 595 as shown in Figure 7.5. They were then connected to Mistras Group™ pre-amplifiers with a 40 dB gain and a built-in band-pass filter of 20-1200 kHz. The pre-amps were in turn connected to a Mistras Group™ PCI2 acquisition unit. The detection settings were 45 dB threshold, sampling rate 5 MHz (as recommended by previous authors including Al-Jumaili [134] and Pearson [156]). Damage initiation and evolution were detected using the traditional AE analysis technique described in Chapter 3 (the improved Delta-T location technique cannot be applied in this case as it requires the use of three sensors [69]).

7.3.1 Pre-cracking

In order to create a crack initiation site in the doubler specimens they were preloaded (this was not necessary for the splice specimens in which the crack naturally grows from the discontinuity at the outer surface). This was achieved by loading the

specimens slowly in tension whilst using the camera system with the high magnification micro-lens described in Section 3.4 to monitor crack initiation and propagation. When the crack length reached 1 mm the test was stopped.

7.3.2 Static testing

Quasi-static tests were conducted on specimens containing each type of joint of (three splice specimens and three pre-cracked doubler specimens were tested as the pristine doubler specimens showed very similar behaviour to the pre-cracked ones). Load was applied through displacement control at a rate of 0.001 mm/s, and specimens were tested until failure. Tests were monitored using a Digital Image Correlation (DIC) system to derive accurate measurements of the in-plane displacement as described above. Further details of work carried out to examine the initiation and propagation of damage in these specimens using acoustic emission (AE) monitoring are explained in Appendix-B.

7.3.3 Fatigue testing

A series of fatigue tests, based on the loads determined from the static tests were then performed. In the case of the doubler, both pristine and pre-cracked specimens were tested. For the splice, only pristine specimens were tested since the termination of the outer aluminium ply acted as a crack initiator. Tests were carried out with a constant load ratio $R = 0.1$ and a frequency of 5 Hz. Different severities were investigated (two each of 30%, 40%, 50% and 60%) based on a maximum fatigue loads calculated from ultimate tensile strengths obtained from quasi-static tests on identical specimens [180] Fatigue tests were terminated after 10^6 cycles as the run out failure cycles. Experiments were initially monitored using the high magnification video camera described in Section 3.4 to monitor crack growth with an example of the results obtained for one of the doubler specimens shown in Figure 7.6, however due to the

field of view achieved at the required level of magnification cracks could only be monitored up to a length of 4 mm. In addition to this, crack opening displacement, particularly at the early stages of crack growth is less than 0.1 mm, making the crack very difficult to detect. It was therefore decided to use data from the experiments of Alderliesten [4] to verify the model (further details are provided in Section 7.4.3.2).

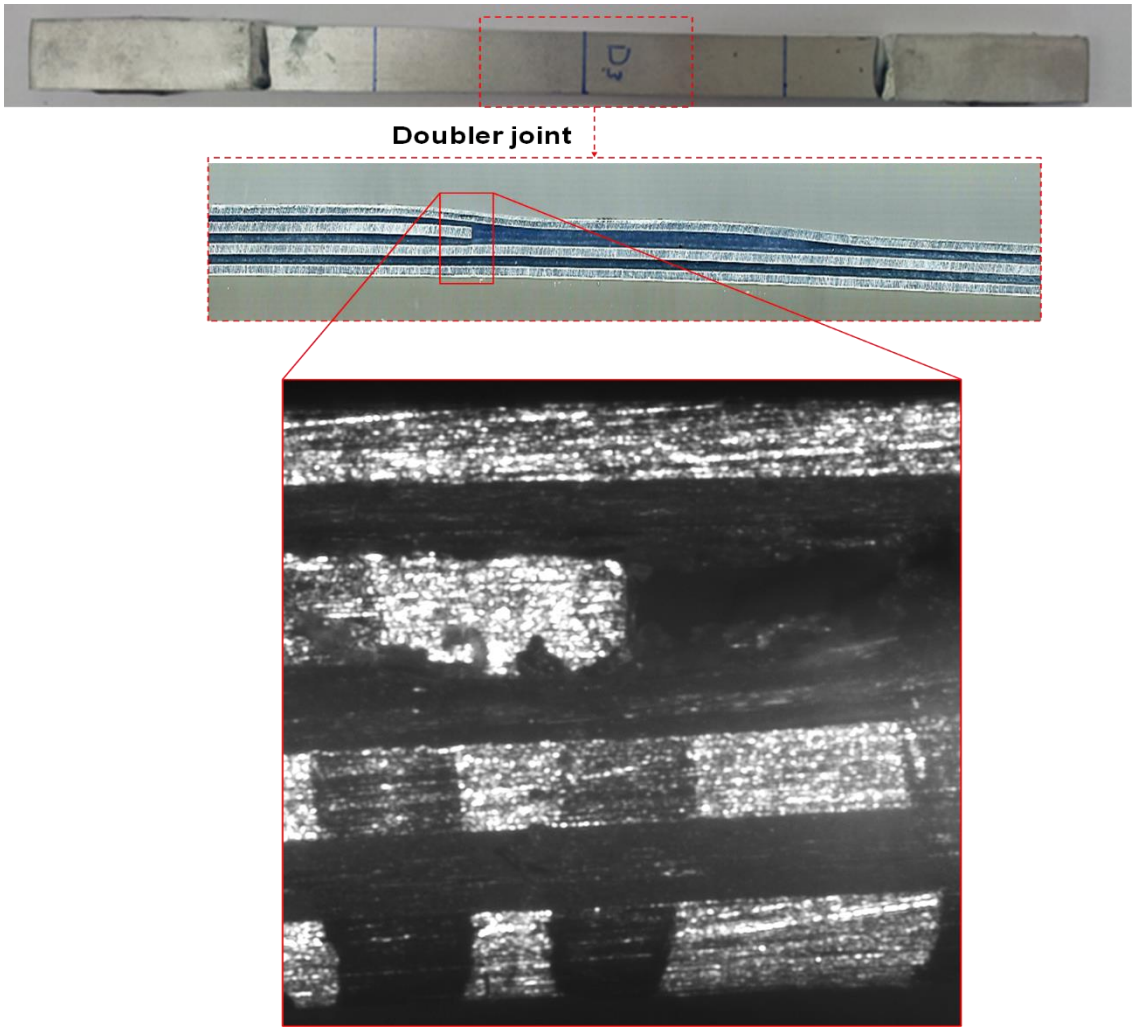

Figure 7.6: Fatigue crack length measurement for doubler specimen using video camera with micro lenses at 50% severity and load ratio $R = 0.1$.

7.4 Results and discussion

7.4.1 Static testing

The load versus displacement results for both crosshead displacement and in-plane displacement measured using MTS machine and DIC system respectively for the static tests for both the splice and the doubler specimens are shown in Figures 7.7 and 7.8.

The average ultimate tensile loads for use in calculating the severities for the fatigue tests are seen to be 12.52 kN in the doubler and 9.47 kN in the splice specimens, respectively.

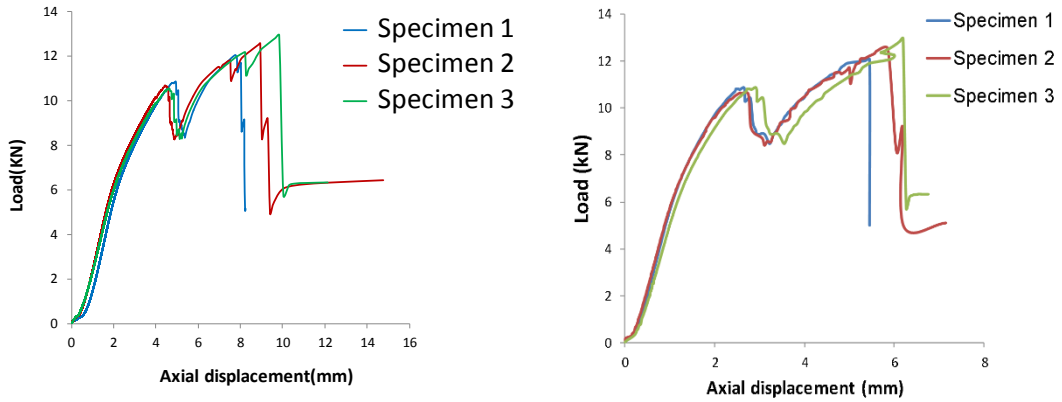

(a) (b)

Figure 7.7: Axial force versus in-plane displacement for doubler specimens; (a) MTS results and (b) DIC results.

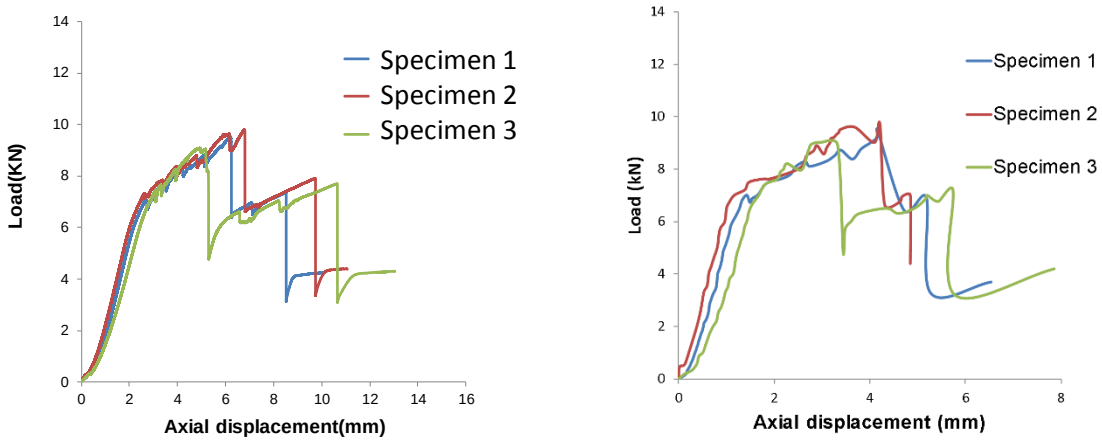

(a) (b)

Figure 7.8: Axial force versus in-plane displacement for splice specimens; (a) MTS results and (b) DIC results.

7.4.2 Fatigue testing

Fatigue test data for the splice and doubler specimens (pristine and pre-cracked) is presented in Table 7.1.

Table 7.1: Fatigue test results for the splice and doubler specimens.

Specimen	Peak load (kN)	Severity (%)	Fatigue life (cycles) Set-1	Fatigue life (cycles) Set-2
Splice	5.682	60	55912	49187
	4.735	50	110055	141878
	4.261	45	185093	180931
	3.788	40	374187	551276
	3.314	35	Run out	Run out
Pristine doubler	6.260	50	35156	48874
	5.008	40	161388	201607
	4.382	35	456228	424827
	3.756	30	896389	769385
	3.130	25	Run out	Run out
Pre-cracked doubler	6.260	50	49547	55945
	5.008	40	169251	174165
	4.382	35	394311	455357
	3.756	30	904207	912823
	3.130	25	Run out	Run out

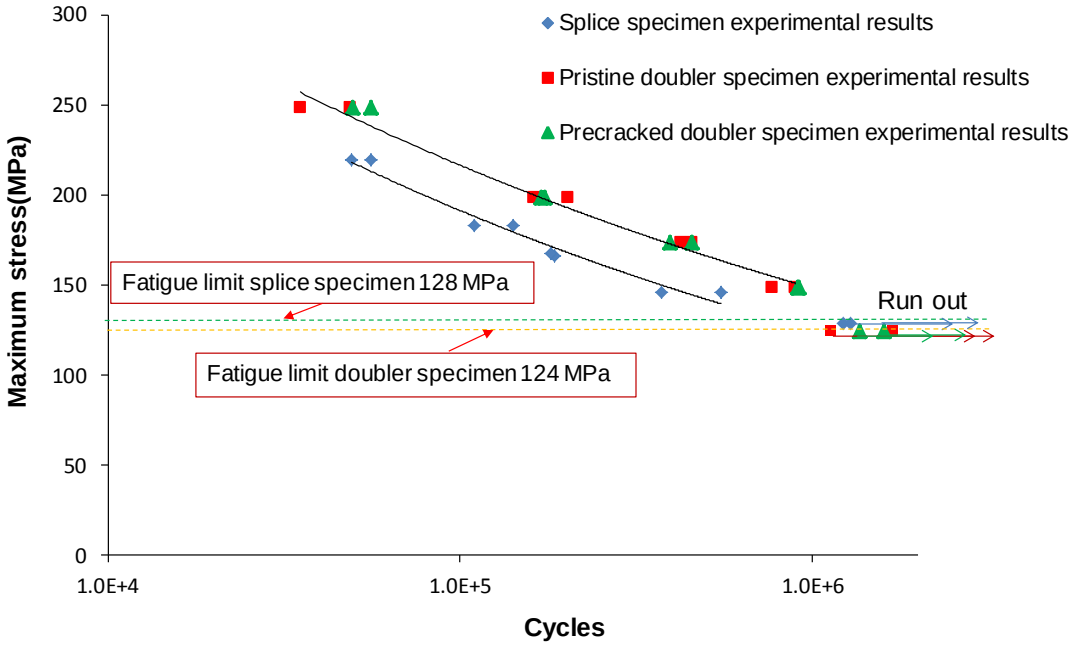

Figure 7.9: Experimental S-N curves for the splice and doubler specimens with a load ratio R = 0.1.

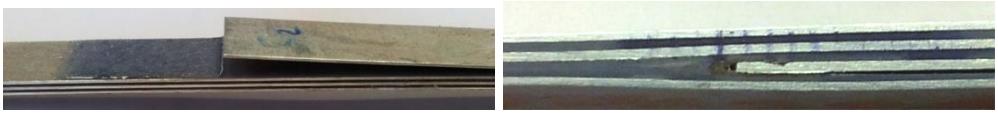

(a) (b)

Figure 7.10: Glare4B specimens after fatigue test at load ratio R = 0.1 and maximum severities (a) 60% (55912 cycles) for splice and (b) 50% (49547 cycles) for doubler.

Pairs of points collected from the experiments at different severities are used to plot S-N curves for both types of specimens in Figure 7.9. Solid lines represent the trend lines. The S-N curves show the expected relationship between stress and average cycles to failure for both the doubler and splice. The results reveal that the fatigue life for the doubler specimens is higher than for the splice specimens, corresponding to the doubler joint exhibiting a higher fatigue damage tolerance compared with the splice joint. This is in agreement with the fact that delamination initiates and grows in the external discontinuous aluminium/ GFRP interfaces for the splice specimens as shown in Figure 7.10 causing significant stiffness degradation, while the doubler specimens do not show any delamination. Final fatigue failure occurred in the outer aluminium layers in the thinner cross-section for both splice and doubler specimens.

Further insight into the initiation and propagation of damage is provided by the AE results. For the splice specimens Figures 7.11 and 7.12 show cumulative energy and amplitude against time respectively. During the first 1,300 seconds of the test (Figure 7.11 region A) whilst axial displacement increases from 0 to 0.3 mm, cumulative energy remains very low and signals are produced with amplitudes in the range of about 45-65 dB (Figure 7.12 region 1). This is potentially due to plastic deformation in the aluminium layers as observed in [181, 182], in which it was observed that plastic deformation in metals was accompanied by pronounced AE activity with an amplitude dependent on the type of metal. Then during the time period 1,300-4,000 s (Figure 7.11- region B) cumulative energy starts to increase gradually, potentially due to matrix cracking as demonstrated by [183, 184] producing signals with an amplitude range of about 45-75 dB (Figure 7.12 – region 2). This is accompanied by a small jump in axial displacement as seen in Figure 7.11.

Delamination initiation and growth is observed in the experiments during the period 5,500-11,000 s and is seen to correspond to a gradual increase in the amplitude of the AE events which reach their highest amplitude range of about (75-98 dB) (Figure 7.12 region 3). This is accompanied by a steady increase in energy followed by a jump at a

time of about 6,500 s. Finally a small number of high amplitude events are seen in the range 87-98 dB (Figure 7.12 region 4) accompanied by a gradual increase followed by a big jump in cumulative energy and axial displacement during time period 11,000-12,000 s, observed to correspond to crack initiation and growth in the aluminium layers of the thinner region of the specimen (Figure 7.2) followed by complete failure of the aluminium and hence the specimen.

For the doubler specimens, AE results show similar behaviour for both pristine and pre-cracked specimens with the results for pristine specimen being presented in Figures 7.13 and 7.14. As for the splice specimens, high amplitude events were recorded at the beginning of the test with an amplitude range (45-77 dB) (Figure 7.14 region 1) while cumulative energy remained constant up to 500 s (Figure 7.13, regionA). This was accompanied by an increase in axial displacement to about 0.5 mm, again it is anticipated, mostly due to plastic deformation in the aluminium layers. During the time period from 550 – 4,000 s, AE activity increases as the test progresses (Figure 7.13 - regionB) alongside an increase in axial displacement up to about 6 mm at time 5,500 s. This is accompanied by a gradual increase in the amplitude of the signals to between 45-87 dB (Figure 7.14 region 2) believed to be caused by matrix cracking in the doubler joint as characterised by this level of amplitude of signal in the work of Liu and Zhuang *et al.* [183, 184]. This is followed during the time period 5,500-6,500 s, by fibre breakage in the discontinuous GFRP layers, characterised by signal amplitudes of between 45-98 dB (Figure 7.14 region 3) again in agreement with the work of Liu and Zhuang *et al.* [185, 186], accompanied by a small jump followed by a large jump in cumulative energy and a noticeable increase in axial displacement as shown in Figure 7.13. Finally a steady increase in signals in the amplitude range of 87-98 dB is noticed (see Figure 7.14 region 3), accompanied by a high jump in cumulative energy and axial displacement, corresponding to the propagation of cracks and then failure of the aluminium layers in the thinner Section of the specimens observed during the test and confirmed by visual inspection of the damaged specimens.

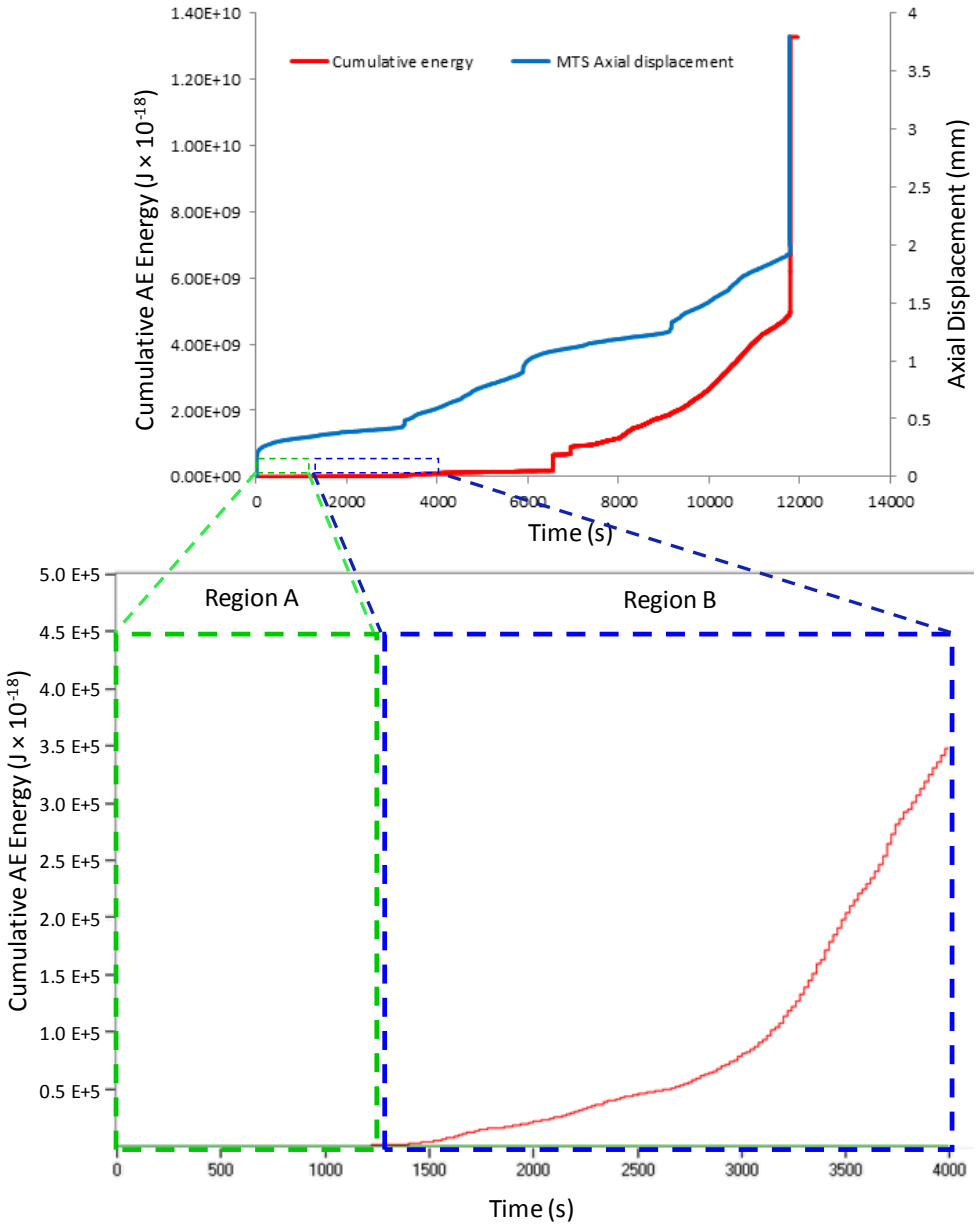

Figure 7.11: (Top) Comparison between cumulative AE energy and axial displacement versus time for splice specimen under fatigue load with severity 60% and R-ratio of 0.1; (bottom) detailed curve of cumulative AE energy versus time for $0 < t < 4{,}000$ s.

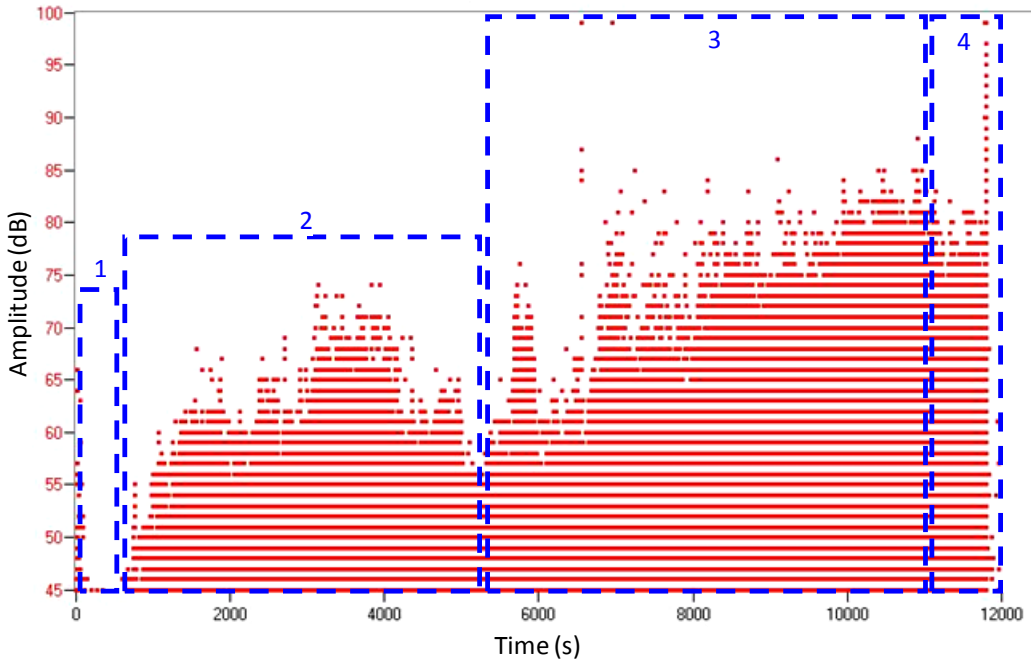

Figure 7.12: Amplitude-versus time for splice specimen under fatigue load with severity 60% and R-ratio 0.1.

7.4.3 Numerical analysis

As described in Section 7.2 two types of analysis were carried out, calculating first the static damage variable, then the fatigue damage variable, and then combining, following the load envelope approach to determine the total damage variable and hence the fatigue damage evolution as discussed in Chapter 6.

7.4.3.1 Quasi-static loading

Traction-separation curves for both splice and doubler specimens are shown in Figures 7.15 and 7.18, respectively.

For the splice model, static results for each of the cohesive elements are similar, therefore only those for element 1 are presented. These show similar behaviour to the simplified model discussed in Section 6.5.3, following the trapezoidal traction-separation law as expected, with stresses exhibiting a linear relationship with a shear stiffness of 83,200 N/mm^3 in the elastic region up to the user defined shear stress of 40 MPa where damage initiation starts at displacement 4.86×10^{-4} mm. After this

stresses remain constant for the constant-stress region while displacement increases up to 0.01518 mm. Finally stresses decrease in a linear manner through the softening region with displacements increasing up to final failure at 0.0353 mm.

For the doubler model, again static results for the cohesive elements are similar, therefore only the results for element 1 are presented. The trapezoidal traction-separation law is again followed correctly, with stresses exhibiting a linear relationship with a shear stiffness of 83,200 N/mm^3 in the elastic region up to a user defined shear stress of 40 MPa where damage initiation starts at a displacement of 4.86×10^{-4} mm. The stress then remains constant during the constant-stress region while displacement increases up to a displacement 0.0176 mm. Finally stress degradation starts and develops in a linear manner up to the final failure at displacement 0.0358 mm.

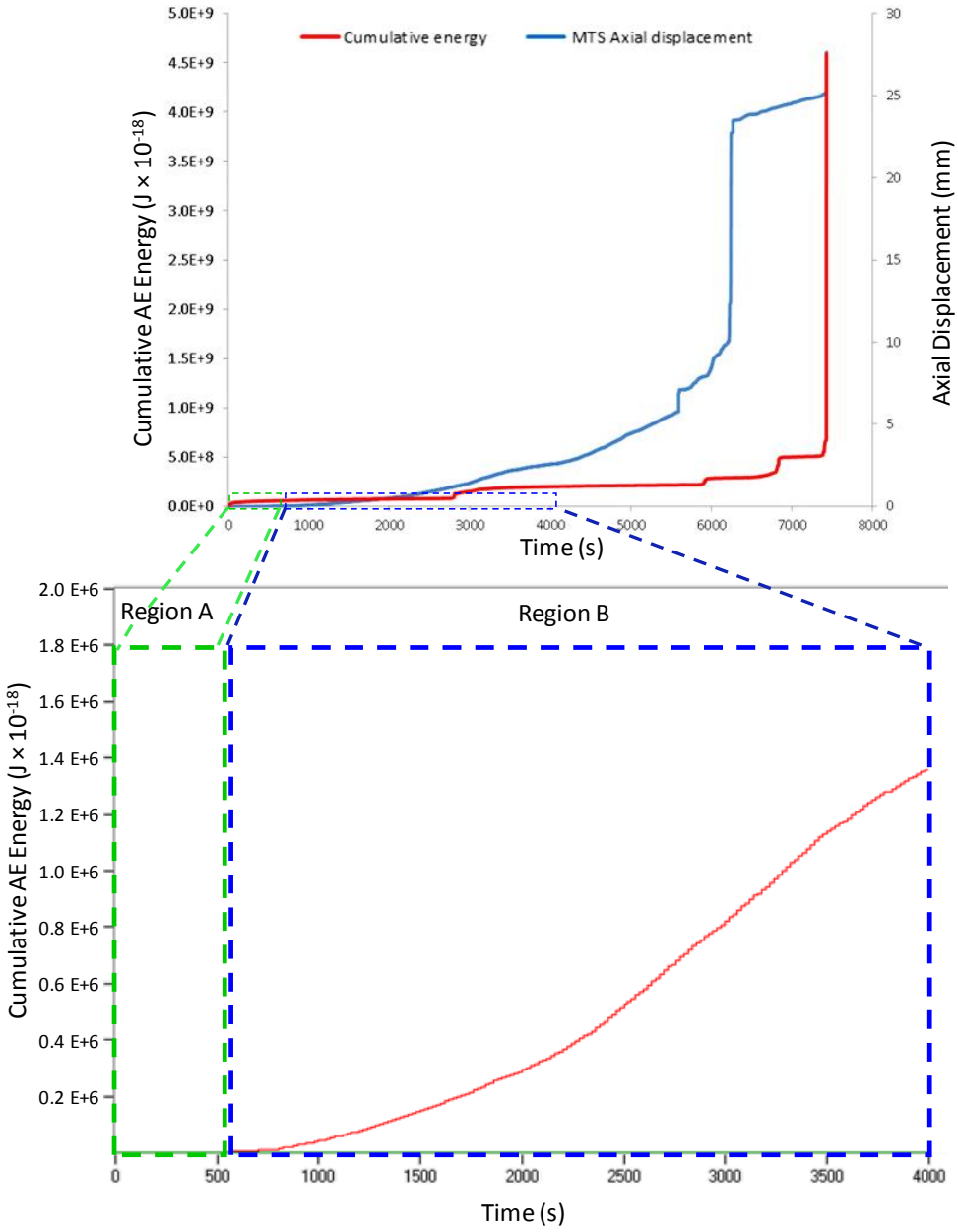

Figure 7.13: (Top) Comparison between cumulative AE energy and axial displacement versus time for a doubler specimen under fatigue load with severity 50% and R-ratio of 0.1; (bottom) detailed curve of cumulative AE energy versus time for $0 < t < 4{,}000$ s.

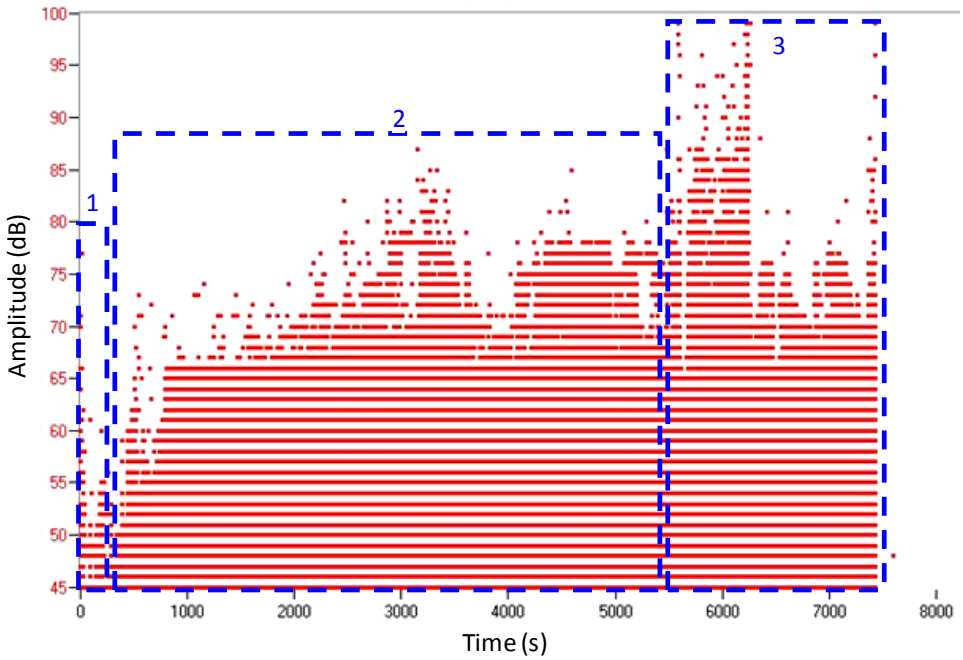

Figure7.14: Amplitude-versus time for pristine doubler specimen under fatigue load with severity 50% and R-ratio 0.1.

7.4.3.2 Fatigue loading

The traction-separation curves for the splice for a series of five cohesive elements in the path of the fatigue crack growth were obtained as shown in Figure 7.15 (b) with damage propagating from left to right *i.e.* from element 1 towards element 5 as expected and in agreement with the experimental observations. It can be seen that for each element these curves follow the static softening curve for a considerable portion of the elastic region, up to the point where the elements become part of the numerical crack front, at which point rapid fatigue degradation takes place. Comparing with the static analysis the VUMAT results show softening starts earlier under fatigue at a displacement of about 0.006 mm as compared to 0.0159 mm under static loading. Further degradation then occurs following the fatigue damage law up to final failure at an average displacement of approximately 0.0125 mm for the selected series of cohesive elements, which is lower than for the static failure that occurs at a displacement of about 0.0352 mm.

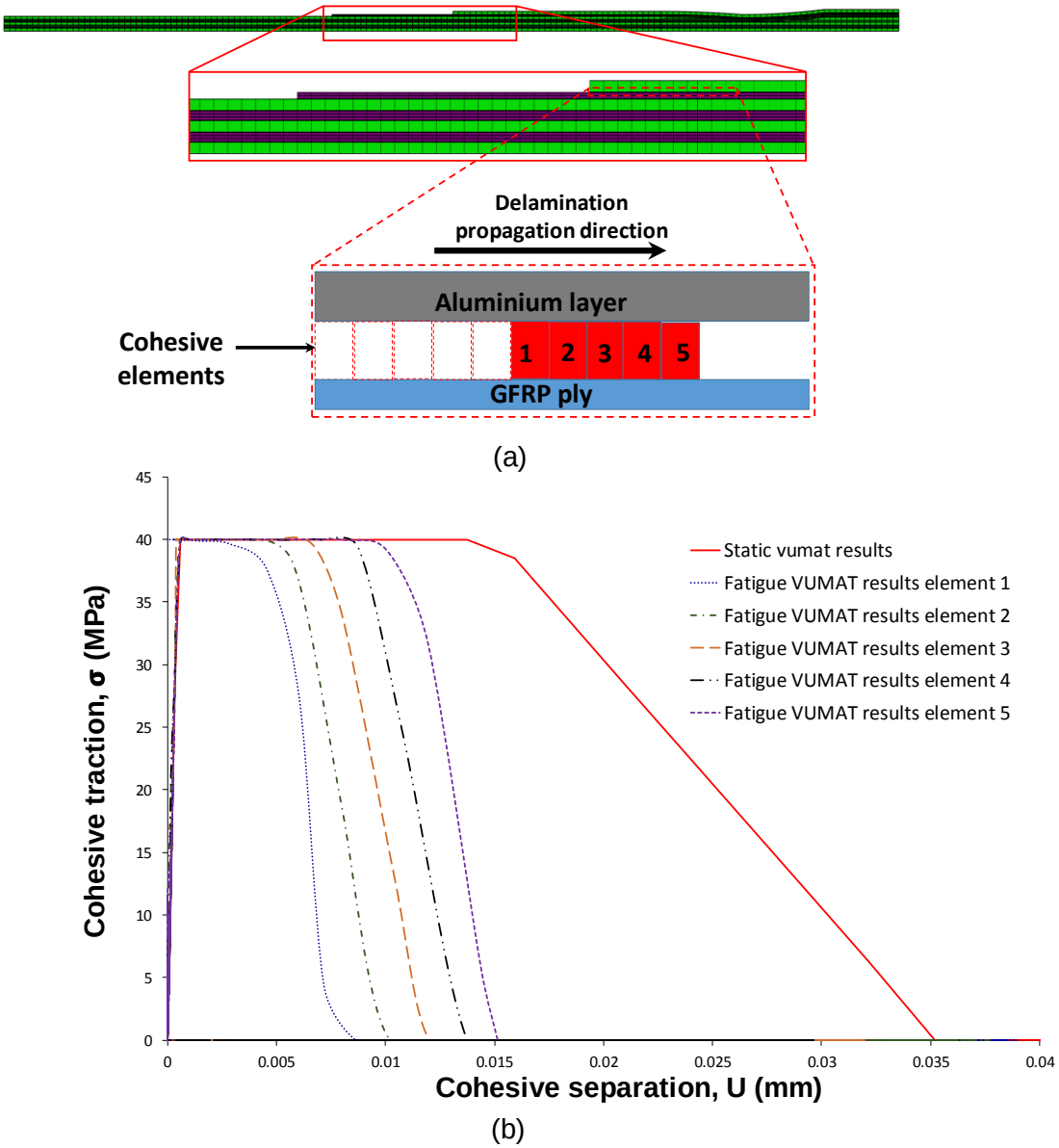

Figure7.15: (a) Location of delamination in splice specimen model, (b) comparison between static and fatigue traction-separation curves using pure mode-II VUMAT codes for the splice model at 50% severity (fine mesh, data sampled in 1 mm intervals starting 5 mm from discontinuous outer aluminium layer interface edge).

In terms of the damage variables, Figure 7.16 shows fatigue damage variable contours at the outer aluminium/GFRP interface for a series of five cohesive elements starting 5 mm from the crack edge), during different regions of the traction-separation curves. These elements were chosen to be far enough away from the unstable behaviour near the crack tip to enable stable propagation to be monitored with zero indicating undamaged elements and one corresponding to fully damaged elements. Contours start from zero in the elastic region corresponding to undamaged cohesive elements

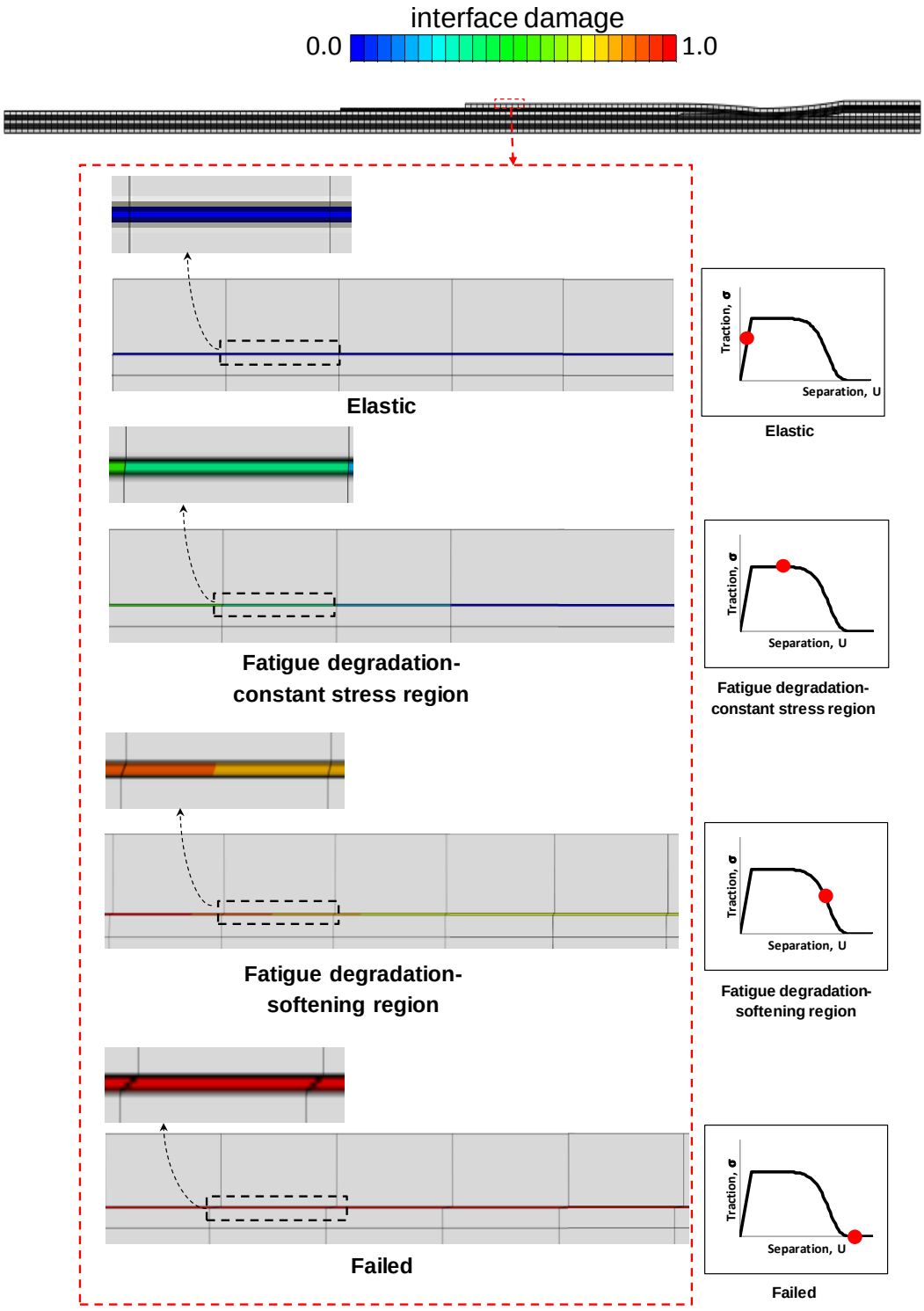

Figure 7.16: (a) Fatigue damage variable contours plots for cohesive elements in splice specimen at 50% severity for elastic region, fatigue degradation constant stress region, fatigue degradation softening region and final failure region, (b) Traction-separation curves pointing baseline fatigue damage formulation.

(blue). As the load is increased delamination propagates in the constant-stress region of the trapezoidal traction-separation law (green - partly damaged interface elements). Then more fatigue degradation occurs in a number of the cohesive elements in the softening region (orange - partly damaged interface elements). Finally the delamination grows across all the cohesive elements (red – damage variable equal to one).

In order to validate the numerical results, failure times from the VUMAT code results were compared with experimental data. Since it was not possible to obtain this data from the specimens tested in-house due to the problems in relation to the field of view as mentioned earlier in Section 7.3.3, Paris law curves recreated from the experimental data obtained by Alderliesten [4] from fatigue tests on Glare® 2 and Glare® 4B specimens giving Paris Law coefficients $C = 0.05$ and $m = 7.5$ were used. These coefficients are used to derive the points on Figure 7.17 corresponding to the five elements in the model, and the best fit line. It can be seen that the numerical VUMAT subroutine results correlate well with these experimentally derived results, with the crack growth rates showing good correlation for all five cohesive elements.

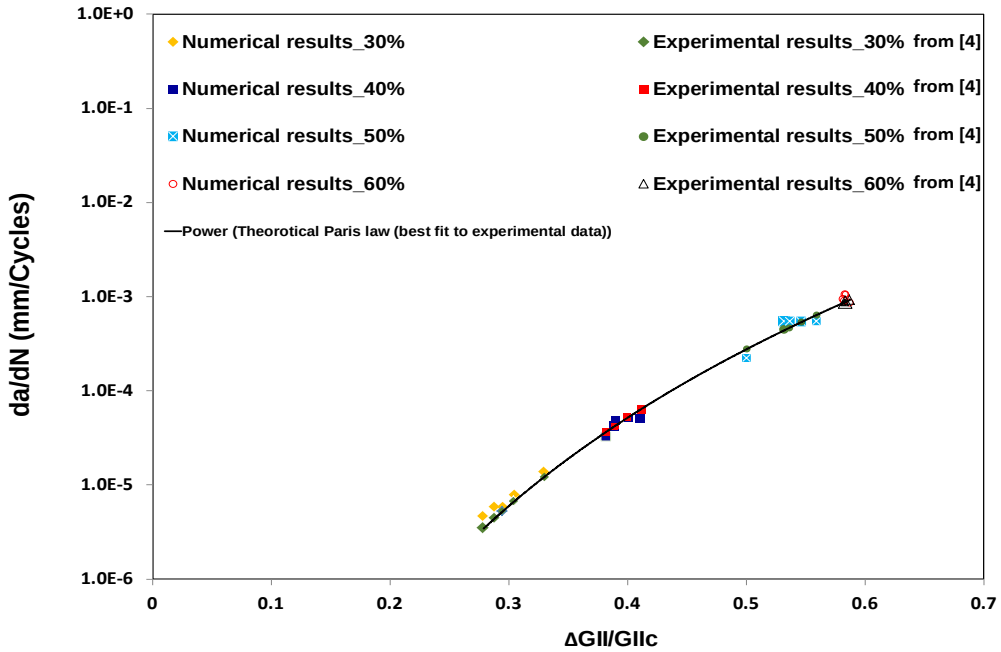

Figure 7.17: Experimentally generated and numerical Paris curve for a series of five cohesive elements (shown in Figure 7.15a) in the splice model at severities 30%, 40%, 50% and 60% and R-ratio 0.1.

For the doubler model, traction–separation curves for a series of five cohesive elements 5 mm from the crack tip in the path of the fatigue crack propagation at the interface between the aluminium layer and the GFRP at the discontinuity in the joint region are shown in Figure 7.18. Again as for the splice specimens these elements were chosen to validate the VUMAT code since at this stage the crack growth is stable. Since the upper and lower interfaces behave in exactly the same way the results from only the lower interface are shown in Figure 7.18 (a). The fatigue traction-separation curves follow the reference (static) softening curve up to the end of elastic region at a displacement of 4.86×10^{-4} mm and stress 40 MPa as for the splice. However, unlike the splice, after this point no fatigue degradation occurs in any of the elements along the interface indicating that delamination does not propagate along either the upper or the lower interface. This is consistent with the experimentally derived S-N curves (Figure 7.9) which show negligible difference in fatigue life between pristine and pre-cracked doubler specimens as would be expected if delamination fails to grow. Confirmation can be obtained from visual inspection of the pre-cracked doubler specimens after testing which shows that there is no crack growth after 49547 cycles (Figure 7.10). The AE results further support this since similar AE activity is seen for both damaged and undamaged doubler specimens consistent with no delamination growth in the discontinuous aluminium layer and GFRP interfaces.

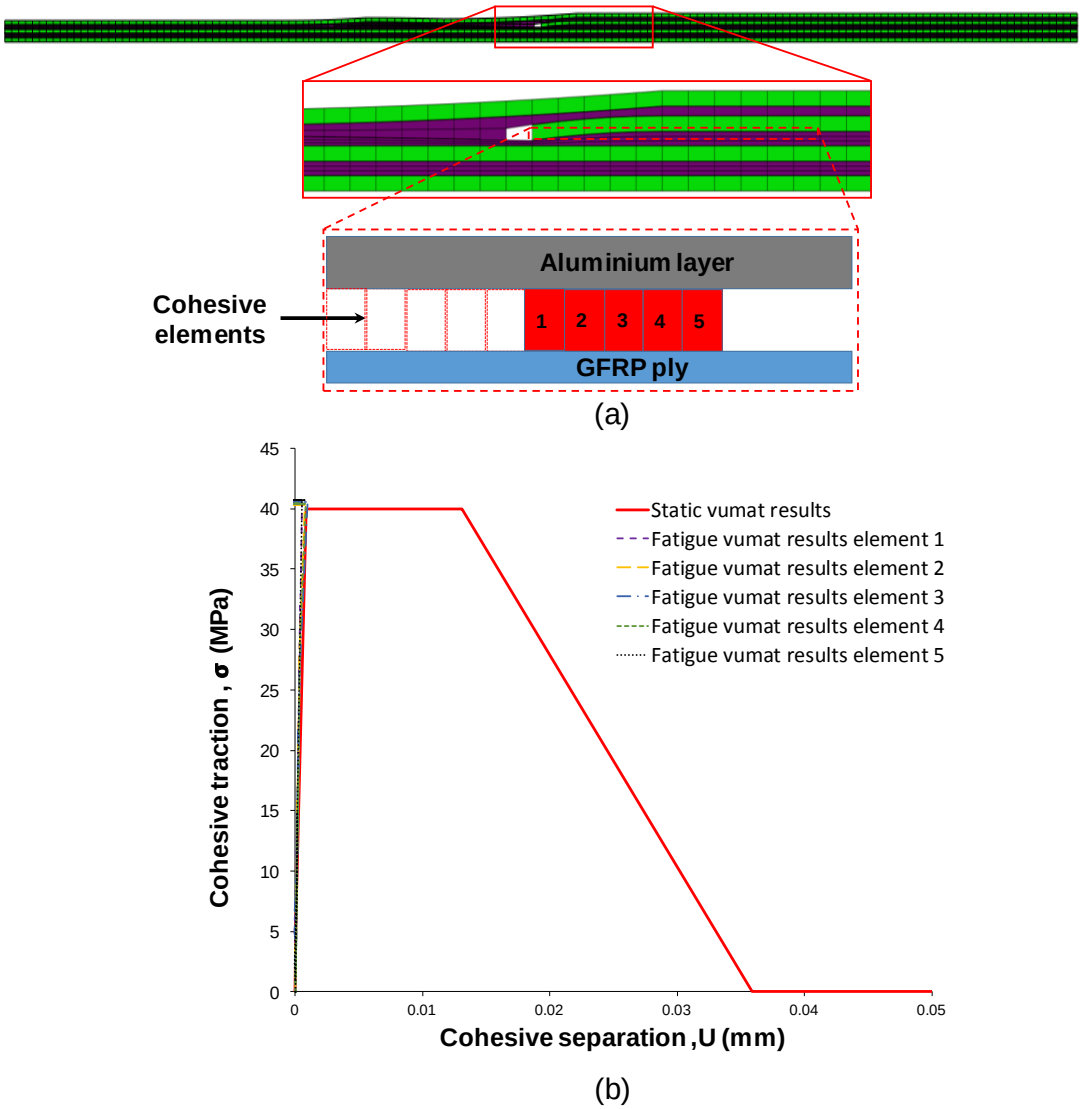

Figure7.18: (a) Location of cohesive elements in pre-cracked doubler specimen model, (b) comparison between static and fatigue traction-separation curves using pure mode-II VUMAT codes for pre-cracked doubler specimen model at 50% severity (fine mesh, data sampled in 1 mm intervals starting 5 mm from discontinues outer aluminium layer interface edge).

7.5 Chapter summary

A novel cohesive zone model incorporating using a mode-II trapezoidal traction law was developed to simulate delamination initiation and growth in splice and doubler joints under static and high-cycle fatigue loading. A series of experiments were performed on both types of specimens under constant amplitude high-cycle fatigue loading to provide data to support model validation. The experimental results showed that the fatigue life for the splice specimens was lower than for the doubler specimens corresponding to lower fatigue damage tolerance. This was shown to be due to the fact

that delaminations initiating in the region of the discontinuous outer aluminium layers at the interface with the GFRP plies in the splice joint continued to propagate under fatigue loading, whilst with the doubler, for both pristine and pre-cracked specimens, no delamination growth occurred under fatigue loading. Good correlation was observed between the predicted FE results and those determined experimentally by Alderliesten [4]. AE results were successfully used to validate numerical fatigue results in which delamination initiation and propagation were identified by the occurrence of high cumulative energy events.

Chapter 8 - Conclusions and Further Work

8.1 Conclusions

The research presented in this thesis has focused on the numerical and experimental investigation of Glare4B laminates including adhesive joints (splices and doublers) incorporating defects representative of those introduced during manufacturing (or impact loading during operation) under static compression and high cycle fatigue loading. The main achievements of this work can be listed as follows:

- The buckling and postbuckling behaviour of the splice and doubler features with and without defects, were successfully investigated through a series of instrumented tests.
- Finite element models generated to model this behaviour showed good agreement with experiments in terms of in-plane and out-of-plane displacement.
- In experiments artificial delaminations representative of those which could potentially be generated during manufacturing had a negligible effect on the compressive strength of both splice and doubler specimens, a finding which was replicated in the numerical results. This is potentially due to the relatively small size of the artificial delaminations.
- The gradual evolution of interface damage (delamination) under compressive loading in the specimens investigated was effectively modelled by a cohesive zone model in the splice specimen model, which also predicted the lack of delamination growth in the doubler specimen model.
- Finite element model results for both splice and doubler specimens subject to compressive loading, showed a considerable amount of energy is dissipated via

plastic deformation of the metallic sheets in both cases.

- Models for both splice and doubler specimens under compression also predict damage in the composite layers, including matrix cracking and shear damage in the matrix resin layers and fibre breakage in the fibre plies.
- Good correlation was observed between the damage predicted by the FE models and Scanning Electron Microscopy (SEM) micrographs for the specimens tested under compression loads.
- Digital image correlation (DIC) monitoring was used for visualisation of three-dimensional full-field in-plane and out-of-plane displacements enabling the study of the buckling and postbuckling behaviour.
- Acoustic Emission (AE) was successfully used to detect and locate damage initiation and propagation during testing with damage correlating with areas of high curvature and AE activity increasing at salient points during loading, corresponding to significant reductions in stiffness.
- The novel AE Delta-T location algorithm was used for the first time to improve this damage location.
- The effect of impact damage represented by artificial circular delamination on the buckling and postbuckling behaviour of Glare® laminates was successfully examined through monitored experimental tests.
- The introduction of a large delamination (covering 62.5% of the width) had a significant effect on this behaviour of the specimen.
- Reductions in postbuckling stiffness due to these delaminations correlated well with high activity events detected by AE. AE data also enabled detection of matrix cracking in the highest curvature region for both pristine specimens and those containing defects.

- AE results for specimens containing artificial circular delaminations showed excellent correlation with FE models, which predicted delamination growth along the specimen's horizontal centreline where the highest curvature is seen and around the edges of the artificial delamination. Also the FE model results predict the lack of delamination in the pristine 'far-field' specimens.
- The load versus in-plane displacement curves predicted by the models for both pristine specimens and those with circular delaminations was also in very good agreement with experimental results demonstrating the ability of the FE models generated to simulate the buckling and postbuckling behaviour of such FML structures.
- A modified cohesive zone model incorporating using mixed-mode trapezoidal traction-separation law was developed to simulate damage initiation and evolution at the metal-fibre interfaces of the FML "Glare® 4B" under both quasi-static and high cycle fatigue tension loadings.
- This model is able to simulate elastic-plastic interfacial damage behaviour and as such is suitable for ductile adhesives including toughened epoxy unlike bilinear cohesive zone models which can only accurately simulate damage in brittle adhesives. This makes it suitable for modelling any material interface which incorporates ductile adhesives.
- A series of experiments were performed under high cycle fatigue loading. The experimental fatigue results show that the fatigue life for the doubler specimens was higher than for the splice specimens, indicating that the doubler joint has a higher fatigue damage tolerance than the splice joint.
- Experimental results revealed that neither pristine doubler specimens nor those containing defects show any delamination propagation under high cycle fatigue loading while in splice specimens delaminations occur in the outer discontinuous

aluminium layers and GFRP interfaces.

- Developed static and fatigue VUMAT codes were successfully implemented and were able to model delamination initiation and propagation in fibre-metal laminate structures including adhesive joints.
- Two simplified models were generated for both mode I and mode II damage failure modes under quasi-static loading in order to validate the static VUMAT code results against Abaqus/Explicit software results and a good correlation was obtained.
- Fatigue FE analyses using this VUMAT code were validated using experimental Paris law results from Alderliesten [4] and a good correlation was observed between the predicted FE results and the experiments, with the model predicting the propagation of damage in the splice joints and lack of delamination in the doubler joints.
- The trapezoidal CZM was shown to be an efficient for modelling interlaminar damage in FML structures (Glare) including adhesively bonded joints. This due to the plastic or constant stress region included in the trapezoidal law which enables simulation of the plastic flow which occurs in such ductile interface materials.
- The effect of relatively small pre-cracks on the fatigue life of Glare® 4B specimens including doubler joint was shown to be negligible.
- AE results were successfully used to validate different fatigue damage mechanisms such as delamination initiation and propagation, matrix cracking, fibre breakage and metal plasticity which were detected via different signal amplitudes.

8.2 Further work

Whilst the work reported in this thesis provides and extensive study of the behaviour of the fibre-metal laminate Glare® under different loading scenarios, several areas of research could not be explored in this project and are left as future work, as discussed below.

- The fatigue models developed in the present work could be further expanded to account for full 3D crack propagation problems. Although the 2D fatigue models developed here are suitable for the analysis of prismatic laminates, full 3D models may be necessary for the analysis of more complex geometries.
- Additional fatigue damage mechanisms in fibre-metal laminates could be accounted for, including damage within the composite plies (matrix cracking, fibre failure) and the metallic layers (metal fatigue). The present work focused on fatigue delamination growth, which is the predominant damage mechanism, and only accounted for the other types of damage in a *pseudo-static* sense, *i.e.* without additional fatigue damage accumulation laws. The consideration of the latter is expected to have only a moderate effect on the predictions presented in the current work, however.
- If possible, detailed damage imaging could be used to further validate the models presented here, and any models implemented in the future. X-ray computed tomography, which is now commonly used for the validation of CFRP and GFRP damage models, is unfortunately not very useful for FMLs since their metallic and composite layers have very different X-ray absorption and scattering properties. Alternatively, high-resolution ultrasonic imaging or ultrasonic microscopy might be more suitable imaging techniques.
- The effects of static and fatigue bending stresses on FMLs with internal features could be considered, in addition to axial stresses. Bending stresses are expected to generate considerably higher mode-II loading, which could result in very different

damage evolution behaviour. It should be noted however that the models presented in this thesis are suitable for such analyses.

- In addition to internal joints such as doublers and splices, other features such as open-holes and bolted-holes could also be analysed. These are representative of bolted and riveted joints which are also commonly found in FML structures.

References

[1] A. Vlot and J.W. Gunnink, Fibre Metal Laminates - An Introduction. London: Kluwer Academic publishers, 2001.

[2] R.C. Alderliesten, M. Hagenbeek, J.J. Homan, P.A. Hooijmeijer, T.J. De Vries, and C. A. J. R. Vermeeren, Fatigue and Damage Tolerance of Glare, Applied Composite Materials, vol. 10, pp. 223–242, 2003.

[3] S.M.O. Tavares, P.P. Camanho, and P. M. S. T. de Castro, Assessment of Materials for Fuselage Panels Considering Fatigue Behavior, Materials Science Forum, vol. 730, pp. 265-270, 2013.

[4] R.C. Alderliesten, Fatigue Crack Propagation and Delamination Growth in Glare, Delft University of Technology, 2005.

[5] M.P. Clarke and M.J. Pavier, Artificial damage techniques for low velocity impact in carbon fibre composites, Composite Structures vol. 25 pp. 113–120, 1993.

[6] M.J. Pavier and M.P. Clarke, Experimental techniques for the investigation of the effects of impact damage on carbon fibre composites, Composites Science and Technology, vol. 55, pp. 157-169, 1995.

[7] H. Gu and A. Chattopadhyay, An experimental investigation of delamination buckling and postbuckling of composite laminates, Composites Science and Technology, vol. 59 pp. 903–910, 1999.

[8] Z. Kutlu and Fu-Kuo Chang, Composite panels containing multiple through-the-width delaminations and subjected to compression. Part II: experiments & verification, Composite Structures vol. 31, pp. 297-314, 1995.

[9] M. Aslan and W.M. Banks, The effect of multiple delamination on postbuckling behavior of laminated composite plates, Composite Structures, vol. 42, pp. 1-12, 1998.

[10] Y. Pekbey and O. Sayman, A Numerical and Experimental Investigation of Critical Buckling Load of Rectangular Laminated Composite Plates with Strip Delamination, Journal of Reinforced Plastics and Composites, vol. 25, pp. 685-697, 2006.

[11] J.L. Verolme, Crippling and short-column buckling of fiber metal laminates, Delft University of Technology, Faculty of Aero. Eng1994.

[12] J.L. Verolme, The initial buckling behavior of flat and curved fiber metal laminate panels, Delft University of Technology, Faculty of Aero. Eng1995.

[13] J.L. Verolme, The development of a design tool for fiber metal laminate compression panel, PhD, Delft University of Technology, 1995.

[14] E.C. Botelho, L.C. Pardini, R.A. Silva, and M. C. Rezende, A Review on the Development and Properties of Continuous Fiber/epoxy/aluminum Hybrid Composites for Aircraft Structures, Materials Research, vol. 9, pp. 247-256, 2006.

[15] D. Hull and T. Clyne, An Introduction to Composite Materials: Cambridge University Press, 1996.

[16] R.J. Mania and C.B. York, Buckling strength improvements for Fibre Metal Laminates using thinply tailoring, Composite Structures, vol. 159 pp. 424–432, 2017.

[17] R.J. Mania, Z. Kolakowski, J. Bienias, P. Jakubczak, and K. Majerski, Comparative study of FML profiles buckling and postbuckling behaviour under axial loading, Composite Structures vol. 134, pp. 216–225, 2015.

[18] M. Kamocka and R.J. Mania, Analytical and Experimental Determination of FML Stiffness and Strength Properties, Mechanics and Mechanical Engineering, vol. 19, pp. 141–159, 2015.

[19] R.M. Frizzell, C.T. McCarthy, and M.A. McCarthy, An experimental investigation into the progression of damage in pin-loaded fibre metal laminates, Composite Part B, vol. 39, pp. 907-925, 2008.

[20] J.J.C. Remmers and R. de Borst, Delamination buckling of fibre–metal laminates,

Composites Science and Technology vol. 61, pp. 2207–2213, 2001.

[21] L.M. Kachanov, Delamination buckling of composite materials. London: Kluwer Academic Publishers, 1988.

[22] W.T. Koiter, The effect of axisymmetric imperfections on the buckling of cylindrical shells under axial compression, 1963.

[23] J.W. Hutchinson, Knockdown factors for buckling of cylindrical and spherical shells subject to reduced biaxial membrane stress, International Journal of Solids and Structures vol. 47 pp. 1443–1448, 2010.

[24] M.W. Hilburger and J.H. Starnes Jr., Effects of imperfections on the buckling response of compression-loaded composite shells International Journal of Non-Linear Mechanics vol. 37, pp. 623–643, 2002.

[25] N.G. Tsouvalis, A.A. Zafeiratou, and V.J. Papazoglou, The effect of geometric imperfections on the buckling behaviour of composite laminated cylinders under external hydrostatic pressure, Composites: Part B vol. 34 pp. 217–226, 2003.

[26] C.A. Featherston, Experimental buckling of a simple aerofoil under combined shear and in-plane bending, Journal of Mechanical Engineering Science, vol. 218, pp. 155-172, 2004.

[27] P.A. Lagace, D.W. Jensen, and D.C. Finch, Buckling of unsymmetric composite laminates, Composite Structures, vol. 5, pp. 101–123, 1986.

[28] E. Eglitis, K. Kalnins, and O. Ozolinsh, The influence of loading eccentricity on the buckling of axially compressed imperfect composite cylinders, Mechanics of Composite Materials, vol. 46, pp. 483-492, 2010/12/01 2010.

[29] R.J. Mania, Comparative static buckling study of FML thin-walled profiles, presented at the ECCM16 – 16th European conference on compositematerials, Seville, Spain, 2014.

[30] D. Banat, Z. Kolakowski, and R.J. Mania, Investigations of FML profile buckling and post-buckling behaviour under axial compression, Thin-Walled Structures vol. 107, pp. 335–344, 2016.

[31] H. Kwon and H. Kim, Buckling and debond growth of partial debonds in adhesively bonded composite splice joints, Composite Structures vol. 79, pp. 590–598, 2007.

[32] R.G. Wang, L. Zhang, J. Zhang, W.B. Liu, and X.D. He, Numerical analysis of delamination buckling and growth in slender laminated composite using cohesive element method, Computational Materials Science, vol. 50, pp. 20-31, 2010.

[33] B. Mohammadi, F. Shahabi, and S.A.M. Ghannadpou, Post-buckling delamination propagation analysis using interface element with de-cohesive constitutive law, Procedia Engineering, vol. 10, pp. 1797-1802, 2011.

[34] Y. Zhang and S. Wang, Buckling, post-buckling and delamination propagation in debonded composite laminates Part 1: Theoretical development, Composite Structures, vol. 88, pp. 121-130, 2009.

[35] S. Wang and Y. Zhang, Buckling, post-buckling and delamination propagation in debonded composite laminates Part 2: Numerical applications, Composite Structures, vol. 88, pp. 131-146, 2009.

[36] I. Chirica and E.-F. Beznea, Buckling analysis of the composite plates with delaminations, Computational Materials Science, vol. 50, pp. 1587-1591, 2011.

[37] S.D. Akbarov, N. Yahnioglu, and E.E. Karatas, Buckling delamination of a rectangular plate containing a rectangular crack and made from elastic and viscoelastic composite materials, International Journal of Solids and Structures, vol. 47, pp. 3426-3434, 2010.

[38] M. Eaton, Acoustic emission (AE) monitoring of buckling and failure in carbon fibre composite structures, PhD, Cardiff, 2007.

[39] V. Obdrzalek and J. Vrbka, On buckling of a plate with multiple delaminations, Engineering Mechanics, vol. 17, pp. 37–47, 2010.

[40] V. Obdržálek and J. Vrbka, On the applicability of simple shapes of delaminations in buckling analyses, Composites Part B: Engineering, vol. 42, pp. 538-545, 2011.

[41] C.T. McCarthy, R.M. Frizzell, and M.A. McCarthy, Simulating damage and delamination in fibre metal laminate joints using a three-dimensional damage model with cohesive elements and damage regularisation, Composite Science and Technology, vol. 71, pp. 1225-1235, 2011.

[42] M.W. Hilburger and J.H. Starnes Jr., Effects of imperfections of the buckling response of composite shells, Thin-Walled Structures vol. 42, pp. 369–397, 2004.

[43] R. Degenhardt, A. Kling, A. Bethge, J. Orf, L. Kärger, R. Zimmermann, et al., Investigations on imperfection sensitivity and deduction of improved knock-down factors for unstiffened CFRP cylindrical shells, Composite Structures vol. 92, pp. 1939–1946, 2010.

[44] S.G.P. Castro, R. Zimmermann, M.A. Arbelo, R. Khakimova, M.W. Hilburger, and R. Degenhardt, Geometric imperfections and lower-bound methods used to calculate knock-down factors for axially compressed composite cylindrical shells, Thin-Walled Structures, vol. 74 pp. 118–132, 2014.

[45] M.S. Ismail, J. Purbolaksono, A. Andriyana, C.J. Tanb, N. Muhammad, and H.L. Liew, The use of initial imperfection approach in design process and buckling failure evaluation of axially compressed composite cylindrical shells, Engineering Failure Analysis, vol. 51, pp. 20-28, 2015.

[46] J. Singer, J. Arbocz, and T. Weller, Buckling Experiments, Experimental Methods in Buckling of Thin-Walled Structures, Volume 2, Shells, Built-up Structures, Composites and Additional Topics: John Wiley &Sons, INC, 2002.

[47] Y. Fu, R. Bi, Y. Tian, and C. Jiang, Buckling and Postbuckling Analysis of Elasto-Plastic Fiber Metal Laminates, Acta Mechanica Solida Sinica, vol. 27, 2014.

[48] T.C. Wittenberg and A.D. Jonge, Plasticity correction factors for buckling of flat rectangular glare plates loaded in compression or shear, presented at the ICAS 2002 congress, Toronto, 2002.

[49] A.D. Crocombe, C.Y. Ong, C.M. Chan, M.M.A. Wahab, and I.A. Ashcroft, Investigating fatigue damage evolution in adhesively bonded structures using backface strain measurement, Journal of Adhesion, vol. 78, pp. 745-776, 2002.

[50] S.R. Swanson, Handbook of fatigue testing, 1974.

[51] A.D. Crocombe and G. Richardson, Assessing stress state and mean load effects on the fatigue response of adhesively bonded joints, International Journal of Adhesion and Adhesives, vol. 19, pp. 19-27, 1999.

[52] P.R. Underhill and D.L. DuQuesnay, The dependence of the fatigue life of adhesive joints on surface preparation, International Journal of Adhesion and Adhesives, vol. 26, pp. 62-66, 2006.

[53] R.R. Gomatam and E. Sancaktar, The effects of stress state, loading frequency and cyclic waveforms on the fatigue behavior of silver-filled electronically-conductive adhesive joints," Journal of Adhesion Science and Technology, vol. 20, pp. 53-68, 2006b.

[54] R. Sarfaraz, A.P. Vassilopoulos, and T. Keller, Modeling the constant amplitude fatigue behavior of adhesively bonded pultruded GFRP joints, Journal of Adhesion Science and Technology, vol. 27, pp. 855–878, 2013.

[55] Z.H. Zhang, J.K. Shang, and F.V. Lawrence, A Backface Strain Technique for Detecting Fatigue-Crack Initiation in Adhesive Joints, Journal of Adhesion, vol. 49, pp. 23-36, 1995.

[56] M. Dessureault and J.K. Spelt, Observations of fatigue crack initiation and propagation in an epoxy adhesive, International Journal of Adhesion and Adhesives, vol. 17, pp. 183-195, 1997.

[57] M. Quaresimin and M. Ricotta, Life prediction of bonded joints in composite materials, International Journal of Fatigue, vol. 28, pp. 1166-1176, 2006.

[58] S. Azari, M. Papini, J.A. Schroeder, and J.K. Spelt, Fatigue threshold behavior of adhesive joints, International Journal of Adhesion and Adhesives, vol. 30, pp. 145-159, 2010.

[59] L.F. Kawashita and S.R. Hallett, A crack tip tracking algorithm for cohesive interface element analysis of fatigue delamination propagation in composite materials, International Journal of Solids and Structures vol. 49, pp. 2898–2913, 2012.

[60] K. Ishii, M. Imanaka, H. Nakayama, and H. Kodama, Evaluation of the fatigue strength of adhesively bonded CFRP/metal single and single-step double-lap joints, Composites Science and Technology, vol. 59, pp. 1675-1683, 1999.

[61] P.T. Cheuk, L. Tong, C.H. Wang, A. Baker, and P. Chalkley, Fatigue crack growth in adhesively bonded composite-metal double-lap joints, Composite Structures, vol. 57, pp. 109-115, 2002.

[62] H. Khoramishad, Modelling fatigue damage in adhesively bonded joints, PhD, University of Surrey, 2010.

[63] S. Khan, Fatigue crack and delamination growth in fibre metal laminates under variable amplitude loading, PhD, Delft Univerisity of Technology, Netherland, 2012.

[64] H.J.K. Lemmen, R.C. Alderliesten, R. Benedictus, J.C.J. Hofstede, and R. Rodi, The power of Digital Image Correlation for detailed elastic-plastic strain measurements, presented at the WSEAS International Conference on Engineering Mechanics, Structures, Engineering Geology (EMSEEG '08), Heraklion, Greece, 2008.

[65] Y.A. Dzenis, Cycle-based analysis of damage and failure in advanced composites under fatigue: 1. Experimental observation of damage development within loading cycles, International Journal of Fatigue, vol. 25, pp. 499-510, 2003.

[66] M.G.R. Sause, T. Müller, A. Horoschenkoff, and S. Horn, Quantification of Failure Mechanisms in Mode-I Loading of Fiber Reinforced Plastics Utilizing Acoustic Emission Analysis, Composites Science and Technology, vol. 72, pp. 167-174, 2012.

[67] E. Maillet, N. Godin, M. R'Mili , P. Reynaud, G. Fantozzi, and J. Lamon, Damage monitoring and identification in SiC/SiC minicomposites using combined acousto-ultrasonics and acoustic emission, Composites Part A: Applied Science and Manufacturing, vol. 57, pp. 8-15, 2014.

[68] M.G. Baxter, R. Pullin, K.M. Holford, and S.L. Evans, Delta T source location for acoustic emission, Mechanical Systems and Signal Processing vol. 21, pp. 1512–1520, 2007.

[69] K.R. Miller and E.K. Hill, Nondestructive Testing Handbook: Acoustic Emission Testing. American Society for Non-Destructive Testing, 2005.

[70] G. Qi, Wavelet-Based AE Characterization of Composite Materials, NDT & E International, vol. 33, pp. 133-144, 2000.

[71] C. Lu, P. Ding, and Z. Chen, Time-frequency Analysis of Acoustic Emission Signals Generated by Tension Damage in CFRP, Procedia Engineering vol. 23, pp. 210-215, 2011.

[72] S. Momon, M. Moevus, N. Godin, M. R'Mili, P. Reynaud, G. Fantozzi, et al., Acoustic emission and lifetime prediction during static fatigue tests on ceramic-matrix-composite at high temperature under air, Composites Part A: Applied Science and Manufacturing, vol. 41, pp. 913-918, 2010.

[73] E. Maillet, N. Godin, M. R'Mili, P. Reynaud, J. Lamon, and G. Fantozzi, Analysis of Acoustic Emission energy release during static fatigue tests at intermediate temperatures on Ceramic Matrix Composites: Towards rupture time prediction, Composites Science and Technology, vol. 72, pp. 1001-1007, 2012.

[74] S.C. Woo and N.S. Choi, Analysis of Fracture Process in Single-Edge-Notched Laminated Composites Based on the High Amplitude Acoustic Emission Events, Composites Science and Technology, vol. 67, pp. 1451-1458, 2007.

[75] X. Zhuang and X. Yan, Investigation of Damage Mechanisms in Self-Reinforced Polyethylene Composites by Acoustic Emission, Composites Science and Technology, vol. 66, pp. 444-449, 2006.

[76] M.M.A. Wahab, I.A. Ashcroft , A.D. Crocombe, and S.J. Shaw, Prediction of fatigue thresholds in adhesively bonded joints using damage mechanics and fracture mechanics, Journal of Adhesion Science and Technology, vol. 15, pp. 763-781, 2001.

[77] M. Imanaka, T. Hamano, A. Morimoto, R. Ashino, and M. Kimoto, Fatigue damage evaluation of adhesively bonded butt joints with a rubber-modified epoxy adhesive, Journal of Adhesion Science and Technology, vol. 17, pp. 981-994, 2003.

[78] I. Hilmy, M.M.A. Wahab, I.A. Ashcroft, and A.D. Crocombe, Measuring of damage parameters in adhesive bonding, Key Engineering Materials, , vol. 324-325, p. 275 278, 2006.

[79] I. Hilmy, M.M.A. Wahab, A.D. Crocombe, I.A. Ashcroft, and A.G. Solana, Effect of triaxiality on damage parameters in adhesive, Key Engineering Materials, vol. 348-349,

pp. 37-40, 2007.

[80] J.E. Ganghoffer and J. Schultz, Interactions between adhesion and friction-1.Theorotical aspects, J.Mech. Phys. Solids, vol. 45, pp. 151-174, 1997.

[81] M. Imanaka, A. Morimoto, R. Ashino, and M. Kimoto, Fatigue damage evaluation of adhesively bonded butt joints with a rubber-modified epoxy adhesive, J Adhes Sci Technol, vol. 17, pp. 981–94, 2003.

[82] M.M.A. Wahab, I.A. Ashcroft, A.D. Crocombe, and P.A. Smith, Numerical prediction of fatigue crack propagation lifetime in adhesively bonded structures, International Journal of Fatigue, vol. 24, pp. 705-709, 2002.

[83] M.M.A. Wahab, I.A. Ashcroft, A.D. Crocombe, and P.A. Smith, Finite element prediction of fatigue crack propagation lifetime in composite bonded joints, Composite Part A: Applied Sience and Manufacturing, vol. 35, pp. 213-222, 2004.

[84] R.H. Martin and G.B. Murri, Characterisation of modeI and modeII delamination growth and threshold in AS4/PEEK composites, in ASTM STP vol. 1057, ed. Philadelphia(PA): American Society for Testing and Materials, 1990, pp. 251-270.

[85] A.J. Curley, H. Hadavinia, A.J. Kinloch, and A.C. Taylor, Predicting the service life of adhesively-bonded joints, International Journal of Fracture, vol. 103, pp. 41-69, 2000.

[86] M. Imanaka, K. Ishii, and H. Nakayama, Evaluation of fatigue strength of adhesively bonded single and single step double lap joints based on stress singularity parameters, Engineering Fracture Mechanics, vol. 62, pp. 409-424, 1999.

[87] G.I. Barenblatt, Equilibrium Cracks Formed on A Brittle Fracture, Doklady Akademii Nauk Sssr, vol. 127, pp. 47-50, 1959.

[88] D.S. Dugdale, Yielding of Steel Sheets Containing Slits, Journal of the Mechanics and Physics of Solids, vol. 8 pp. 100-104, 1960.

[89] G. Barenblatt, The Mathematical Theory of Equilibrium Cracks in Brittle Fracture, Advances in Applied Mechanics, vol. 7, pp. 55-129, 1962.

[90] A. Hillerborg, M. Modeer, P-E. Petersson, Analysis of crack formation and crack growth in concrete by means of fracture mechanics and finite elements, Cem Concr Res, vol. 6, pp. 773–81, 1976.

[91] A. Needleman, A continuum model for void nucleation by inclusion debonding, Journal of Applied Mechanics, vol. 54, pp. 525–531, 1987.

[92] A. Needleman, An analysis of tensile decohesion along an interface, J Mech Phys Solids, vol. 38, pp. 289–324, 1990.

[93] U. Mi, M. Crisfield, and G. Davies, Progressive delamination using interface elements, Journal of Composite Materials, vol. 32, pp. 1246-1272, 1998.

[94] V. Tvergaard and J.W. Hutchinson, The relation between crack growth resistance and fracture process parameters in elastic-plastic solids, J. Mech. Phys. Solids, vol. 40, pp. 1377-1397, 1992.

[95] G. Alfano and M.A. Crisfield, Finite element interface models for the delamination analysis of laminated composites: mechanical and computational issues, International Journal for Numerical Methods in Engineering, vol. 7, pp. 1701–1736, 2001.

[96] O. Nguyen, E. Repetto, M. Ortiz, and R. Radovitzky, A cohesive model of fatigue crack growth, International Journal of Fracture, vol. 4, pp. 351–369, 2001.

[97] B.F. Sørensen, Cohesive law and notch sensitivity of adhesive joints, Acta Materialia, vol. 5, pp. 1053–1061, 2002.

[98] D. Xie and J.S.B. Biggers, Progressive crack growth analysis using interface element based on the virtual crack closure technique, Finite Elements in Analysis and Design, vol. 11, pp. 977–984, 2006.

[99] D. Xie and A.M. Waas, Discrete cohesive zone model for mixed-mode fracture using finite element analysis, Engineering Fracture Mechanics, vol. 13, pp. 1783– 1796, 2006.

[100] P.A. Gustafson and A.M. Waas, T650/AFR-PE-4/FM680-1 mode I critical energy release rate at high temperatures: experiments and numerical models, presented at the AIAA/ASME/ASCE/AHS/ASC 48th Structures, Structural Dynamics, and Materials Conference, Honolulu, 2007.

[101] C. Sun, Fracture of plastically deforming adhesively bonded structures: experimental

and numerical studies, PhD, University of Michigan, 2007.

[102] P.A. Gustafson and A.M. Waas, Efficient and robust traction laws for the modeling of adhesively bonded joints, presented at the AIAA/ASME/ASCE/ AHS/ASC 49th Structures, Structural Dynamics, and Materials Conference, Schaumburg, 2008.

[103] P.A. Gustafson and A.M. Waas, The influence of adhesive constitutive parameters in cohesive zone finite element models of adhesively bonded joints, International Journal of Solids and Structures, vol. 46 pp. 2201–2215, 2009.

[104] K.L. Roe and T. Siegmund, An irreversible cohesive zone model for interface fatigue crack growth simulation, Engineering Fracture Mechanics, vol. 70, pp. 209-232, 2003.

[105] P.W. Harper and S.R. Hallett, A fatigue degradation law for cohesive interface elements – Development and application to composite materials, International Journal of Fatigue vol. 32, pp. 1774–1787, 2010.

[106] M.F.S.F. de Moura and J.P.M. Gonçalves, Cohesive zone model for high-cycle fatigue of composite bonded joints under mixed-mode I+II loading, Engineering Fracture Mechanics vol. 140, pp. 31–42, 2015.

[107] W. Van Paepegem and J. Degrieck, Fatigue degradation modelling of plain woven glass/epoxy composites, Composites Part A-Applied Science and Manufacturing, vol. 32, pp. 1433-1441, 2001.

[108] A. Ural and K. Papoulia, Modeling of fatigue crack growth with a damage-based cohesive zone model, presented at the 4th European Congress on Computational Methods in Applied Sciences and Engineering, Finland, 2004.

[109] D. Cojocaru and A.M. Karlsson, A simple numerical method of cycle jumps for cyclically loaded structures, International Journal of fatigue, vol. 28, pp. 1677-1689, 2006.

[110] A. Turon, J. Costa, P.P. Camanho, C.G. Da´vila, Simulation of delamination in composites under high-cycle fatigue, Composites: Part A vol. 38 pp. 2270–2282, 2007.

[111] P. Robinson, U. Galvanetto, D.Tumino, G. Bellucci, and D. Violeau, Numerical simulation of fatigue-driven delamination using interface elements, International Journal for Numerical Methods in Engineering, vol. 63, pp. 1824–1848, 2005.

[112] R. Marissen, Fatigue crack growth in ARALL A hybrid aluminium-aramid composite material, PhD, 1988.

[113] T. Takamatsu, T. Matsumura, N. Ogura, T. Shimokawa, and Y. Kakuta, Fatigue crack growth properties of a GLARE 3-5/4 Fiber Metal Laminate, Engineering Fracture Mechanics, vol. 63 pp. 253-272, 1999.

[114] X.R. Wu and Y.J. Guo, Fatigue behaviour and life prediction of fibre reinforced metal laminates under constant and variable amplitude loading, Fatigue & Fracture of Engineering Materials & Structures, vol. 25, pp. 417-432, 2002

[115] R.C. Alderliesten and J.J. Homan, Fatigue and damage tolerance issues of Glare in aircraft structures. International Journal of Fatigue, 28, pp. 1116-1123, 2006.

[116] R.C. Alderliesten, On crack tunneling and plane-strain delamination in laminates, International Journal of Fracture, vol. 148, pp. 401-414, 2007.

[117] T.S. Austin, M.M. Singh, P.J. Gregson, and P.M. Powell, Characterisation of fatigue crack growth and related damage mechanics in FRP-metal hybrid laminates, Composite Science and Technology, vol. 68, pp. 1399-1412, 2008.

[118] H. Khoramishad, A.D. Crocombe, K.B. Katnam, and I. A. Ashcroft, Predicting fatigue damage in adhesively bonded joints using a cohesive zone model, International Journal of Fatigue vol. 32, pp. 1146–1158, 2010.

[119] K.B. Katnam, A.D. Crocombe, H. Khoramishad, and I.A. Ashcroft, Load ratio effect on the fatigue behaviour of adhesivelly bonded joints: an enhanced damage model, The journal of Adhesion, vol. 86, pp. 257-272, 2010.

[120] S. Sugiman and A.D. Crocombe, The static and fatigue response of metal laminate and hybrid fibre-metal laminate doublers joints under tension loading, Composite Structures, vol. 94, pp. 2937–2951, 2012.

[121] M. Gupta, R.C. Alderliesten, and R. Benedictus, A novel approach for estimation of crack paths in fibre metal laminates, presented at the The 4th International Conference on Crack Paths (CP 2012), Gaeta (Italy), 2012.

[122] J. Yang, T.H. Hahn, H. Seo, P. Chang, and P. Yeh., Damage tolerance and durability of

fibre metal laminates for aircraft structures, Univeristy of California, Los AngelesOctober 2010.

[123] G.S. Wilson, Fatigue Crack Growth Prediction for generalized fiber metal laminates and hybrid materials, Master, Delft University of Technology, Netherland, 2013.

[124] A. Chlupová and V. Kozák, Fatigue crack growth and delamination in fibre metal laminate (Glare) during loading with positive mean stress, presented at the 18th Intenational Conference Engineering Mechanics, Svratka, Czech Republic, 2012.

[125] F. Mazaheri and H. Hosseini-Toudeshky, Low-cycle fatigue delamination initiation and propagation in fibre metal laminates, Fatigue Fract Engn g Mater Struct, vol. 38, pp. 641–660, 2015.

[126] S.G. Prolongo and A. Urena, Effect of surface pre-treatment on the adhesive strength of epoxy –aluminium joints, International Journal Adhesion and dhesives, vol. 29, pp. 23-31, 2009.

[127] T. Sinmazçelik, E. Avcu, M.Ö. Bora, and O. Çoban, A review: Fibre metal laminates, background, bonding types and applied test methods, Materials and Design, vol. 32 pp. 3671–3685, 2011.

[128] A.J. Kinloch, M.S.J. Little, and J.F. Watts, The role of the interphase in the environmental failure of adhesive joints, Acta Mater, vol. 48, pp. 4543-4553, 2000.

[129] S.Y. Sang Park, W.J. Choi, H.S. Choi, H. Kwon, and S.H. Kim, Effects of surface pre-treatment and void content on Glare laminate process characterisations, J. Mater Process Technol, vol. 210, pp. 1008-1016, 2010.

[130] G.W. Critchlow, Pretreatments for Metal to Metal bonding, PhD, Loughborough University, 1997.

[131] P.G. Sheasby and R. Pinner, The surface treatment and finishing of aluminium and its alloys, 6th Edition: Finishing Publications Ltd. and ASM International, 2001.

[132] C. Pitzer and J.M. Yang, Hybrid Metal Laminate (HML) Manufacturing Planning Evaluation and Assessment, Department of Materials Science and Engineering,University of California 2008.

[133] J.Y. Sheikh-Ahmad., Machining of Polymer Composites. United Arab Emirates, 2009.

[134] S. Al-jumaili, Damage Assessment In Complex Structures Using Acoustic Emission, PhD, Cardiff University, 2016.

[135] K.R. Miller and E.K. Hill, Nondestructive Testing Handbook, Third Edition: Volume 6, Acoustic Emission Testing, American Society for Non-Destructive Testing, 2005.

[136] S. Rippengill, K. Worden, K.M. Holford, and R. Pullin, Automatic Classification of Acoustic Emission Patterns, Strain, vol. 39, pp. 31-41, 2003.

[137] Y.Z. Pappas, A. Kontsos, T.H. Loutas, and V. Kostopoulos, On the Characterization of Continuous Fibres Fracture by Quantifying Acoustic Emission and Acousto-Ultrasonics Waveforms, NDT & E International, vol. 37, pp. 389-401, 2004.

[138] H. Vallen, AE testing fundamentals, equipment, applications, Journal of Nondestructive Testing(Germany), vol. 7, pp. 1-30, 2002.

[139] H.J. Rindorf, Acoustic Emission Source Location in Theory and in Practice: Bruel & Kjaer 1981.

[140] A. Pollock, Classical Wave Theory in Practical AE Testing, Progress in Acoustic Emission III, Proceedings of the Eighth International Acoustic Emission Symposium, The Japanese Society for Nondestructive Testing, pp. 708 - 721, 1986.

[141] M.R. Gorman and W.H. Prosser, AE source orientation by plate wave analysis, 1991.

[142] R. Svečko, D. Kusić, T. Kek, A. Sarjaš, A. Hančič, and J. Grum, Acoustic Emission Detection of Macro-Cracks on Engraving Tool Steel Inserts during the Injection Molding Cycle Using PZT Sensors, Sensors, vol. 13, pp. 6365-6379, 2013.

[143] M.G. Baxter, Damage assessment by Acoustic Emission (AE) during landing gear fatigue testing, Cardiff University, UK, 2007.

[144] ASTM, Standard method for primary calibration of acoustic emission sensors, vol. E1106-86, ed. American Society for Testing and Materials, 1986.

[145] ASTM, Standard guide for mounting piezoelectric acoustic emission sensors," vol. E650-97, ed. American Society for Testing and Materials, 1997.

[146] N.N. Hsu and F.R. Breckenridge, Characterization and Calibration of Acoustic Emission Sensors, Materials Evaluation, vol. 1, pp. 60-68, 1981.

[147] ASTM, A standard guide for determining the reproducibility of acoustic emission sensor response, American Society for Testing and Materials, vol., E976, 1994.

[148] K.R. Miller and E.K. Hill, Nondestructive Testing Handbook, Acoustic Emission Testing vol. 6: American Society for Non-Destructive Testing, 2005.

[149] F.F. Barsoum, Acoustic emission monitoring and fatigue life prediction in axially loaded notched steel specimens, J. Acoustic Emission, vol. 27, pp. 40-63, 2009.

[150] R. Pullin, A. Clarke, M.J. Eaton, K.M. Holford, S.L. Evans, J.P. McCrory, Detection of Cracking in Gear Teeth Using Acoustic Emission, Applied Mechanics and Materials vols. 24-25, pp. 45-50, 2010.

[151] D.D. GmbH, ISTRA 4D,Software Manual, Q-400 System, 2011.

[152] C. Herbst and K. Splitthof. Q-400, Dantec Dynamics Technical Note [Online].

[153] M. Hilburger and M. Nemeth, Application of Video Image Correlation Techniques to the Space Shuttle External Tank Foam Materials, presented at the In 47th AIAA/ASME/ASCE/AHS/ASC Structures, Structural Dynamics, and Materials Conference 14th AIAA/ASME/AHS Adaptive Structures Conference 7th (p. 2199). 2005.

[154] Y. Wang, P. Lava, S. Coppieters, M.D. Strycker, P.Houtte, and D. Debruyne, Investigation of the Uncertainty of DIC under Heterogeneous Strain States with Numerical Tests, Strain, vol. 48, pp. 453-462, 2012.

[155] O. Büyüköztürk and M.A. Taşdemir, Nondestructive Testing of Materials and Structures: Springer Science & Business Media, 2012.

[156] M. Pearson, Developement of Lightweight Structural Health Monitoring Systems for Aerospace Applications, PhD, Cardiff, 2013.

[157] M.J. Eaton, R. Pullin, and K.M. Holford, Acoustic emission source location in composite materials using Delta T Mapping, Composites: Part A vol. 43, pp. 856–863, 2012.

[158] Ahmad S.M. Al-Azzawi, L.F. Kawashita, and C.A. Featherston, Buckling and postbuckling behaviour of Glare laminates containing splices and doublers. Part 2: Numerical modelling, manuscript accepted for publication, Composite Structures, 2017.

[159] P. Linde, J. Pleitner, H. de Boer, and C. Carmone, Modelling and Simulation of Fibre Metal Laminates, presented at the ABAQUS Users' Conference, 2004

[160] P. Naghipour, K. Schulze, J. Hausmann, and M. Bartsch, Numerical and experimental investigation on lap shear fracture of Al/CFRP laminates, Composites Science and Technology vol. 72, pp. 1718–1724, 2012.

[161] L. Kawashita, A. Kinloch, D. Moore, and J. Williams, The influence of bond line thickness and peel arm thickness on adhesive fracture toughness of rubber toughened epoxyaluminium alloy laminates, International Journal of Adhesion & Adhesives, vol. 28, pp. 199-210, 2008.

[162] K.B. Katnam, A.D. Crocombe, H. Sugiman, H. Khoramishad, and I.A. Ashcroft, Static and fatigue failures of adhesively bonded laminate joints in moist environments, International Journal of Damage Mechanics, vol. 20, 2011.

[163] A. Seyed-Yaghoubi and B. Liaw, Experimental and numerical approaches on behavior of Glare 5 beams: Influences of thickness and stacking sequence, in Topics in Modal Analysis II, Volume 6: Proceedings of the 30th IMAC,, J. D. C. in: R. Allemang, C. Niezrecki, J. Blough (Eds.),, Ed., ed Springer New York, 2012, pp. 7-16.

[164] Cytec Engineering Materials, FM® 94 Adhesive Film Technical Data Sheet, Ed., 2010.

[165] M. Hagenbeek, Characterisation of Fibre Metal Laminates under Thermo-mechanical Loadings, PhD, Delft University of Technology, 2005.

[166] V. Rooijen, Bearing Strength Characteristics of Standard and Steel Reinforced GLARE, PhD, Delft University of Technology, Faculty of Aerospace Engineering, P.O. Box 5058, 2600 GB Delft, the Netherlands, 2006.

[167] DuPont. PFA Fluorocarbon lm properties bulletin (H-04321-4) [Online]. Available: http://www2:dupont:com/Teflon Industrial/en US/assets/downloads/h04321:pdf

[168] DuPont ®, Teflon Fluoropolymer resin properties handbook (H-37051-3), 2004.

[169] Dassault Systemes, Abaqus analysis user's manual version 6.12, 2012.

[170] Z. Hashin, Failure criteria for unidirectional fibre composites, ASME Journal of Applied Mechanics, vol. 47, pp. 329-334, 1980.

[171] Abaqus Analysis User's Manual, Dassault Systemes Corp., "Explicit dynamic analysis", 2012.

[172] Ahmad S.M. Al-Azzawi, J. McCrory, L. Kawashita, C. Featherston, R. Pullin, and K. Holford, Buckling and post-buckling behaviour of glare laminates containing splices and doublers. Part 1: Instrumented tests, manuscript accepted for publication, Composite Structures 2017.

[173] G. Mohamed, Modelling damage and fracture of fibre metal laminates subject to blast loading, PhD, Department of Mechanical Engineering, University of Sheffield, 2012.

[174] G.S. Makandar, N.K. Chhapkhane, and S.M. Sawant, Progressive failure analysis of compression-loaded composite flat panel with cutout, International Journal on Theoretical and Applied Research in Mechanical Engineering (IJTARME), vol. 3, pp. 2319-3182, 2014.

[175] R.D.S.G. Campilho, M.D. Banea, J.A.B.P. Neto, and L.F.M. da Silva, Modelling adhesive joints with cohesive zone models: effect of the cohesive law shape of the adhesive layer, International Journal of Adhesion & Adhesives, vol. 44, pp. 48–56, 2013.

[176] Wen-Guang Jiang, S.R. Hallett, B.G. Green, and M.R. Wisnom, Aconcise interface constitutive law for analysis of delamination and splitting in composite materials and its application to scaled notched tensile specimens, International Journal for Numerical methods in Engineering, vol. 69, pp. 1982-1995, 2007.

[177] M. Vesco and J. Sinke, Response and Damage Evolution in glare Laminates under Indentation Loads - Experimental Results, Delft University of Technology 2005.

[178] P. Camanho and S.R. Hallett, Composite Joints and Connections, Principles, Modelling and Testing: Woodhead Publishing limited, 2011.

[179] A. Amiri-Rad, M. Mashayekhi, F. P. Van der Meer, and H. Hadavinia, A two-scale damage model for high cycle fatigue delamination in laminated composites, Composite Science and Technology, vol. 120, pp. 32-38, 2015.

[180] H. Hadavinia, A.J. Kinloch, M.S.G. Little, and A.C. Taylor, The prediction of crack growth in bonded joints under cyclic-fatigue loading II. Analytical and finite element studies, International Journal of Adhesion and Adhesives, vol. 23, pp. 463-471, 2003.

[181] J. Miloš, K. Robert, D. Patrik, C. František, Š. Vladimír, and F. Holländer, Mechanisms of plastic deformation in AZ31 magnesium alloy investigated by acoustic emission and transmission electron microscopy, Materials Science and Engineering: A, vol. 462, pp. 311-315, 2007.

[182] A. Vinogradov, D. Orlov, A. Danyuk and Y. Estrin, Effect of grain size on the mechanisms of plastic deformation in wrought Mg-Zn-Zr alloy revealed by acoustic emission measurements, Acta Materialia, vol. 61, pp. 2044-2056, 2013.

[183] P.F. Liu, J.K. Chu, Y.L. Liu and J.Y. Zheng, A study on the failure mechanisms of carbon fiber/epoxy composite laminates using acoustic emission Materials & Design, vol. 37, pp. 228-235, 2012.

[184] X. Zhuang and X. Yan, Investigation of Damage Mechanisms in Self-Reinforced Polyethylene Composites by Acoustic Emission, Composites Science and Technology, vol. 66, pp. 444-449, 2006.

[185] Ahmad S.M. Al-Azzawi, L.F. Kawashita, and C.A. Featherston, A constitutive model for elastic-plastic behaviour and delamination damage in fibre metal laminates, Proceedings of the 25th UKACM Conference on Computational Mechanics, University of Birmingham, United Kingdom, 12 –13 April 2017.

[186] Ahmad S.M. Al-Azzawi, L.F. Kawashita, and C.A. Featherston, Modelling Fatigue Damage in Fibre Metal Laminate Adhesive Joints, accepted for presentation at 21st International Conference on composite Materials (ICCM-21), in Xi'an, China, 20-25 August 2017.

Appendix A - Sensitivity analysis

A.1 Sensitivity analysis for VUMAT fatigue code

A.1.1 Simplified model

The results of a study to determine the sensitivity of the mesh for the three element model used in Chapter 6: Section 6.6 shown in Figure A.1 are presented here. The analysis is based on a comparison of the traction-separation curves for cohesive elements predicted using the VUMAT subroutine based on the trapezoidal traction law for mode II under fatigue loading. As described previously, the simplified model incorporates three cohesive elements with a constant thickness of 0.01 mm and different element lengths namely 2 mm, 1.5 mm, 1 mm and 0.5 mm. Element 1 is subjected to a horizontal load or displacement representing the mode II damage failure mode whilst the other two elements are fixed in both the x and y-axes. The properties of the cohesive materials used are as given in Table 5.4.

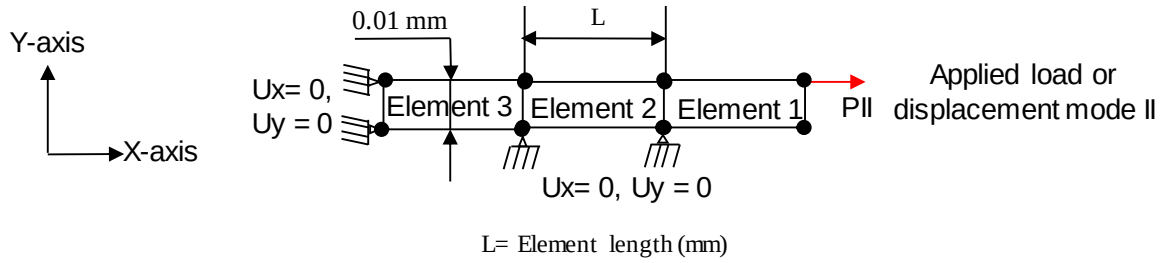

Figure A.1: Three element model(adapted from [185]).

A.1.2 Results and discussion

Figure A.2 shows traction-separation curves for the four different mesh sizes under fatigue with 80% severity using the pure mode II VUMAT code for this simplified three element model. Fatigue results are again presented only for element 1 since no damage occurs in elements 2 and 3 due to fixing the boundary conditions assigned to

them in order to simplify the analysis. The traction–separation curves plotted in Figure A.2 show identical behaviour for different sized meshes both in the purely elastic region and at the beginning of the static softening region before fatigue damage occurs. Following this fatigue damage starts at a user-defined start time (0.0015 s in this example) in the constant-stress region at a stress of 40 MPa leading to early degradation in stresses at a displacement of 0.0055 mm for mesh sizes 1mm and 0.5 mm and 0.006 mm for mesh size 1.5 mm whilst a cohesive element with mesh size 2 mm starts softening at a displacement of 0.01 mm. Elements with mesh sizes 0.5mm and 1 mm fail at a displacement of 0.011 mm under fatigue whilst the failure displacements are 0.012 mm and 0.014 mm for elements with mesh sizes 1.5 mm and 2 mm, respectively. An element size of 1mm is therefore chosen for use in the model to achieve the desired balance between accuracy and computational efficiency.

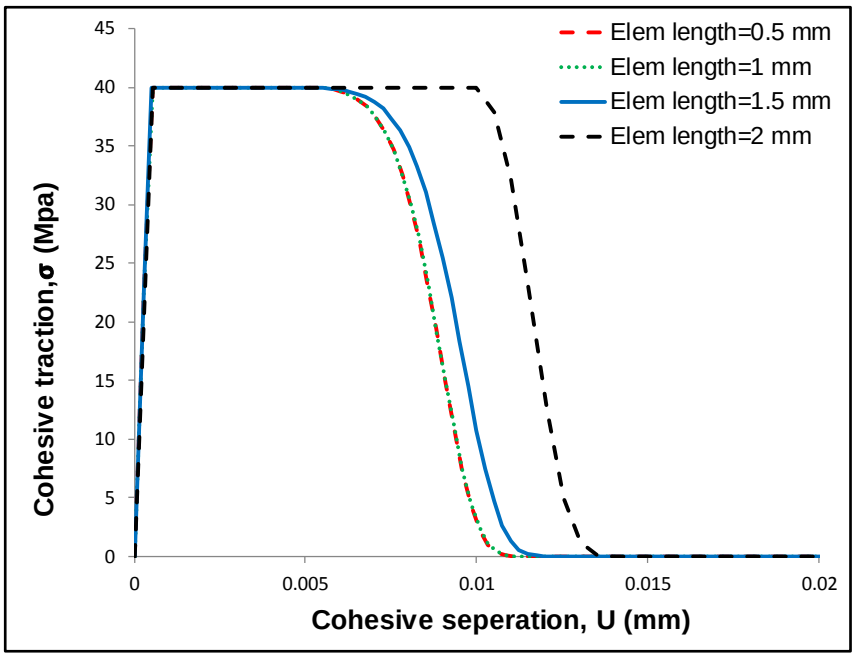

Figure A.2: Traction-separation curve for four different mesh sizes under fatigue 80% severity using pure mode II VUMAT code for simplified three element model.

A.2 Sensitivity analysis for buckling model

A.2.1 Far-field no defect specimen model

To examine mesh sensitivity in terms of its effect on models predicting buckling behaviour the far-field specimen described in Chapter 5: Section 5.2 shown in Figure A.3 was studied. The analysis in this appendix compares load versus in-plane displacement curves for far-field specimen models without defects but with different mesh densities. The far-field model incorporates three layers of aluminium and two layers of GFRP representing the Glare4B- 3/2 standard Glare specimen. Cohesive layers with a constant thickness of 0.01 mm are inserted at each metal-fibre interface. Further details in relation to material properties and element types can be found in Section 5.2. Different element lengths (2 mm, 1.5 mm, 1 mm and 0.5 mm) were chosen to mesh the continuum and cohesive layers.

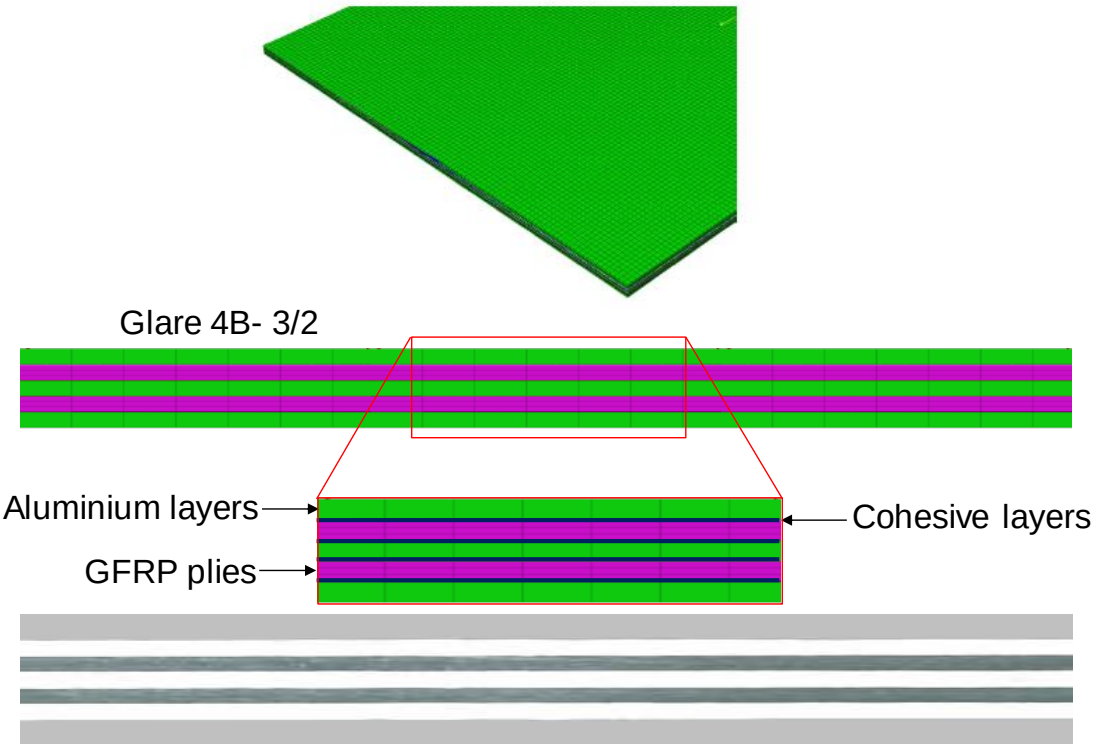

Figure A.3: Finite element mesh for far-field no defect specimen (top) based on optical scans of real specimens (bottom) (images resized for clarity, not to scale).

A.2.2 Results and discussion

Figure A.4 shows load versus in-plane displacement curves for the four different mesh sizes under compressive loading for the far-field no defect model. The buckling and postbuckling results in Figure A.4 show identical behaviour in the purely elastic region until buckling occurs. Following this, in the postbuckling region from approximately 7.5 kN axial load onwards, for mesh sizes 2 mm and 1.5 mm the load starts to be overestimated in comparison to the results obtained using a size of 1 mm. For both 1mm and 0.5 mm mesh sizes load versus in-plane displacement curves show similar behaviour, therefore a mesh size 1 mm was chosen as the optimum value.

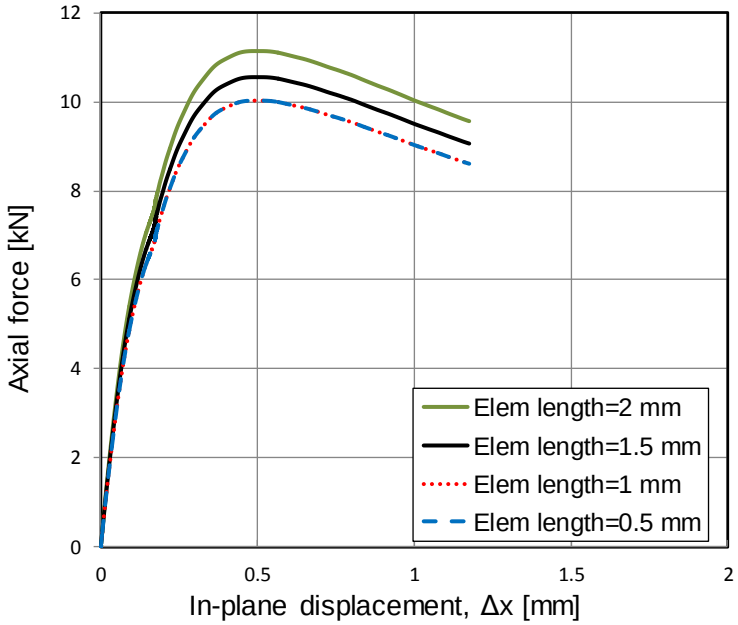

Figure A.4: Axial force versus in-plane displacement for far-field no defect specimen at four different mesh sizes under compression using buckling model.

A.3 Sensitivity analysis for imperfection

A.3.1 Splice with defect specimen model

To examine the effect of the amplitude of the geometric imperfections introduced the splice with defect specimen model described in Chapter 5 Section 5.2 was studied. The load versus in-plane displacement curves for different amplitudes of geometrical

imperfections (2 mm, 1.5 mm, 1 mm and 0.5 mm) were compared. In each case imperfections took the form of the first eigenmode.

A.3.2 Results and discussion

Figure A.5 shows load versus in-plane displacement curves for the four different imperfection amplitudes under compressive loading for the splice with defect model. The results show identical behaviour in the purely elastic region until buckling occurs for imperfection values 1 mm and 0.5 mm, however a reduction in buckling stiffness is noticed for imperfection values 2 mm and 1.5 mm. Following this, in the postbuckling region from a load of approximately 10.5 kN onwards, a reduction in postbuckling stiffness is predicted for amplitudes 2 mm and 1.5 mm compared with results for smaller imperfection values (1 mm and 0.5 mm) although the results converge again further into the postbuckling region. An imperfection amplitude of 1mm was therefore used throughout the thesis which is in agreement with the value measured for the specimens tested.

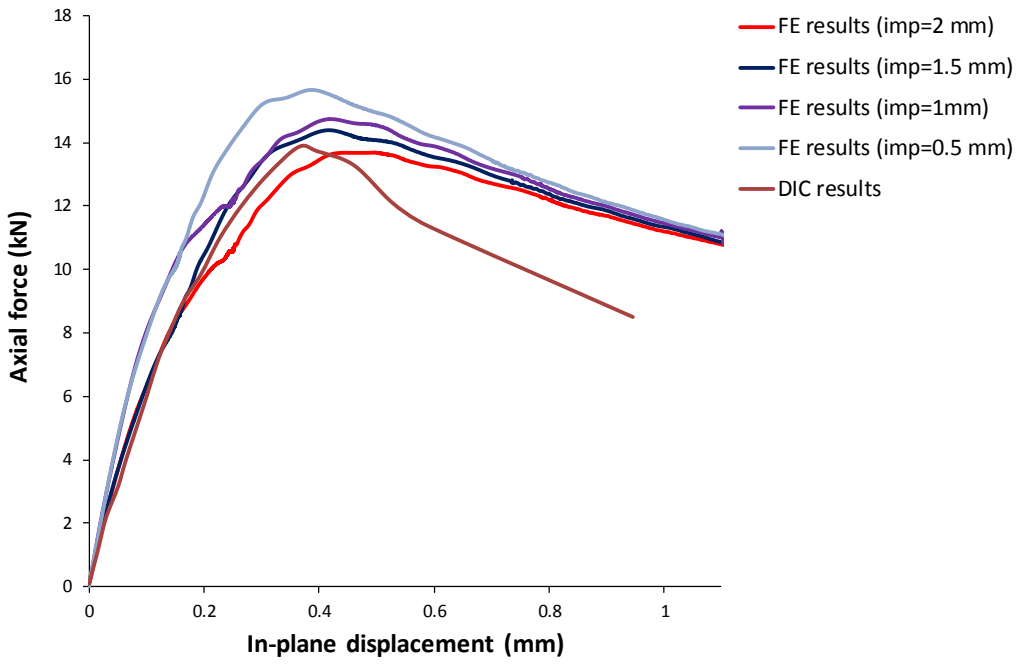

Figure A.5: Axial force versus in-plane displacement for splice with defect specimen at four different geometrical imperfection values under compression load.

Appendix B - Quasi-Static Experiments

B.1 Introduction

The progressive damage and fracture behaviour of Glare® fibre-metal laminates (FMLs) containing adhesive joints (splices and doublers) was investigated experimentally. A series of specimens of both types were tested under quasi-static tensile loads. Tests were monitored using digital image correlation (DIC) for visualisation of three-dimensional full-field displacements whilst acoustic emission (AE) monitoring enabled the detection of damage events. Large numbers of AE events were recorded at the splice and doubler joints during elastic and elastic-plastic regimes, suggesting that the AE techniques used is suitable for the monitoring of matrix cracks in addition to delaminations initiation and growth in the internal features in Glare® laminates. Finally, good correlation was observed between the fibre breakage and a rapid increase in cumulative AE energy, demonstrating that as well as indicating interlaminar damage, AE monitoring is able to indicate quite clearly when the bulk material damage was occurred.

B.2 Test setup

A Zwick / Roell servo-hydraulic testing machine (maximum force 100 kN) was used for quasi-static tensile tests as shown in Figure B.1. Tests were conducted on a series of specimens made of Glare® 4B included two features (splices and doublers). A displacement control load was applied at a rate of 0.001 mm/s. Specimens measuring (153 mm × 13.5 mm) were manufactured in-house, incorporating splice and doubler features as shown in Figure B.2. They consisted of 0.4 mm thick sheets of aluminium alloy 2024-T3 and Cytec™ S2-glass/FM94 glass fibre reinforced polymer (GFRP) unidirectional prepreg with a lay-up corresponding to the specification for Glare® 4B[1].

Each GFRP 'layer' had 3 plies with the layup [90°/0°/90°] and a cured ply thickness of 0.133 mm. The layup one side of the joint was '3/2' (three layers of aluminium and two layers of GFRP prepreg) and on the other '4/3' (four layers of aluminium and three layers of prepreg). Static tests were monitored using DIC to derive accurate measurements of the in-plane displacement. The DIC system and set-up were as described in Chapter 3.

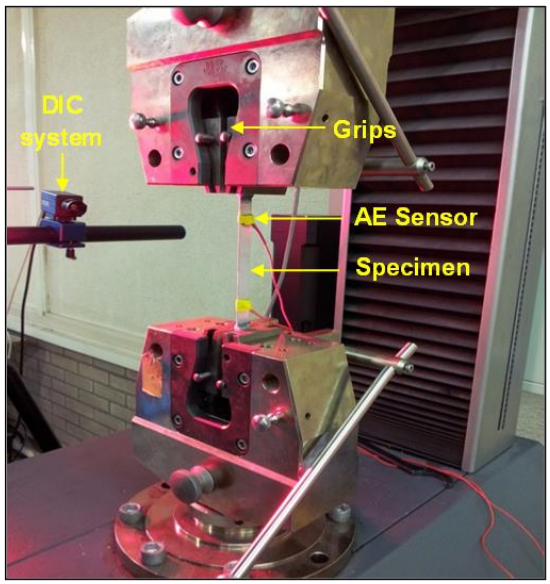

Figure B.1: Experimental quasi-static test set-up.

Two Nano-30 Acoustic Emission (AE) sensors were mounted on the specimens to monitor damage events during static tests. These sensors; supplied by Mistras Group™ have a mid-band frequency range of 125-750 kHz. They were chosen due to their small size (8mm diameter) they could easily be mounted on the relatively small surfaces of the specimen available. In addition to this practical consideration, the Nano-30 AE sensor has a resonant response up to 300 kHz and a good frequency response making it suitable for monitoring the signals expected. They were bonded to the specimens using multi-purpose silicone sealant *Loctite*™ 595. They were then connected to Mistras Group™ pre-amplifiers with a 40 dB gain and a built-in band-pass filter of 20-1200 kHz. The pre-amps were in turn connected to a Mistras Group™ PCI2 acquisition unit. The detection settings were 45 dB threshold, sampling rate

5 MHz (as recommended by previous studies including Al-jumaili [134] and Pearson [156]). Located signals between the sensors were detected using the traditional AE analysis technique (a detailed description of this method is given by Miller [148]) (the improved Delta-T location technique cannot be applied in this case as it requires the use of three sensors [69].)

B.3 Results and discussion

B.3.1 Doubler specimen

The first experiments were quasi static tensile tests in order to get ultimate tensile strength for Glare4B doubler specimens. These results for three specimens (presented in Section 7.4), showed that average ultimate tensile load for doubler specimens is 12.52 kN. Experimental results for the axial displacement (presented in Section 7.4) exhibit a good representation of deboning between discontinuous aluminium layer and resin pocket in the doubler joint as reduction in displacement occurs at load 10.63 kN for all tested specimens. Then at load 10.59 kN delamination onset observed followed by delamination quick growth then at load 9.25 kN fibre breakage noticed from test visualisation in the discontinues GFRP layers (curved cross section), afterwards delamination propagated consciously up to another fibre breakage at load 12.52 kN.

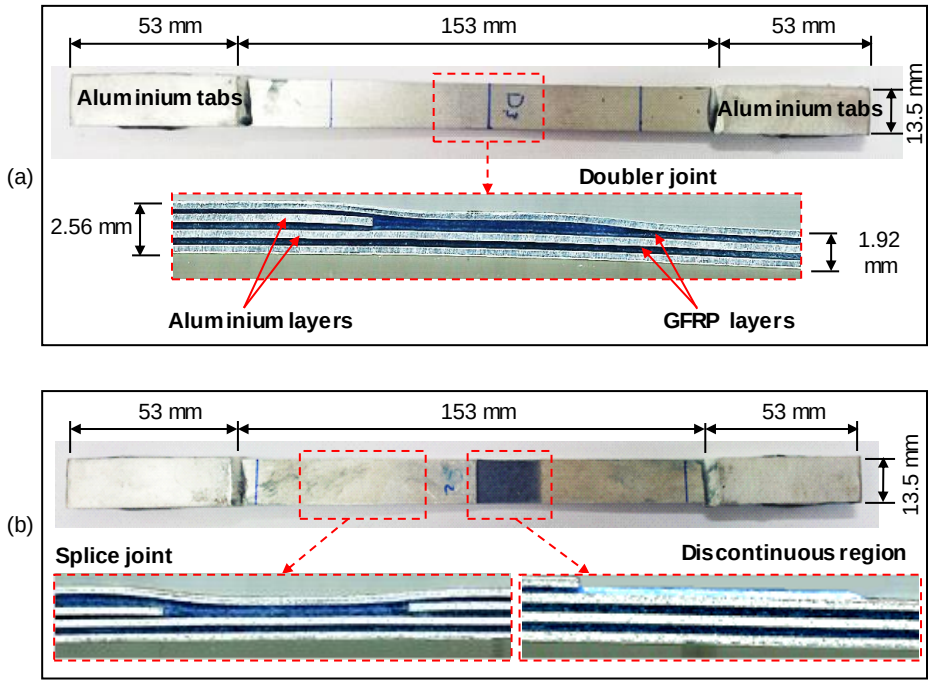

Figure B.2: Specimen design for (a) doubler (b) splice (images resized for clarity, not to scale)(after [186]).

These results were confirmed using in-plane DIC results (presented in Section 7.4). DIC results for the in-plane displacements exhibit good representation of debonding as reduction in displacements at average load 10.63 kN for the three specimens, Then at load 10.59 kN delaminations onset occurs followed by delaminations quick growth accompanied with drop in axial loads down to 9.25 kN which is mostly fibre breakage noticed near doubler joint in the top discontinues GFRP plies (curved cross stion). Afterwards delamination propagated consciously with axial load increasing subsequently up to another fibre breakage at peak load.

Experimental observation for the damage behaviour of Glare 4B laminate with doubler joint was confirmed by Acoustic Emission (AE) results through cumulative energy and load versus time curve (Figure B.3). AE results show a gradual increase in elastic energy at time period (0-4,000 s) mostly due to matrix cracks followed by deboning between discontinued aluminium layer and resin pocket in the doubler joint at time period (4,500-5,000 s) as observed in the experiments. This was followed by a jump in energy during time period (5,200-5,500 s) mostly due to fibre breakage. A gradual

increase in cumulative energy accompanied by rapid increase in axial load was observed at time period (5,500-8,000 s) is likely as a result of delamination initiation and growth in the aluminium /fibre interfaces. Then a large jump in energy was noticed at time (8,200 s) which could be due to fibre breakage in the discontinues fibre layers near doubler joint .Finally cumulative energy remain constant when the aluminium layers plastically deformed up to the final failure of aluminium which is not considered in this study.

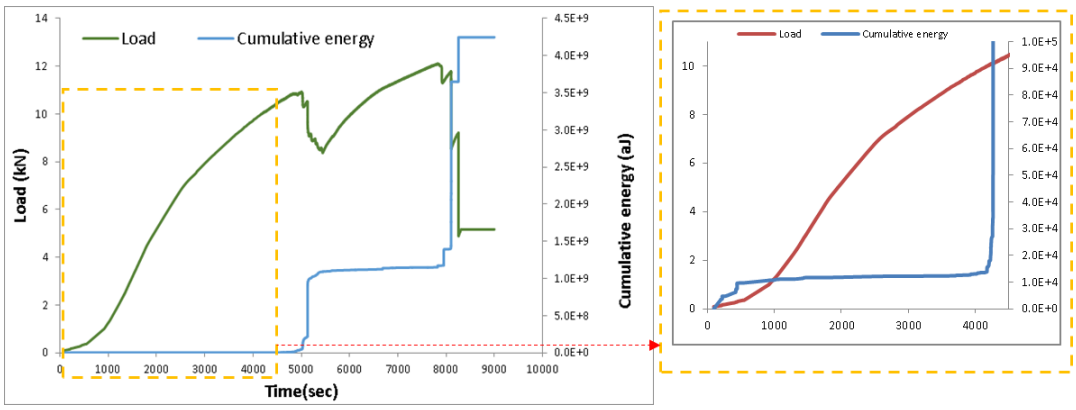

Figure B.3: Load and cumulative AE energy versus time for the doubler specimen.

B.3.2 Splice specimen

Quasi static tensile tests were conducted in order to obtain ultimate tensile strength for Glare4B splice specimens. Experimental results from both Zwick / Roell machine and DIC system (presented in Section 7.4), show that the average ultimate tensile load for splice specimens is 9.47 kN which can be used later to calculate maximum fatigue load. Also the in-plane displacement results exhibited good representation of delaminations initiation and growth in the aluminium/GFRP interfaces of the discontinuous regions in splice specimens as reduction in displacements at average load 7.4 kN for all tested specimens, respectively. Then at average load of 8.6 kN, delaminations onset and growth in the splice joints occurred in the three specimens. This was followed by fibre breakages in the splice joint at average ultimate load 9.47 kN for all tested specimens, respectively. Finally loads were slightly increased due

to plastic deformation in aluminium layers and remain constant at average load 4.2 kN up to final failure by aluminium layers breaks as noticed through experimental tests. However, as aluminium breaks take long time of test life so the test was terminated. Experimental observation for the damage behaviour of Glare 4B laminate with splice joint was confirmed by AE cumulative energy and load versus time results (Figure B.4) which shows a small increase in energy at time period (0 -880 s) mostly due to matrix cracks followed by a small jumps in cumulative energy mostly caused by delamination initiation between discontinuous outer Aluminium layer and the discontinuous two GFRP plies. This is followed by a stepped increase in energy at time period (1150-1600 s) delamination propagation between discontinuous outer Aluminium layer and discontinuous GFRP plies. This was followed by a gradual increase in energy starts at time (2000 s) accompanied by a small drop in axial load which mostly due to delamination in splice joint. This was followed by a high jump in cumulative energy with a big drops in axial load at time about (2300 s) mostly caused by fibre breakage in splice joint. Consequentially energy remains constant and load increased gradually at time period about (2300-3250 s).This was followed by another jump in energy with a high drop in load down to 3.42 kN mostly as a results of fibre breakage and delamination growth in other aluminium/GFRP interfaces as observed during tests. Finally cumulative energy continued to be constant while load is slightly recovered up to 4.36 kN and then remain constant as a result of plastic deformation in aluminium layers up to final failure of aluminium layers. Aluminium breaks is not recorded as this stage takes long time which is expensive in terms of AE recording and also out of scope for this study.

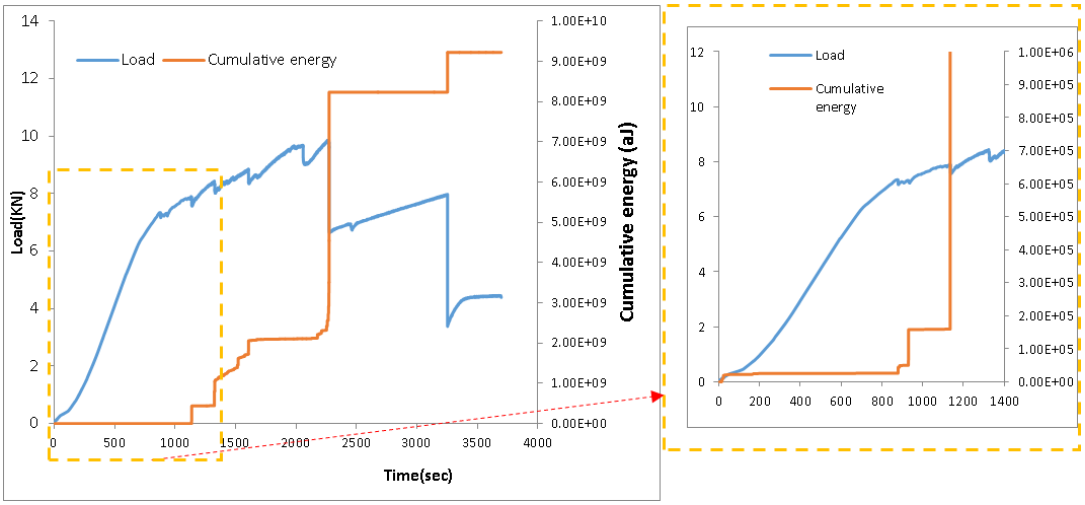

Figure B.4: Load and cumulative AE energy versus time for the splice specimen.